Forschungszentrum Karlsruhe
in der Helmholtz-Gemeinschaft

Wissenschaftliche Berichte

FZKA 7520

Fluid Dynamic Design of Complex Mixing Chambers

A. Wank

Institut für Kern- und Energietechnik

Oktober 2009

Forschungszentrum Karlsruhe

in der Helmholtz-Gemeinschaft

Wissenschaftliche Berichte

FZKA 7520

Fluid Dynamic Design of Complex Mixing Chambers

Alexander Wank

Institut für Kern- und Energietechnik

Von der Fakultät für Maschinenbau der Universität Karlsruhe (TH)
genehmigte Dissertation

Forschungszentrum Karlsruhe GmbH, Karlsruhe

2009

Forschungszentrum Karlsruhe GmbH
Postfach 3640, 76021 Karlsruhe

Mitglied der Hermann von Helmholtz-Gemeinschaft
Deutscher Forschungszentren (HGF)

ISSN 0947-8620

urn:nbn:de:0005-075206

Fluid Dynamic Design of Complex Mixing Chambers

Zur Erlangung des akademischen Grades eines

Doktors der Ingenieurwissenschaften

der Fakultät für Maschinenbau der Universität Karlsruhe (TH)

genehmigte

Dissertation

von

Dipl. Ing. Alexander Wank

aus Reutlingen

Tag der mündlichen Prüfung:	12.10.2009
Vorsitzender:	Prof. Dr.-Ing. H.-J. Bauer
Hauptreferent:	Prof. Dr.-Ing. T. Schulenberg
Korreferent:	o. Prof. Prof. e.h. Dr.-Ing. habil. H. Oertel

Vorwort:

Die vorliegende Arbeit entstand während meiner Tätigkeit als wissenschaftlicher Mitarbeiter am Institut für Kern und Energietechnik (IKET) des Forschungszentrums Karlsruhe GmbH.

Herrn Prof. Dr.-Ing. T. Schulenberg, Leiter des Instituts für Kern und Energietechnik (IKET) des Forschungszentrums Karlsruhe GmbH und Hauptreferent dieser Arbeit gilt mein herzlichster Dank. Sein persönlicher Einsatz, die stets vorhandene Unterstützung und Diskussionsbereitschaft sowie die sehr persönliche Betreuung haben in außerordentlichem Maß zum Gelingen dieser Arbeit beigetragen.

Dem Leiter des Instituts für Strömungslehre (ISL) der Universität Karlsruhe (TH), Herrn Prof. Dr.-Ing. H. Oertel danke ich besonders für die Übernahme des Koreferats dieser Arbeit, sein großes Interesse und die verschiedenen anregenden Diskussionen.

Für die fachliche Unterstützung sowie die persönliche Förderung danke ich meinem Gruppenleiter Dr.-Ing. J. Starflinger. Außerdem möchte ich mich bei den Mitarbeitern des Instituts, besonders bei Herrn Prof. Dr.-Ing. habil. A. Class und Herrn Dr.-Ing. Grötzbach für die wertvollen Ratschläge, die ermutigenden Worte und die fachliche Betreuung bedanken.

Allen Kollegen, Studien- und Diplomarbeitern danke ich für ihre Hilfsbereitschaft, das hervorragende Arbeitsklima und ihren Einsatz. Besonderer Dank gilt Herrn Dr.-Ing. B. Vogt, Herrn Dr.-Ing. K. Fischer sowie Herrn Dipl.-Ing. C. Pfeifer und Herrn Dipl.-Ing. C. Bruzzese für ihre Unterstützung und die vielen anregenden Diskussionen. Speziell danke ich auch meinem langjährigen Mitbewohner, Kollegen und guten Freund Herrn Dipl.-Ing. C. Haasi.

Ganz besonders herzlich danke ich meiner Familie für ihre uneingeschränkte Unterstützung, Hilfe und Motivation während meiner gesamten Ausbildungszeit sowie meinen ehemaligen Gasteltern Carol und Bob Decker, die geduldig die erste Version probegelesen haben. Schließlich danke ich von ganzem Herzen meiner Frau Tati für die tatkräftige Unterstützung, die gute Teamarbeit in allen Bereichen und ihre Liebe.

Karlsruhe, im Oktober 2009 Alexander Wank

Kurzfassung:

Strömungsmechanische Auslegung komplexer Mischkammern

Ein Ansatz für die Simulation von komplexen Mischkammern mit vergleichbar geringem numerischem Aufwand ist ein interessantes Werkzeug für Auslegungsprozesse von Mischkammern sowie von andern komplexen Geometrien in Strömungen. Vor allem in Designprozessen müssen oft mehrere Simulationen einer Geometrie durchgeführt werden um optimale Anordnungen zu entwickeln. Aus diesem Grund sind Methoden, die zwar alle Einflüsse einer komplexen Geometrie auf die Strömung berücksichtigen, den numerischen Aufwand aber drastisch reduzieren von großem Interesse. In dieser Arbeit wird ein Ansatz vorgestellt, in dem die, die Strömung beeinflussende Geometrie nicht detailliert aufgelöst wird, ihr Einfluss auf die Strömung aber erhalten bleibt. In der so genannten Vereinfachungsmethode kommen Quellterme in den Strömungsmechanischen Gleichungen zum Einsatz. Diese Quellterme repräsentieren die nicht berücksichtigten Geometrieelemente in heutzutage standardisierten CFD Simulationen. Als Anwendung für die Vereinfachungsmethode wurde die obere Mischkammer des High Performance Light Water Reactor (HPLWR) ausgewählt. Anhand der komplexen Geometrie der Mischkammer wurde die verwendete Methode ausgearbeitet. In der oberen Mischkammer werden verschiedene Einlassströme unterschiedlicher Temperatur vermischt. Ziel ist dabei eine gute Homogenisierung der Temperatur um eine Weitergabe heißer Strähnen in eine folgende Aufheizungsstufe zu vermeiden. Eine weitere Herausforderung bei der Berechnung der Vermischung resultiert daraus, dass überkritisches Wasser nahe dem Pseudokritischen Punkts vermischt werden soll. Die besonders starken Änderungen in den relevanten Stoffeigenschaften müssen in das Modell integriert werden um mögliche temperaturabhängige Effekte, wie z.B. Auftrieb zu berücksichtigen. Beide Herausforderungen, das Abbilden der komplexen Geometrie sowie die Berücksichtigung temperaturabhängiger Effekte werden unabhängig voneinander angegangen. Das Anwenden der Vereinfachungsmethode auf die obere Mischkammer führt zu einem vereinfachten Modell, das jedoch die globale Strömungsstruktur in der Mischkammer wiedergibt. Das vereinfachte Modell wird dann optimiert und erst im Anschluss werden die Vereinfachungen mit Quelltermen ins Modell integriert. Zur Bestimmung der erforderlichen Quellterme wurden einfache Handrechnungen auf Basis des Impulssatzes sowie Druckverlustkorrelationen verwendet. Die erhaltenen Ergebnisse wurden dann mit einer Simulation eines Detailausschnitts der oberen Mischkammer, in dem alle geometrischen Details aufgelöst wurden, validiert. Für die Berücksichtigung temperaturabhängiger Effekte wurden Funktionen für die relevanten Stoffeigenschaften in das Modell aufgenommen. Obwohl Auftriebseffekte keine dominante Rolle spielen, hat die Berücksichtigung der variablen Stoffeigenschaften doch einen Einfluss auf die Strömung und die Vermischung. Gesamtergebnisse, die sowohl die abgebildete komplexe Geometrie als auch temperaturabhängige Effekte enthalten wurden für das Referenzdesign sowie für ein optimiertes Design erzeugt.

Die vorgestellten Methoden, die für die Optimierung der oberen Mischkammer verwendet wurden, sind grundsätzlich für jede andere Mischkammer oder komplexe Geometrie in einer Strömung anwendbar.

Abstract:

Fluid Dynamic Design of Complex Mixing Chambers

An approach to simulate complex mixing chambers with comparably little numerical effort is introduced, which makes this approach an interesting tool for design processes of mixing chambers and also to some extent for other systems with complex geometries. Especially in design processes, where various simulations under the same constraints are necessary to find optimal configurations, methods reducing the numerical effort, while still capturing the dominant influences on the flow are interesting. In this work, a method has been developed, with which complex geometrical structures in a flow are not resolved in detail, while still including their effects. This so-called simplification method uses source terms in the equations describing the flow and thus accounts for disregarded geometric details in state of the art CFD simulations. As an exemplary application of the simplification method, the very complex upper mixing chamber of the High Performance Light Water Reactor (HPLWR) has been used and the method has been developed with the given geometry of this rather complex mixing chamber. In the upper mixing chamber, different inlet flows with different temperatures are mixed to achieve a good temperature homogenization of all inlet flows. Thus, the propagation of hot streaks to a following heat-up section is avoided. The fact that the upper mixing chamber shall mix water, at supercritical conditions close to the pseudo critical point leads to an additional challenge, which is the consideration of the very large gradients that occur in the fluid properties. They have to be introduced into the applied models to be able to analyze temperature dependant effects, such as buoyancy. Both challenges, the reproduction of the complex geometry and the introduction of the temperature dependant effects into the model are tackled independently. Applying the simplification method to the upper mixing chamber leads to a much more simplified model, which to some extent still resembles the global flow structure in the mixing chamber. This simplified model is then optimized, before the effects of the simplifications are introduced by source terms. To derive the necessary source terms, simple hand calculations based on the integral balance of momentum as well as on pressure drop correlations are used. The obtained results are validated with simulations of a detailed cut-out model of the upper mixing chamber, in which all geometric entities are included. To account for temperature dependant effects in the flow, functions describing the strong changes in the different fluid properties are included into the model. Even though buoyancy effects do not play a dominant role, temperature dependant effects still have some visible influences on the flow field in the upper mixing chamber and therefore on the mixing. Integrated results containing both, the influences of the complex geometry and the consideration of temperature dependant effects are presented for the reference case and the optimized case of the upper mixing chamber.

The methods to optimize the upper mixing chamber should be generally applicable to any other mixing chamber or flow in or around complex geometries.

TABLE OF CONTENTS

TABLE OF CONTENTS - DETAILED

1 Introduction

Complex mixing chambers with different functions are found in many industries. Examples include the mixing of chemical components in the chemical or petrol industry, processes in the metallurgy, and many others. In the sector of power production, mixing to reduce temperature peaks in flows, e.g. to ensure sufficient cooling of components and surfaces sometimes also requires very complex mixing chambers.

In this work, a method to optimize the mixing of water at supercritical pressure in the very complex upper mixing chamber of the High Performance Light Water Reactor (HPLWR), which is a new concept of light water reactors, is developed and applied. The basic principle of this method should be generally applicable for complex mixing chambers or complex internal flows. In the upper mixing chamber, different inlet flows with different temperatures are mixed to achieve a good temperature homogenization of all inlet flows and thus the propagation of hot streaks to the following heat-up section is avoided. This temperature homogenization is a crucial aspect of the feasibility of the HPLWR, which makes the upper mixing chamber an important part within the reactor design.

Two main aspects are discussed and ways to model them are presented in this work. The challenge of reproducing the very complex structures and their influences on the flow and therefore on the mixing is the leading subject. Also, it is expected that the presented solution of this problem will find broader application in different fields. Another challenge is the consideration of the distinctive aspects occurring when analyzing water at supercritical pressures. Here, very large gradients occur in the fluid properties that have to be introduced into the applied models.

1.1 Fluid Mixing in Complex Systems – Concepts and Modeling

Mixing systems can be classified in different ways. According to the book of Kraume [38] and the book of Schubert [67], mixers can be divided in continuous and discontinuous mixing systems. While in continuous mixers a constant stream from the inlet to the outlet side is found, discontinuous mixers are loaded with batches. Here the mixing process can be divided into different steps like filling, mixing, and emptying. Another classification for mixing applications is the division in static and dynamic mixers. While either internals or the whole chamber is moving in dynamic mixers, no moving parts are found in static or motionless mixers and the mixing is a result of the energy introduced into the system by the flow field. All static mixers are by definition continuous mixers. Here the flow usually passes through the mixing volume and the mixing is enhanced with included passive / non moving internals. Also, mixer systems can be characterized by the components which have to be mixed. Mixer systems differ strongly weather solid substances or fluids are mixed. In this work, only static mixers for one single phase fluid are analyzed.

For static or motionless mixers, different methods of operation can be found. The ones working with, what sometimes is referred to as “free turbulence”, consist of alignments where jets interact with each other or a global swirl is imposed. A typical alignment is presented in the

catalog by Pfaudler in [59]. Other mixers mainly use the effects of flow separation and changes in the flow direction. Common design features include many of the same passive elements introduced into the flow one after the other to change the flow direction significantly in each step. An overview of different motionless mixers is delivered in [56]. The evaluation of the achieved mixing quality in a mixture is often described with the statistical deviation of samples around a mean value as described in detail in the book of Oldshue [55].

Difficulties arise in the designing and dimensioning of complex mixer systems. For comparable small mixing systems or mixers with a limited complexity, numerical simulations are the state of the art in industrial design processes as described in the paper by Arimond and Ervin [1]. Essential advances in the simulation of static mixers are presented by Hobbs and Muzzio in [28] and another, more recent example for the numerical simulation of the flow in mixing applications is given by Visser et al. in [80]. Here it is shown that the periodically repeating structure of the mixer is used and only a small section of the complex geometry is modeled, thus simplifying the task significantly. Similar approaches using the periodically repeating structure of the analyzed mixing systems are found in [37] and a more recent analysis in [61]. Good results have been obtained by Bertolotto et al., who have compared their simulation results to experiments carried out for a double T-junction in [6]. In their setup, it can be seen that already for a small and rather simple geometry, a very large number of numerical meshes are necessary and therefore the numerical effort is very high. Another recently published, promising approach that delivers good results, while reducing the numerical effort, is presented in [70]. However, all presented studies have only been successful for small structures or structures for which it is possible to extract a small, representative geometry.

On the other hand, for many large and highly complex mixers, numerical simulations often lead to a very large numerical effort and are not feasible within satisfactory time limits, which play an important role, especially in design processes. Therefore, the design of many mixing systems in industrial use today is based on empirical data as described for example by [59], in which the design process of the Pfaudler Werke GmbH is briefly summarized for one mixer type. An overview of the application and the design process of static mixers is given in [57]. Here, also the empirical design process and the different design criteria are summed up exemplarily. The interest in efficient simulation methods describing complex mixing elements or just any complex flow structures was also affirmed by the industry (among others by Bürkert [10] and Pfaudler [58]). Especially interesting are methods applicable in design processes, where many simulations are necessary to develop optimized structures.

In this work, an approach to simulate complex mixing chambers with comparably little numerical effort is introduced, which makes this approach an useful tool for design processes of mixing chambers and also to some extent other systems with complex flow geometries. As application of the method, the upper mixing chamber of the HPLWR, which is explained in detail in the following chapter, has been defined. Being a nuclear reactor system, the reliability of the mixing chamber at all times is crucial, therefore moving parts are not permitted. This avoids additional maintenance and control of the system. The upper mixing chamber, which is explained in more detail in chapter 1.4, is an example for a very complex static mixing chamber.

1.2 High Performance Light Water Reactor – HPLWR

The High Performance Light Water Reactor HPLWR is a new concept of light water reactors, cooled and moderated with supercritical steam. It is currently developed as one of the Generation IV advanced nuclear systems according to the generation IV technology roadmap [78]. The idea was to develop a system, which is based on well established Light Water Reactor (LWR) concepts, but is more efficient and leads to further improvement in an economical point of view. Oka has presented a review of water cooled reactors with supercritical pressures in [54]. A first conceptual design of such a reactor has been proposed by Dobashi et al. in [16]. An improved core design has been presented by Yamaji et al. in [87] and in [88].

The key advantages of the HPLWR concept are the use of a single phase fluid in the core, which avoids steam separators and dryers, a direct once through steam cycle, and the support by the long term experience of supercritical steam cycles for fossil fired power plants. Also, a high thermal efficiency of around 44% shall be enabled, as summarized by Squarer et al in [72].

The capital costs of a Super-Critical Light Water Reactor (SCWR) system, such as the HPLWR, can be reduced significantly in comparison with today's nuclear power plants. Reasons for the competitive economical advantage of these systems are the very compact reactor, a smaller pressure vessel leading to a smaller containment and therefore a smaller reactor building. Other components used in today's LWRs, like steam separators, steam dryers, and steam generators can be omitted in this design. Bittermann et al. [7] estimated the very low construction costs in the vicinity of 1000€ per kW_e and also expected very low electricity production costs in the range of 3 to 4 cents per kWh.

At supercritical pressure conditions of around 25 MPa, liquid water shall enter the core at a temperature of 280°C and exit as superheated steam of around 500°C. For comparison, the HPLWR steam cycle as proposed by Bittermann et al. in [8] and a reference LWR steam cycle are shown in the temperature-entropy (T-s) diagram in Fig. 1-1. It can be seen that the temperature in the reactor of the HPLWR stays above the two-phase region throughout the entire heat up and the area surrounded by the curve describing the steam cycle is much larger than for the LWR reference design, explaining the higher thermal efficiency.

Using supercritical steam in the reactor leads to challenges due to the very high pressures and temperatures. Important aspects are the testing and development of eligible materials, e.g. concerning corrosion behavior, as well as the investigation of heat transfer deterioration under supercritical conditions. In addition a plant design has to be developed, components within the HPLWR steam cycle have to be designed and dimensioned, safety systems have to be planed and analyzed, and a reactor pressure vessel with all its internals has to be designed. While Schulenberg and Starflinger have described different core design concepts in [69], the design of the core for the HPLWR presented by Fischer et al. in [20] shall be explained in more detail, since all analyses presented in this work are based on this design.

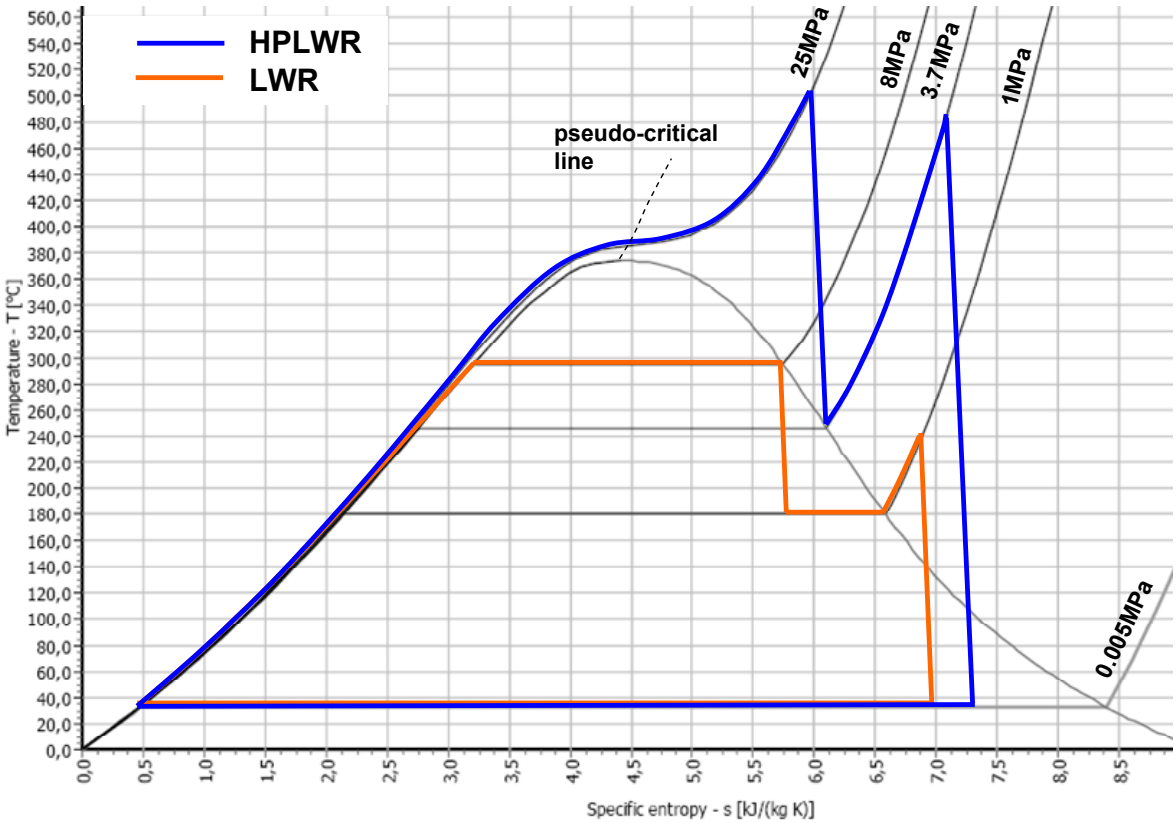

Fig. 1-1 The HPLWR steam cycle and a reference LWR steam cycle in the T-s diagram

Water above the critical pressure is called supercritical. It is a single phase fluid with liquid like properties at low temperatures and steam like properties at high temperatures. The critical point of water is found at the critical temperature $T_C = 374°C$ and the critical pressure $p_C = 22.1MPa$. A pseudo-critical line can be defined by the peak values of the specific heat, called the pseudo-critical points, at a given pressure. Along this line, the gradients of the fluid properties, the viscosity, conductivity and density are very strong.

The modeling of the changes in the fluid properties due to temperature changes in the upper mixing chamber of the HPLWR is presented in chapter 6 (Analysis of Temperature Depending Effects). Here, also the influences on the flow and therefore on the mixing of such effects are discussed.

1.3 Three Pass Core Design

The enthalpy rise of the cooling water from core inlet to outlet is almost 2000kJ/kg, thus exceeding the enthalpy rise of pressurized water reactors by a factor of 8. This large enthalpy rise leads to concerns for the hottest sub-channel in the core. It is assumed that the worst case hot channel experiences a larger enthalpy rise than a nominal subchannel due to several, so called hot channel factors, as described by Strauß in [73], containing certain statistical uncertainties instead of absolute tolerances. First predictions with thermal-hydraulic analyses by Schulenberg et al. [68] were assuming the following hot channel factors:

1) A radial form factor, considering differences in the power distribution and in the mass flux distribution in the core.

2) A local peaking factor, regarding similar differences not in the entire core, but within each fuel assembly cluster.

The differences taken into account by these two hot channel factors arise due to differences in the fuel composition and distribution, in the water density distribution, in the size and distribution of subchannels, in neutron leakage, and differences due to burn up effects. They also take into account differences in the positions of the control rods and differences arising due to the usage of burnable poisons. Additional factors are:

3) An uncertainty factor including all statistical uncertainties regarding the core design.

This factor includes all uncertainties concerning materials, fluid properties, neutron physical and thermohydraulical modeling, manufacturing tolerances, deformations, differences in the inlet temperature distribution, as well as measurement uncertainties of the installed measurement systems.

4) A factor regards concessions in the plant operation, like power, flow, and pressure control, as well as small transients during operation.

If these hot channel factors are multiplied, a total hot channel factor of 2.0 is obtained. The total hot channel factor should be multiplied with the enthalpy rise of a nominal sub-channel to model the hottest sub-channel under worst case conditions. Cladding materials available today suggest that a maximum cladding temperature of 620°C should not be exceeded. Considering this hot channel factor and the maximum cladding temperature, the high core outlet temperature can only be achieved with a stepwise heat up, e.g. in three stages, and with intermediate mixing to avoid hot streaks.

Each of the three heating stages of the coolant includes 52 assembly clusters. In the central part of the core, the first stage is situated, the so-called evaporator, which has upward flow. Another 52 assembly clusters with downward flow acting as a first superheater are arranged around the evaporator. The second and final superheater, again with upward flow, also made of 52 assembly clusters is situated at the outer periphery of the core. This way, superheater II, which has the highest coolant temperatures, is at the periphery of the core, where the neutron flux and therefore the pin power are lowest. Between the evaporator and the superheater I, the flow is mixed in the upper mixing chamber and between the two superheaters, in the lower mixing chamber. The concept of this three pass core and the actual cluster arrangement in the cross section of a quarter of the core are depicted in Fig. 1-2.

Certain fuels in nuclear reactors, like uranium with a certain amount of $^{235}_{92}U$, require neutrons with energy below 1keV to sustain the chain reaction, since the fission probability for these neutrons is much higher. These neutrons are called thermal neutrons, because their kinetic energy is in the range of the energy due to the thermal molecular motion within the material of the reactor. The neutrons produced by fission have an average kinetic energy of 2MeV, which means that these fast neutrons have to be decelerated for the continuous chain reaction

in the reactor as explained by Smidt in [71] and in the books of Todreas [75] and [76]. The deceleration is accomplished with so-called moderators, in which the neutron dispenses its energy due to elastic collisions with the nucleuses of the moderator material. In the HPLWR, which is designed as a thermal reactor, water should be used as moderator, which has the advantage that the chain reaction decreases if the density is reduced with increasing temperature. This leads to additional safety, since the core switches off automatically if the temperature becomes too high.

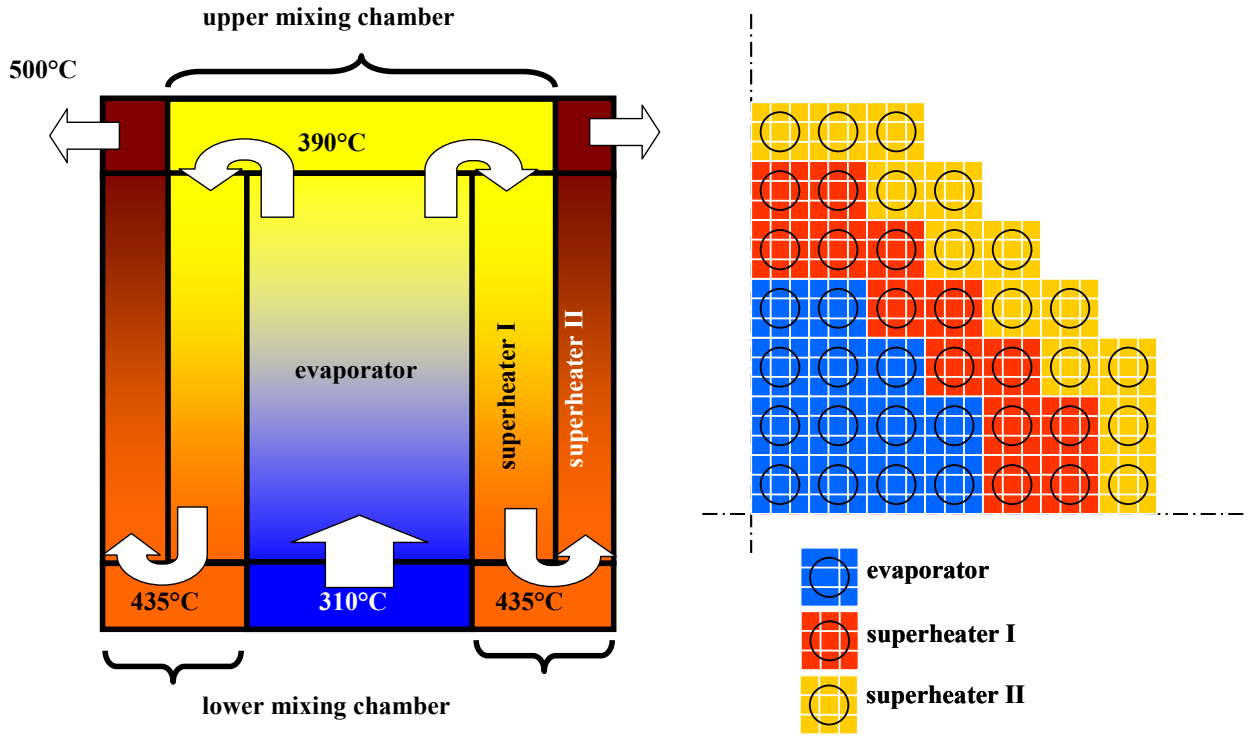

Fig. 1-2 Concept of the HPLWR three pass core with three different heat up steps as proposed in [68]

In the HPLWR, the density ratio between the core outlet steam and the inlet feed water is very high exceeding a factor of eight, which leads to an uneven moderation in the core. Therefore, Hofmeister et al. proposed a fuel element design in [30] and [31] according to first analyses of Cheng et al. [15] in which the moderator water should flow downwards through moderator boxes and through the gaps between the fuel assemblies, while the coolant flows upwards in the subchannels, which are the various channels between the fuel rods. The fuel assemblies have to be enclosed by a fuel assembly box and in the center of the assemblies, a moderator box has to be introduced. A mechanical analysis of the fuel assembly box of the HPLWR has been carried out by Himmel et al. in [26]. Another aspect, when designing fuel elements is the neutron absorption by structure material is in the core. Hofmeister et al. [30] identified that small fuel assemblies need less structural material than large ones, which leads to a design with small fuel elements. Square fuel assemblies have been designed, because Cheng et al. [15] expected that they have a more uniform heat up than hexagonal arrangements.

Since the selected fuel assembly only has an outer width of 70mm, it is not possible to equip each fuel assembly with a control rod. Moreover, because so many small fuel assemblies are necessary, they become very difficult to handle during revision, refueling, and shuffling. To

overcome these difficulties, a fuel element cluster has been proposed consisting of nine small and housed fuel assemblies in a 3x3 arrangement, with 40 fuel rods and a moderator rod each. The design of the fuel elements and a cut out of one cluster are depicted in Fig. 1-3.

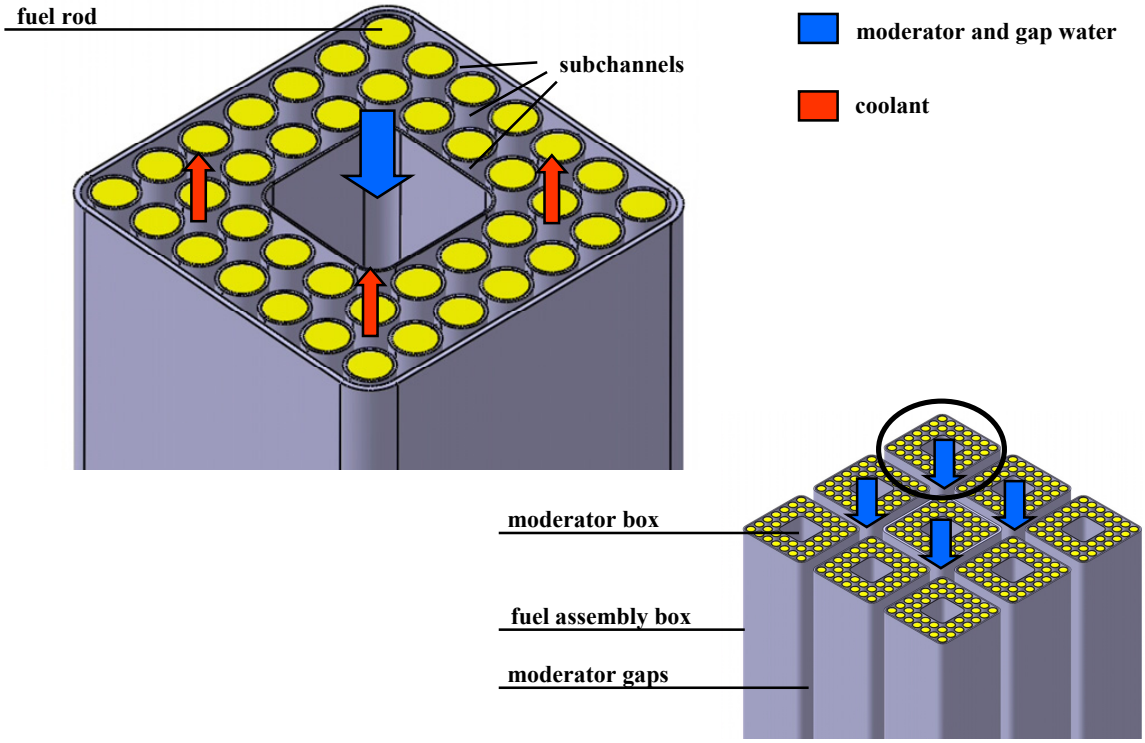

Fig. 1-3 Fuel element of the HPLWR [31]

Each cluster has a common headpiece and footpiece. To actively control the reactivity and thus to control the power output and to shut down the reactor, control rods, made out of neutron absorbing materials, are used. A cross shaped design, the control rod spider, is proposed by Hofmeister et al. [31] with a common drive from the top into 5 of the 9 moderator boxes of one cluster. For the corner moderator boxes, no control rods are foreseen, since no straight access through the headpiece geometry is possible. The headpiece and footpiece of a fuel element cluster are depicted in Fig. 1-4. As spacers between the fuel rods, wire wraps have been proposed by Himmel et al. in [25]. Wire wraps around each fuel rod provide good mixing of the coolant. Their effect on the flow and on the mixing between the subchannels of a fuel assembly has also been analyzed by Himmel et al. in [24].

The design of the reactor and its internals has been carried out and presented by Fischer et al. in [19] and [20]. A stress analysis of the reactor pressure vessel (RPV) has been presented by Fischer et al. in [18]. In Fig. 1-5, a general overview of the RPV and its internals is given and it is shown how the fuel element clusters are arranged in the core. The footpieces are inserted into the lower plenum and the headpieces are inside the steam plenum above the core. In these two plena, the steam is collected before it is passed on to the next heat up stage. The steam plenum is divided into two regions. The upper mixing chamber in the center contains all the evaporator and superheater I clusters. Here the mixing between these two heat up stages takes place. An outer region, where the coolant is collected before it leaves the core, is built around this mixing chamber. The lower plenum is also separated in an inner and outer region. In the

inner region, the coolant is mixed before it enters the evaporator, whereas in the outer region of the lower plenum, the so-called lower mixing chamber, the coolant is mixed between the two superheaters.

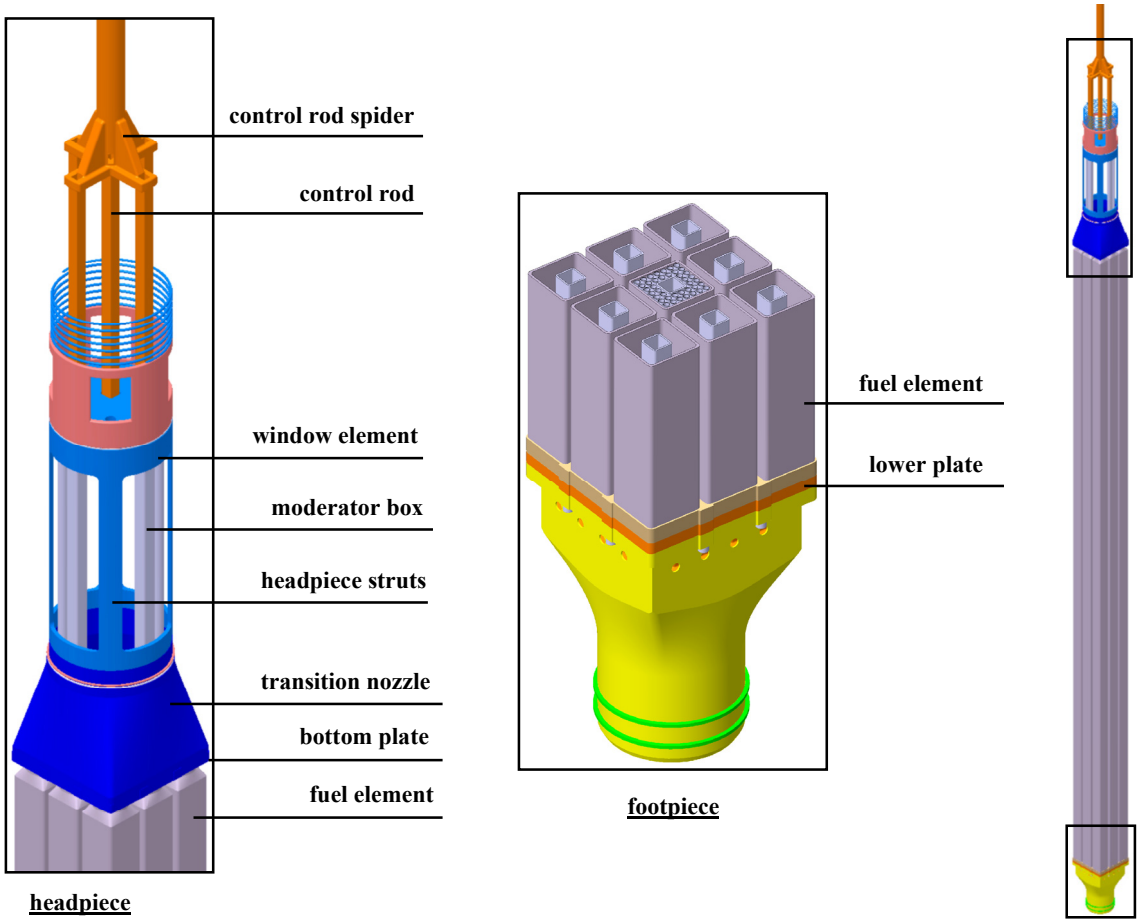

Fig. 1-4 headpiece and footpiece of the HPLWR fuel assembly cluster [19]

Surrounding the fuel element clusters, a steel reflector is introduced to reduce neutron leakages from the core. This way, a more uniform power distribution is achieved and the RPV is protected from aging due to high neutron flux. All internals in the RPV are contained and fixated in the core barrel. The core barrel is a cylindrical structure, which hangs in the RPV to allow thermal expansion due to different temperatures of the different parts in the RPV. The control rods enter the core from the top, therefore control rod guiding tubes are placed above the steam plenum containing and guiding the control rods/the control rod spiders for each cluster. On the top of the RPV, the vessel is closed with the closure head. Two redundant o-ring seals are foreseen to assure the leaktightness of the vessel. On top of the vessel the penetrations for the control rods need to be foreseen. The height of the RPV is determined by the active length of the core, which is 4.2m (including fission gas plena, the fuel rods have a length of 4.7m) and the height of the extended control rods on top. Its smallest possible diameter is found, when adding up the diameter of the core, the thickness of the steel reflector and the core barrel, the downcomer, and the smallest possible thickness of the RPV. Thus, the height of the RPV is 14.3m and the inner diameter of the vessel is 4.47m with a maximum shell thickness of 0.56m. The detailed design of the HPLWR three pass core is thoroughly explained by Fischer et al. in [19]. To understand the concept of the HPLWR, the coolant flow pass will be explained in more detail.

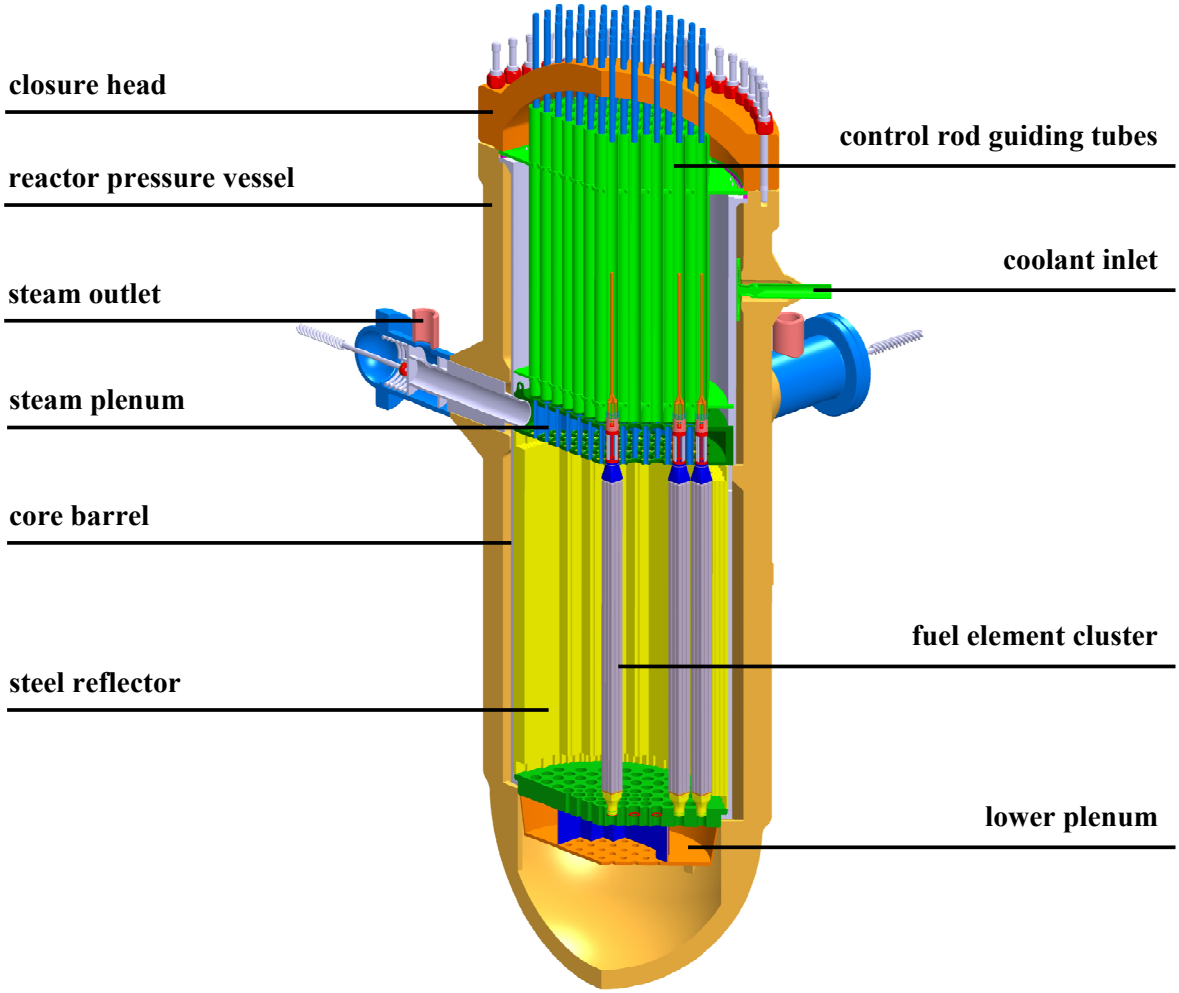

Fig. 1-5 The HPLWR Core and its internals according to [19] and [20]

The coolant entering the core is split up; 25% of the cooling water entering the reactor pressure vessel shall be supplied to gaps between the assemblies and to moderator rods inside the assemblies. The flow pass of this gap and moderator water is indicated on the left side in Fig. 1-6. It flows upwards in the pressure vessel, passing the closure head of the reactor pressure vessel, and reaches the core from the top. Thus, the region in the RPV above the steam plenum is entirely filled with the gap and moderator water. From here, 2/3 of this flow is lead through connection tubes in the steam plenum, to be kept outside the fuel assemblies as gap water. The remaining moderator water flows downwards in the moderator boxes inside the fuel assemblies. The lower plate of each footpiece, which is indicated in Fig. 1-4, has two levels. The moderator boxes are extended to the lower level, where the moderator water is collected and then released to the outside of the footpiece, where it is mixed with the gap water surrounding the assemblies. The combined gap and moderator water is then led through holes in the central part of the lower plenum.

The other 75% of the cooling water entering the core, the downcomer water, flow downwards in the gap between the RPV and the core barrel and enters the central part of the lower plenum from below via holes. The flow pass of this downcomer water is shown in the center of Fig. 1-6.

In the inner mixing chamber of the lower plenum, which is indicated with the black rectangle in Fig. 1-6, the gap and moderator water is mixed with the downcomer water. At the core inlet, above the central part of the lower mixing plenum, the temperature of the mixed coolant is expected to be around 310°C. The mixing of the moderator water by jets of the downcomer water in the footpieces has been analyzed by Hofmeister et al. in [29] and appeared to be very effective.

On the right side of Fig. 1-6, the flow pass inside the three pass core is depicted. Each heat up zone, the evaporator and the two superheaters are indicated with only one fuel element cluster exemplarily. The colors of the arrows indicating the flow direction stand for the temperature of the coolant in a qualitative way. The temperature of the gap and moderator water, as well as of the downcomer water is close to the core inlet temperature. In the evaporator and the two superheaters, the coolant is heated up significantly before it exits the core with a core outlet temperature of approximately 500°C.

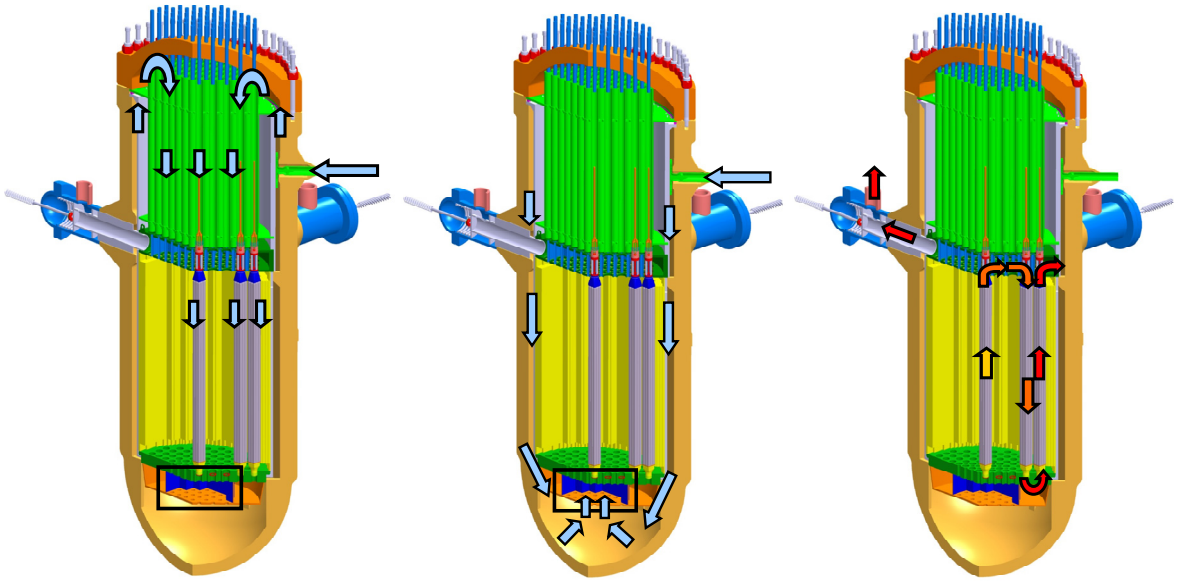

Fig. 1-6 Coolant flow pass in the HPLWR
left: gap and moderator water, center: downcomer water right: heat up in the three pass core

The coolant enters the reactor through four inlets circumferentially positioned at the cylindrical part of the vessel, well above the four outlets. Inlets and outlets are positioned every 90°, while the inlets have a 45° offset to the outlets. To avoid high thermal stresses in the RPV, high temperature gradients have to be avoided. To achieve this, the inside surface of the RPV should only be in contact with coolant close to the inlet temperature of the core. Therefore, the hot steam outlet pipes are surrounded by a thermal sleeve, realized with an alignment of to coaxial pipes. The downcomer water flows around the hot outlet pipe, shielding the RPV from the high temperatures as analyzed by Foulon et al. in [22].

All analyses presented in this work are based on the design proposed by Fischer et al. in [19] and [20].

1.4 The Upper Mixing Chamber

The inner part of the steam plenum is called the upper mixing chamber. Considering the flow pass of the coolant in the reactor, it is located above the core between the evaporator and superheater I. It is separated from the outer part by a wall welded into the plenum. The steam plenum with the upper mixing chamber is depicted in Fig. 1-7. Since no moving parts are included, the upper mixing chamber is an example for a static mixing chamber with the aim to achieve good mixing in order to accomplish homogenization of the temperature.

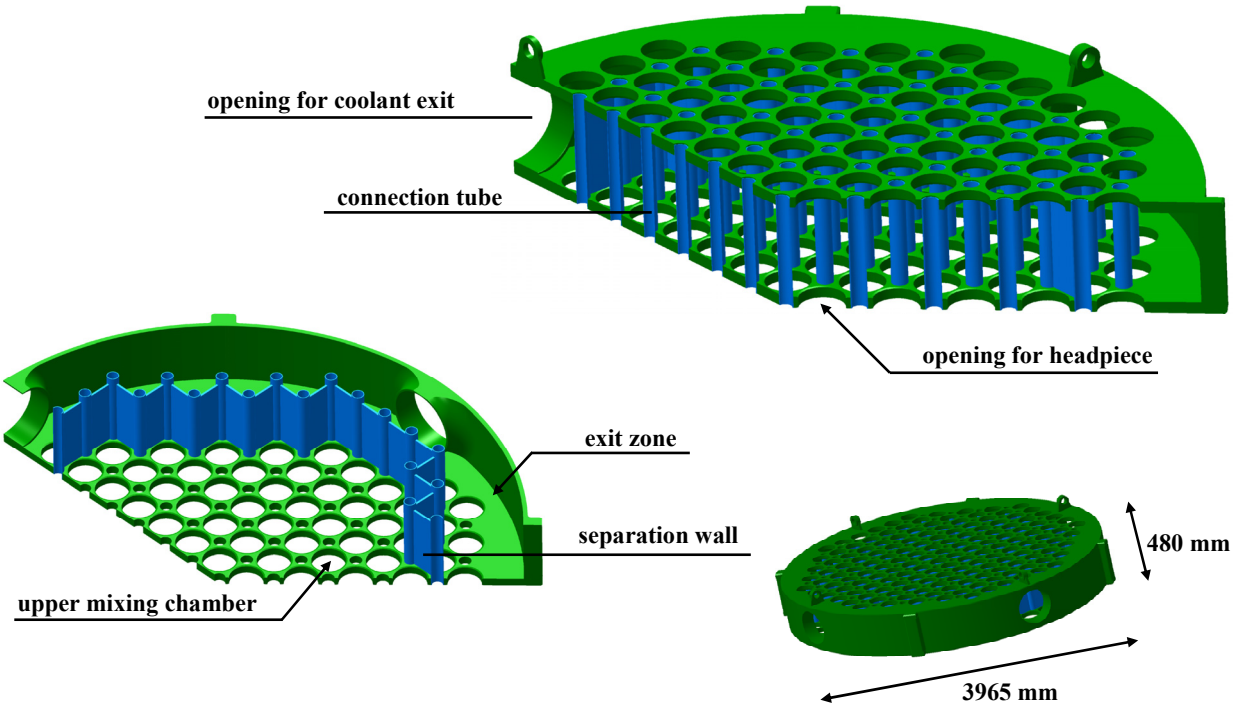

Fig. 1-7 HPLWR Steam plenum – upper mixing chamber [19]

The outer part has a rather simple geometry with only few obstacles in the flow. Here the supercritical coolant is collected before leaving the reactor through the connected steam outlet pipes. The inner part has a very complex geometry due to the many headpieces forming the in- and outlets to the upper mixing chamber. In addition to the headpieces, a high number of connections tubes are encountered in the upper mixing chamber, transporting the gap water to the gaps between the fuel assembly clusters. A cross section of the upper mixing chamber with indications of the coolant flow and of the flow of the gap and moderator water through the connection tubes and the moderator boxes within the headpieces is shown in Fig. 1-8. Again, one exemplary cluster is shown representing each heat up stage.

All headpieces are captured by the steam plenum, thus separating the inner and outer region, while mixing the flow coming from the evaporator and guiding the flow coming from superheater II to the reactor outlets. The diameter of the steam plenum is 3965mm, almost 4m; its height is 480mm, while the outer diameter of one headpiece is 218mm and the outer diameter of each connection tube is 82mm.

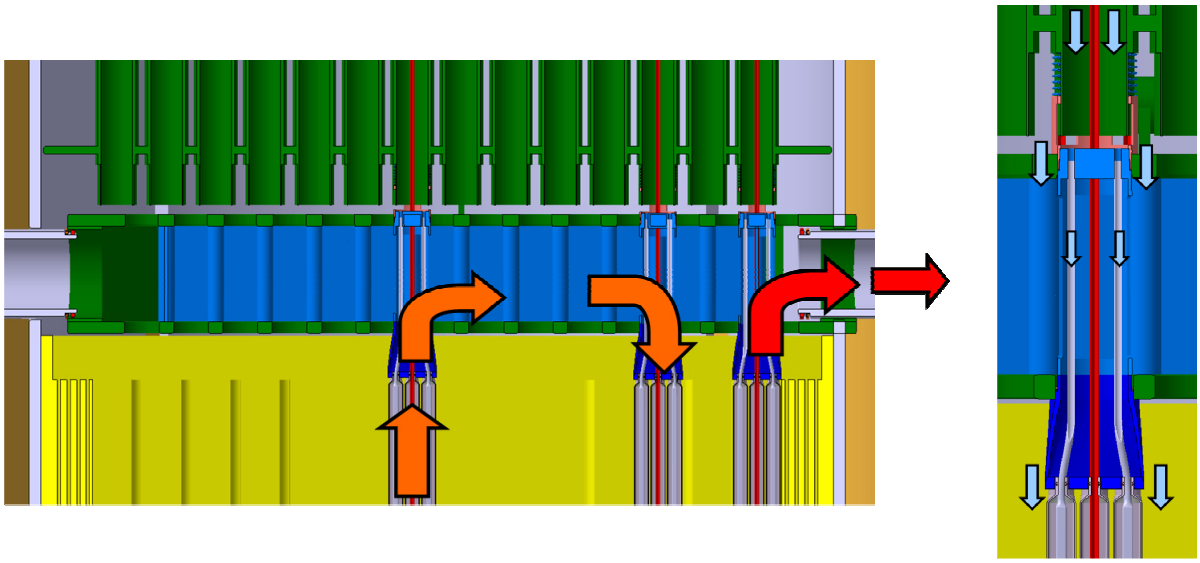

Fig. 1-8 Coolant flow in / moderator and gap water flow through the upper mixing chamber

The complexity of the upper mixing chamber becomes more evident when looking at Fig. 1-9. Here, a cut through the steam plenum is shown with all introduced fuel element clusters. The space in the upper mixing chamber is filled with either connection tubes or headpieces with their struts and moderator boxes to a significant amount. The mixing of the flows coming from the different evaporator fuel element clusters is strongly influenced by the large amount of obstacles in the flow field. Challenges arise when modeling the flow in the mixing chamber due to this complicated structure and due to the fact that the mean coolant temperature in the upper mixing chamber is 390°C, thus being close to the pseudo-critical point. High gradients of the fluid properties are expected.

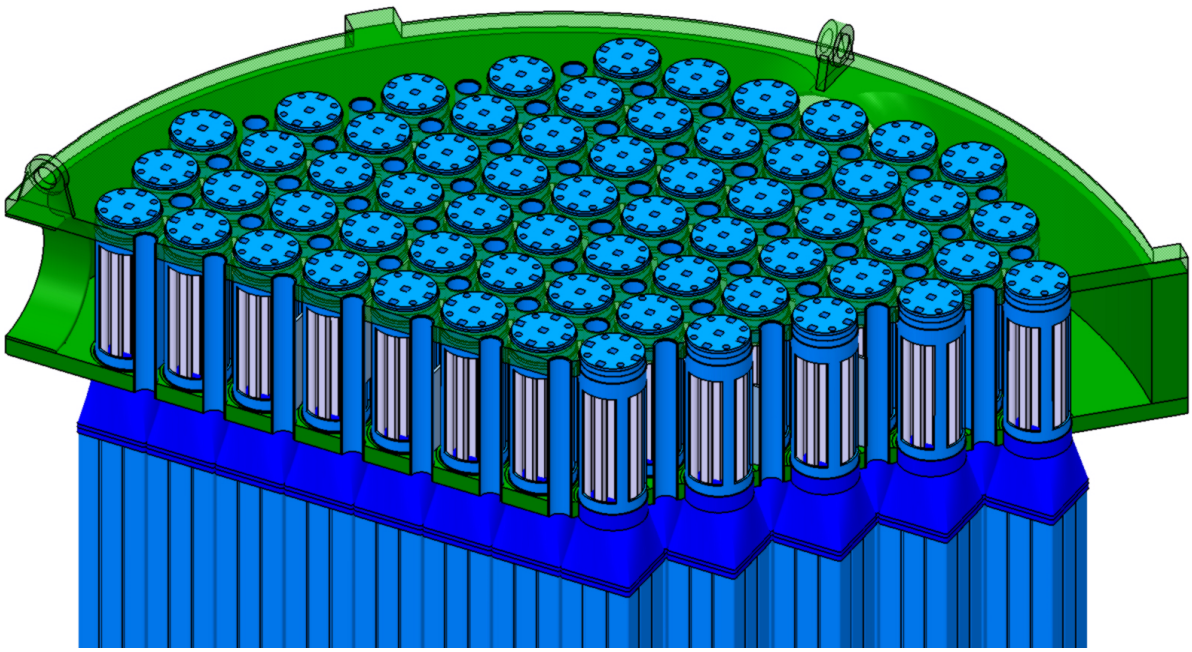

Fig. 1-9 Cut through the steam plenum with introduced fuel element clusters [19]

1.5 The Lower Mixing Chamber

The lower mixing chamber is the outside ring of the mixing plenum. Unlike the upper mixing chamber, which is a rather full structure (connection tubes, headpieces) the lower mixing chamber can be characterized as an empty volume with no flow obstacles inside to influence mixing. In Fig. 1-10 the lower plenum with its two mixing chambers, the inner mixing chamber and the lower mixing chamber between superheater I and II is depicted. The footpieces of the fuel element clusters are introduced in the foreseen openings of the core support plate. Thus, the core support plate, which is supported by the core barrel, is carrying the weight of the clusters.

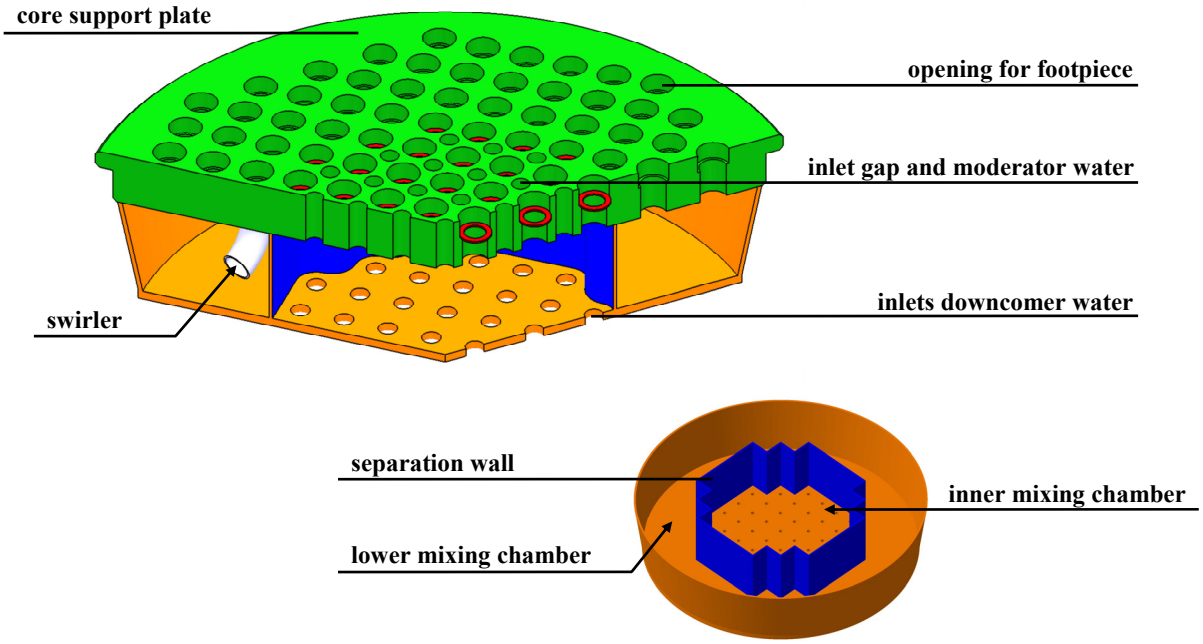

Fig. 1-10 HPLWR lower plenum – lower mixing chamber [19]

Sufficient mixing in the lower mixing chamber is accomplished with so-called swirlers, indicated in Fig. 1-10. These swirlers are welded to the bottom of the core support plate at the outlet openings of the superheater I footpieces. Since no flow obstacles are found in the lower mixing chamber, a global swirl is created, extending the mixing length between in- and outlet of the lower mixing chamber. The analysis of the mixing in the lower chamber with and without swirlers has been presented by Wank et al. in [85]. It has been shown that a global swirl can be created leading to good mixing. Thus, the lower mixing chamber can be characterized according to the introduced classification as a static mixer using “free turbulence”. A more detailed analysis of the mixing in the lower mixing chamber is presented in Annex A.

1.6 Aim and Outline of this Work

The aim of this work is to develop a method for the fluid dynamic design of complex mixing chambers, using the example of the complex upper mixing chamber of the HPLWR. When analyzing the flow in the upper mixing chamber, two challenges are encountered:

1) The consideration of the complex structure with the very high number of complex obstacles, such as headpieces and connection tubes

2) The consideration of the very large gradients in the fluid properties due to different inlet temperatures near the pseudo-critical point in the upper mixing chamber as a result of differences in the heat up of the evaporator clusters

Since more than a single analysis is necessary for a design optimization, many different simulations need to be carried out. Therefore the need for an analysis method arises, using Computational Fluid Dynamics (CFD), which requires only little computing and preparation time while leading to results capturing the dominating effects of the mixing.

Using such analyses, the technical objective is to develop a design of the complex upper mixing chamber that ensures good mixing of the different inlet flow to homogenize the temperature and thus to avoid the propagation of hot streaks into the superheater I fuel element clusters. In Fig. 1-11 the process of the analysis and optimization of the upper mixing chamber is outlined.

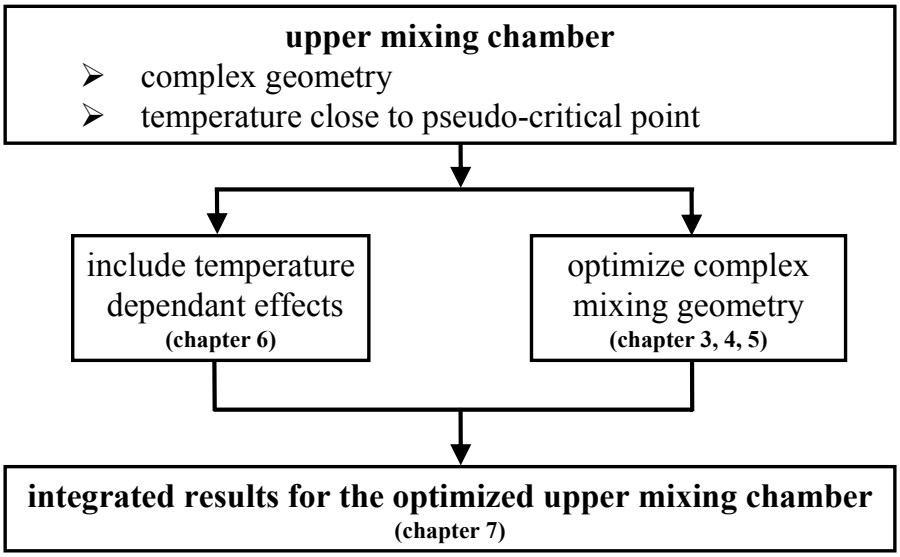

Fig. 1-11 Process of the analysis and optimization of the upper mixing chamber

The challenges for the analysis which are explained above are tackled independently in different steps. Thus, the task at hand is split up in several independent modules. In chapter 3, 4, and 5 the complex structures are included in the simulation and a design optimization of the mixing chamber is carried out. In chapter 6 the temperature dependant effects are handled, before an integrated result including all different aspects is presented in chapter 7.

Outline of the thesis

In the first chapter (Introduction), the scientific and technical tasks as well as the HPLWR have been described. The focus lies hereby on the flow pass in the three pass core and on the necessary mixing chambers. The technical design of the HPLWR is presented, leading to the design of the upper mixing chamber.

Chapter 2 (Governing Equations) gives an overview of the analyzed flow in the upper mixing chamber in the context of fluid dynamics. The equations describing the flow are derived. Also, the applied turbulence models are explained and the evaluation strategy for the mixing is introduced.

In chapter 3 (Method for the Analysis of Complex Mixing Chambers), the method for the analysis is explained. It is shown how it is intended to deal with complex structures in mixing chambers. In addition, the numerical model is described and a verification of the numerical model, a grid sensitivity analysis, is shown. Also the Validation of the applied CFD model is presented. Therefore, an experiment of a similar mixing chamber is described and compared with the carried out simulations for the same settings.

In chapters 4 (Design optimization using the simplified model) and 5 (Including the Effects of the Omitted Structures), the actual design optimization is carried out and the approach, introduced in chapter 3 is applied.

The effects on the flow due to the large changes in the fluid properties with temperature are discussed in chapter 6 (Analysis of Temperature Depending Effects).

The consideration of both analyzed aspects, the complex geometry and the large gradients in the fluid properties, combined in one analysis set is shown in chapter 7 (Integrated Results for the Upper Mixing Chamber). The conclusions are presented in chapter 8 (Summary and Conclusion).

2 Governing Equations

In this chapter, the analyzed problem will be concerted into the context of the field of fluid mechanics. Therefore, the analyzed flow will be described with characteristic dimensionless numbers. Then, the governing equations necessary for the performed analyses in this work are introduced. In the case of the adiabatic approach, these are the mass conservation equation and the momentum conservation equations. For further analyses, also the energy conservation equation and an equation for the transport of a scalar magnitude are introduced.

2.1 Characterization of the Flow in the Upper Mixing Chamber

Based on a one dimensional thermal-hydraulic analysis, Schulenberg et al. [68] predicted an average temperature of 390°C and a pressure of around 25MPa at the evaporator outlet. The coolant mass flow was 1160kg/s, which yields 22.3kg/s per assembly cluster. The fluid properties of water at this point were defined according to [81]. Due to the complicated structure of the upper mixing chamber the characteristic dimensionless numbers, defined by Oertel in [50], [52] and Schlichting in [66] vary strongly according to where they are defined. The geometrical parameters used for their definition are shown in Fig. 2-1.

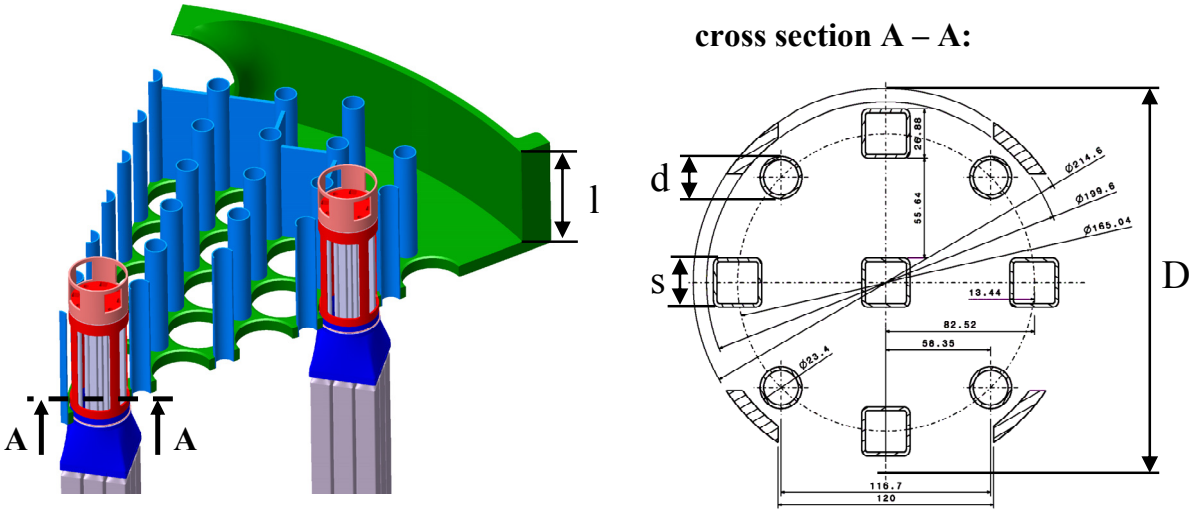

Fig. 2-1 Definition of the lengths for the dimensionless numbers describing the flow
With: $D = 199.6mm$, $d = 23.4mm$, $s = 26.88mm$.

The hydraulic diameter d_h is defined according to:

$$d_H = 4 \cdot \frac{A}{P}$$

with the cross section area A and the wetted perimeter P, defined as:

$$A = \frac{\pi D^2}{4} - 4 \cdot \frac{\pi d^2}{4} - 5 \cdot s^2 = 25957.5 mm^2 ,$$

$$P = \pi D + 4 \cdot \pi d + 5 \cdot 4 \cdot s = 1458.7 mm .$$

This leads to the hydraulic diameter:

$$d_H = 4 \cdot \frac{A}{P} = 71.2 mm .$$

In Tab. 2-1, the fluid properties at the evaporator outlet are listed.

Pressure:	$p = 25 MPa$
Temperature:	$T = 390°C$
Density:	$\rho = 215.189 \frac{kg}{m^3}$
Dynamic viscosity:	$\mu = 31.704 \cdot 10^{-6} \frac{kg}{ms}$
Kinematic viscosity:	$\nu = 0.147 \cdot 10^{-6} \frac{m^2}{s}$
Specific heat:	$c_p = 28461 \frac{J}{kgK}$
Conductivity:	$\lambda = 0.2398 \frac{W}{mK}$
Thermal diffusivity:	$a = 0.553 \cdot 10^{-6} \frac{m^2}{s}$
Sound velocity:	$c = 403.34 \frac{m}{s}$
Volumetric thermal expansion coefficient:	$\alpha = 0.042 K^{-1}$

Tab. 2-1 Fluid properties at the evaporator outlet

The analysis of Schulenberg et al. [68] results in the following average inlet velocity into to the mixing chamber, defined with the given density, mass flow, and inlet cross section area, which corresponds to the inner cross section at the inlet of a headpiece:

Inlet velocity: $$u = \frac{\dot{m}}{\rho A} = \frac{1160 kg/s}{52} \cdot \frac{1}{\left(215.2 kg/m^3\right) \cdot \left(0.2596 m^2\right)} = 3.997 \frac{m}{s}$$

In order to characterize the flow, different characteristic, dimensionless numbers are introduced. The different characteristic dimensionless numbers describing the flow are defined as:

Mach-number:
$$\mathrm{M} = \frac{flow\ \ velocity}{sound\ \ velocity}\frac{u}{c} = 0.0099$$

Reynolds-number at inlet cross section:
$$\mathrm{Re}_{in} = \frac{inertia}{friction} = \frac{\rho u d_h}{\mu} = \frac{u d_h}{\nu} = 1.9 \cdot 10^6$$

Reynolds-number with inner height:
$$\mathrm{Re}_l = \frac{inertia}{friction} = \frac{\rho u l}{\mu} = \frac{u l}{\nu} = 1.3 \cdot 10^7$$

Prandtl-number:
$$\mathrm{Pr} = \frac{viscous\ \ diffusivity}{thermal\ \ diffusivity} = \frac{\nu}{a} = 3.76$$

Peclet-number:
$$\mathrm{Pe} = \mathrm{Re}\,\mathrm{Pr} = \frac{convective\ \ heat\ \ transfer}{diffusive\ \ heat\ \ transfer} = \frac{u d_h}{a} = 7.3 \cdot 10^6$$

Grashof-number inside the mixing chamber:
$$\mathrm{Gr} = \frac{buoyancy\ \ force}{viscous\ \ force} = \frac{\alpha g l^3 (\mathrm{T} - \mathrm{T}_0)}{\nu^2} = 1.1 \cdot 10^{14}$$

The Mach-number is defined with the flow velocity u and the sound velocity c. In the Reynolds-number, the kinematic viscosity ν and the hydraulic diameter d_h/the inner height l are used. And in the Prandtl-number, a is the thermal diffusivity. In the Grashof-number, α represents the volumetric thermal expansion coefficient, g the acceleration due to gravity, and T the temperature. The characteristic length for buoyancy effects entered into the Grashof-number, is the height of the mixing chamber.

Two Reynolds-numbers are defined: one with the hydraulic diameter d_h at the inlet of the mixing chamber and another one with the inner height of the mixing chamber. The very high Reynolds-number at the inlet of more than 10^6 implies that the flow is highly turbulent, since the critical Reynolds number for a pipe flow is approximately 2300. Also, the very complex geometry with wire wrap spacers to enhance the mixing between the different subchannels of the fuel element clusters, through which the flow has to pass before entering the upper mixing chamber, suggests that the flow is highly turbulent at the mixing chamber inlet. The other Reynolds-number, built with the height of the mixing chamber, is necessary for the characterization of buoyancy influences as presented in chapter 2.3 and applied in chapter 6.

The Prandtl-number has a value of 3.8. Thus, it lies between the one of water (Pr = 7) and air (Pr = 0.7) at a pressure of 1bar and a temperature of 20°C.

Due to the very low Mach-number of 0.0099, the flow can be regarded as incompressible, which means that the density variation with pressure is negligible compared with the density variation with temperature.

The large Peclet-number shows that the heat transfer due to diffusion can be disregarded and the convective heat transfer predominates. This has an influence on the analysis strategy explained in chapter 2.5. A criterion if buoyancy effects have a significant effect on the flow is derived in chapter 2.3 (Characterization of Buoyancy Influences). The Grashof-number, which is defined with the inner height l of the upper mixing chamber, is very high at a value of 10^{14}. A discussion, weather buoyancy effects have an influence on the flow can be found in chapter 6.

2.2 Conservation Equations

The governing equations for the mass, momentum, and energy conservation are derived from an infinitesimal small volume at an arbitrary position within the analyzed flow according to [43]. All of the conservation equations have the same structure, where the time dependant change of the conserved quantity within the analyzed volume equals the flow of the conserved quantity in and out of the volume plus corresponding sources and sinks influencing the transported quantity. The notation according to the book of Oertel and Laurien [43] is generally used.

2.2.1 Conservation of Mass

Applying a mass balance to the analyzed fluid volume in which the time dependant changes of the mass equal the difference of the mass flow entering and exiting the fluid volume results in the mass conservation equation:

$$\frac{\partial \rho}{\partial t} + \frac{\partial (\rho u)}{\partial x} + \frac{\partial (\rho v)}{\partial y} + \frac{\partial (\rho w)}{\partial z} = 0 . \tag{2.1}$$

In this equation ρ represents the density and u, v, w are the velocities in the different spatial directions. The flow in all analyzed applications in this work can be regarded as incompressible and the density therefore is only a function of the temperature ($\rho = \rho(T)$). In cases, where temperature dependant effects are disregarded and the density in the flow is constant, the mass conservation equation is simplified to:

$$\frac{\partial u}{\partial x} + \frac{\partial v}{\partial y} + \frac{\partial w}{\partial z} = 0 . \tag{2.2}$$

Applying vector notation, the continuity equation for flows with constant density is written as:

$$\nabla \cdot \vec{v} = 0 . \tag{2.3}$$

2.2.2 Conservation of Momentum

The Navier-Stokes Equations, which describe the conservation of momentum, can be derived when looking at the time dependant changes of the momentum in an analyzed fluid volume, which are the sum of the momentum fluxes in and out of the analyzed fluid volume, the shear and normal stresses, and the forces acting on the volume. For the change in momentum in x-direction, the following equation can be derived:

$$\frac{\partial(\rho u)}{\partial t}+\frac{\partial(\rho uu)}{\partial x}+\frac{\partial(\rho uv)}{\partial y}+\frac{\partial(\rho uw)}{\partial z}=F_x+\frac{\partial \tau_{xx}}{\partial x}+\frac{\partial \tau_{yx}}{\partial y}+\frac{\partial \tau_{zx}}{\partial z}. \tag{2.4}$$

The pressure acts as a negative normal stress, thus it can be written as:

$$p=-\frac{\tau_{xx}+\tau_{yy}+\tau_{zz}}{3}. \tag{2.5}$$

The three normal stresses τ_{xx}, τ_{yy}, and τ_{zz} can be written as a composite of the pressure p and the contributions due to the friction of the fluid σ_{xx}, σ_{yy}, and σ_{zz}:

$$\tau_{xx}=\sigma_{xx}-p, \qquad \tau_{yy}=\sigma_{yy}-p, \qquad \tau_{zz}=\sigma_{zz}-p. \tag{2.6}$$

Applying the relationship found in (2.6) leads to:

$$\rho\left(\frac{\partial u}{\partial t}+u\frac{\partial u}{\partial x}+v\frac{\partial u}{\partial y}+w\frac{\partial u}{\partial z}\right)=F_x-\frac{\partial p}{\partial x}+\frac{\partial \sigma_{xx}}{\partial x}+\frac{\partial \tau_{yx}}{\partial y}+\frac{\partial \tau_{zx}}{\partial z}, \tag{2.7}$$

$$\rho\left(\frac{\partial v}{\partial t}+u\frac{\partial v}{\partial x}+v\frac{\partial v}{\partial y}+w\frac{\partial v}{\partial z}\right)=F_y-\frac{\partial p}{\partial y}+\frac{\partial \tau_{xy}}{\partial x}+\frac{\partial \sigma_{yy}}{\partial y}+\frac{\partial \tau_{zy}}{\partial z}, \tag{2.8}$$

$$\rho\left(\frac{\partial w}{\partial t}+u\frac{\partial w}{\partial x}+v\frac{\partial w}{\partial y}+w\frac{\partial w}{\partial z}\right)=F_z-\frac{\partial p}{\partial z}+\frac{\partial \tau_{xz}}{\partial x}+\frac{\partial \tau_{yz}}{\partial y}+\frac{\partial \sigma_{zz}}{\partial z}. \tag{2.9}$$

Further relations for Newtonian fluids according to [89] lead to the Navier-Stokes equations for flows with variable density.

$$\begin{aligned}\rho\left(\frac{\partial u}{\partial t}+u\frac{\partial u}{\partial x}+v\frac{\partial u}{\partial y}+w\frac{\partial u}{\partial z}\right)=F_x&-\frac{\partial p}{\partial x}+\frac{\partial}{\partial x}\left[\mu\left(2\frac{\partial u}{\partial x}-\frac{2}{3}(\nabla\cdot\vec{v})\right)\right]\\&+\frac{\partial}{\partial y}\left[\mu\left(\frac{\partial u}{\partial y}+\frac{\partial v}{\partial x}\right)\right]+\frac{\partial}{\partial z}\left[\mu\left(\frac{\partial w}{\partial x}+\frac{\partial u}{\partial z}\right)\right],\end{aligned} \tag{2.10}$$

$$\begin{aligned}\rho\left(\frac{\partial v}{\partial t}+u\frac{\partial v}{\partial x}+v\frac{\partial v}{\partial y}+w\frac{\partial v}{\partial z}\right)=F_y&-\frac{\partial p}{\partial y}+\frac{\partial}{\partial y}\left[\mu\left(2\frac{\partial v}{\partial y}-\frac{2}{3}(\nabla\cdot\vec{v})\right)\right]\\&+\frac{\partial}{\partial z}\left[\mu\left(\frac{\partial v}{\partial z}+\frac{\partial w}{\partial y}\right)\right]+\frac{\partial}{\partial z}\left[\mu\left(\frac{\partial u}{\partial y}+\frac{\partial v}{\partial x}\right)\right],\end{aligned} \tag{2.11}$$

$$\begin{aligned}\rho\left(\frac{\partial w}{\partial t}+u\frac{\partial w}{\partial x}+v\frac{\partial w}{\partial y}+w\frac{\partial w}{\partial z}\right)=F_z&-\frac{\partial p}{\partial z}+\frac{\partial}{\partial z}\left[\mu\left(2\frac{\partial w}{\partial z}-\frac{2}{3}(\nabla\cdot\vec{v})\right)\right]\\&+\frac{\partial}{\partial x}\left[\mu\left(\frac{\partial w}{\partial x}+\frac{\partial u}{\partial z}\right)\right]+\frac{\partial}{\partial z}\left[\mu\left(\frac{\partial v}{\partial z}+\frac{\partial w}{\partial y}\right)\right].\end{aligned} \tag{2.12}$$

These can be further simplified for flows with constant density introducing the continuity equation and assuming constant viscosity. The Navier-Stokes equations for constant density and constant viscosity can be written as:

$$\rho\left(\frac{\partial u}{\partial t}+u\frac{\partial u}{\partial x}+v\frac{\partial u}{\partial y}+w\frac{\partial u}{\partial z}\right)=F_x-\frac{\partial p}{\partial x}+\mu\left(\frac{\partial^2 u}{\partial x^2}+\frac{\partial^2 u}{\partial y^2}+\frac{\partial^2 u}{\partial z^2}\right), \tag{2.13}$$

$$\rho\left(\frac{\partial v}{\partial t}+u\frac{\partial v}{\partial x}+v\frac{\partial v}{\partial y}+w\frac{\partial v}{\partial z}\right)=F_y-\frac{\partial p}{\partial y}+\mu\left(\frac{\partial^2 v}{\partial x^2}+\frac{\partial^2 v}{\partial y^2}+\frac{\partial^2 v}{\partial z^2}\right), \tag{2.14}$$

$$\rho\left(\frac{\partial w}{\partial t}+u\frac{\partial w}{\partial x}+v\frac{\partial w}{\partial y}+w\frac{\partial w}{\partial z}\right)=F_z-\frac{\partial p}{\partial z}+\mu\left(\frac{\partial^2 w}{\partial x^2}+\frac{\partial^2 w}{\partial y^2}+\frac{\partial^2 w}{\partial z^2}\right). \tag{2.15}$$

Using vector notation, these equations can be summed up as:

$$\rho\left(\frac{\partial \vec{v}}{\partial t}+(\vec{v}\cdot\nabla)\vec{v}\right)=\vec{F}-\nabla p+\mu\Delta\vec{v}\,. \tag{2.16}$$

For flows with constant density, the Navier-Stokes equations (2.16) together with the continuity equation (2.3) describe the analyzed flow. These equations form a system of four nonlinear, second-order partial differential equations, which has to be solved for given initial and boundary conditions as exemplarily described in chapter 2.4.7. The four unknowns are: u, v, w, and p.

If temperature dependant effects are regarded and the density is not regarded as constant, the analyzed flow is described by the Navier -Stokes equations according to (2.10), (2.11), (2.12), and the continuity equation according the (2.1). In this case, an additional equation is necessary, since the density is also an unknown.

2.2.3 Conservation of Energy

For flows with constant density, the energy equation describing the conservation of energy is not a constitutive equation for the density, but merely a transport equation for the energy; otherwise it is necessary to close the equation system describing the flow. The energy equation describes the time dependant change of the inner and kinetic energy in an analyzed fluid volume due to the energy fluxes in and out of the volume, the energy fluxes in and out of the volume by means of conduction, the work done on the volume due to pressure forces, shear and normal stresses, the energy from outside, and the work due to volumetric forces.

$$\underbrace{\frac{\partial\left(\rho\left[e+\frac{V^2}{2}\right]\right)}{\partial t}}_{\text{Change of total energy}} = \underbrace{-\left(\frac{\partial\left(\rho\left[e+\frac{V^2}{2}\right]u\right)}{\partial x}+\frac{\partial\left(\rho\left[e+\frac{V^2}{2}\right]v\right)}{\partial y}+\frac{\partial\left(\rho\left[e+\frac{V^2}{2}\right]w\right)}{\partial z}\right)}_{\text{Convective terms}}$$

$$+\underbrace{\left(\frac{\partial}{\partial x}\left[\lambda\frac{\partial T}{\partial x}\right]+\frac{\partial}{\partial y}\left[\lambda\frac{\partial T}{\partial y}\right]+\frac{\partial}{\partial z}\left[\lambda\frac{\partial T}{\partial z}\right]\right)}_{\text{Change by means of heat conduction}} \tag{2.17}$$

$$+\underbrace{\begin{array}{l}\left(-\frac{\partial(pu)}{\partial x}+\frac{\partial(\sigma_{xx}u)}{\partial x}+\frac{\partial(\tau_{xy}v)}{\partial x}+\frac{\partial(\tau_{xz}w)}{\partial x}\right)+\left(-\frac{\partial(pv)}{\partial y}+\frac{\partial(\tau_{yx}u)}{\partial y}+\frac{\partial(\sigma_{yy}v)}{\partial y}+\frac{\partial(\tau_{yz}w)}{\partial y}\right)\\ +\left(-\frac{\partial(pw)}{\partial z}+\frac{\partial(\tau_{zx}u)}{\partial z}+\frac{\partial(\tau_{zy}v)}{\partial z}+\frac{\partial(\sigma_{zz}w)}{\partial z}\right)\end{array}}_{\text{pressure, normal, and shear stress forces}}$$

$$+\underbrace{\vec{F}\cdot\vec{v}+\rho\dot{q}_S}_{\text{work by volume forces and outside energy}}.$$

Here e is the internal energy, the kinetic energy is [ρ V^2/2], and λ is the thermal conductivity. The velocity magnitude is calculated with the velocity components in the different spatial directions, as: $V^2 = u^2 + v^2 + w^2$. When excluding the term [e+V^2/2] from the term describing the change of total energy and from the convective terms, it is found that one multiplier is the continuity equation, which equals 0. This and the approach used for the normal and shear stresses for Newtonian fluids analogue as for the conservation of momentum, leads to:

$$\rho\left(\frac{\partial e}{\partial t}+u\frac{\partial e}{\partial x}+v\frac{\partial e}{\partial y}+w\frac{\partial e}{\partial z}\right)=\left(\frac{\partial}{\partial x}\left[\lambda\frac{\partial T}{\partial x}\right]+\frac{\partial}{\partial y}\left[\lambda\frac{\partial T}{\partial y}\right]+\frac{\partial}{\partial z}\left[\lambda\frac{\partial T}{\partial z}\right]\right) \tag{2.18}$$
$$-p(\nabla\cdot\vec{v})+\mu\Phi+\vec{F}\cdot\vec{v}+\rho\dot{q}_S,$$

with the dissipation function Φ:

$$\Phi=2\left[\left(\frac{\partial u}{\partial x}\right)^2+\left(\frac{\partial v}{\partial y}\right)^2+\left(\frac{\partial w}{\partial z}\right)^2\right] \tag{2.19}$$
$$+\left(\frac{\partial v}{\partial x}+\frac{\partial u}{\partial y}\right)^2+\left(\frac{\partial w}{\partial y}+\frac{\partial v}{\partial z}\right)^2+\left(\frac{\partial u}{\partial z}+\frac{\partial w}{\partial x}\right)^2-\frac{2}{3}\left(\frac{\partial u}{\partial x}+\frac{\partial v}{\partial y}+\frac{\partial w}{\partial z}\right)^2.$$

Rewriting the energy equation for the enthalpy, defined as:

$$h=e+\frac{p}{\rho},$$

with:

$$dh=\left(\frac{\partial h}{\partial T}\right)_p dT+\left(\frac{\partial h}{\partial p}\right)_V dp\text{, with}\quad c_p=\left(\frac{\partial h}{\partial T}\right)_p,$$

Assuming that the pressure is constant, the change in enthalpy can be written as:

$$dh=c_p dT.$$

This leads to the energy equation expressed with the enthalpy, when disregarding radiation, work imposed by outside forces, and the usually very small dissipation:

$$\rho\left(\frac{\partial h}{\partial t}+u\frac{\partial h}{\partial x}+v\frac{\partial h}{\partial y}+w\frac{\partial h}{\partial z}\right)=\frac{\partial}{\partial x}\left(\frac{\lambda}{c_p}\frac{\partial h}{\partial x}\right)+\frac{\partial}{\partial y}\left(\frac{\lambda}{c_p}\frac{\partial h}{\partial y}\right)+\frac{\partial}{\partial z}\left(\frac{\lambda}{c_p}\frac{\partial h}{\partial z}\right). \tag{2.20}$$

For all the introduced conservation equations no restrictions were made. They are valid in general, describing all homogeneous flows of Newtonian fluids.

2.3 Characterization of Buoyancy Influences

As the flow is incompressible, the change in density due to changes in the pressure is negligible. The change in the density with temperature due to thermal expansion, however, is very significant. In convective flows this is the origin of buoyancy effects as described in detail by Turner in [77] and in the book of Kakac [35].

The Boussinesq approximation holds for flows, in which the change in density can be disregarded in all equations except the buoyancy term in the momentum equation. Temperature dependant effects are only taken into account by this gravity term. This lift term accelerates the flow in the opposite direction of the gravity:

$$g(\rho - \rho_\infty). \tag{2.21}$$

This term is approximated in the momentum equation in the direction of gravity describing the volumetric buoyancy force $\rho(T)g$ in which $\rho(T)$ is linearized as:

$$\rho(T) = \rho_\infty[1 - \alpha(T - T_\infty)]. \tag{2.22}$$

Here, ρ_∞ is the reference density, α the thermal expansion coefficient, and T_∞ a reference temperature. $\rho = \rho(T)$ is only introduced in this term, in all other terms the density change will be neglected. The Boussinesq approximation also implies that all other fluid properties are constant.

To obtain a criterion if buoyancy effects have a significant effect on the flow, the dimensionless Boussinesq equations are needed. The following dimensionless quantities are introduced to derive them:

$$x_i^* = \frac{x_i}{l}, \text{ with } i = 1,2,3;\ \ \vec{v}^* = \frac{l}{a_\infty}\vec{v};\ T^* = \frac{T - T_\infty}{T_W - T_\infty};\ p^* = (p + \rho_\infty g x_3)\frac{l^2}{\rho_\infty \nu_\infty a_\infty}. \tag{2.23}$$

Whereas the thermal diffusivity a_∞, the acceleration due to gravity g, the kinematic viscosity ν_∞, and a characteristic length scale l are defined for the bulk. Introducing these dimensionless quantities lead to the dimensionless Boussinesq equations, however formulated for the temperature in steady state flow (Oertel [52]):

$$\nabla \cdot \vec{v}^* = 0, \tag{2.24}$$

$$\frac{1}{\mathrm{Pr}}(\vec{v}^* \cdot \nabla)\vec{v}^* = -\nabla p^* + \Delta\vec{v}^* + \mathrm{Ra}T^*\begin{pmatrix}0\\0\\1\end{pmatrix}, \tag{2.25}$$

$$\vec{v}^* \cdot \nabla T^* = \Delta T^*. \tag{2.26}$$

Ra is the dimensionless Rayleigh-number, which describes the ratio of the buoyancy accelerating the flow against the gravity to the retaining friction. The Rayleigh-number is defined as:

$$\mathrm{Ra}_\infty = \frac{g l^3}{a_\infty \nu_\infty}\alpha(T - T_\infty). \tag{2.27}$$

Introducing the following dimensionless numbers:

$$\mathrm{Re}_{l,\infty} = \frac{u_\infty l}{\nu_\infty}, \qquad \mathrm{Pr}_\infty = \frac{\nu_\infty}{a_\infty}, \qquad \mathrm{Pe}_\infty = \mathrm{Re}_{l,\infty}\,\mathrm{Pr}_\infty = \frac{u_\infty l}{\nu_\infty}\frac{\nu_\infty}{a_\infty} = \frac{u_\infty l}{a_\infty}, \tag{2.28}$$

together with another definition for a dimensionless velocity:

$$\vec{v}' = \frac{\vec{v}}{\vec{v}_\infty}, \qquad \vec{v}^* = \frac{l\vec{v}_\infty \vec{v}'}{a_\infty}, \qquad \vec{v}^* = \frac{l}{a_\infty}\vec{v} = \mathrm{Re}_\infty\,\mathrm{Pr}_\infty\,\vec{v}' = \mathrm{Pe}_\infty \vec{v}', \tag{2.29}$$

and then inserting this dimensionless velocity into the Boussinesq equations, the following equation for the momentum in the direction of gravity is obtained:

$$\frac{\mathrm{Pe}^2}{\mathrm{Pr}}\left(u'\frac{\partial w'}{\partial x} + v'\frac{\partial w'}{\partial y} + w'\frac{\partial w'}{\partial z}\right) = -\frac{\partial p^*}{\partial z} + \mathrm{Pe}\mu\left(\frac{\partial^2 w'}{\partial x^2} + \frac{\partial^2 w'}{\partial y^2} + \frac{\partial^2 w'}{\partial z^2}\right) + \mathrm{Ra}T^*. \tag{2.30}$$

Dividing equation (2.30) with (RePe) leads to:

$$\underbrace{\left(u'\frac{\partial w'}{\partial x} + v'\frac{\partial w'}{\partial y} + w'\frac{\partial w'}{\partial z}\right)}_{\textit{convection}} = \underbrace{+\frac{1}{\mathrm{Re}}\mu\left(\frac{\partial^2 w'}{\partial x^2} + \frac{\partial^2 w'}{\partial y^2} + \frac{\partial^2 w'}{\partial z^2}\right)}_{\textit{friction}} \underbrace{-\frac{1}{\mathrm{RePe}}\frac{\partial p^*}{\partial z}}_{\textit{pressure}} + \underbrace{\frac{\mathrm{Ra}}{\mathrm{RePe}}T^*}_{\textit{buoyancy}} \tag{2.31}$$

A limit can be defined for the significance of buoyancy effects in flows with the coefficient of the buoyancy term in (2.31). The introduction of the Grashof-number, defined as $\mathrm{Gr} = \mathrm{Ra}/\mathrm{Pr}$, leads to the rewritten coefficient in the buoyancy term: $\mathrm{Gr}/\mathrm{Re}^2$.

We conclude from equation (2.31) that buoyancy effects are negligible if:

$$\frac{\mathrm{Gr}}{\mathrm{Re}^2} << 1. \tag{2.32}$$

If the changes in the fluid properties are larger, the linear approximation (2.22) will not be valid and the specific heat, viscosity, and thermal conductivity will vary with temperature as well. In such cases, this criterion can only lead to an approximate evaluation of buoyancy effects, since is derived with the simplified Boussinesq approximation.

2.4 Turbulent Flows

In comparison with laminar flows, turbulent flows are characterized by local fluctuations of the flow magnitudes leading to additional exchange of momentum and of energy as described among others in the book by Pope [85]. The smooth and straight laminar flow in a pipe, for instance, becomes turbulent at higher velocities, thus at higher Reynolds numbers. It is highly irregular and is full of eddy motions. The velocity fluctuations, which are superimposed on the flow lead to a higher pressure drop and to better mixing of the flow.

The transition from laminar to turbulent flows is characterized by the critical Reynolds number Re_c for each flow type. The laminar flow is influence by small perturbations, which aren't damped away at high enough Reynolds numbers. If the critical Reynolds number is obtained in the flow, the laminar flow is superimposed with two dimensional perturbating waves (Tollmien-Schlichting waves). Further downstream, three dimensional perturbations lead to so called Λ-vortices decaying into local turbulent spots, which lead to the fully turbulent flow. The onset of turbulence/the laminar-turbulent transition is described in [52] and [51].

The most accurate way of simulating turbulent flow is the so-called Direct Numerical Simulation DNS as described in the book of Ferziger and Peric [17]. Here, the Navier-Stokes equations are solved without averaging or the use of approximations. The only errors arise due to the numerical discretization, which can be estimated and controlled. The disadvantage of this approach is the high numerical effort, which makes it not applicable as a design tool. Also, the very detailed information often exceeds the demand.

An approach in which the large scales, which are in general much more energetic and thus transport most of the conserved properties, are simulated and the small scales, usually containing much less energy are modeled, is called Large Eddy Simulation LES. The numerical effort is decreased significantly in comparison with the DNS, but it is still very high when considering the use of computational methods for fluid dynamics.

An effective approach to model complex turbulent flows is the Reynolds-Averaged Navier Stokes (RANS) approach. Here, the turbulent fluctuations are regarded, without resolving them. All simulations presented in this work use this approach, which is explained in more detail below.

2.4.1 Reynolds Equations for Turbulent Flows

Even though the derived equations in chapter 2.2 are valid for all flows, solving them for turbulent flows, which are encountered in many technical applications, is linked to an enormous computational effort. To reduce the computational effort and thus, to enable the analysis of very complex, technical flows, these equations are modified to simpler equations, which still describe the significant aspects of the flow according to [43]. The modified Navier-Stokes equations for turbulent flows are called Reynolds equations. To derive them for fluids with constant density (ρ = const.), the Reynolds ansatz, which splits all the velocity components: u, v, w, and the pressure p into time-averaged values according to (2.34) and a fluctuating value denoted with a dash.

Doing so, it is possible to separate the global unsteady flow from the local turbulent fluctuations. This way, time averaging the equations including the separated flow magnitudes leads to the time averaged continuity equation and the Reynolds equation, without losing the products of the local fluctuations. These then have to be modeled.

$$u = \overline{u} + u', \qquad v = \overline{v} + v', \qquad w = \overline{w} + w', \qquad p = \overline{p} + p' \tag{2.33}$$

The flow magnitudes are Reynolds averaged:

$$\overline{u} = \frac{1}{T}\int_0^T (u)dt\,. \tag{2.34}$$

This ansatz is now introduced into (2.4):

$$\frac{\partial\rho(\overline{u}+u')}{\partial t} + \frac{\partial\rho(\overline{u}+u')^2}{\partial x} + \frac{\partial\rho(\overline{u}+u')(\overline{v}+v')}{\partial y} + \frac{\partial\rho(\overline{u}+u')(\overline{w}+w')}{\partial z} = F_X + \frac{\partial\tau_{xx}}{\partial x} + \frac{\partial\tau_{yx}}{\partial y} + \frac{\partial\tau_{zx}}{\partial z}. \tag{2.35}$$

The Reynolds averaged magnitudes describe the global unsteady flow, whereas the turbulent fluctuations are present in the additional fluctuation terms on the right side of (2.38), (2.39), and (2.40). The additional fluctuation terms are called Reynolds stresses. The separation of the velocity component in x-direction is shown exemplarily in Fig. 2-2.

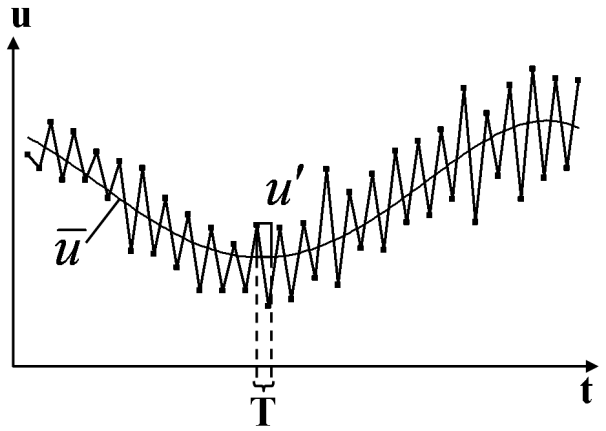

Fig. 2-2 Separation of u velocity in time-averaged and turbulent fluctuation component

When time averaging (2.35), in which all flow parameters have been separated into a time averaged and fluctuating term, it has to be considered that:

$$\bar{\bar{f}} = \bar{f} \qquad \overline{f}' = 0 \qquad \overline{f\overline{f}'} \neq 0\,. \tag{2.36}$$

Here, f represents any flow magnitude. Due to the definition of the Reynolds averaging $\overline{f}' = 0$, as shown exemplarily for the u velocity:

$$\overline{u} = \frac{1}{T}\int_0^T (u)dt = \overline{u} = \frac{1}{T}\int_0^T (\overline{u}+u')dt = \frac{1}{T}\int_0^T (\overline{u})dt + \frac{1}{T}\int_0^T (u')dt \Rightarrow \overline{u} = \overline{u} + \overline{u}';\Rightarrow \overline{u}' = 0\,.$$

Thus, the time averaged continuity equation for flows with constant density is written as:

$$\frac{\partial \overline{u}}{\partial x}+\frac{\partial \overline{v}}{\partial y}+\frac{\partial \overline{w}}{\partial z}=0\,. \tag{2.37}$$

And the Reynolds equations for flows with constant density are:

$$\begin{aligned}&\frac{\partial(\rho\overline{u})}{\partial t}+\frac{\partial(\rho\overline{u}\,\overline{u})}{\partial x}+\frac{\partial(\rho\overline{u}\,\overline{v})}{\partial y}+\frac{\partial(\rho\overline{u}\,\overline{w})}{\partial z}=F_x-\frac{\partial \overline{p}}{\partial x}+\frac{\partial \overline{\sigma}_{xx}}{\partial x}+\frac{\partial \overline{\tau}_{yx}}{\partial y}+\frac{\partial \overline{\tau}_{zx}}{\partial z}\\&-\left(\frac{\partial(\rho\overline{u'u'})}{\partial x}+\frac{\partial(\rho\overline{u'v'})}{\partial y}+\frac{\partial(\rho\overline{u'w'})}{\partial z}\right),\end{aligned} \tag{2.38}$$

$$\begin{aligned}&\frac{\partial(\rho\overline{v})}{\partial t}+\frac{\partial(\rho\overline{v}\,\overline{u})}{\partial x}+\frac{\partial(\rho\overline{v}\,\overline{v})}{\partial y}+\frac{\partial(\rho\overline{v}\,\overline{w})}{\partial z}=F_y-\frac{\partial \overline{p}}{\partial y}+\frac{\partial \overline{\tau}_{xy}}{\partial x}+\frac{\partial \overline{\sigma}_{yy}}{\partial y}+\frac{\partial \overline{\tau}_{zy}}{\partial z}\\&-\left(\frac{\partial(\rho\overline{v'u'})}{\partial x}+\frac{\partial(\rho\overline{v'v'})}{\partial y}+\frac{\partial(\rho\overline{w'v'})}{\partial z}\right),\end{aligned} \tag{2.39}$$

$$\begin{aligned}&\frac{\partial(\rho\overline{w})}{\partial t}+\frac{\partial(\rho\overline{w}\,\overline{u})}{\partial x}+\frac{\partial(\rho\overline{w}\,\overline{v})}{\partial y}+\frac{\partial(\rho\overline{w}\,\overline{w})}{\partial z}=F_z-\frac{\partial \overline{p}}{\partial z}+\frac{\partial \overline{\tau}_{xz}}{\partial x}+\frac{\partial \overline{\tau}_{yz}}{\partial y}+\frac{\partial \overline{\sigma}_{zz}}{\partial z}\\&-\left(\frac{\partial(\rho\overline{w'u'})}{\partial x}+\frac{\partial(\rho\overline{w'v'})}{\partial y}+\frac{\partial(\rho\overline{w'w'})}{\partial z}\right).\end{aligned} \tag{2.40}$$

2.4.2 Energy Equation for Turbulent Flows

Analogue to the approach leading to the Reynolds equations, the Reynolds ansatz is introduced to the energy equation for incompressible flows as:

$$h=\overline{h}+h'\,. \tag{2.41}$$

Thus, the energy equation describing turbulent flows with constant density can be written as:

$$\begin{aligned}&\rho\left(\frac{\partial \overline{h}}{\partial t}+u\frac{\partial \overline{h}}{\partial x}+v\frac{\partial \overline{h}}{\partial y}+w\frac{\partial \overline{h}}{\partial z}\right)=\frac{\partial}{\partial x}\left(\frac{\lambda}{c_p}\frac{\partial \overline{h}}{\partial x}\right)+\frac{\partial}{\partial y}\left(\frac{\lambda}{c_p}\frac{\partial \overline{h}}{\partial y}\right)+\frac{\partial}{\partial z}\left(\frac{\lambda}{c_p}\frac{\partial \overline{h}}{\partial z}\right)+\overline{\vec{F}}\cdot\overline{\vec{v}}+\rho\dot{q}\\&-\left(\frac{\partial(\rho\overline{h'u'})}{\partial x}+\frac{\partial(\rho\overline{h'v'})}{\partial y}+\frac{\partial(\rho\overline{h'w'})}{\partial z}\right).\end{aligned} \tag{2.42}$$

2.4.3 Equations for Turbulent Flows with Variable Density

For flows in which the density changes, as analyzed in chapters 6 (Analysis of Temperature Depending Effects) and 7 (Integrated Results for the Upper Mixing Chamber), another approach is used. Mass-averaged quantities are introduced as:

$$\widetilde{u} = \frac{\overline{\rho u}}{\overline{\rho}}, \qquad \widetilde{v} = \frac{\overline{\rho v}}{\overline{\rho}}, \qquad \widetilde{w} = \frac{\overline{\rho w}}{\overline{\rho}}, \qquad \widetilde{h} = \frac{\overline{\rho h}}{\overline{\rho}}. \tag{2.43}$$

The flow magnitudes are Favre averaged:

$$\overline{\rho u} = \frac{1}{T}\int_0^T (\rho u)dt\,. \tag{2.44}$$

According to the approach for flows without density changes, the different quantities are made up of time averaged and fluctuating quantities. For the mass averaged quantities the fluctuations will be denoted by two dashes. The density and the pressure do not have to be mass averaged. This leads to the Reynolds ansatz for flows with variable density:

$$\begin{aligned} u &= \widetilde{u} + u'', \quad & v &= \widetilde{v} + v'', \quad & w &= \widetilde{w} + w'', \quad & h &= \widetilde{h} + h'', \\ p &= \overline{p} + p', & \rho &= \widetilde{\rho} + \rho''. \end{aligned} \tag{2.45}$$

In addition it has to be considered that:

$$\overline{f}'' \neq 0\,, \qquad \overline{\rho}\overline{f}'' = 0\,, \qquad \overline{\rho}'\widetilde{u} = 0\,, \qquad \overline{\rho u}'' = 0\,. \tag{2.46}$$

Introducing the Reynolds ansatz for flows with variable density in the continuity equation, the Navier Stokes equations, and the energy equation describing all flows with variable density leads to the time averaged continuity equation for flows with variable density:

$$\frac{\partial\overline{\rho}}{\partial t} + \frac{\partial(\overline{\rho}\widetilde{u})}{\partial x} + \frac{\partial(\overline{\rho}\widetilde{v})}{\partial y} + \frac{\partial(\overline{\rho}\widetilde{w})}{\partial z} = 0\,, \tag{2.47}$$

the Reynolds equations for flows with variable density:

$$\begin{aligned} &\frac{\partial(\overline{\rho}\widetilde{u})}{\partial t} + \frac{\partial(\overline{\rho}\widetilde{u}\widetilde{u})}{\partial x} + \frac{\partial(\overline{\rho}\widetilde{u}\widetilde{v})}{\partial y} + \frac{\partial(\overline{\rho}\widetilde{u}\widetilde{w})}{\partial z} = F_x - \frac{\partial\overline{p}}{\partial x} + \frac{\partial\overline{\sigma}_{xx}}{\partial x} + \frac{\partial\overline{\tau}_{yx}}{\partial y} + \frac{\partial\overline{\tau}_{zx}}{\partial z} \\ &-\left(\frac{\partial(\overline{\rho u''u''})}{\partial x} + \frac{\partial(\overline{\rho u''v''})}{\partial y} + \frac{\partial(\overline{\rho u''w''})}{\partial z}\right), \end{aligned} \tag{2.48}$$

$$\begin{aligned} &\frac{\partial(\overline{\rho}\widetilde{v})}{\partial t} + \frac{\partial(\overline{\rho}\widetilde{v}\widetilde{u})}{\partial x} + \frac{\partial(\overline{\rho}\widetilde{v}\widetilde{v})}{\partial y} + \frac{\partial(\overline{\rho}\widetilde{v}\widetilde{w})}{\partial z} = F_y - \frac{\partial\overline{p}}{\partial y} + \frac{\partial\overline{\tau}_{xy}}{\partial x} + \frac{\partial\overline{\sigma}_{yy}}{\partial y} + \frac{\partial\overline{\tau}_{zy}}{\partial z} \\ &-\left(\frac{\partial(\overline{\rho v''u''})}{\partial x} + \frac{\partial(\overline{\rho v''v''})}{\partial y} + \frac{\partial(\overline{\rho w''v''})}{\partial z}\right), \end{aligned} \tag{2.49}$$

$$\begin{aligned} &\frac{\partial(\overline{\rho}\widetilde{w})}{\partial t} + \frac{\partial(\overline{\rho}\widetilde{w}\widetilde{u})}{\partial x} + \frac{\partial(\overline{\rho}\widetilde{w}\widetilde{v})}{\partial y} + \frac{\partial(\overline{\rho}\widetilde{w}\widetilde{w})}{\partial z} = F_z - \frac{\partial\overline{p}}{\partial z} + \frac{\partial\overline{\tau}_{xz}}{\partial x} + \frac{\partial\overline{\tau}_{yz}}{\partial y} + \frac{\partial\overline{\sigma}_{zz}}{\partial z} \\ &-\left(\frac{\partial(\overline{\rho w''u''})}{\partial x} + \frac{\partial(\overline{\rho w''v''})}{\partial y} + \frac{\partial(\overline{\rho w''w''})}{\partial z}\right), \end{aligned} \tag{2.50}$$

with:

$$\begin{aligned}\overline{\sigma}_{ii} &= \mu\left(2\frac{\partial\widetilde{u}_i}{\partial x_i}-\frac{2}{3}\left(\nabla\cdot\widetilde{\vec{v}}\right)\right)+\mu\left(2\frac{\partial\overline{u_{ii}''}}{\partial x_i}-\frac{2}{3}\left(\nabla\cdot\overline{\vec{v}''}\right)\right),\\ \overline{\tau}_{ii} &= \mu\left(\frac{\partial\widetilde{u}_i}{\partial x_j}+\frac{\partial\widetilde{u}_j}{\partial x_i}\right)+\mu\left(\frac{\partial\overline{u_i''}}{\partial x_j}+\frac{\partial\overline{u_j''}}{\partial x_i}\right),\end{aligned} \tag{2.51}$$

and the time averaged energy equation for flows with variable density:

$$\begin{aligned}&\left(\frac{\partial(\overline{\rho}\widetilde{h})}{\partial t}+\frac{\partial(\overline{\rho}\widetilde{h}\widetilde{u})}{\partial x}+\frac{\partial(\overline{\rho}\widetilde{h}\widetilde{v})}{\partial y}+\frac{\partial(\overline{\rho}\widetilde{h}\widetilde{w})}{\partial z}\right)=\frac{\partial}{\partial x}\left(\frac{\lambda}{c_p}\frac{\partial\widetilde{h}}{\partial x}\right)+\frac{\partial}{\partial y}\left(\frac{\lambda}{c_p}\frac{\partial\widetilde{h}}{\partial y}\right)+\frac{\partial}{\partial z}\left(\frac{\lambda}{c_p}\frac{\partial\widetilde{h}}{\partial z}\right)\\ &-\left(\frac{\partial\left(\overline{\rho}\overline{h''}\overline{u''}\right)}{\partial x}+\frac{\partial\left(\overline{\rho}\overline{h''}\overline{v''}\right)}{\partial y}+\frac{\partial\left(\overline{\rho}\overline{h''}\overline{w''}\right)}{\partial z}\right).\end{aligned} \tag{2.52}$$

This Reynolds Averaged Navier-Stokes approach for the conservation of momentum and energy allows accounting for the local fluctuations in turbulent flows without resolving them detailed in time and space.

2.4.4 Turbulence Modeling

The additional fluctuation terms in the Reynolds equations, as well as in the energy equation for turbulent flows have to be modeled using so-called turbulence models. Starting point are the equations describing flows with constant density. The models for flows with variable density are derived in analogy. The additional fluctuation terms can be summarized in a tensor for the Reynolds equations and in a vector for the turbulent energy equation.

$$\tau^t=-\rho\begin{pmatrix}\overline{u'u'} & \overline{u'v'} & \overline{u'w'}\\ \overline{v'u'} & \overline{v'v'} & \overline{v'w'}\\ \overline{w'u'} & \overline{w'v'} & \overline{w'w'}\end{pmatrix}\qquad q^t=-\rho\begin{pmatrix}\overline{u'h'}\\ \overline{v'h'}\\ \overline{w'h'}\end{pmatrix} \tag{2.53}$$

Due to symmetry of the matrix, 6 Reynolds stresses and 3 turbulent heat fluxes have to be modeled. The Reynolds equations and the turbulent energy equation are written as follows:

$$\rho\left(\frac{\partial\overline{\vec{v}}}{\partial t}+\left(\overline{\vec{v}}\cdot\nabla\right)\overline{\vec{v}}\right)=\overline{\vec{F}}-\nabla\overline{p}+\nabla\,\overline{\tau}+\nabla\,\tau_t\,, \tag{2.54}$$

$$\rho\left(\frac{\partial\overline{h}}{\partial t}+\overline{\vec{v}}\cdot\nabla\overline{h}\right)=\frac{\partial}{\partial x}\left(\frac{\lambda}{c_p}\frac{\partial\overline{h}}{\partial x}\right)+\frac{\partial}{\partial y}\left(\frac{\lambda}{c_p}\frac{\partial\overline{h}}{\partial y}\right)+\frac{\partial}{\partial z}\left(\frac{\lambda}{c_p}\frac{\partial\overline{h}}{\partial z}\right)-q^t\,. \tag{2.55}$$

The eddies in turbulent flows lead to additional mixing and transport of mass, momentum, and energy, thus leading to higher forces and heat transfer at walls. Considering the fact, that in a microscopic scale, momentum and energy are transported by diffusion, the turbulent transport will be modeled in analogy. This approach leads to the eddy-viscosity model for the Reynolds stresses.

2.4.4.1 Eddy Viscosity Approach

To enable a more compact way of writing the necessary equations, the velocity components in x-, y-, and z-direction will be written as u_1, u_2, and u_3 or u_i, u_j, respectively. The Reynolds stresses will be modeled in analogy to the approach for Newtonian fluids applied in (2.13), (2.14), (2.15), as:

$$-\rho\overline{u_i'u_j'} = \mu_t\left(\frac{\partial\overline{u}_i}{\partial x_j}+\frac{\partial\overline{u}_j}{\partial x_i}\right)-\frac{2}{3}\rho K\delta_{ij}, \qquad \delta_{ij}=1, \text{ for } i=j \text{ and } \delta_{ij}=0, \text{ for } i\neq j. \tag{2.56}$$

In this equation μ_t is the eddy viscosity. In laminar flows, the average velocity can be described as the mean velocity of all molecules. The specific velocity of the molecules is averaged over a certain, very small length scale. The Reynolds averaged velocity in turbulent flows is the averaged velocity of the specific, local turbulent eddy structures, also averaged over an adequate turbulent length scale.

The numerical effort of these, so called eddy viscosity models is smaller compared to models, in which all the additional terms are modeled separately. The turbulent kinetic energy per mass K, which is used in (2.56), is defined as:

$$K=\frac{1}{2}\overline{u_i'u_i'}=\frac{1}{2}\left(\overline{u_1'}^2+\overline{u_2'}^2+\overline{u_3'}^2\right). \tag{2.57}$$

The turbulent heat fluxes are assumed to be proportional to the gradient of the mean enthalpy and are modeled as:

$$-\rho\overline{u_i'h'}=\lambda_t\frac{\partial\overline{h}}{\partial x_i} \qquad \text{or} \qquad -\overline{u_i'h'}=a_t\frac{\partial\overline{h}}{\partial x_i}. \tag{2.58}$$

Either λ_t, which is the turbulent thermal conductivity or a_t, the turbulent thermal diffusivity has to be modeled. Considering the fact that the eddy viscosity and the turbulent thermal diffusion are transported by the same turbulent fluctuations, it can be seen that they are not independent from each other and are linked by the turbulent Prandtl-number, defined as:

$$\mathrm{Pr}_t=\frac{\nu_t}{a_t}. \tag{2.59}$$

For fluids with small heat conductivity as used in the analyses presented in this work $\nu_t \approx a_t$, and Pr_t is constant and close to one.

In the k-ε model defined by Launder and Spalding in [42], the eddy viscosity μ_t is expressed as:

$$\mu_t=\rho C_\mu\frac{K^2}{\varepsilon}. \tag{2.60}$$

For the turbulent kinetic energy K and the dissipation ε, transport equations are solved, to identify the local distribution of the eddy viscosity μ_t in the flow. The k-ε model is only applicable to completely turbulent flows. K is describing the energy of the turbulent fluctua-

tions, while ε is describing their decay due to friction. Both magnitudes are produced, transported, and dissipated in the flow.

$$\frac{\partial(\rho K)}{\partial t}+\frac{\partial(\rho\overline{u}_j K)}{\partial x_j}=\underbrace{\mu_t\frac{\partial\overline{u}_i}{\partial x_j}\left(\frac{\partial\overline{u}_i}{\partial x_j}+\frac{\partial\overline{u}_j}{\partial x_i}\right)}_{Production}+\underbrace{\frac{\partial}{\partial x_j}\left(\mu\frac{\partial K}{\partial x_j}+\frac{\mu_t}{\sigma_k}\frac{\partial K}{\partial x_i}\right)}_{Diffusion}+ \underbrace{\mu_t\frac{g_i}{\mathrm{Pr}_t}\frac{1}{\rho}\frac{\partial\rho}{\partial x_i}}_{Buoyancy}-\underbrace{\rho\varepsilon}_{Destruction} \tag{2.61}$$

$$\frac{\partial(\rho\varepsilon)}{\partial t}+\frac{\partial(\rho\overline{u}_j\varepsilon)}{\partial x_j}=\underbrace{C_{\varepsilon1}\frac{\varepsilon}{K}\mu_t\frac{\partial\overline{u}_i}{\partial x_j}\left(\frac{\partial\overline{u}_i}{\partial x_j}+\frac{\partial\overline{u}_j}{\partial x_i}\right)}_{Production}+\underbrace{\frac{\partial}{\partial x_j}\left(\mu\frac{\partial\varepsilon}{\partial x_j}+\frac{\mu_t}{\sigma_\varepsilon}\frac{\partial\varepsilon}{\partial x_i}\right)}_{Diffusion} + \underbrace{C_{\varepsilon3}\rho\frac{\varepsilon}{K}\mu_t\frac{g_i}{\mathrm{Pr}_t}\frac{1}{\rho}\frac{\partial\rho}{\partial x_i}}_{Buoyancy}-\underbrace{C_{\varepsilon2}\rho\frac{\varepsilon^2}{K}}_{Destruction} \tag{2.62}$$

With the following empirical model parameters defined in the model: C_μ=0.09, $C_{\varepsilon1}$=1.44, $C_{\varepsilon2}$=1.92, σ_K=1.0, σ_ε=1.3. The left side of the K and ε equations is composed of the time dependant and convective terms. The first term on the right side of both equations represents the production, the second one diffusive term, the third one describes buoyancy influences, with g_i being the vector of the acceleration due to gravity, and the last term in the K-equation is the sink term. $C_{\varepsilon3}$ in the buoyancy term of the ε equation describes the ration between the flow velocity parallel and orthogonal to the direction of gravity.

Turbulent structures emerge due to instabilities. First, large structures or eddies are produced which eventually decay into small structures. The large structures carry most of the energy and can be associated with the turbulent kinetic energy K. The turbulent kinetic energy is mostly dissipated in the smaller structures, which therefore can be associated with ε. For industrial applications, where shear stresses or heat fluxes at the wall do not play the dominant role, the k-ε model has become the most widely used turbulence model. The flow patterns within the flow field are described well in the k-ε model.

Other turbulence models have been developed for different applications. In the ERCOFTAC best practice guidelines [11] a general overview is given over the performance of turbulence models for different flows. The k-ϖ model, among other sources described in the book of Wilcox [86], for instance, performs very well for boundary layer flows close to the wall. Besides the k-equation, a transport equation for the frequency of the large eddies ϖ is solved. A compromise between these two most widely used models (k-ε and k-ϖ) is realized with the k-ϖ SST (shear stress transport) model proposed by Menter in [48]. This model maintains the good solutions obtained by the k-ϖ model close to the wall and blending into the better suited k-ε model away from the wall.

Reynolds Stress Models and Non-Linear Models

To capture anisotropic effects of the flow, e.g. strong swirls, two different approaches have been conducted. These are non-linear eddy viscosity models and the Reynolds stress models RSM. In Reynolds stress models, each of the 6 independent Reynolds stresses are modeled separately, thus, not only two additional equations have to be solved to account for the turbulent fluctuations, but six. Since the goal of this work is a method for design optimization, which requires many simulations and the numerical effort of the Reynolds stress models is much higher, they aren't applied in this work. Non-linear eddy viscosity models, however, might be a promising approach. Here, non-linear relationships between the Reynolds stresses and the rate of strain are adopted as described in the methodology of Star-CD [14].

The choice of an adequate turbulence model for the analysis of the flow in the upper mixing chamber is based on the comparison between an experiment and the obtained results for this chosen experiment as shown in chapter 3.3.

2.4.5 Applied Boundary Conditions

Inlet Boundary

At the inlets to the fluid domain, the velocity components u_i in all directions are defined. Also, the density ρ, for non-isothermal simulations, the temperature T and values for the turbulent kinetic energy K and the dissipation ε have to be given.

Outlet Boundary

At the outlets, specifications for the velocity components u_i, the temperature T, and the turbulent variables are required. In general, the boundary condition at the outlet should only have a weak influence on the upstream flow and therefore it is defined far away from the analyzed geometry. In this work, so called pressure boundaries are applied for all simulations. At the outlet, the pressure is defined at a certain value, whereas the gradients of all other variables are set to zero. Thus, the flow variables can adjust to the main flow.

Wall Boundary

Directly at the wall, the fluid velocity is equal to the velocity of the wall, since a viscous fluid sticks to the wall. Here, all walls are motionless, which means that the velocity at the wall is zero for all simulations carried out within this work. Thus, the gradients in the flow variables close to the wall become extremely large as the wall distance reduces to zero. To resolve the flow in the boundary layer close to the wall, a large number of cells would be necessary in this region. Due to the fact that the viscous effects close to the wall become dominant, since the turbulent fluctuations are damped, the standard turbulence models are not valid in this region and have to be adapted. For the here applied turbulence models, the near-wall region is not explicitly resolved, but so-called wall functions are applied, reducing the numerical effort significantly.

The stationary turbulent flow close to a solid surface can be described for the dimensionless velocity u^+ with the dimensionless wall distance y^+, defined with the friction velocity u_τ according to Versteeg and Malalasekera [79] as:

$$u^+ = \frac{u}{u_\tau}, \qquad y^+ = \frac{\rho \Delta y u_\tau}{\mu}, \qquad u_\tau = \sqrt{\frac{\tau_w}{\rho}}. \tag{2.63}$$

Here, Δy is the wall distance and τ_w is the wall shear stress.

The near wall region can be divided into three parts. In the viscous sublayer, which is in contact with the wall, it is assumed that they are no turbulent eddying motions due to the wall and thus, in the absence of turbulence, the shear stress is constant and equal to the wall shear stress τ_w throughout the layer. The viscous sublayer layer is very thin, it starts at $y^+ = 0$ and ends at $y^+ = 5$. Due to $u^+ = y^+$, it is also called linear sublayer.

The log-law layer is the region just outside of the viscous sublayer. Here, viscous and turbulent effects influence the flow and the log-law is valid describing the functional relationship between u^+ and y^+:

$$u^+ = \frac{1}{\kappa} \ln y^+ + C, \tag{2.64}$$

with $\kappa = 0.41$ and $C = 5.5$. For the applied models in this work, wall functions are used at the wall according to the following relationship:

$$u^+ = \begin{cases} y^+ & ; y^+ \le {y^+}_m \\ \frac{1}{\kappa} \ln y^+ + C & ; y^+ \ge {y^+}_m \end{cases}. \tag{2.65}$$

The two equations meet at ${y_m}^+ \approx 12$. To obtain good results when using high-Reynolds turbulent models with wall functions, the criteria $30 \le y^+ \ge 100$ should be applied for the cell centers, according to the best practice guidelines ([11]).

2.4.6 Symmetry Boundary

Symmetry boundaries are applied to the planes, where the analyzed geometry model has been cut. They are defined that all flow variables in one side of the surface are a mirror image to the ones on the other side. This means that the velocities orthogonal to the symmetry plane disappear. The applied inlet, wall, and symmetry boundaries are called Dirichlet boundary, which means that the values of the flow variables are defined directly, whereas the pressure boundary at the outlet is a Neumann boundary condition. Here, the gradients of the flow variables are specified.

2.4.7 Numerical Methods

The equations describing general flows usually aren't solvable analytically. The approach is to discretize them and then solve the coupled system of discretized equations iteratively as described by Oertel and Laurien [43] and Ferziger and Peric [17].

Discretization

In this work, only steady state simulations are carried out, which is why the discretization in time is not regarded. After the governing set of equations for the analyzed problem has been chosen, a discretization method has to be selected to approximate the differential equations leading to algebraic equations. Star CD, being the used program in this work, uses the finite volume method (FVM). The fluid domain is divided into a number of contiguous volumes or cells connected by nodes, which represent the limitation of each cell. In the center of the cells, the fluid variables are calculated applying the conservation equations; therefore, the Gauss theorem is applied, which states that the change of a magnitude in a volume is equal to the fluxes over the regarded volume's surface area. Since the position of the cell centers, where all fluid variables are defined differs from the position where the fluxes are calculated, an interpolation method has to be selected to approximate the surface integrals.

The applied interpolation methods in this work are the Upwind Differencing Scheme (UD) and the Quadratic Upstream Interpolation of Convective Kinematics (QUICK). For the UD Scheme, the value for each fluid variable is approximated from the value of the cell, where the flow comes from. For the QUICK method, the value of the neighboring cell is not approximated by a straight line, but by a quadratic function. Therefore, three points, respectively cell values are needed, not only one or two neighboring cells. To construct the quadratic function, the two neighboring cell values are used and the third point is taken from an additional cell on the upstream side.

Solution Method

After discretizing the equations describing the flow, the remaining system of non-linear algebraic equations has to be solved. For the analyses presented in this work, the Semi-Implicit Method for Pressure Linked Equations (SIMPLE), which suitable for steady state conditions has been used. Here, the velocity components of the momentum equations are calculated with a guessed pressure field. The solution of this calculation is the velocity field u_{*_i}, which holds for the momentum equations. Since the velocity field has to also hold for the continuity equation, a pressure correction equation that includes the continuity constraint is solved with the velocity components u_{*_i}. With the corrected pressure field, corrected velocity components u_{*_i} are calculated. This process is carried out iteratively until the obtained velocity field converges, respectively until the changes for the velocity components from one iteration to the previous one stay within a certain limit.

Numerical Errors

There are different sources for errors in numerical simulations. The model error is the difference the applied models show in comparison to reality. A validation, which means the comparison of the simulation with an experiment, needs to be carried out to quantify the model error. Another error is the discretization error due to the discretization method and the grid resolution. Generally speaking, regions with large gradients in the flow variables need to be resolved much higher. Thus, it needs to be checked if the solution is not dependent on the discretization and the discretization method.

2.5 Analysis Strategy

The exact temperature distribution at the inlet of the upper mixing chamber will continue to be unknown. As outlined in chapter 1.3, it will depend on power and mass flow distribution in the evaporator assemblies, which vary with burn-up and time, but also with statistical effects like tolerances, uncertainties, local perturbations, and fluctuations of the operating conditions. The hot channel factor of 2, estimated by Schulenberg et al. in [68] can in general occur in any assembly of the evaporator. The strategy for optimization of the mixing chamber is therefore to limit the influence of a temperature perturbation in any inlet to the mixing chamber on any of its outlets.

An effective method to study the mixing of several inlet flows with different temperatures in one single CFD analysis is the use of passive scalars as markers. Applying this strategy, each inlet is charged with a passive scalar for which a transport equation is solved; pictured can this idea with the coloring of the different inlet flows. The inlet scalar distribution is then evaluated at each outlet. This method is applicable to first, preliminary analyses in which isothermal flow is assumed, as well as to cases with a certain temperature distribution at the inlet side. The transport equations for the energy, here expressed with the temperature T (2.66) and for an exemplary scalar Y_m (2.67) for turbulent flows are defined as follows:

$$\frac{\partial \overline{T}}{\partial t} + \frac{\partial}{\partial x_j}\left(\overline{u_j}\,\overline{T}\right) = \frac{\partial}{\partial x_j}\left[\left(a + \frac{\nu_t}{\mathrm{Pr}_t}\right)\frac{\partial \overline{T}}{\partial x_j}\right], \tag{2.66}$$

$$\frac{\partial \overline{Y_m}}{\partial t} + \frac{\partial}{\partial x_j}\left(\overline{u_j}\,\overline{Y_m}\right) = \frac{\partial}{\partial x_j}\left[\left(D + \frac{\nu_t}{\mathrm{Sc}_t}\right)\frac{\partial \overline{Y_m}}{\partial x_j}\right]. \tag{2.67}$$

It can be seen that the two equations only differ in the diffusion terms a, describing the thermal diffusivity and D, describing the diffusion coefficient of the transported scalar and in the turbulent Prandtl-number Pr_t and turbulent Schmidt-number Sc_t.

The very high Peclet-number with a value of $\mathrm{Pe} = 7.3 \cdot 10^6$ calculated in chapter 2.1 suggests that the thermal diffusivity a is very small compared to the turbulent term and can be neglected. Also, since the transport of the scalar should reflect the energy transport in the flow, Sc_t is set equal to Pr_t, thus leading to the possibility of applying the described strategy of using passive scalars for the evaluation of the mixing and this way of the temperature homogenization, if the thermal diffusivity a and the diffusion coefficient D is set to equal zero.

The great advantages when using these scalars are:

1) For a potential hot outlet, not only the increased temperature can be identified, but also the inlet from which the transported hot streak is derived.

2) Predictions for the mixing performance of a mixing chamber used for temperature homogenization can be made in one single simulation, rather than evaluating various given inlet temperature distributions and the enthalpy distribution at the outlets.

A vital requirement for this applied evaluation strategy is that the used scalars are passive, which means that they do not influence the flow and each other.

The analyzed flow has been characterized as incompressible ($\rho = \rho(T)$) and turbulent. Also, only steady state analyses are performed and mixing shall be evaluated with passive scalars. In case of small temperature perturbations, we can describe the flow with constant density with the following equations:

The time averaged continuity equation:

$$\frac{\partial \overline{u}_i}{\partial x_i} = 0\,, \tag{2.68}$$

the steady-state Reynolds equations, describing turbulent flows:

$$\rho\left(\overline{u}_j \frac{\partial \overline{u}_i}{\partial x_i}\right) = -\frac{\partial \overline{p}_i}{\partial x_i} + \frac{\partial}{\partial x_i}\left[\left(\mu + \mu_t\right)\left(\frac{\partial \overline{u}_i}{\partial x_j} + \frac{\partial \overline{u}_j}{\partial x_i}\right)\right], \tag{2.69}$$

the steady-state transport equations for the turbulent quantities K and ε :

$$\frac{\partial\left(\rho \overline{u}_j K\right)}{\partial x_j} = \mu_t \frac{\partial \overline{u}_i}{\partial x_j}\left(\frac{\partial \overline{u}_i}{\partial x_j} + \frac{\partial \overline{u}_j}{\partial x_i}\right) + \frac{\partial}{\partial x_j}\left(\mu \frac{\partial K}{\partial x_j} + \frac{\mu_t}{\sigma_k}\frac{\partial K}{\partial x_i}\right) + \mu_t \frac{g_i}{\mathrm{Pr}_t}\frac{1}{\rho}\frac{\partial \rho}{\partial x_i} - \rho\varepsilon\,, \tag{2.70}$$

$$\begin{aligned}\frac{\partial\left(\rho \overline{u}_j \varepsilon\right)}{\partial x_j} &= C_{\varepsilon 1}\frac{\varepsilon}{K}\mu_t \frac{\partial \overline{u}_i}{\partial x_j}\left(\frac{\partial \overline{u}_i}{\partial x_j} + \frac{\partial \overline{u}_j}{\partial x_i}\right) + \frac{\partial}{\partial x_j}\left(\mu \frac{\partial \varepsilon}{\partial x_j} + \frac{\mu_t}{\sigma_\varepsilon}\frac{\partial \varepsilon}{\partial x_i}\right) \\ &+ C_{\varepsilon 3}\rho\frac{\varepsilon}{K}\mu_t \frac{g_i}{\mathrm{Pr}_t}\frac{1}{\rho}\frac{\partial \rho}{\partial x_i} - C_{\varepsilon 2}\rho\frac{\varepsilon^2}{K},\end{aligned} \tag{2.71}$$

which are linked with the equations (2.69) by the equations: (2.53), (2.56), and (2.60).

For the transport of a scalar $\overline{Y}_i$, including energy, a transport equation is solved according to:

$$\rho\left(\overline{u}_j \frac{\partial \overline{Y}_i}{\partial x_i}\right) = \frac{\partial}{\partial x_i}\left(\left(D + D_t\right)\frac{\partial \overline{Y}_i}{\partial x_i}\right). \tag{2.72}$$

A system of 6 non-linear differential equations, together with a variable amount for the different scalars transported, has to be solved, whereas, in cases where the energy equation has an influence on the flow field, the equations describing flows with variable density have to be solved.

3 Method for the Analysis of Complex Mixing Chambers

3.1 Simplification Method

The applied method for the analysis of the upper mixing chamber that should be applicable to other complex mixing chambers is based on the simplification of the geometry. If complex structures in the flow are disregarded, their effects on the flow are not taken into account as well. For flows in or around complex geometries, simulations are often linked to a very high numerical effort since a large number of cells is necessary to resolve the geometric details. Especially for design optimization using CFD methods, this leads to very long computing and preparation times for the simulations, in particular if many simulations are necessary, like here. The different steps of the simplification model procedure are also outlined in [84].

The simplification method describes the approach in which a simplified grid is used to calculate flows in and around complex geometries by applying source terms in the equations describing the flow.

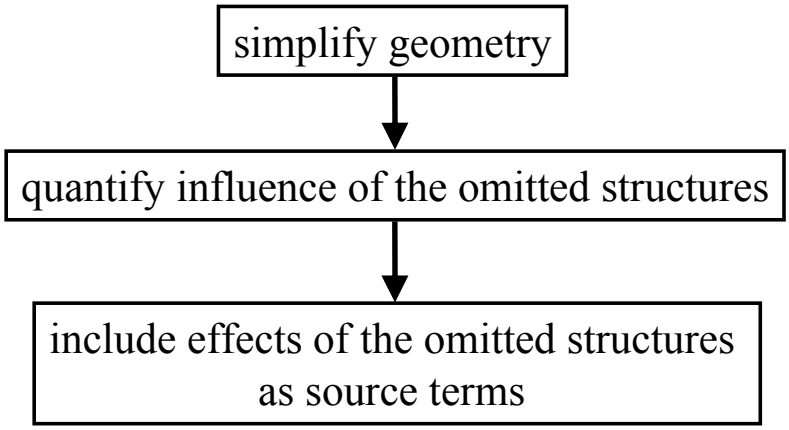

Fig. 3-1 Procedure of the simplification method

The idea is to economize the numerical effort significantly, while still taking into account the effects, complex geometries have on the flow. However, the complex structures shall not be resolved in a detailed way. For the highly anisotropic flow in the upper mixing chamber with a rather distinctive global flow field, source terms in the Reynolds equations seem to be the most promising approach. Therefore, volumetric forces are introduced to the right side of (2.69) leading to:

$$\rho\left(\overline{u}_j \frac{\partial \overline{u}_i}{\partial x_i}\right) = -\frac{\partial \overline{p}_i}{\partial x_i} + \frac{\partial}{\partial x_i}\left[\left(\mu + \mu_t\right)\left(\frac{\partial \overline{u}_i}{\partial x_j} + \frac{\partial \overline{u}_j}{\partial x_i}\right)\right] + \underbrace{F_{iS}}_{volumetric\ \ forces} . \tag{3.1}$$

Since these volumetric forces F_{iS} represent complex geometries, their definition is the crucial aspect to successfully apply them instead of resolving the detailed geometry.

The definition of the adequate forces differs from mixing chamber to mixing chamber. For the upper mixing chamber, different approaches were pursued as described in chapter 5 (Including the Effects of the Omitted Structures).

The first step of the simplification method is:

1) Simplifying the geometry.

Applying this first step of the simplification method to the upper mixing chamber of the HPLWR leads to the simplified model. In this model the geometry is simplified by disregarding the complex headpiece structure. Thus, the moderator boxes and the thickness of the headpiece struts are omitted and only the outer contour of the headpieces struts, the window elements with 2-dimensional, impermeable baffle cells as shown in Fig. 3-2 are introduced.

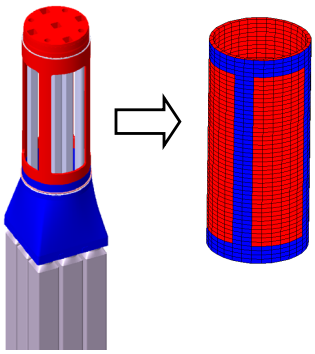

Fig. 3-2 Headpiece geometry in the simplified model – reduced to window element

The simplified model is shown on the right side of Fig. 3-3, while the actual geometry of the upper mixing chamber is shown on the left side. Even though the structure of the simplified model is still rather complicated, it is much simpler than the actual geometry. Adequate results for the mixing and the pressure drop now are achieved with less then one million cells, when regarding 1/8th of the geometry.

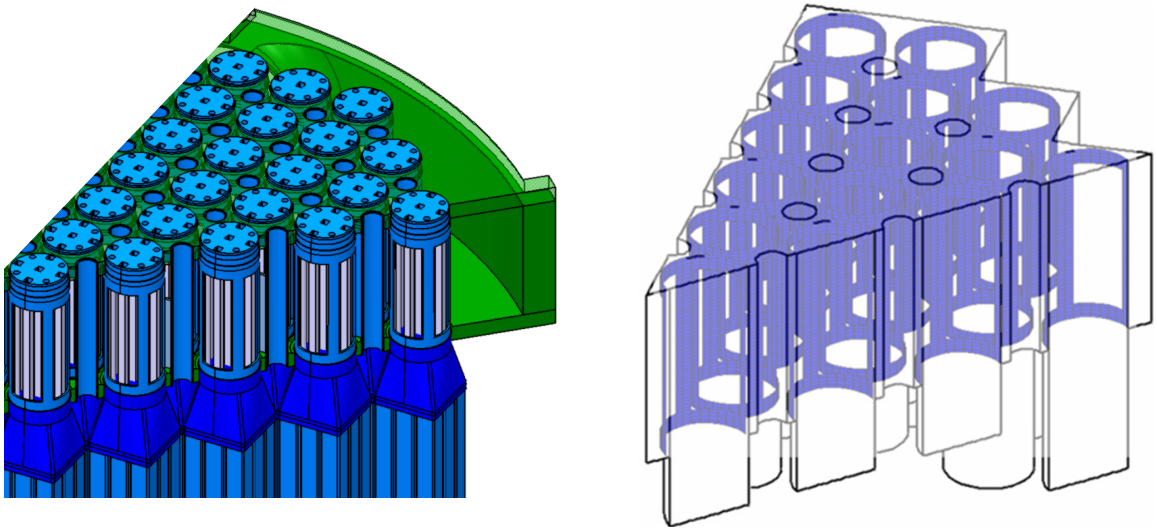

Fig. 3-3 Upper mixing chamber: actual geometry vs. simplified model

The next two steps, when applying the simplification method to the upper mixing chamber are:

2) Quantifying the influences of the disregarded headpiece structures on the mixing and

3) Introducing these influences via source terms (in this case via volumetric forces in the Reynolds equations) into the simplified model.

These two steps are presented in chapter 5, while in this chapter the numerical model for the simplified model is described. Also, a validation of the used code Star-CD and the applied numerical methods is presented and a grid sensitivity study as verification is shown for the simplified model. In the following Fig. 3-4, it is outlined how the simplification method is applied within the design process of the upper mixing chamber.

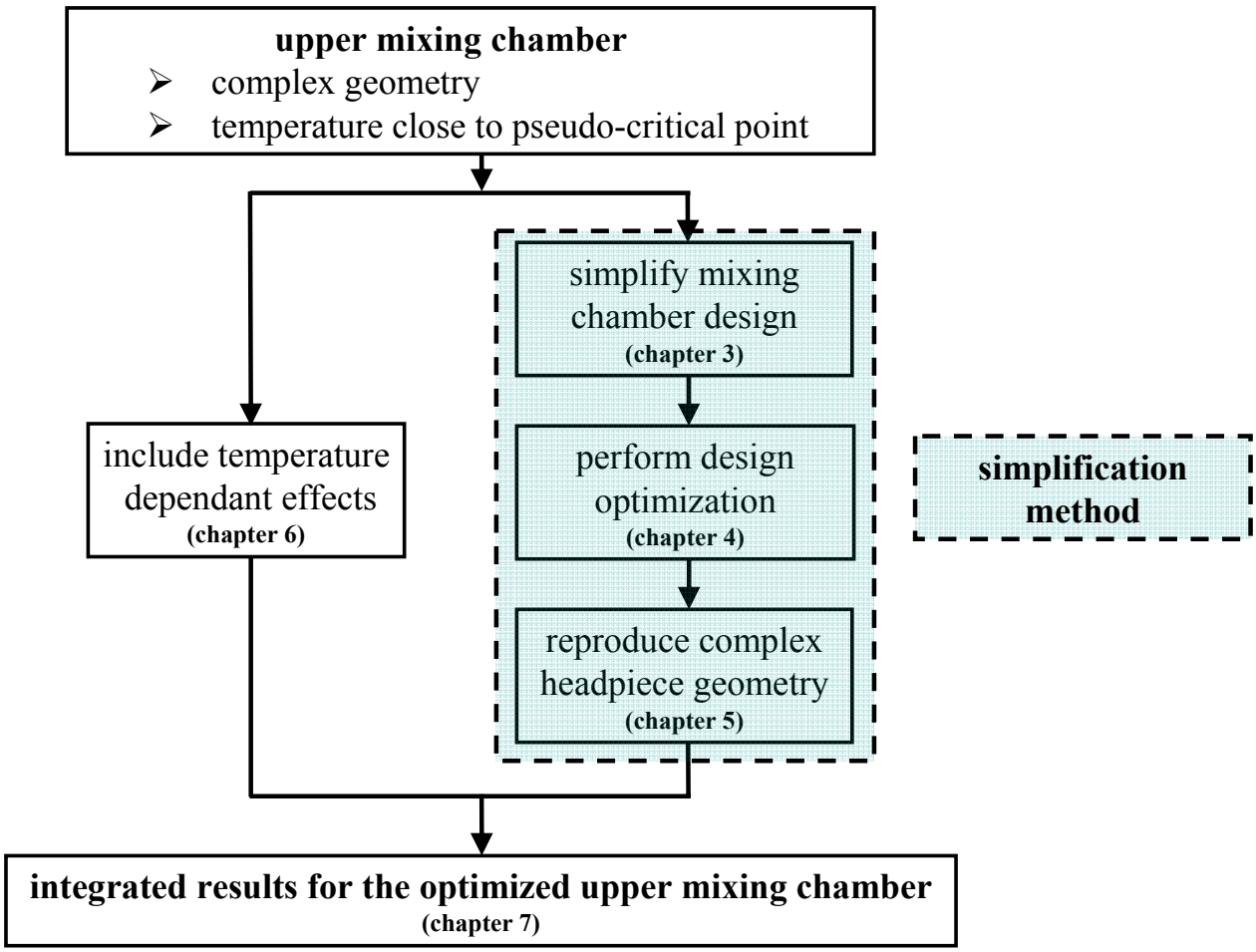

Fig. 3-4 Outline of the design process of the HPLWR upper mixing chamber with emphasis on the included simplification method

3.2 Simplified Model

3.2.1 Numerical Model for the Simplified Geometry

All calculations have been carried out with the CFD software package STAR-CD version 3.26. Moderator boxes and the thickness of the headpiece struts have been omitted. The mixing of the inlet flows is modeled with passive scalars for which the transport equation (2.72), the Reynolds equations (2.69), the mass balance equation (2.68), and the K and ε equations (2.70), (2.71) of the introduced $k-\varepsilon$ model were solved. Only steady state analyses have been performed. For this first analysis step, the flow is assumed to be isothermal so that fluid properties were assumed to be constant. As RANS-turbulence model, the standard high-Reynolds $k-\varepsilon$ together with the standard wall function has been chosen.

Only 1/8th of the total mixing chamber has been modeled and the sidewalls of the fluid domain, where the mixing chamber has been cut, were modeled as symmetry boundary conditions, since no circumferential effects are expected. The radial limitation of the upper mixing chamber model is formed by the separation wall. As only one eight of the upper mixing chamber is modeled, there are eight inlets and seven outlets as sketched from below in Fig. 3-5. These include also half in- and outlet regions as a result of the cutting plane that runs through several headpieces.

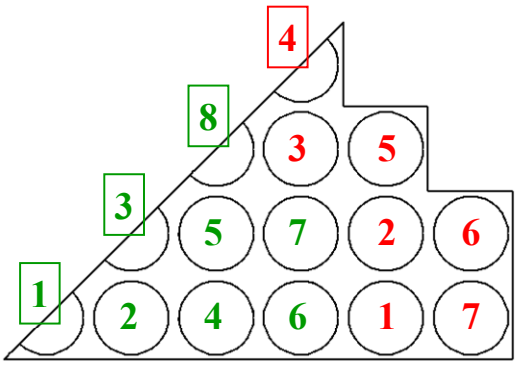

Fig. 3-5 Inlet (green) and outlet (red) numbering

To minimize errors due to numerical diffusion in the mesh, a block structured mesh has been created for the analyses as can be seen in Fig. 3-6. The mesh consists of approximately one million cells, of which about 21,000 are baffle cells. Cells near the walls have been arranged to adjust the dimensionless wall distance y^+ to a value in between 30 and 100 for most of the cells for the application of high-Reynolds-turbulence models in combination with laws-of-the-wall. The headpiece structure is created with a so-called o-grid, which is a standard procedure to mesh round tubes with hexahedral cells. At the outer periphery of these o grids, the two dimensional baffle cells are created as shown in Fig. 3-2. The created o-grids are extended to the bottom to enlarge the distance between the mixing chamber and the applied boundaries. The outlet extensions are longer, since the effects of the boundaries on the flow shall be minimized. A pressure drop of around 10^5 Pa in first superheater assemblies, between the upper mixing chamber and the lower mixing chamber, has been estimated by Schulenberg et al. [68]. The pressure difference in the fuel assembly clusters of the first superheater has been implemented by three layers of porous media cells at the end of the outlet pipes as shown in

Fig. 3-6. The resistance coefficients of this porous media have been defined such that the estimated pressure drop of about 100kPa will be obtained.

Since the connection tubes are included in the simplified model, their geometry is omitted in the mesh. Four blocks are created around them as shown on the lower left side in the picture below. The introduced cells are refined towards the walls of the connection tubes to capture the effects at the walls adequately.

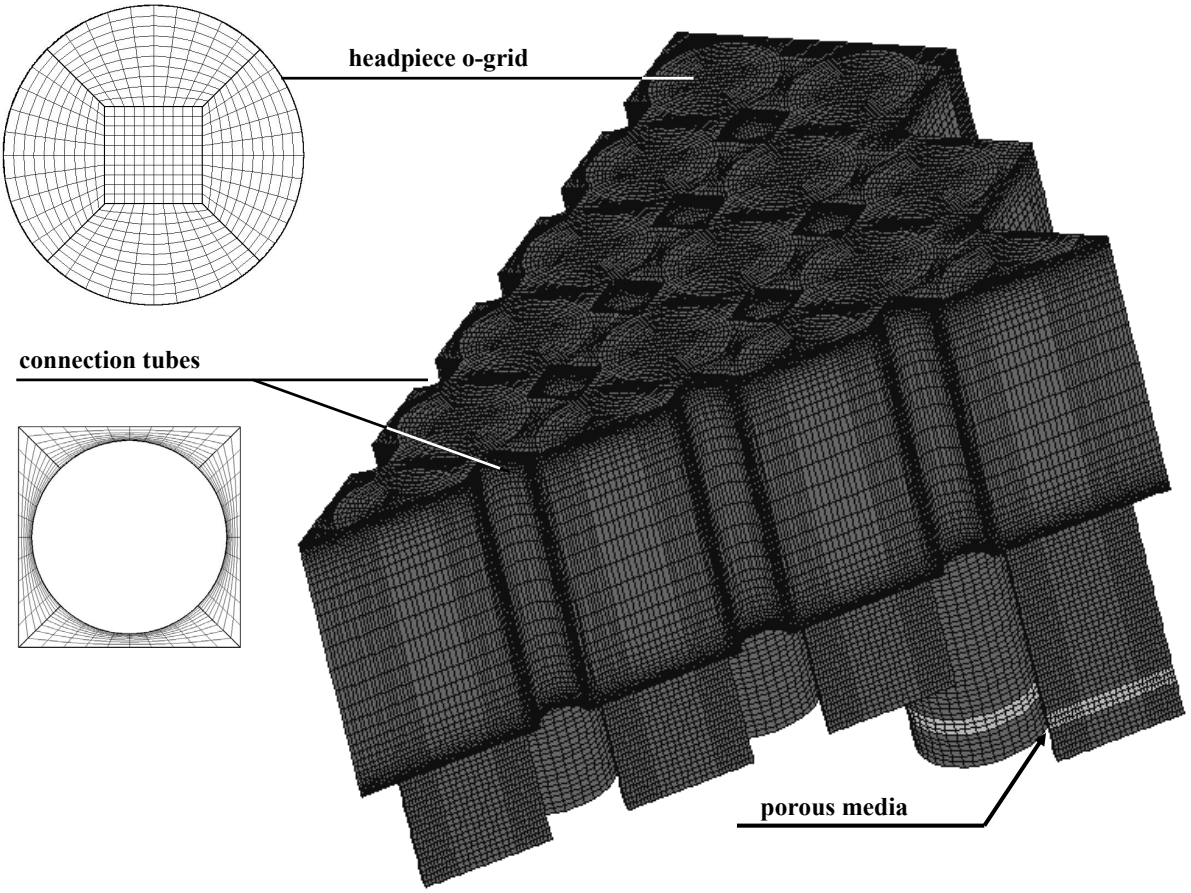

Fig. 3-6 Numerical mesh of the upper mixing chamber

All boundaries are indicated in Fig. 3-7. The two cutting planes are defined as symmetry boundaries, as indicated in blue, whereas all other surfaces are defined as no-slip walls. As the moderator boxes are omitted, a smaller and uniform inlet velocity in vertical direction ($w = 2.78 m/s$) is defined according to the average mass flow in each cluster for all eight inlet areas indicated with the green circles. The values for the turbulent energy K and the turbulent dissipation ε at the inlet are taken from the analysis by Himmel et al. [24]. At the outlets, pressure boundaries are defined indicated with the red circles. Since the pressure boundaries are located very far away from the analyzed flow field and the pressure drop of the superheater I elements is realized with the introduced porous media cells in the model, the value for the pressure at the boundaries does not influence the result. A constant pressure of $p \approx 25 MPa$ is applied.

Here, each evaporator outlet shall be marked with a different passive scalar which allows to differentiate between the contributions of different inlet flows into the mixing chamber to

individual outlet flows into each superheater cluster. Buoyancy forces will be neglected in this analysis. Assuming a certain inlet temperature distribution instead of these markers, on the other hand, would require a separate CFD analysis for each case, so that mixing could only be studied exemplarily.

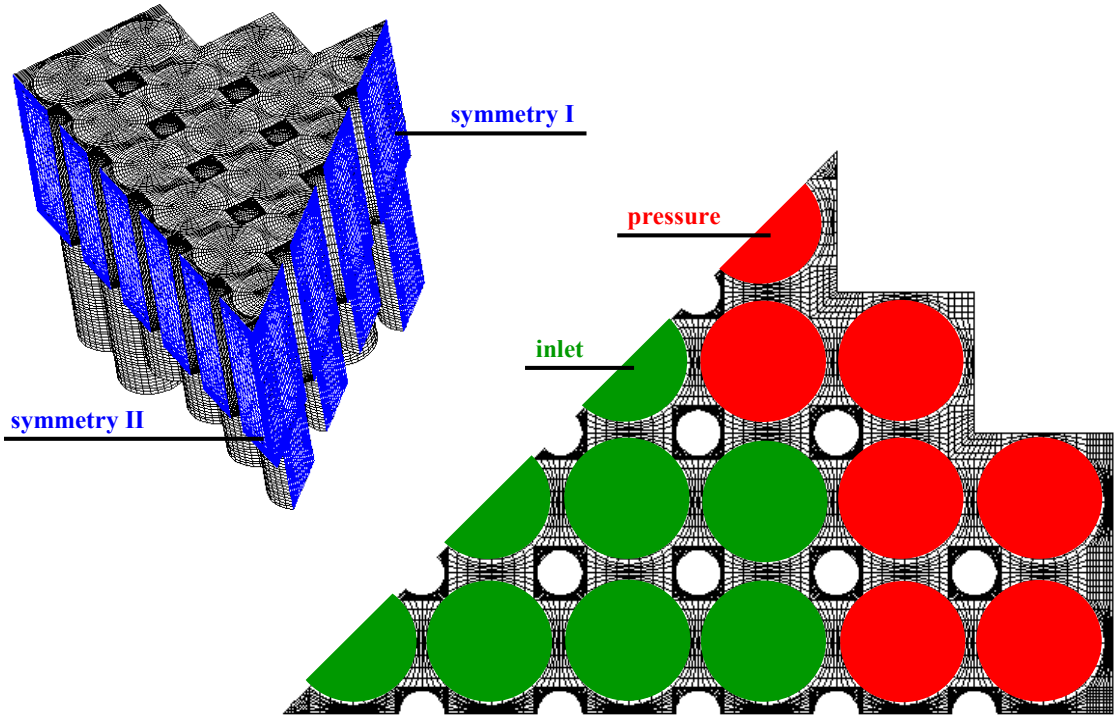

Fig. 3-7 Boundaries applied to the upper mixing chamber

All model variables are summarized in:

Fluid:	water at a pressure of $p = 25MPa$ and a temperature of 390°C
Fluid properties:	Density: $\rho = 215kg/m^3$ Dynamic viscosity: $\mu = 31.704 \cdot 10^{-6} kg/ms$ Conductivity: $\lambda = 0.2398W/mK$ Specific heat: $c_p = 28.461kJ/kgK$
Boundaries:	Inlet: $u = 2.78m/s$, $K = 0.002m^2/s^2$, $\varepsilon = 0.0007m^2/s^3$ ([24]) Outlet: $p \approx 250MPa$ Wall: no slip conditions Cutting planes: symmetry conditions

Tab. 3-1 Boundary conditions for the numerical model of the simplified model

In chapter 6 (Analysis of Temperature Depending Effects), buoyancy effects are analyzed and a distinctive, defined temperature distribution will be shown in chapter 6.2 (Case with a Specified Inlet Temperature Distribution).

3.2.2 Reference Case of the Simplified Model

The first analysis has been performed for the design of the upper mixing chamber by Fischer et al. [20]. Here, no extra measures have been introduced to enhance mixing. For this reference case, the procedure to analyze the mixing of passive scalars will be shown exemplarily and the evaluation of the obtained results will be presented.

The quality of mixing is expressed by the marker concentrations in the outlets, shown in Fig. 3-8. The colors represent the concentrations of each of the 8 scalars used as markers in the analysis, in the arbitrary scale from 0 to 1. A red inlet color indicates the origin of the particular marker, whereas blue regions are occupied only by the other seven inlet scalars in this case. For the visual evaluation, the distribution of each scalar is plotted from underneath. The summary of all the distributions in one graph leads to a general impression of the flow distribution in the upper mixing plenum. Fig. 3-8 shows the marker distribution for the base case without measures to enhance mixing.

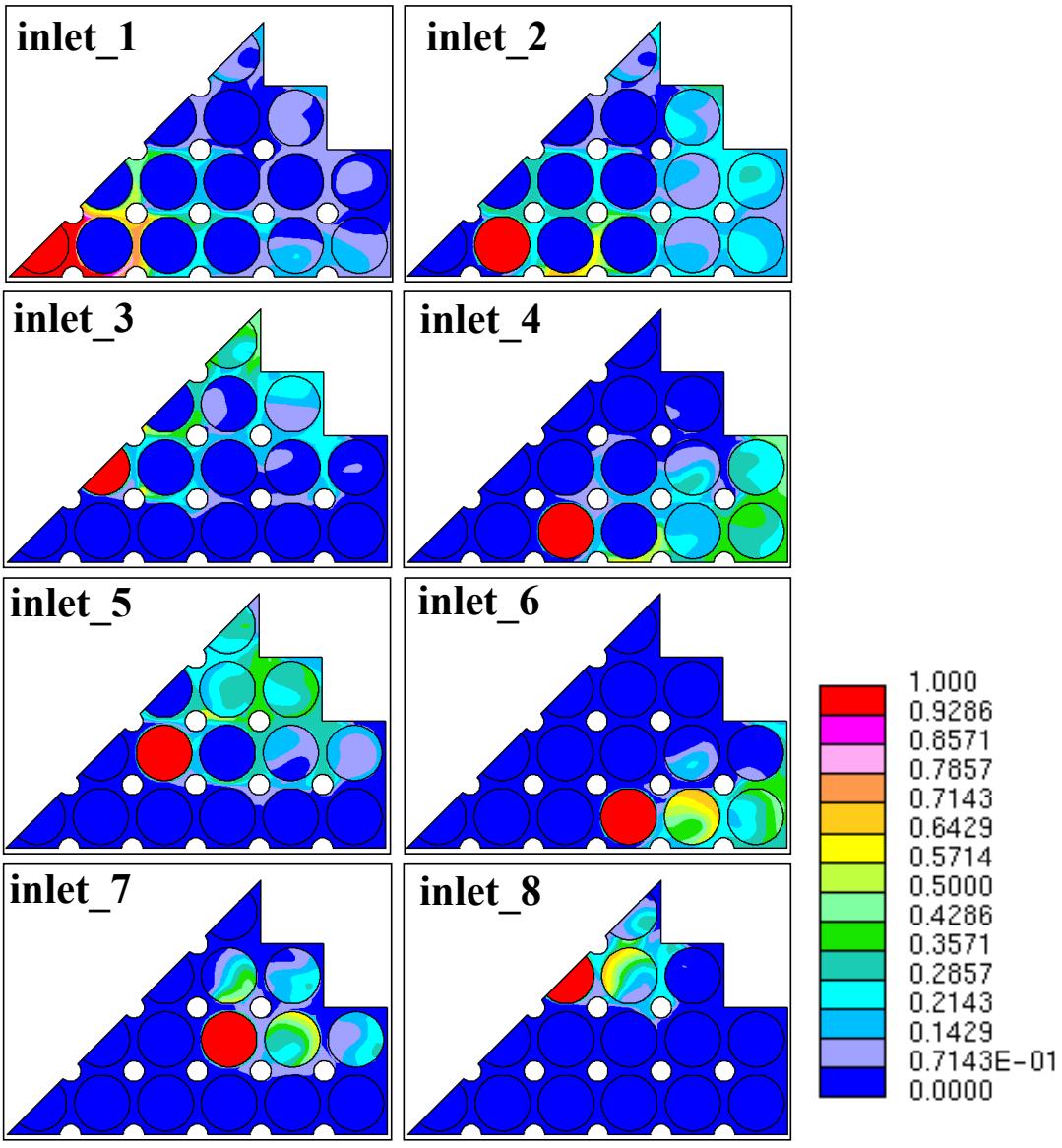

Fig. 3-8 Scalar/ marker concentrations in the upper mixing chamber, seen from underneath

It is noticeable that the inlet flows 1 to 4, which enter in the center of the upper mixing chamber and do not have a neighboring outlet, are distributing their scalars already rather uniformly to the outlets in the outer part of the chamber. Inlets 6 to 8, however, which are close to the outlets 1, 2, and 3, are disposing their scalars primarily there, such that the outlet concentrations are exceeding even 70% locally. The scalar distribution of the inlet 6 scalar is shown in the following Fig. 3-9. It describes the worst case.

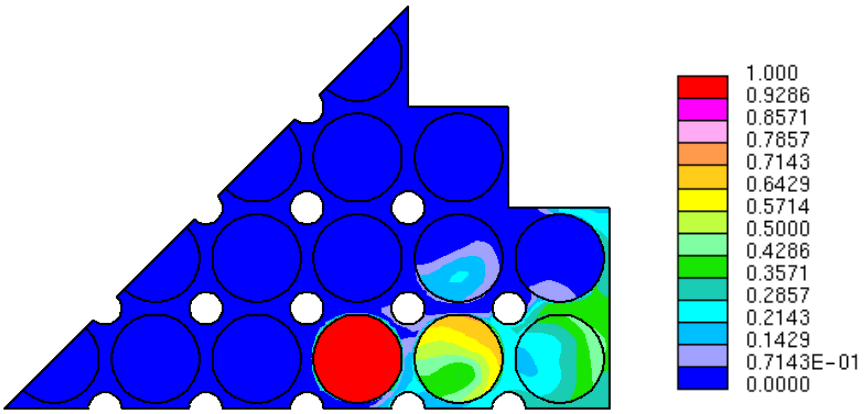

Fig. 3-9 Distribution of the inlet 6 scalar

This result can be explained by a horizontally layered flow structure with short cuts for neighboring in- and outlets. In Fig. 3-10 this layered flow structure is demonstrated. It shows a vertical cut through the upper mixing chamber, parallel to the cutting plane with symmetry boundary II, shown in Fig. 3-7. The cut runs through the inlets 1, 2, 4, 6, and through the outlets 1 and 7, marked on the right side in Fig. 3-10. It can be seen that the central inlet flows are obstructed by the inlet flows closer to the outlets. As expected, the concentration of the inlet markers at the outlets are higher the closer the in- and outlets come together.

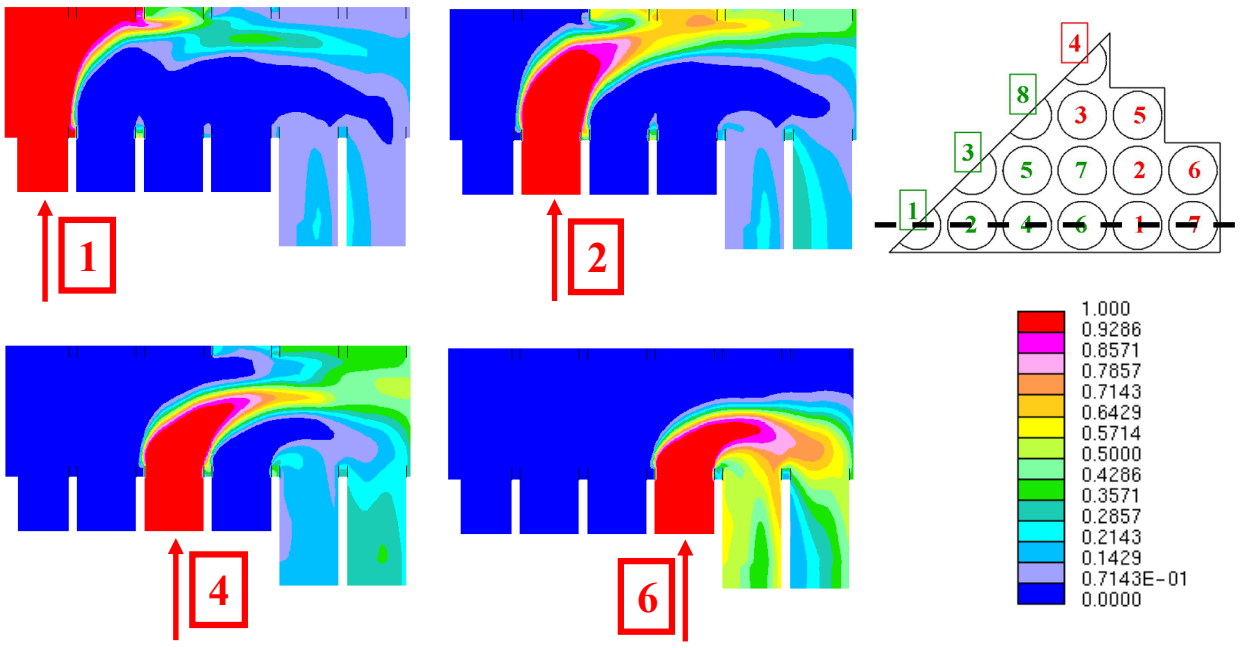

Fig. 3-10 Vertical cut through the upper mixing chamber and distribution of the scalars: inlet_1, inlet_2, inlet_4, and inlet_6

For quantitative evaluation of the mixing performance, the concentration of each of the eight inlet scalars is evaluated in the one cell layer of each outlet just above the porous media cells. The value of the concentration for each scalar is readout for each cell and then both, a volume averaged concentration, as well as the local maxima for the concentration are calculated in each outlet region. The volume averaged value is obtained by multiplying the value for each scalar in one cell with its volume, building the sum of all the cell values and then dividing the obtained value by the volume of all evaluated cells. The index j stands for the inlet scalar; i represents the cell number.

$$\bar{c}_j = \frac{1}{V_{total}} \sum c_i V_i \quad , \quad j = 1,...,8 \tag{3.2}$$

$\bar{c}_j$ is the volume averaged concentration of each scalar at the analyzed outlet,
c_i is the concentration of each scalar at the analyzed cell,
V_i is the volume of the analyzed cell,
V_{total} is the sum of all the cell volumes per outlet

Thus, an average value for each scalar is received at each outlet. For later analyses, not only the averaged values will be of interest, but also local hot spots, so that the maximum values for each scalar ($c_{j,\max}$) were analyzed as well.

The results for the reference case of the upper mixing chamber without any additional mixing devices are shown in Fig. 3-11. The outlets are displayed on the x-coordinate and an inlet marker distribution is shown for each outlet; each bar indicates the value for one scalar (marker), according to the color scale situated underneath the diagram. The diagram in Fig. 3-11 shows the marker concentration of each inlet averaged over the cross section of each outlet, whereas the diagram in Fig. 3-12 shows the peak values for each inlet marker at the outlets.

To evaluate the mixing the standard deviation σ can be introduced. This way each configuration for the later presented design optimization can be characterized by only one number. The standard deviation, as the dispersion of the analyzed variable around its mean value, can be used to characterize the mixing quality. The standard deviation applied for the evaluation of the mixing according to e.g. [23] is defined as:

$$\sigma = \sqrt{\frac{1}{n-1} \sum_{i=1}^{n} \left(x_i - \bar{x}\right)^2} \tag{3.3}$$

x_i is the value of each inlet scalar averaged over each outlet,
$\bar{x}$ is the mean value of all inlet scalars at all outlets,
n is the number of evaluated values for the inlet scalars. Since 8 inlet scalars are evaluated at 7 outlets, $n = 56$.

Using the standard deviation for the evaluation of the mixing quality serves well, since the mean value of the inlet scalars at the outlet corresponds to the ideal value for perfect mixing in the upper mixing chamber. Therefore, the indicated deviation, or dispersion, is an adequate specification for the mixing quality in the upper mixing chamber, since it quantifies the difference between the achieved mixing and the perfect mixing. The obtained standard deviation

for the reference case of the simplified model is: $\sigma = 12.1\%$. For comparison, Schulenberg et al. [68] assumed in their analysis a standard deviation of $\sigma = 5\%$ only. Thus, the mixing can not yet be considered sufficient.

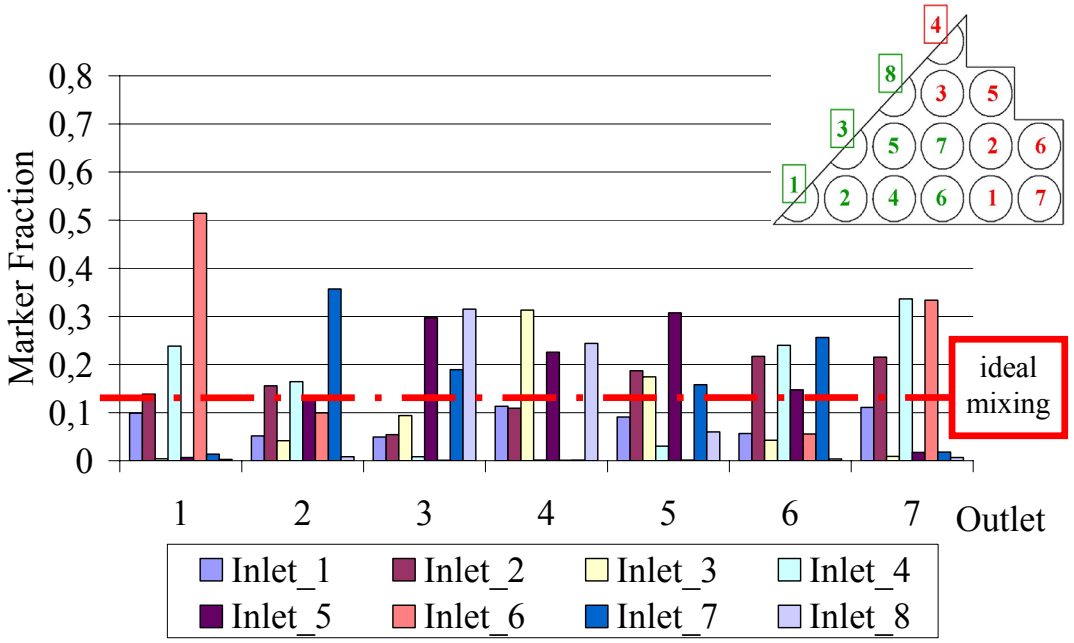

Fig. 3-11 Scalar concentrations, averaged over each outlet cross section

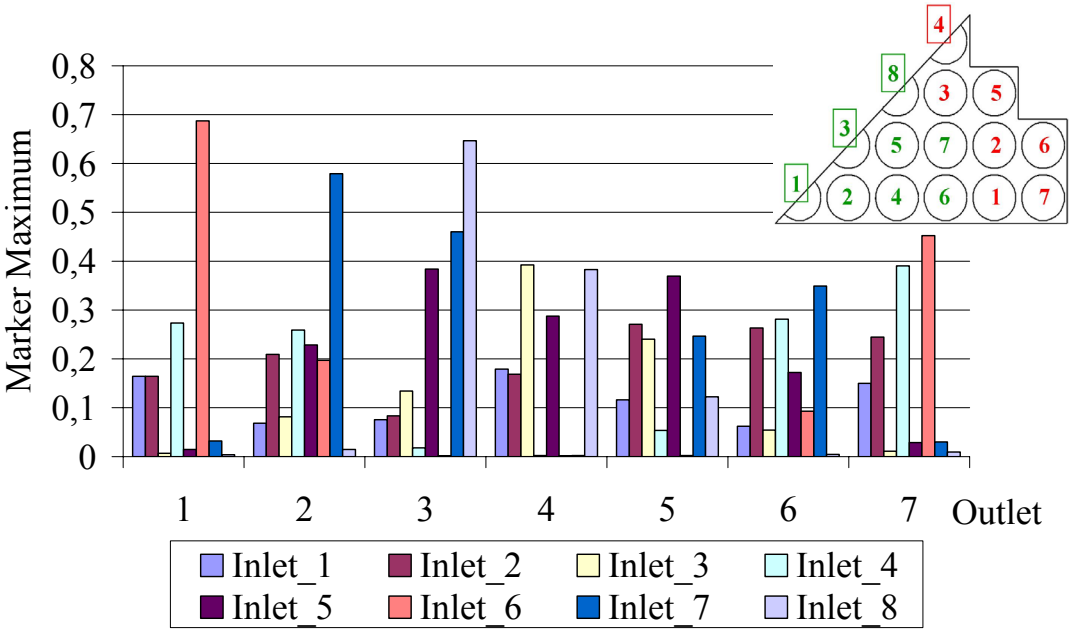

Fig. 3-12 Peak values of the scalar concentrations in each outlet cross section

As an example, outlet 1 receives a high marker fraction of more than 50% in average from the neighboring inlet 6, while the local maximum of inlet scalar 6 is almost 70% at outlet 1. Outlet 3, for example, gets a high peak fraction of 65% from inlet 8, while the average value of the inlet 8 scalar at outlet 3 is just above 30%.

The red line in the top graph shows the ideal marker distribution. For ideal mixing, one eighth, or 12.5% of each inlet should leave the upper mixing plenum at each outlet. Obviously, the present distribution is far from ideal. They highest marker concentration, averaged over each outlet cross section, is 4 times the ideal homogeneous concentration.

Another important aspect for the design of the upper mixing chamber is the created pressure drop, which should be minimized, since the pressure drop in the core of the HPLWR is directly linked to the thermal efficiency of the entire power plant. Analyses for the steam cycle of the HPLWR and the influence of the core pressure drop have been presented by Schlagenhaufer et al. in [64] and in [65], as well as by Brandauer et al. in [9]. The obtained pressure drop for the reference case of the simplified model is:

$\Delta p \approx 4 \cdot 10^3 \, Pa$.

It is measured as the pressure difference between the inlets and the outlets of the mixing chamber.

Different ways to enhance mixing and an optimized design of the upper mixing chamber are presented in chapter 4 (Design optimization using the simplified model).

3.3 Validation

To ensure that adequate results for the carried out simulations are gained and an adequate turbulence model is used, a simulation applying the same numerical methods for an existing experiment has to be compared to the obtained experimental results in the experiment. Validation therefore means the procedure of testing the extent to which the model accurately represents the reality. The chosen validation experiment should be comparable to the analyzed geometry, the upper mixing chamber, and should especially exhibit the same flow features as expected in the analyzed geometry.

When looking at the flow in the upper mixing chamber, two characteristic flow features are found:

1) A strong redirection of the flow of 180°

2) Flow separation at a large number of obstacles in the upper mixing chamber such as connection tubes and headpiece structures

In an adequate validation experiment, the same flow features should be contained.

The major function of the comparison between an experiment and the applied numerical model is the selection of the best suitable turbulence model. Therefore different turbulence models, which according to the best practice guidelines [11] seem promising to capture the main flow feature, have been compared.

An appropriate experiment was carried out by Inagaki et al. [33] in 1990. Here, the core bottom structure (CBS) of the gas cooled high temperature engineering test reactor (HTTR) as presented in [34], developed by the Japan Atomic Energy Research Institute (JAERI), has been analyzed. Other tests of the CBS have also been presented in [41].The CBS is a complex passive mixing chamber, used to mix gas at different inlet temperatures to achieve a rather homogeneous temperature distribution at the outlet of the mixing chamber to avoid hot spots in following high temperature components. Thus, the task of this mixing chamber is somehow comparable to the upper mixing chamber of the HPLWR. For the presented experimental study, however, water at a pressure of 0.3MPa was used as test fluid and a one-seventh scale test model of the CBS was analyzed.

The temperature and flow rates were measured with thermocouples and electromagnetic flow meters, respectively. For the temperature the measurement errors were within $\pm 0.6°C$ and for the flow rate within $\pm 0.5\%$. The analyzed test section is shown in Fig. 3-13. It is made of acrylic resin and consists of a plenum, an outlet nozzle underneath the plenum, and seven inlet nozzles above the plenum. Inlet nozzle number 1 is placed in the center of the test model and is surrounded by the others concentrically, which are numbered 2 to 7. All inlets are indicated by red circles in Fig. 3-13.

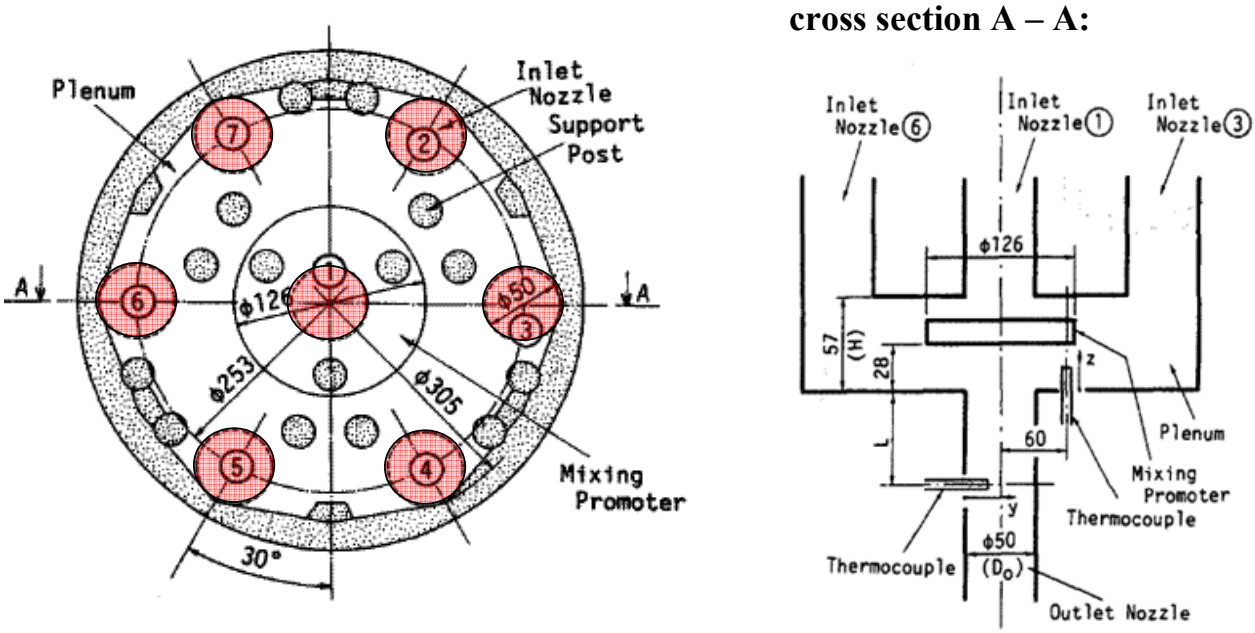

Fig. 3-13 CBS – mixing chamber of the HTTR test section analyzed in [33]

In the plenum 15 cylinders, the so-called support posts, as well as a disc to promote the mixing of the coolant are inserted. The flow rate of the water in each inlet nozzle was controlled by control valves to maintain equality. Hot water at a temperature of 55°C enters through inlet nozzle 1 in the center, while cold water at a temperature of 25°C enters the plenum through all other inlets. Water passing through the inlet nozzles, is then mixed in the plenum before it exits the mixing chamber through the outlet nozzle. Thus, the temperature difference analyzed in this setting is 30°C and the Reynolds number in the outlet nozzle defined with the diameter of the nozzle is $Re = 45000$. The positions of the thermocouples in the plenum and in the outlet nozzle are indicated in Fig. 3-13 and in Fig. 3-14.

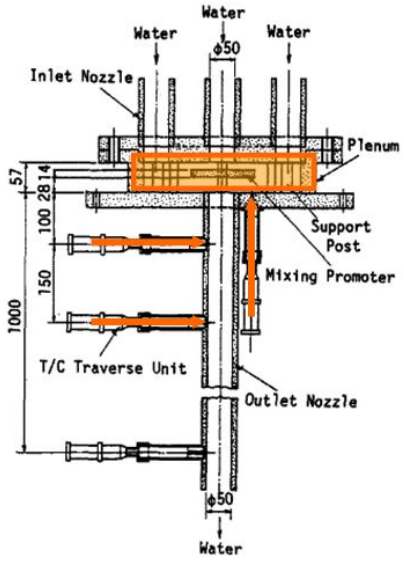

Fig. 3-14 Cut through the CBS –mixing chamber with indicated positions of thermocouples

In Fig. 3-14 the measurement positions that are compared to the simulation are highlighted. Inside the plenum, the temperature is measured within cross section A-A at a radius of $r = 60mm$ between the bottom of the plenum and the indicated mixing promoter. In the outlet nozzle, the measurements at two positions behind the plenum, at 100mm and 750mm, are compared to the simulation. The characteristics of the numerical model for the CBS – mixing chamber are summarized in Tab. 3-2. At the inlets, the velocity profile of a fully developed pipe flow with a mean velocity of $u = 0.11m/s$ and the corresponding values for the turbulent magnitudes has been defined, according to the fully developed pipe flow guaranteed in the experiment (by Inagaki [32]). At the outlet an arbitrary pressure has been defined at a satisfactory distance from the analyzed flow field, with zero gradient conditions for all other flow variables and all walls are assumed to be adiabatic. The high Reynolds $k-\varepsilon$ model has been used for the first simulation, thus the flow at the wall is calculated with the standard wall function. When building the Reynolds number with the velocity $u = 0.11m/s$, the kinematic viscosity $\nu(T = 25°C) = 0.89 \cdot 10^{-6} m^2/s$, and the diameter $d_h = 50mm$, all at an inlet nozzle, $\mathrm{Re} = \mathrm{u d_h} / \nu \approx 6000$ is obtained. To use the Reynolds number in the applied criteria (2.32) for the consideration of buoyancy effects, it is built with the height of the mixing chamber as characteristic length $H = 57mm$. However, only small changes in the value of the Reynolds number are obtained ($\mathrm{Re} \approx 6180$). The Grashof number, built with the volumetric thermal expansion coefficient $\alpha = 1.9K^{-1}$, the acceleration due to gravity $g = 9.81m/s^2$, the kinematic viscosity $\nu(T = 25°C) = 0.89 \cdot 10^{-6} m^2/s$, the temperature difference between the hot inlet 1 and the cold inlets 2 to 7 $(T - T_0) = 30K$, and the height of the plenum as characteristic length $H = 57mm$, is $\mathrm{Gr} = \alpha g \mathrm{H}^3 (\mathrm{T} - \mathrm{T_0})/\nu^2 = 1.3 \cdot 10^{11}$. Applying the criteria (2.32) concerning the consideration of buoyancy:

$$\frac{\mathrm{Gr}}{\mathrm{Re}^2} \approx 3400 >> 1$$

Buoyancy effects need to be taken account for the simulation of the CBS – mixing chamber. To account for buoyancy effects the Boussinesq-Approximation is applied to the model as described in 2.3 Characterization of Buoyancy Influences.

Fluid:	water at a pressure of $p = 0.3MPa$ and a temperature between 25°C and55°C
Fluid properties: (at $p = 0.3MPa$ and 25°C)	Dynamic viscosity: $\mu = 0.8900 \cdot 10^{-6} kg/ms$ Conductivity: $\lambda = 0.6073W/mK$ Specific heat: $c_p = 4.18kJ/kgK$ Density: Boussinesq-Approximation
Boundaries:	Inlet: $u = 0.11m/s$, $K = 0.00013m^2/s^2$, $\varepsilon = 0.0002m^2/s^3$ Outlet: $p \approx 0Pa$, else zero gradient Wall: no slip, adiabatic

Tab. 3-2 Boundary conditions for the numerical model of the CBS – mixing chamber

The grid used in the analysis of the CBS – mixing chamber consists of 400,000 tetrahedral cells. Different grids have been tested and no significant influence on the result has been observed.

The temperature distribution in the CBS – mixing chamber is depicted in Fig. 3-15. On the left side of the figure, the plenum with all inlet nozzles and the upper end of the outlet nozzles is shown. It can be seen how the hot streak entering in the center is flowing around the mixing promoter, being mixed with the cold streaks entering the plenum from the periphery. On the right side of Fig. 3-15 the A-A cut through the geometry, as indicated in Fig. 3-13, can be seen. The temperature of the water in the outlet nozzle is already fairly homogeneous right after the plenum. Two measurement positions are indicated with the letters y and z. At the measurement position z, fairly larger gradients of the temperature are noticeable.

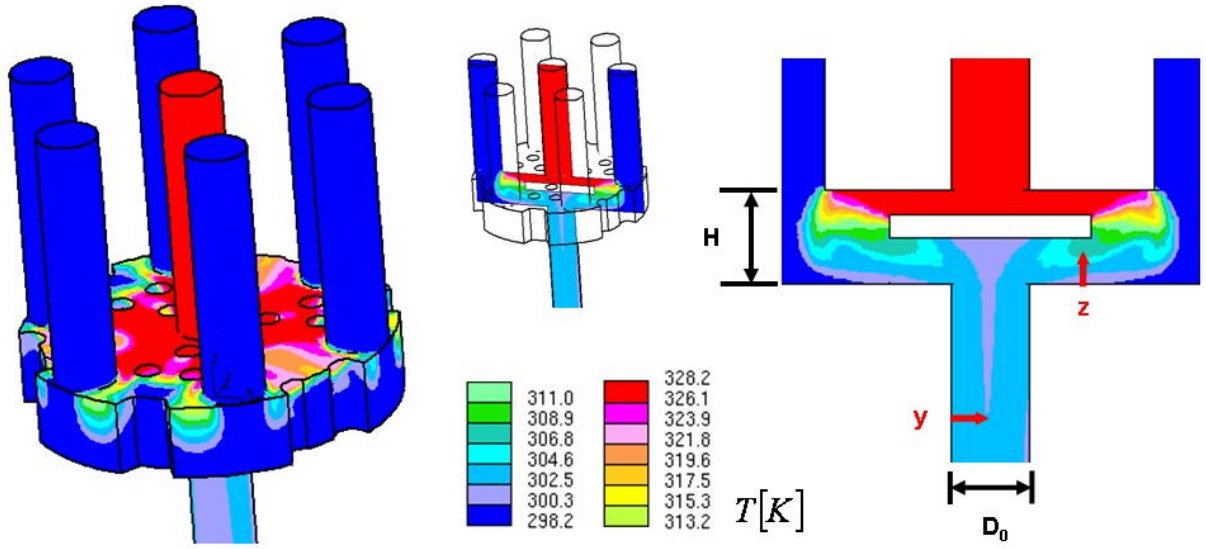

Fig. 3-15 Result for the temperature distribution in the CBS –mixing chamber

In Fig. 3-16 the results of the experiment and the numerical simulation are compared across the vertical direction in the plenum. Inagaki et al [33] have introduced the dimensionless temperature Θ, which is plotted on the y-axis as follows:

$$\Theta = \frac{T - T_{cold}}{\Delta T} \tag{3.4}$$

In which ΔT represents the difference between the inlet temperatures of the hot and the cold inlets. The dimensionless temperature $\Theta = 1$ represents the hot and $\Theta = 0$ the cold water in the inlet nozzles, respectively. The error for the temperature, which can be included in the presented diagrams, is indicated as error margin for each blue point showing the result of the measurement (Experiment – Ex. z/H), at a certain height. The x-axis shows the dimensionless distance from the bottom of the plenum z / H. The red line represents the results for the simulation.

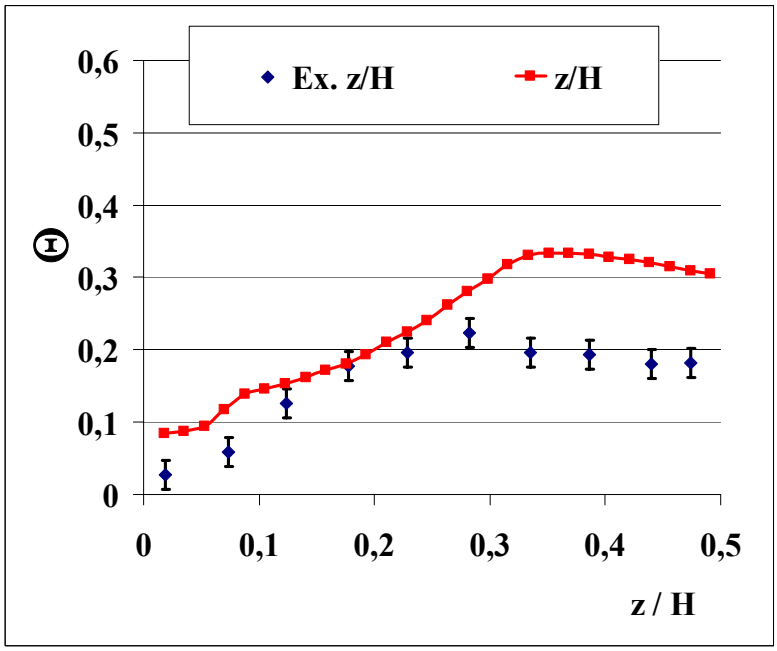

Fig. 3-16 Temperature distribution across the vertical direction in the plenum – experiment (blue) and simulation (red)

It can be seen that the results for the experiment and the simulations agree well close to the bottom of the plenum, while the discrepancy close to the mixing promoter is significant. Reasons for this difference in temperature could be within the applied numerical model. Also, the influence of the thermocouple on the local flow field seems likely to have a large impact. Due to the high gradients in the temperature in the region of the measurement position indicated in Fig. 3-15 with z, vary small variations of the measurement position lead to noticeable changes in the temperature distribution. In Fig. 3-17 the view from the top onto a horizontal cross section through the CBS – mixing chamber is shown. The extension of the mixing promoter is outlined by the black circle. The measurement position, indicated with the black arrow, is located right in one of the hot streaks underneath the mixing promoter. Small influences on the flow field are bound to change the temperature distributions in this region significantly.

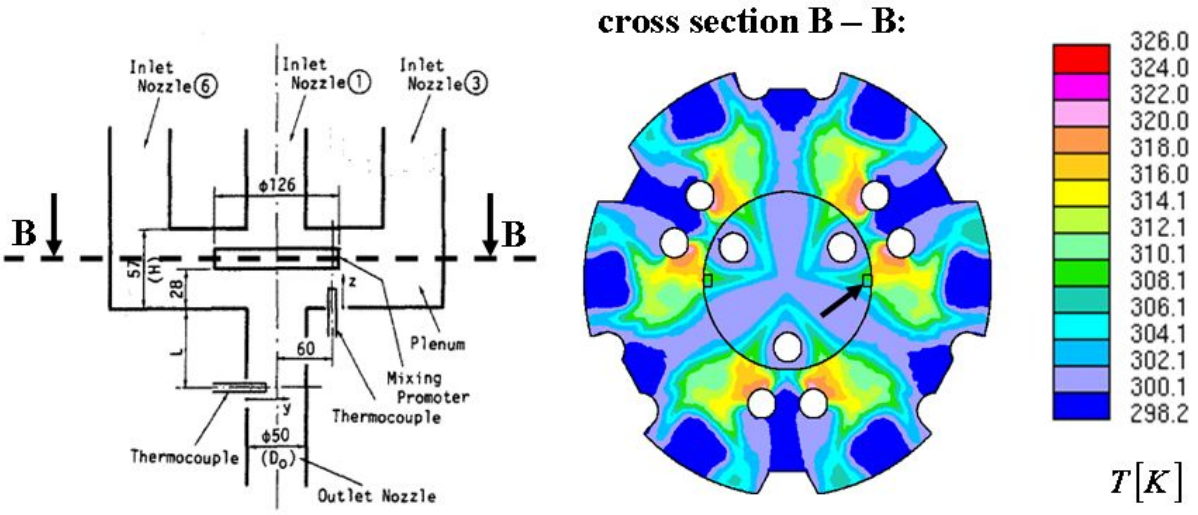

Fig. 3-17 Temperature distribution at the surface underneath the mixing promoter

The results for the temperature distribution in the outlet nozzle according to the experimental data and the numerical results are shown in Fig. 3-18. The x-axis shows the dimensionless distance diagonal in the outlet nozzle. On the left side, the temperature distribution at a distance of 2 nozzle diameters and on the right side at a distance of 5 nozzle diameters is shown. It can be seen that the dimensionless temperature Θ obtained in the simulation stays well within the range of the measurement errors in the experiment.

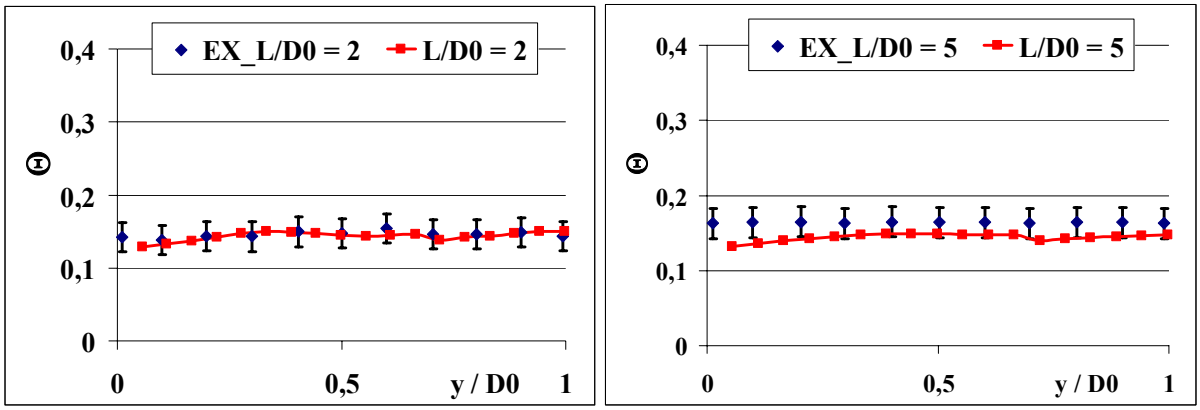

Fig. 3-18 Temperature distribution in the outlet nozzle – experiment (blue) and simulation (red)

Using the same set-up, other turbulence models have also been tested. Several recommendations for the appliance of different turbulence models are suggested. Literature examples are ERCROFTAC [11], MARNET-CFD [2], and QNET-CFD [12]. According to the best practice guidelines [11], the $k-\omega-Shear\ Stress\ Transport\ (SST)$ model proposed by Menter in [48] and [47] is very suitable for flow separation phenomena. For highly anisotropic flows and turbulence driven secondary flows $non-linear\ k-\varepsilon$ models are recommended. The in this work tested $non-linear\ k-\varepsilon$ model has been presented by Baglietto et al in [13], [4] and [5]. It has been developed for fuel bundle simulations, but is not limited to nuclear applications, since it is expected to deliver improved results for anisotropic flows and improved sensitivity to secondary strains.

In Fig. 3-19 the results for the temperature distribution obtained when applying the different turbulence models are compared. Again, the experimental data is plotted and is indicated with the blue dots marked Ex. z/H, Ex. y/D0, respectively. The red line shows the results obtained for the standard $k-\varepsilon$ model marked as KE. The $non-linear\ k-\varepsilon$ model from Baglietto is described by the light blue line marked as quadKE-Bag, while the $k-\omega-Shear\ Stress\ Transport\ (SST)$ model is depicted in the diagram by the orange line, marked as SST.

Comparing the results obtained for the different turbulence models, no significant changes in the results are noticeable. According to Baglietto [3], this can be explained by the fact that the global flow structure dominates compared to local turbulent effects. Also, no differences in the results for the different turbulence models are obtained, when applying them to finer grids.

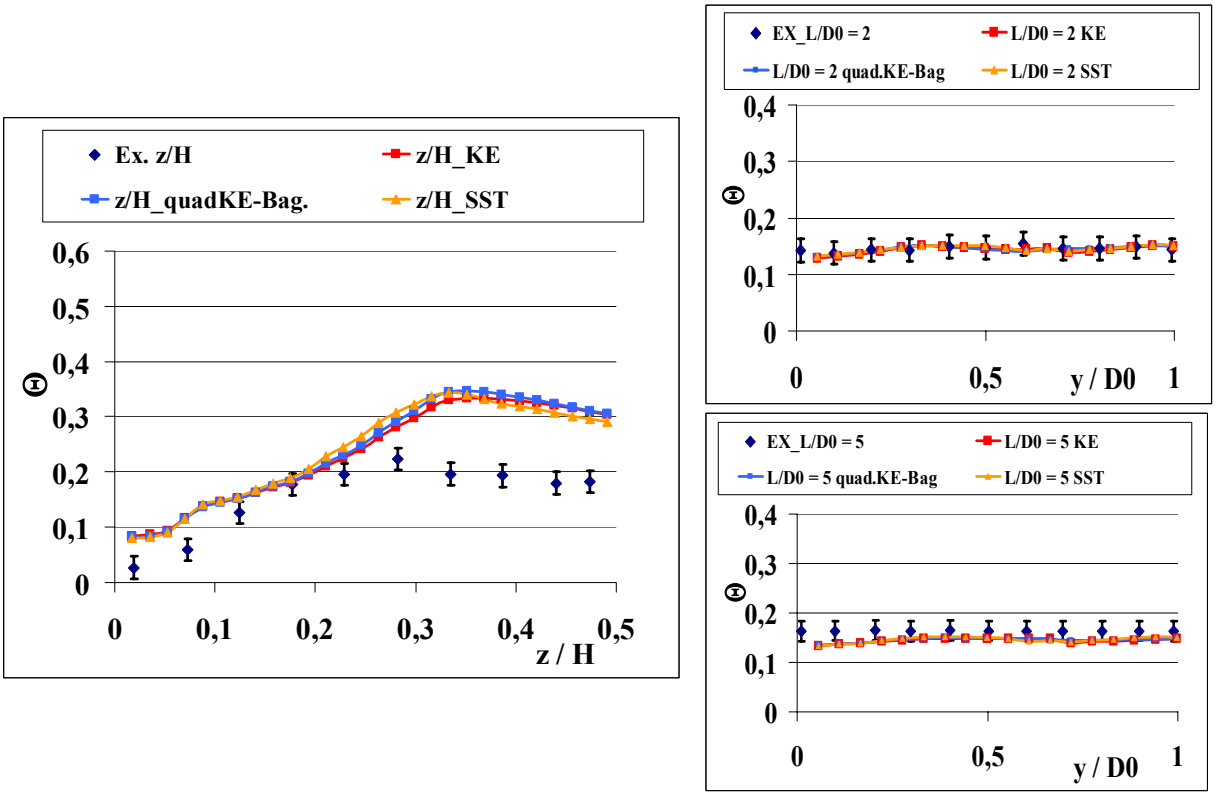

Fig. 3-19 Temperature distribution in the plenum and in the outlet nozzle, obtained in the experiment (Ex. z/H, Ex. y/D0) and by numerical results with different turbulence models

As expected, again no noticeable differences in the results are found, when applying the same different turbulence models to the simplified model of the upper mixing chamber. Therefore, the standard high Reynolds $k-\varepsilon$ turbulence model, which in comparison generates the least numerical effort, is chosen for the analyses and design optimization of the upper mixing chamber. It can be stated that the chosen numerical model is well applicable to the physical problem and the numerical model can be regarded as validated, especially in the region behind the mixing chamber, which corresponds to the results of interest in the analysis of the upper mixing chamber.

3.4 Verification – Grid Sensitivity Analysis

To evaluate the influence of the numerical resolution on the mixing, a grid sensitivity study has been carried out in which the same simulation has been performed with five different grids. To satisfy the validity of the applied wall functions for each model, the cell layer next to the wall is kept inside the limit for the y^+-value, while the progressing cell layers are adapted for the refinement. The coarsest grid, consisting of around 300.000 cells has been refined in several steps to the finest grid with around 1 million cells. In the grid sensitivity study, no baffles have been applied which means that no additional internals, like the window elements to account for the headpieces are regarded. For the grid sensitivity analysis, the regions where the largest gradients were expected have been refined. In vertical direction the number of cell layers has been increased, to provide a better resolution of the in- and outlet regions, also the regions around the connection tubes in the upper mixing chamber have been refined. This way, zones with strong changes in the flow direction as well as regions where flow separation is expected, have been refined. The two evaluated qualities in the grid sensitivity study are the maximum of the volume averaged scalar concentration for all outlets and the total pressure.

For the pressure, the difference between the inlet and outlet pressure is evaluated. In Fig. 3-20, the difference in total pressure for each grid is plotted over 1/N, where N represents the number of cells in the model. The difference between the pressure drop obtained for the coarsest and the fines grid is around 100Pa, which is almost two orders of magnitude smaller than the pressure drop of interest for the performed analyses. The first order interpolation scheme UD and the third order interpolation scheme QUICK for the spatial discretization have been tested for the five different refinement models.

When extrapolating the values obtained with the first order interpolation scheme UD and implying that the results decrease in a linear manner, as expected for the first order scheme, the numerical error for the different grids can be approximated using the Richardson-extrapolation as defined by Roache in [63]. The values of the pressure drop for the different grids are extrapolated to the y-axis which represents an infinite fine mesh. For the finest grid, with just over 1.000.000 cells, an estimated error of 3.5% is found, when comparing it to the extrapolated value from the Richardson extrapolation.

The other quantity evaluated in the grid sensitivity study is the maximum inlet scalar concentration, which is the maximum value of all averaged inlet scalars at all outlets, or the maximum averaged value, which is detected at any outlet. It is the maximum percentage of any inlet detected at an outlet, thus representing the least mixed streak. In Fig. 3-21 it is shown that the maximum inlet scalar is not grid dependent.

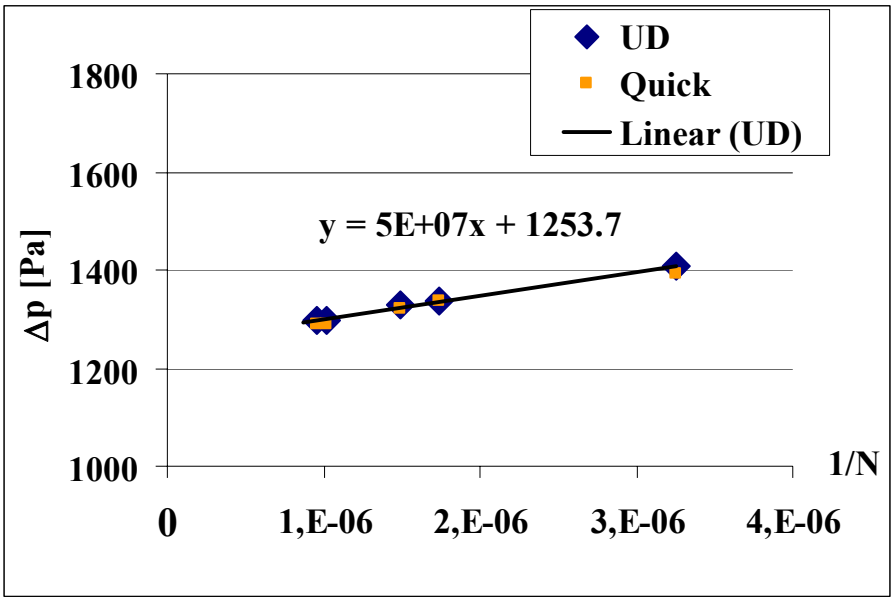

Fig. 3-20 Grid sensitivity study – pressure drop for different grids using the UD and QUICK interpolation scheme, with the Richardson extrapolation applied to the UD scheme

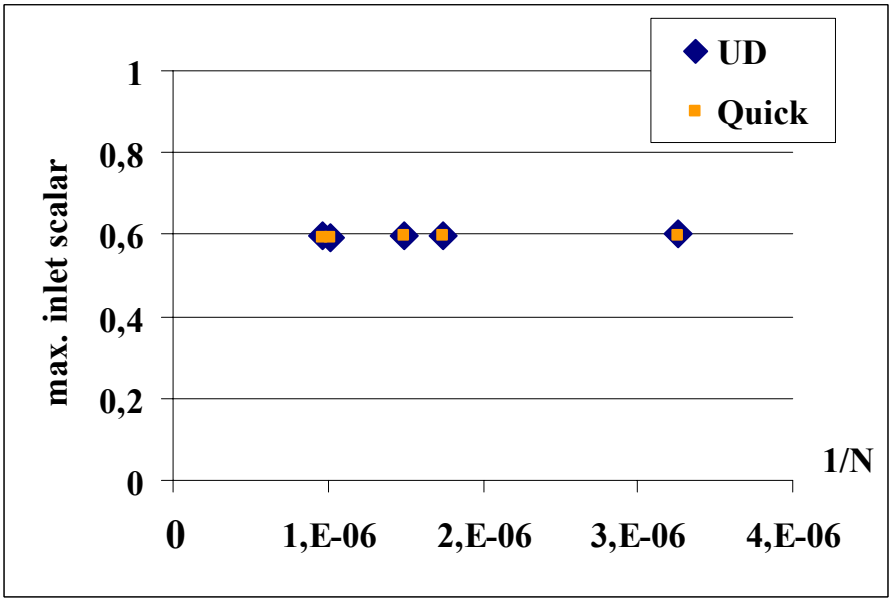

Fig. 3-21 Grid sensitivity study – maximum inlet scalar for different grids using the UD and QUICK interpolation scheme

It can be seen that the values obtained with both interpolation schemes, UD and Quick, only differ insignificantly, leading to the conclusion that the first order interpolation scheme UD is sufficient and will be used in future analyses. For further investigations with the simplified model, the finest grid shall be used to minimize the estimated error.

4 Design optimization using the simplified model

Due to the results for the reference case of the simplified model presented in chapter 3.2.2 (Reference Case of the Simplified Model), a design optimization leading to improved mixing, while limiting the pressure drop to an acceptable value, becomes necessary. According to the simplification method proposed in chapter 3, the design optimization is carried out for the simplified model. After an adequate design is found, the omitted geometry elements will be introduced into the relevant models, applying the simplification method.

The reference design of the upper mixing chamber had originally been designed such that the pressure losses in the mixing chamber are smallest. In Fig. 4-1, the velocities in x-, y-, and z-direction in a horizontal cut through the upper mixing chamber at half its height are plotted. The depicted distinctive flow field consists of several pronounced streaks, facing almost no obstacles.

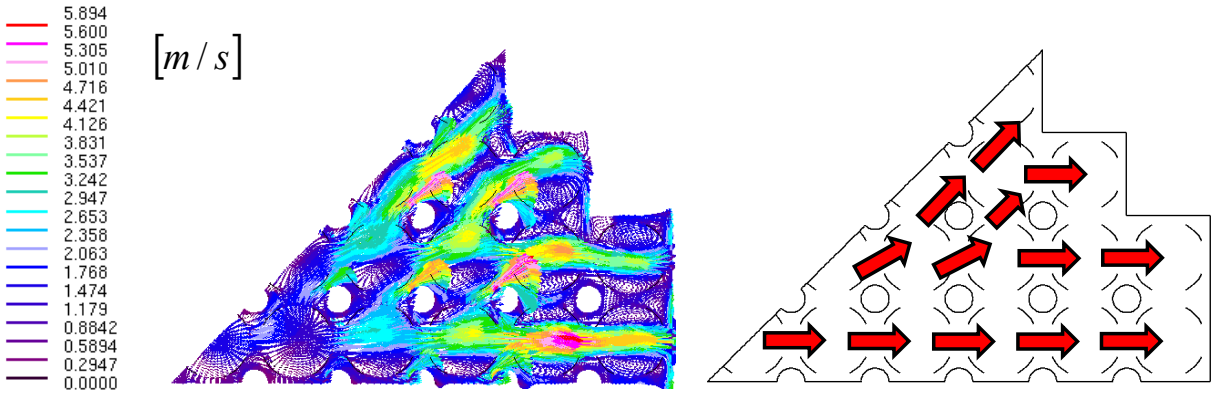

Fig. 4-1 u-, v-, w- velocity plot at a horizontal cut through the upper mixing chamber at half its height

Several modifications to break up this distinctive flow structure and to introduce additional turbulence to enhance the mixing have been analyzed. The different design modifications have been evaluated according to the standard deviation σ for the mixing and the established pressure drop of the upper mixing chamber. Regarding mixing, also the volume averaged inlet scalar distribution (marker fraction) and the peak values for each inlet scalar at the outlets (marker maximum) have been evaluated.

4.1 Turned Headpieces

As described above, the reference design had been designed to minimize the pressure drop. Accordingly, windows in the headpieces of different clusters are facing each other and the struts are placed close to the connection tubes. An idea to increase mixing caused by additional obstacles in the flow could be to turn the head piece by 45°. The change of the distinct flow structure and the introduction of additional turbulence have been expected by this modification. As the fuel element clusters with its headpieces need to be interchangeable among each other for burn-up optimization, all head pieces need to be turned simultaneously. Now, the inlet and outlet window elements do not face each other any more, and direct short cuts, as

in the reference case without mixing devices, are avoided. The averaged scalar concentration and peak values of the scalar concentration for this modification with headpieces turned by 45° are shown in Fig. 4-2. Comparing the results of this modification to the reference case of the simplified model, we see that the situation became even worse.

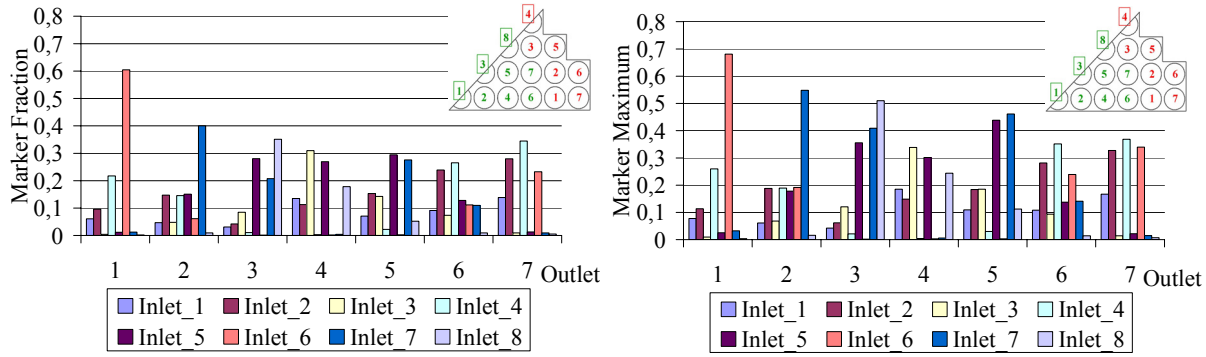

Fig. 4-2 Scalar concentrations, cross section averaged (left) and peak (right) in the upper mixing chamber with headpieces turned by 45°

Outlet 1 receives even 60% of the markers from inlet 6. Slightly better results are obtained for the local peak values of outlet 3, which receives only 50% from inlet 4 now. The reason for this mixing deterioration can be seen, when looking at the u-, v-, w- velocity plot in a horizontal cross section at half its height as shown in Fig. 4-3.

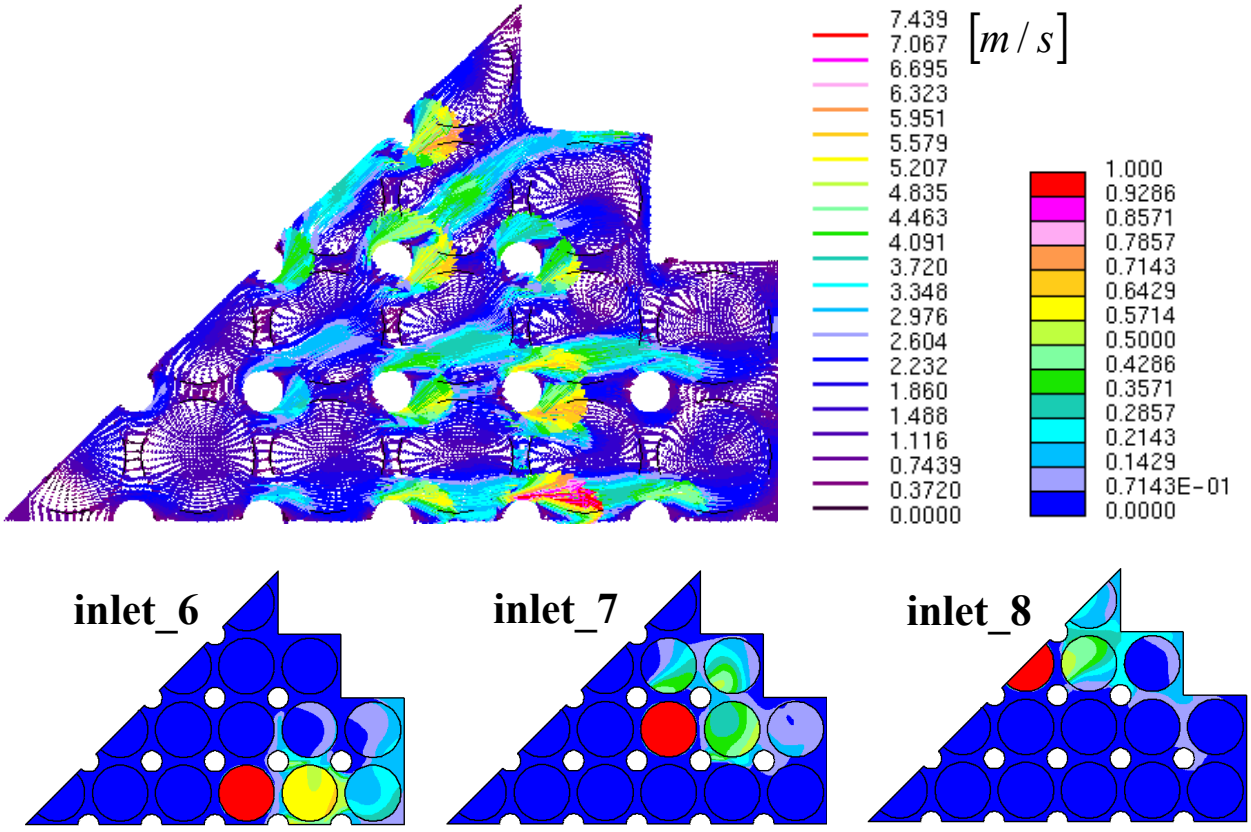

Fig. 4-3 u-, v-, w- velocity plot at a horizontal cut at half its height with turned headpieces and the results for the inlet scalars close to the outlet side

The results for inlet 6 and 7 are even worse in comparison to the reference case, when looking at the cross section averaged values, while the peak values are slightly better, as a result of the enhanced local turbulence. The flows coming from inlet 6 and 7 are now directed towards the connection tubes framing the headpieces of the inlet headpieces towards the outlet side. When colliding with the connection tubes which block the way of the inlet flows, these inlet flows are directed even more towards its neighboring outlets. The standard deviation for the mixing for this configuration has a value of $\sigma = 12.9\%$ ($\sigma = 12.1\%$), so it is slightly increased in comparison to the reference case. Also the pressure drop of the upper mixing chamber with the turned headpieces is slightly increased in comparison to the reference case; for this configuration its value is $\Delta p \approx 7 \cdot 10^3\, Pa$ ($\Delta p \approx 4 \cdot 10^3\, Pa$).

In conclusion, the configuration with the headpieces turned by 45° leads to worse results for both the mixing as well as for the pressure drop.

4.2 Outlets Shielded from Inlet Side

Another measure to improve mixing is to close the window elements of the outlet headpieces on the side facing the inlets, as shown in Fig. 4-4. This measure is similar to the turned head pieces that it also focuses on influencing the in-/ outlet geometry in the mixing chamber although it is more effective. This can be accomplished using plates that are welded into the upper mixing chamber so that assembly clusters still remain exchangeable.

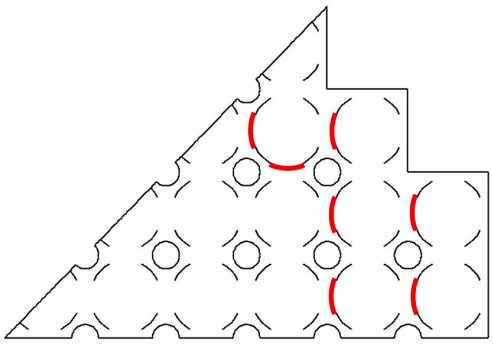

Fig. 4-4 Positions of the closed windows for the relevant window elements of the outlet headpieces

The results for this modification are shown in Fig. 4-5. The advantage of this modification is a reduction of the local peak value from the maximum of almost 70% to just over 50% for scalar 6 at outlet 1. Even though local mixing has been improved, the average marker fraction is still high; with 3.7 times the ideal homogeneous mixing we are still far from optimum.

These additional obstacles, which have been welded in, extend the mixing length locally, thus reducing the problem of the short cuts to some extent. The value of the standard deviation for the mixing has been reduced with this configuration to a value of $\sigma = 11.0\%$ ($\sigma = 12.1\%$). Along with the better mixing, however, the pressure drop in the upper mixing chamber, between the inlets and outlets, has been increased to $\Delta p \approx 0.18 \cdot 10^5\, Pa$ ($\Delta p \approx 4 \cdot 10^3\, Pa$), which it is still small compared to the pressure drop of the fuel assembly clusters.

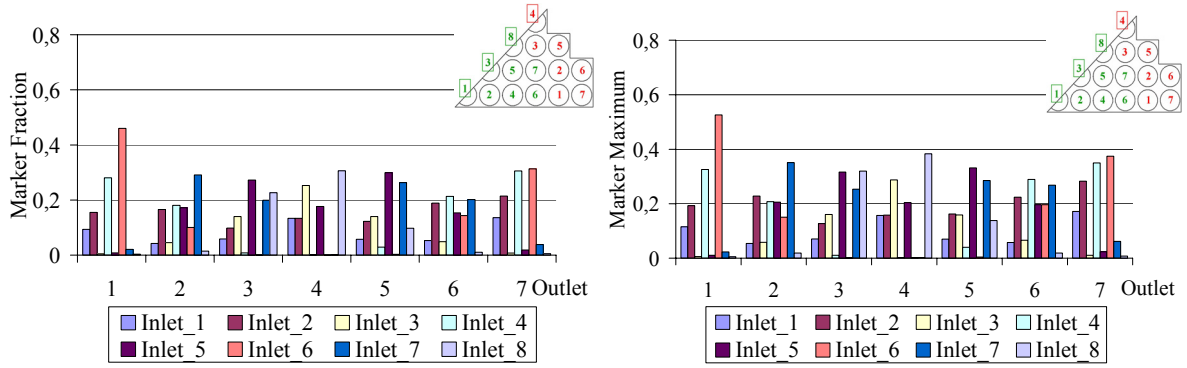

Fig. 4-5 Scalar concentrations, cross section averaged (left) and peak (right) in the upper mixing chamber with closed windows of window elements in headpieces of outlet clusters

Shielding the outlet side from the inlets is a very promising approach. It serves well to break up a flow structure with any short circuits between certain in- and outlets. However, the proposed walls, welded into the mixing chamber, which act as mixing promoters for this configuration, do not yet lead to sufficient mixing.

4.3 In- and Outlets at Different Heights

Since the reference case showed a horizontally layered flow structure, a modification with reduced inlet and outlet openings at different heights has been analyzed as a further modification. The idea is to break up the horizontal layers, to extend the mixing length, and to separate the neighboring inlets and outlets. This shall be realized with a design depicted in Fig. 4-6. The windows of the in- and outlet headpieces are partly closed with cans which are welded into the upper mixing chamber so that all head pieces are still the same and thus exchangeable. In the model, these cans are realized with baffle cells, like the headpiece geometry. The vertical positions of cans and openings are also shown in Fig. 4-6. L stands for low, whereas H stands for a high position of the opening, meaning that the opening is located at the bottom or at the top of the upper mixing chamber, respectively. The dashed line indicates the cans, which are displayed underneath to give a better impression of how the openings are realized at different heights.

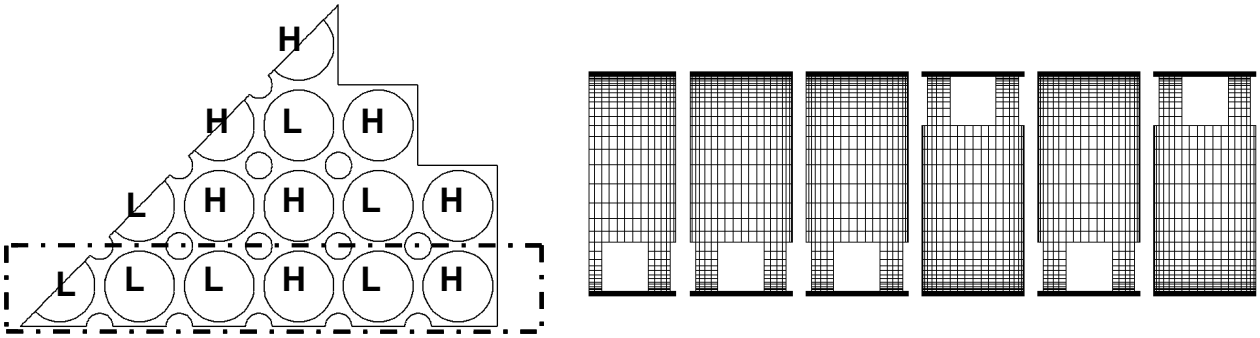

Fig. 4-6 Positions of high and low in- and outlet openings; left side: distribution of top and bottom openings; right side: vertical positions of the openings

The results for the constellation with in- and outlets at different heights indicate that the distribution has shifted drastically, as shown in Fig. 4-7. However, even though the short cuts

between neighboring in- and outlets have been eliminated, very high concentrations, volume averaged as well as for the local peak values, are obtained. As an example, outlet 7 receives 66% of the scalar released from inlet 6 and outlet 4 receives 60% from inlet 8. It appears that inlet and outlet head pieces, having their openings at the same height, find a short cut even if they are not neighboring. A very efficient mixing appears only if two head pieces have openings at different heights.

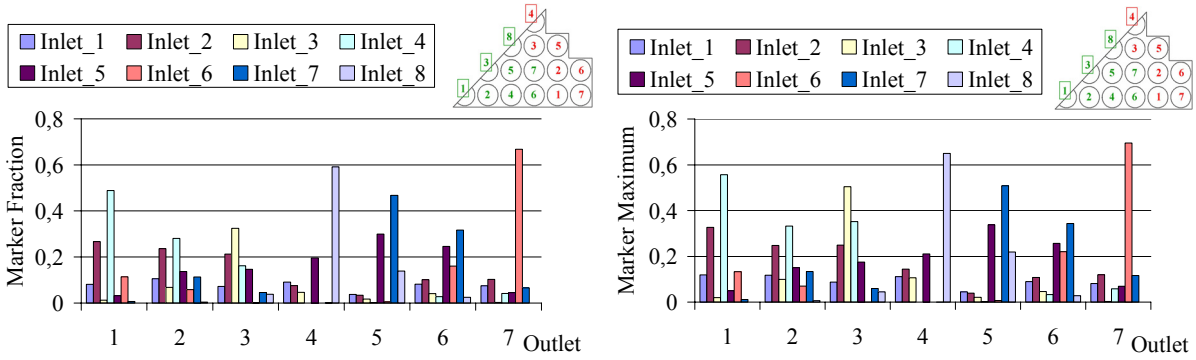

Fig. 4-7 Average and peak scalar concentration in the upper mixing chamber in case that in- and outlets are at different height

In general it can be seen that the scalar transport takes place mainly between in- and outlets at the same height. This effect even outranges the short cuts found between neighboring in- and outlets for the reference case. In Fig. 4-8, this effect is shown by looking at the inlet scalars 4 and 6 exemplarily, in the formerly presented vertical cross section.

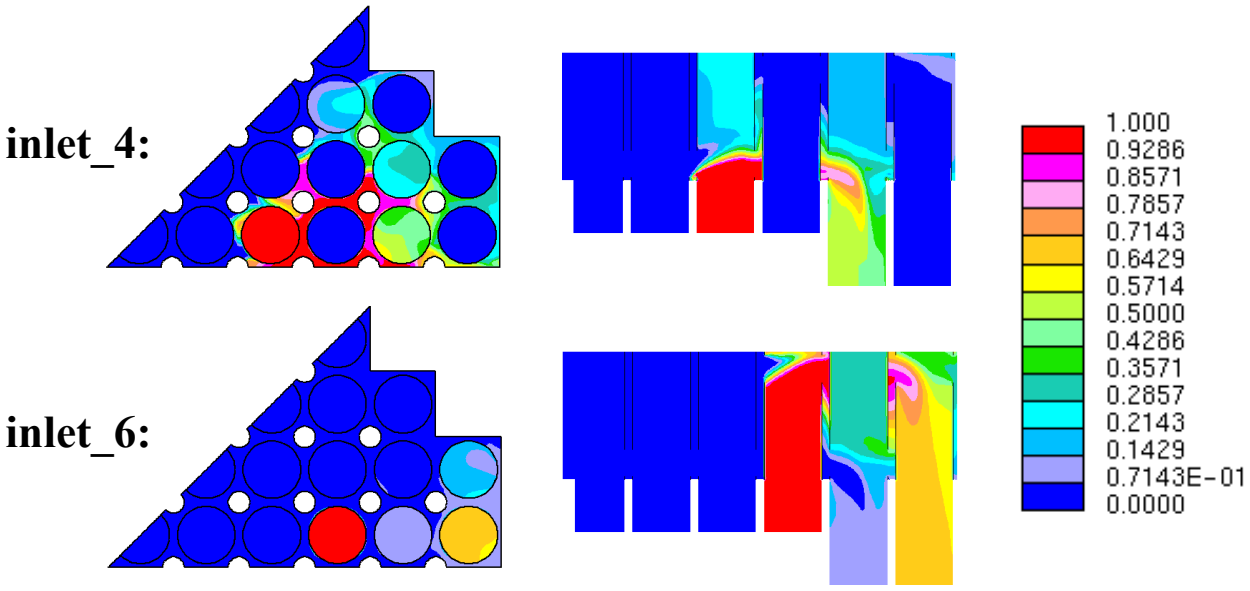

Fig. 4-8 Exemplary results for the configuration with in- and outlet openings at different heights

While the pictures on the left, showing the view from underneath, give an overview of the scalar distribution in a more general way, the short cut effect between the in- and outlets at the same height is captured in the cross sections depicted on the right side of Fig. 4-8. Inlet scalar

4 hardly interacts with its neighboring inlet 6 and is transported mainly to outlet1, while inlet scalar 6 hardly leaves the mixing chamber via its neighboring outlet 1 and is transported to the next outlet in radial direction, outlet 7. The pressure difference between the inlet and outlet side, on the other hand, is found to be around $\Delta p \approx 0.29 \cdot 10^5\, Pa$ ($\Delta p \approx 4 \cdot 10^3\, Pa$). Thus, it is still small compared with the pressure drop in the fuel assemblies.

The proposed configuration shows that the inlet distribution is influenced strongly when the in- and outlets of the mixing chamber are located at different heights. However, other and more severe short cuts are established between in- and outlets at the same height leading to deteriorated mixing and a standard deviation of $\sigma = 15.1\%$ ($\sigma = 12.1\%$).

4.4 Collection and Re-distribution of the Inlet Flows

Up to now, all modifications studied to enhance mixing focused on influencing the flow locally. Approaches were focused on changes to the direction of the inlet flows, or enhancing mixing with introduced obstacles. A different approach is to collect the inlet flows, before distributing them again to the different outlets.

Constructively, this can be realized by simply welding a vertical wall with a slot at the top between the inlet and outlet side of the upper mixing chamber. This way, the inlet flows are collected on the evaporator side of the wall before being forced to pass through a defined small cross section. In Fig. 4-9 the position of the wall between evaporator and superheater assembly clusters is depicted. For the presented first analysis, the wall covers 46 cm of the total chamber height of 48 cm, leaving a slot of 2 cm underneath the top cover of the mixing chamber.

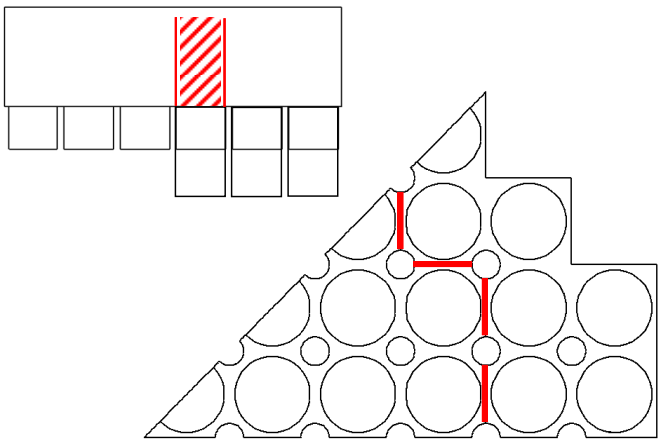

Fig. 4-9 Collecting and re-distribution of inlet flows; separation wall with gap between inlet and outlet regions

The results for the scalar distribution of this case are shown in Fig. 4-10. A much better scalar distribution is obtained. Outlet 1 receives only 35% of inlet 6 and outlet 7 receives 34% of inlet 7, being the worst cases of the averaged inlet scalars. Peak values for the concentration are below 38% in worst cases. This mixing is much better than in the reference case. Averaged inlet scalar concentrations are less than 2.8 times the ideal, homogenized distribution,

and local peak concentrations achieve only 3 times the values of the case with ideal mixing. The obtained standard deviation for this case is $\sigma = 9.3\%$ ($\sigma = 12.1\%$).

Along with the good mixing, on the other hand, a very high pressure drop of about $\Delta p \approx 10^6\,Pa$ ($\Delta p \approx 4 \cdot 10^3\,Pa$) is obtained for the rather small slot. Compared with the pressure drop in the fuel elements, this pressure drop is very high and can hardly be accepted.

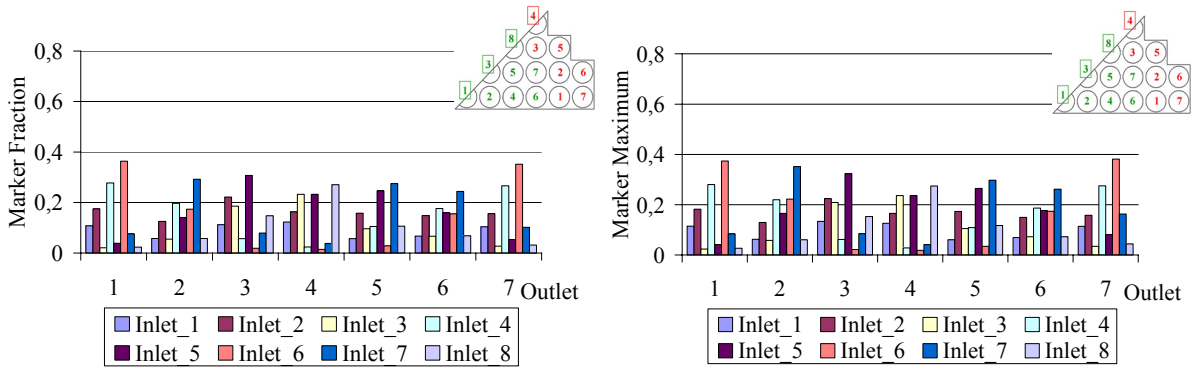

Fig. 4-10 Average and peak scalar concentration of the configuration with a separation wall between the in- and outlet side

4.5 Collection and Re-distribution of the Inlet Flows –Meander Alignment

After evaluating several cases, which separate the inlet from the outlet side, an alignment with three stages has been found as the best way to enhance mixing while keeping the pressure drop within acceptable limits. In Fig. 4-11 such a meander structure and the results for exemplary inlet scalars are depicted. The size of the gaps between the mixing stages has been optimized to a certain limit. Further optimization can be achieved with a finer grid. The gap for the first introduced wall is defined as 18cm, the second gap is 18cm as well, and the value for the third gap is 14cm.

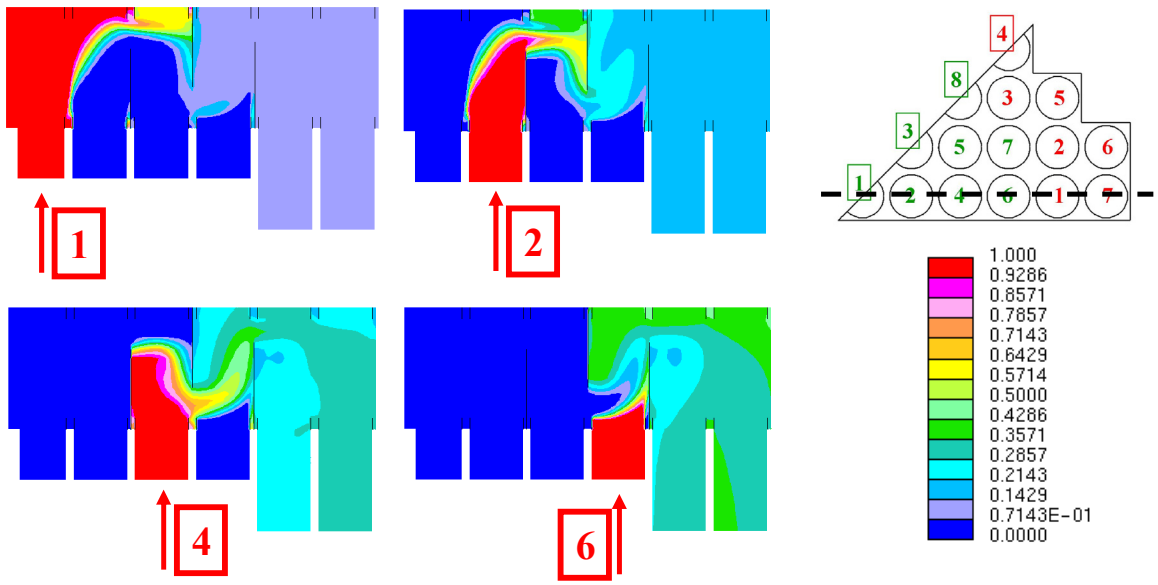

Fig. 4-11 Meander structure dividing the upper mixing chamber in three stages

When comparing the results for the mixing obtained for this meander structure, similar results as for the case with only one separation wall and a very small gap are obtained. The obtained standard deviation is $\sigma = 8.8\%$ ($\sigma = 12.1\%$). Outlet 7 receives 37% percent of inlet 6. The peak values are also small and stay below 39% as can be seen in Fig. 4-12. The pressure drop for this constellation is, however, acceptable with a value of $\Delta p \approx 0.5 \cdot 10^5\, Pa$ (0.5 bar).

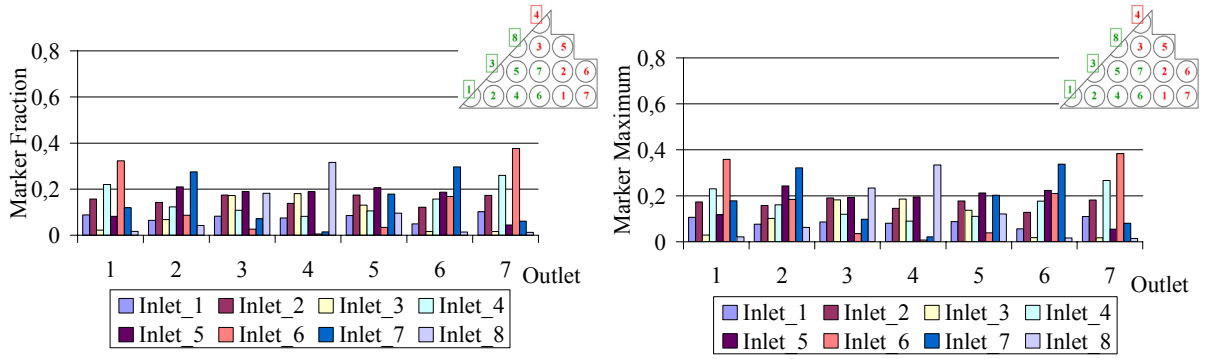

Fig. 4-12 Average and peak scalar concentration of the scalar distributions in the upper mixing chamber with a meander structure, separating the upper mixing chamber into three stages

In Fig. 4-13, the histogram for the results shown in Fig. 4-12 is depicted. It confirms that the standardized normal distribution (Gaussian distribution) has been reached approximately but not ideally.

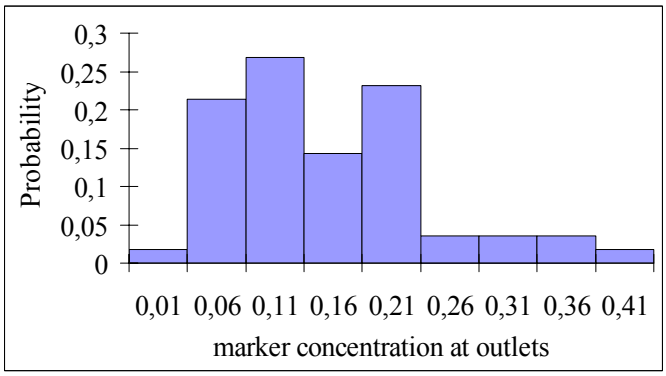

Fig. 4-13 Probability that an inlet marker reaches a certain outlet

4.6 Evaluation of the Different Modifications

Target values for the standard deviation describing the mixing and for the pressure drop have been given by Schulenberg in [68]. For the mixing a standard deviation of $\sigma = 5\%$ and for the pressure drop a value of 0.15bar have been assumed.

Without any measures to enhance mixing (reference case), the scalar distribution at the outlets is exceeding acceptable limits by far. Simply turning the headpieces, by 45 °, as presented in 4.1 does not lead to an improvement as well; the results for the scalar distribution overall are even worse. Better results for the mixing are achieved by introducing obstacles in the flow. When the outlet headpieces are shielded from the inlet side, presented in 4.2, an improvement for the volume averaged mixing is achieved and local peak values are decreased. In compari-

son to this configuration, the configurations without additional obstacles do experience a negligible additional pressure drop. The pressure drop, of course, depends on how much resistance is introduced into the upper mixing chamber by blockages, obstacles, etc. For the evaluated case with baffles cells at the windows of the outlet headpiece window elements facing the inlet flow, a small and thus acceptable, additional pressure drop is obtained. Influencing the mixing by arranging the in- and outlet openings at different, individual heights, discussed in 4.3, does have a strong influence on the mixing. Due to more severe short cuts between in- and outlets at the same height, this configuration provides even worse results than for the reference case, the mixing reacts very sensitive to the introduced changes and the pressure drop is still relatively small.

Concerning the mixing, a very effective approach is to separate the inlet and outlet regions to achieve a collection of the inlet flows before distributing them to the outlets, like presented in 4.4. This approach of collecting and then distributing the different inlet flows leads to best results for the mixing. Due to the small gap between the separating wall and the top of the mixing chamber, however, a very high pressure drop of around 1MPa is obtained. Thus, the pressure drop in the upper mixing chamber exceeds the pressure drop in the fuel assemblies by a factor of more than 5. The best result concerning both mixing and the created additional pressure drop is achieved with the alignment presented in chapter 4.5, the presented meander structure, with which the upper mixing chamber is divided into three stages. In this configuration the gaps between the different zones of the mixing chamber can be enlarged, achieving even better results for the mixing but decreasing the pressure drop significantly. A comparison of the assumed values with the achieved values for the mixing and the pressure drop is shown in the HPLWR is shown in Tab. 4-1. The results for the lower mixing chamber are presented in Annex A (Lower Mixing Chamber), for the upper mixing chamber, the meander alignment proposed in 4.5 is used.

	upper mixing chamber	
	assumed	**achieved**
standard dev. of coolant mixing	5%	8.8%
pressure drop	0.15bar	0.5bar
	lower mixing chamber	
	assumed	**achieved**
standard dev. of coolant mixing	5%	5.5%
pressure drop	1bar	0.2bar

Tab. 4-1 Comparison of assumed and achieved values for the mixing chamber in the HPLWR

Comparing the cases with enhanced mixing of the simplified model and the assumed values for the mixing chambers in the three pass core proposal by Schulenberg et al [68], it is found that the mixing is approximately within the assumed limits. The assumed standard deviation for the mixing in both mixing chambers has been 5%. For the upper mixing chamber a value of 8.8% and for the lower mixing chamber a value of 5.5% has been achieved, which is still acceptable. The pressure drop of 0.5bar for the upper mixing chamber exceeds the assumed value of 0.15bar, whereas the obtained value of 0.2bar for the lower mixing chamber is significantly lower compared to the assumed value of 1bar. The proposed solution for the optimized mixing chamber is shown in Fig. 4-14. For this picture, the top of the upper mixing chamber has been removed to allow an insight. The introduced vertical walls forming the meander structure are shown in grey.

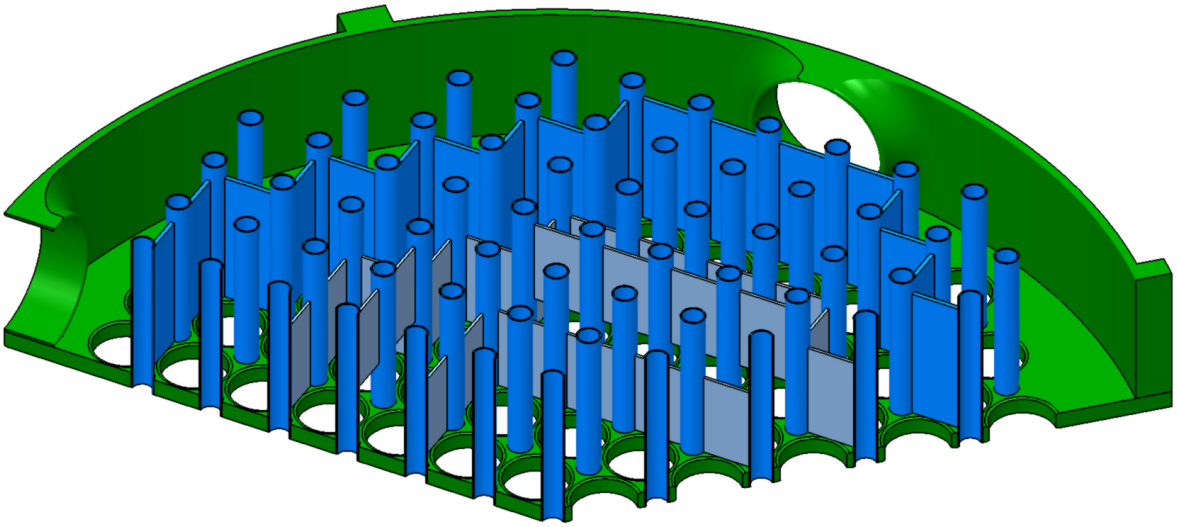

Fig. 4-14 Design of the optimized upper mixing chamber

According to the simplification method presented in this work, so far all analyses for the upper mixing chamber of the HPLWR have been performed for the simplified model. The next step when applying the method for the analysis of complex mixing chambers outlined in chapter 3.1 (Simplification Method) is described in the following chapter.

5 Including the Effects of the Omitted Structures

The first step of the method to analyze complex mixing chambers, which has been introduced in chapter 3.1, has been performed already by building and optimizing the simplified model as described in the chapters before. The moderator boxes, as well as the thickness of the headpiece struts however, will have an influence on the mixing. In the following sections, their influences will be quantified and added to the simplified model by applying the simplification method to the upper mixing chamber of the HPLWR. The required steps are listed in the beginning of chapter 3.1, they are:

1) Simplifying the geometry

2) Quantifying the influences of the disregarded headpiece structures on the mixing

3) Introducing these influences via source terms into the simplified model.

To carry out the second step, a model of the headpiece geometry in all relevant detail has to be built.

5.1 Detailed Analysis of the Flow in the Headpiece Structures

5.1.1 Detailed Headpiece Model

Modeling the upper mixing chamber without all the rather complicated headpiece structures served as a first step of the analysis. It has to be checked how much the omitted structures influence the mixing. An analysis of a single headpiece in the transverse flow field of the upper mixing chamber and an analysis of two neighboring headpieces without a transverse flow field have been performed by Möbius et al. [49]. The results of this analysis show good mixing between the neighboring in- and outlet headpiece, as well as great influence of the headpiece's inner obstacles on the flow field of the upper mixing chamber. For further analysis, neighboring in- and outlet headpieces have been evaluated in the flow field of the upper mixing chamber. In Fig. 5-1, the grid of one single headpiece and the extended grid with two headpieces and additional fluid volumes to apply the necessary boundary conditions used in the presented analysis are shown.

The configuration applied to the detailed headpiece model is a combination of the inlet 6 and the outlet 1 cluster, thus representing the worst case detected in the reference case using the simplified model.

All presented results are based on the grid shown in the center of Fig. 5-1, which will be referred to as the detailed headpiece model. Additional fluid volumes are added to the sides of the model to minimize the influence of the boundaries on the evaluated flow.

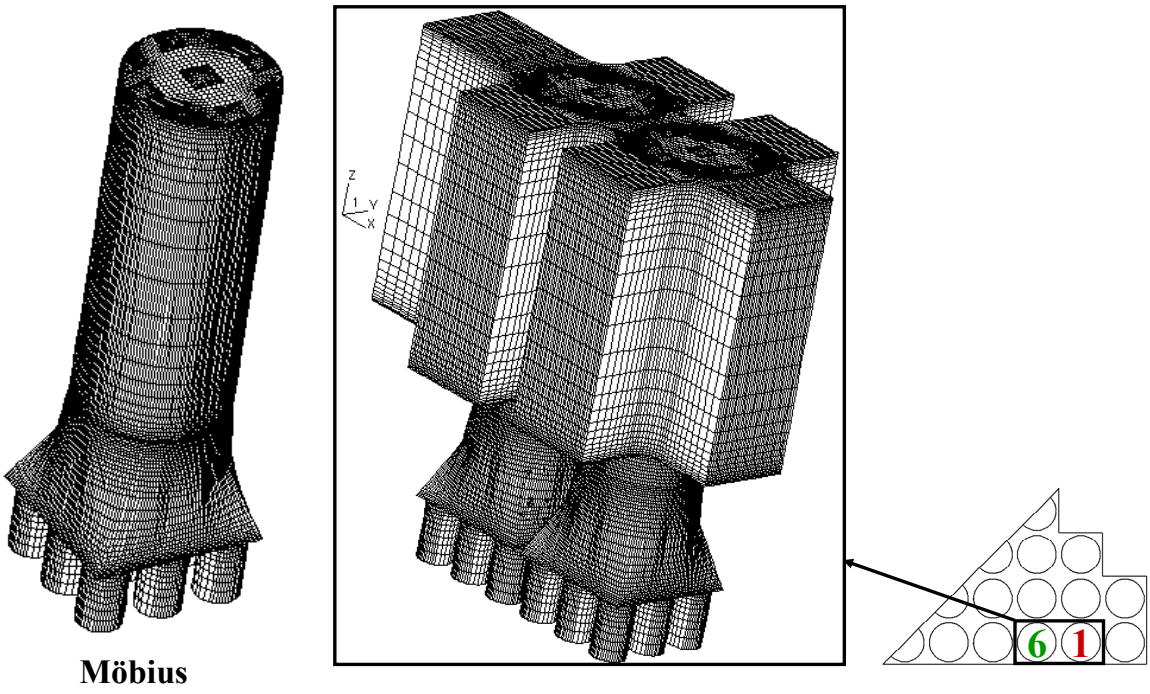

Fig. 5-1 Numerical mesh of a single headpiece proposed by Möbius [49] and of two neighboring headpieces in a transverse flow field

The applied boundary conditions are depicted in Fig. 5-2; here all inlets are depicted with yellow-red color. At the bottom of the headpieces there are either nine inlets or nine outlets for each headpiece representing the fuel elements united in one cluster. A transverse flow is applied with the extracted boundary conditions from the solution of the simplified model. The side inlet of the model introducing the transverse flow of the upper mixing chamber is approximated with a block profile with an inlet velocity of 2m/s.

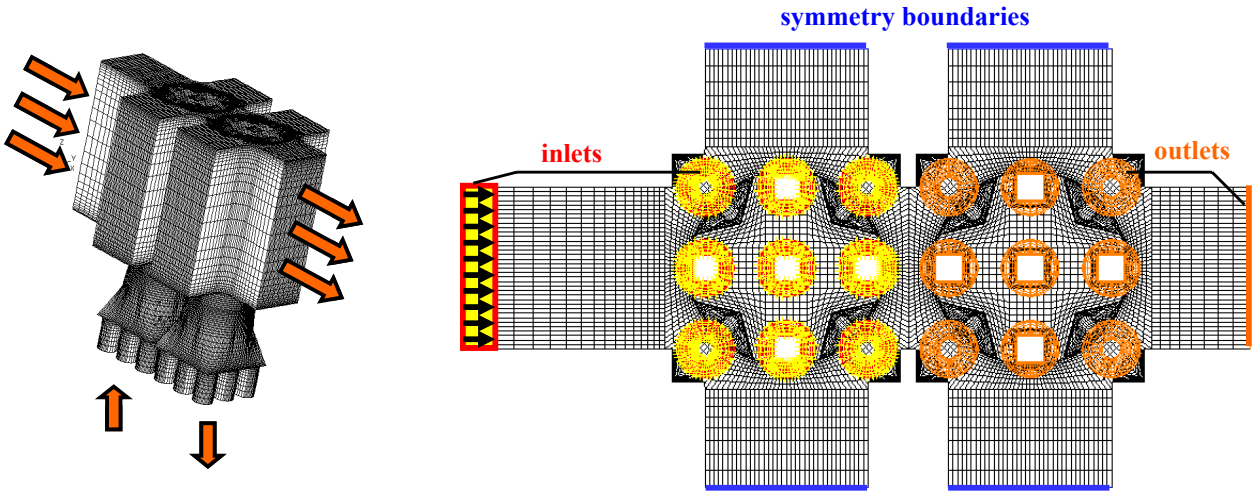

Fig. 5-2 Boundaries applied to the detailed headpiece model

For the headpiece representing the evaporator cluster, block profiles in vertical direction are applied to the inlets on the bottom of the model with a velocity of 5.7m/s for the inlets in the corners of the cluster and 4.6m/s for the other inlets. The inlet velocity for each inlet is esti-

mated using the mass flow and the inlet cross section of the nine inlets. No inlet velocity component in tangential direction has been added, even though the wire wrap spacers proposed by Himmel in [25] are likely to introduce a swirl to each fuel element. Effects of these global inlet swirls applied to each of the nine inlets have been analyzed by Möbius et al. in [49], but are found to be negligible. The boundaries applied to the outlets are pressure boundaries (brown). They are applied to the bottom of the model for the modeled superheater I headpiece and to the outlet side of the model in radial direction. On the sides orthogonal to the main flow directions, symmetry boundaries (blue) are applied as a first guess.

In this detailed headpiece model, all geometry features of the headpieces design are included as demonstrated in Fig. 5-3. The transition nozzle of the headpiece geometry has been rebuilt and all connection tubes are now included in the model. As in the simplified model, the window elements are included by adding baffle cells to the headpiece outer diameter, thus framing the windows by two-dimensional, impermeable cells. It can be seen that the grid is refined towards the window elements and towards the moderator boxes since here the largest gradients are expected in the flow field.

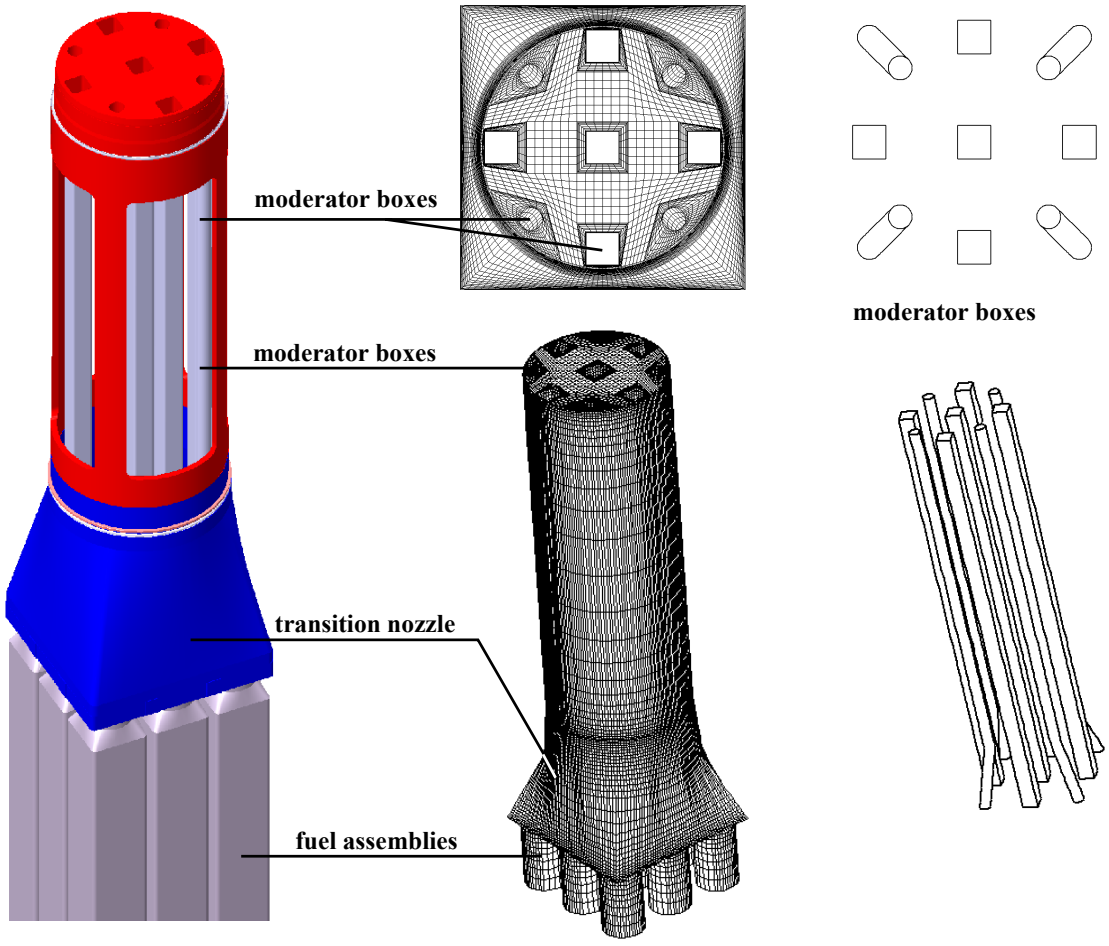

Fig. 5-3 Level of detail fort he detailed headpiece model of the headpiece geometry

The inlet boundary condition for the side inlet, with which the transverse flow is introduced, has been extracted from the simplified model. In Fig. 5-4, the u-,v-,w- velocities in a horizontal cutting plane of the mixing chamber are shown, the red line shows the position where the

cross flow velocities have been extracted. They have been averaged, to apply them to the detailed model.

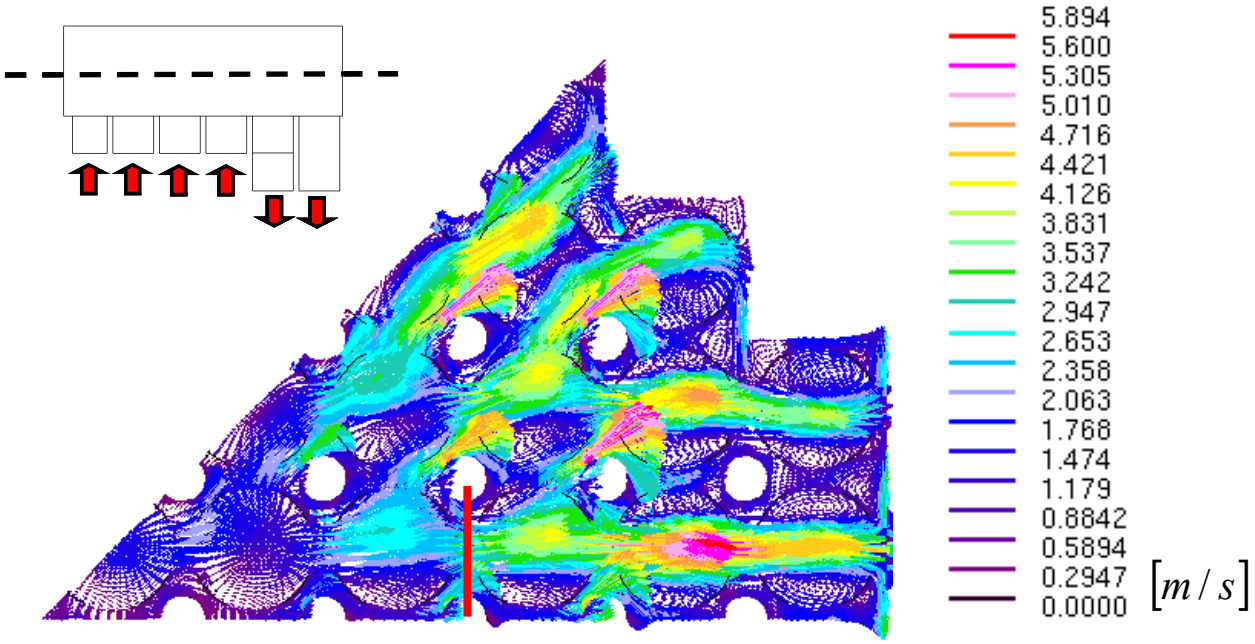

Fig. 5-4 Velocities at a horizontal cross section of the simplified model

5.1.2 Verification – Grid Sensitivity Analysis of the Detailed Headpiece Model

Another grid sensitivity analysis has been performed for the detailed headpiece model to determine the influence of the numerical resolution on the evaluated magnitudes. Again, both the pressure drop and the mixing will be evaluated and plotted over 1/N, where N represents the number of cells in the model. Also, for all analyzed grids, the y^+-values are kept inside the predetermined limits.

Five grids in a range between around 120.000 cells for the coarsest and 1.300.000 cells for the finest grid have been analyzed. Again, any baffles are disregarded for the grid sensitivity analysis. To refine especially the regions where the largest gradients were expected, the number of cell layers around the introduced moderator boxes and the number of cell layers in vertical direction has been increased. The two evaluated qualities are again, the maximum of the volume averaged scalar concentration for all outlets and the total pressure. The first order interpolation scheme UD and the third order interpolation scheme QUICK for the spatial discretization have been tested.

This time, the difference between the inlet and outlet pressure is evaluated, between the evaporator and superheater I fuel elements, respectively, that is the in-/ outlets from the bottom of the detailed headpiece model. The maximum inlet scalar concentration, or the maximum percentage of any inlet detected at an outlet, is obtained in the same way as for the simplified model, explained in 3.4 (Verification – Grid Sensitivity Analysis). Now, each of the nine inlets is charged with a separate scalar and the distribution is then evaluated at the outlets. The result of the grid sensitivity analysis for the detailed headpiece model is shown in Fig. 5-5.

The difference between the pressure drop of the coarsest and the finest grid is around 480Pa, which is much smaller (2 orders of magnitude) than the pressure drop of interest. For the maximum inlet scalar almost no significant change is visible, when comparing the obtained values of the different grids. Also, for both quantities no differences are detected between the UD and the QUICK scheme. For further analysis, the UD scheme is chosen in combination with a grid consisting of around 250.000 cells to reduce the numerical effort, while ensuring adequate results.

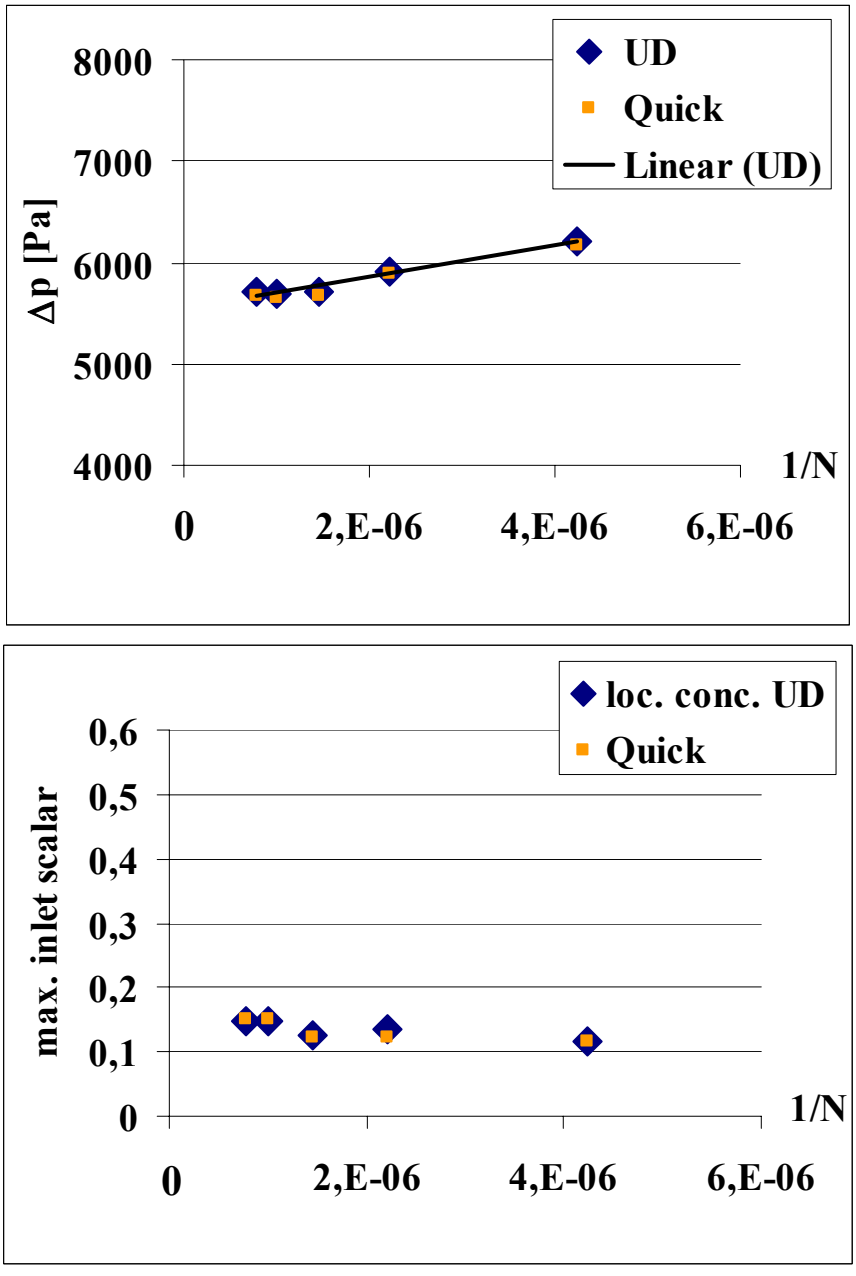

Fig. 5-5 Grid sensitivity analysis of the detailed headpiece model

5.1.3 Simplified Headpiece Model

When comparing the results obtained for this detailed model with the local result for the simplified model, it has to be taken into account that the flow field in the upper mixing chamber is strongly influenced by the other inlet flows. A better comparison can be achieved, when comparing the detailed model with a cutout model of the simplified model, the so-called simplified headpiece model. Again, the same neighboring in- and outlet headpieces are modeled, but without any details like waterboxes or the reducing diameter in the lower part of the model.

Also, a simple transverse flow as applied in the detailed headpiece model can not lead to a quantitative comparison for the mixing and pressure drop of the simplified model and the detailed headpiece model. However, it can serve as a basis to quantify the influences of the disregarded headpiece geometry.

The nine inlets representing the fuel elements are combined in one inlet, respectively one outlet as in the simplified model. This is possible, since the inlets on the bottom of the model, representing any cluster of the mixing chamber neighboring an outlet cluster have to be charged with only one passive scalar for all the nine inlets, to evaluate the mixing in the detailed headpiece model as well. This way, the mixing of this scalar can be compared to the simplified model, where the scalars are applied to each cluster. The simplified headpiece model is shown in Fig. 5-6; it consists of a much lower number of cells than the detailed headpiece model. However, its boundaries applied correspond to the ones of the detailed model as do the dimensions of the added fluid volumes.

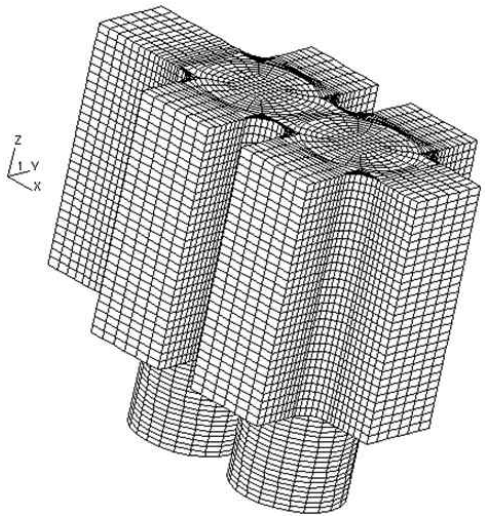

Fig. 5-6 Grid of the simplified headpiece model

Refining the grid of the simplified headpiece model only towards the connection tubes and treating all geometry elements exactly as treated in the simplified model leads to a grid for the simplified headpiece model consisting of less than 45.000 cells. Quantifying the influences of the detailed headpiece geometry omitted in the simplified model, can be done by comparing the results for the two headpiece models: the detailed headpiece model, based on the actual geometry and the simplified headpiece geometry, based on the simplified model according to the simplification method.

5.1.4 Comparison of the Detailed and Simplified Headpiece Model

When comparing the detailed and the simplified headpiece model, large differences in the models as well as in the results are found. The two different models are displayed in Fig. 5-7; on the bottom of the picture, a top view of each model is shown. Obviously, the numerical effort for the simplified headpiece model consisting of around 45.000 cells is significantly reduced in comparison to the detailed headpiece model with 230.000 cells. Also, the analyzed flow structure is much simpler.

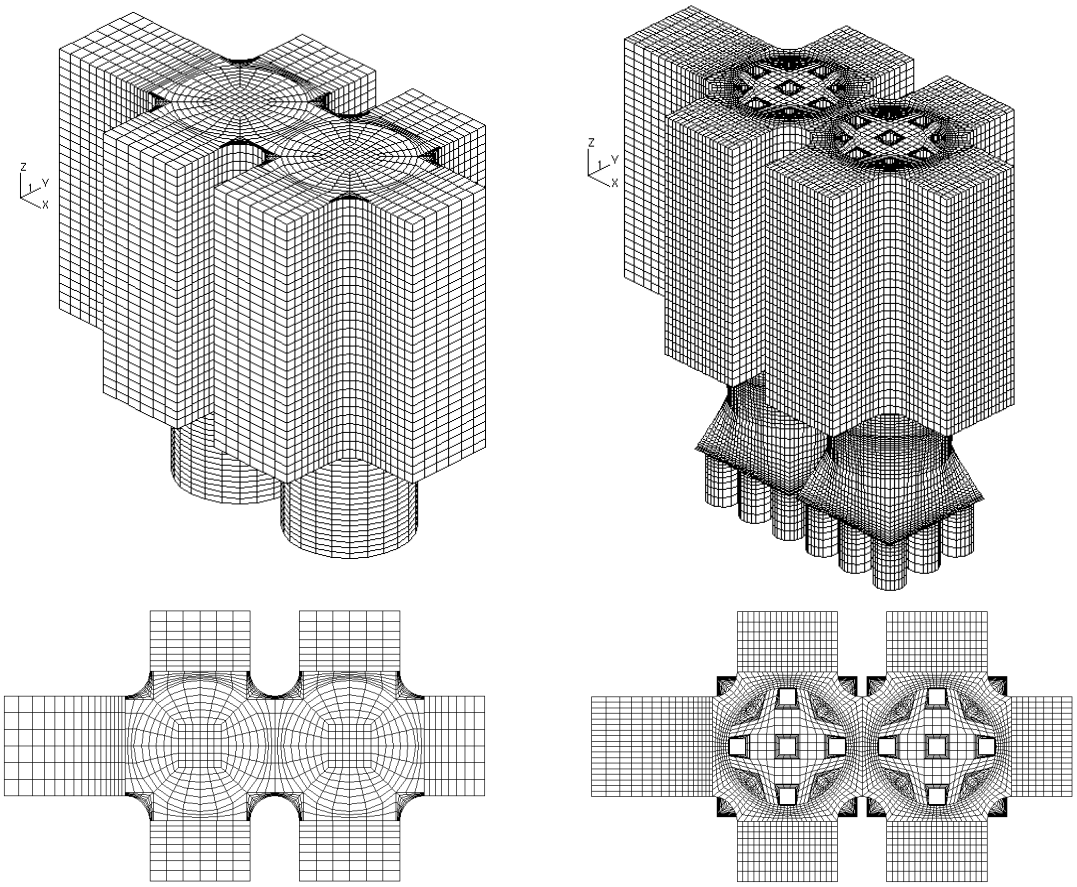

Fig. 5-7 Comparison of the simplified (left) and detailed (right) headpiece model

The results for the mixing of the simplified headpiece and of the detailed headpiece model can be seen in Fig. 5-8 from underneath. Whereas 53.5% of the inlet scalar 6 is transported to outlet 1 in the simplified model, only 40.5% of the inlet scalar reaches the neighboring outlet in the simplified headpiece model. When comparing the models where only two headpieces are regarded, the difference due to the disregarded details is higher than due to the simplified boundaries applied to the cutout section with simplified boundary conditions.

In the simplified headpiece model, the difference between the highest and lowest value for the neighboring inlet scalar varies between 29.8% and 62.6%. For the detailed model, a more homogenized flow is found for the outlets on the bottom of the model; the scalar concentration varies between 25.4% and 40.0%. There is also a large difference in the overall amount of the inlet scalar reaching the neighboring outlet. For the detailed headpiece model, only

35.7% reaches the neighboring outlet, while in the simplified headpiece model this number is higher at a value of 42.3%.

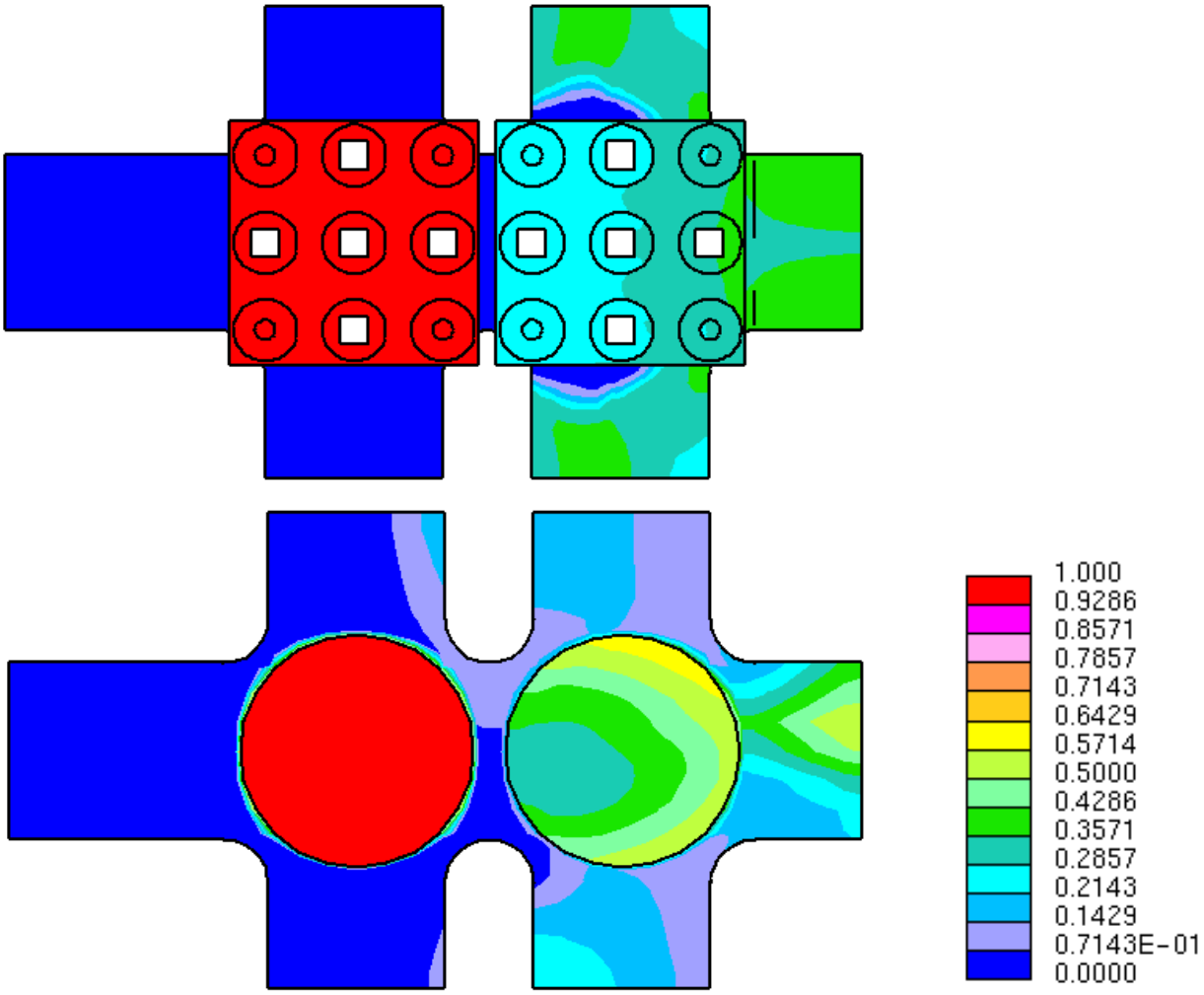

Fig. 5-8 Distribution of the inlet scalar in the neighboring outlet – top: detailed headpiece model, bottom simplified headpiece model

The large differences in the mixing of the fluid are caused by the disregarded moderator boxes. These boxes act as obstacles on the flow, leaving only small gaps where the water can pass through the headpieces. In these smaller gaps, local jets are formed resulting in a better transport of the inlet scalar beyond the neighboring outlet headpieces. Also, the velocities in the lateral direction are much higher due to the flow obstacles leading to a better mixing of the inlet flow charged with the scalar and the transverse flow in the mixing chamber. In Fig. 5-9 the velocity fields of the two headpieces models at a cross section at half the height of the model, as indicated on the right side of the figure, are displayed.

Two very distinctive jets are shaped by the waterboxes in the detailed headpiece model. Here the flow is accelerated strongly and additional turbulence is introduced by the obstacles in the flow. Also, the transverse flow hitting the headpieces is in some extent deflected to the sides. This distinct flow structure leads to a much higher transport of the inlet scalar past the neighboring headpiece, representing outlet 1 of the simplified model. In addition, the mixing

of the inlet 6 scalar is enhanced significantly, which is noticeable by the more homogeneous distribution at outlet 1.

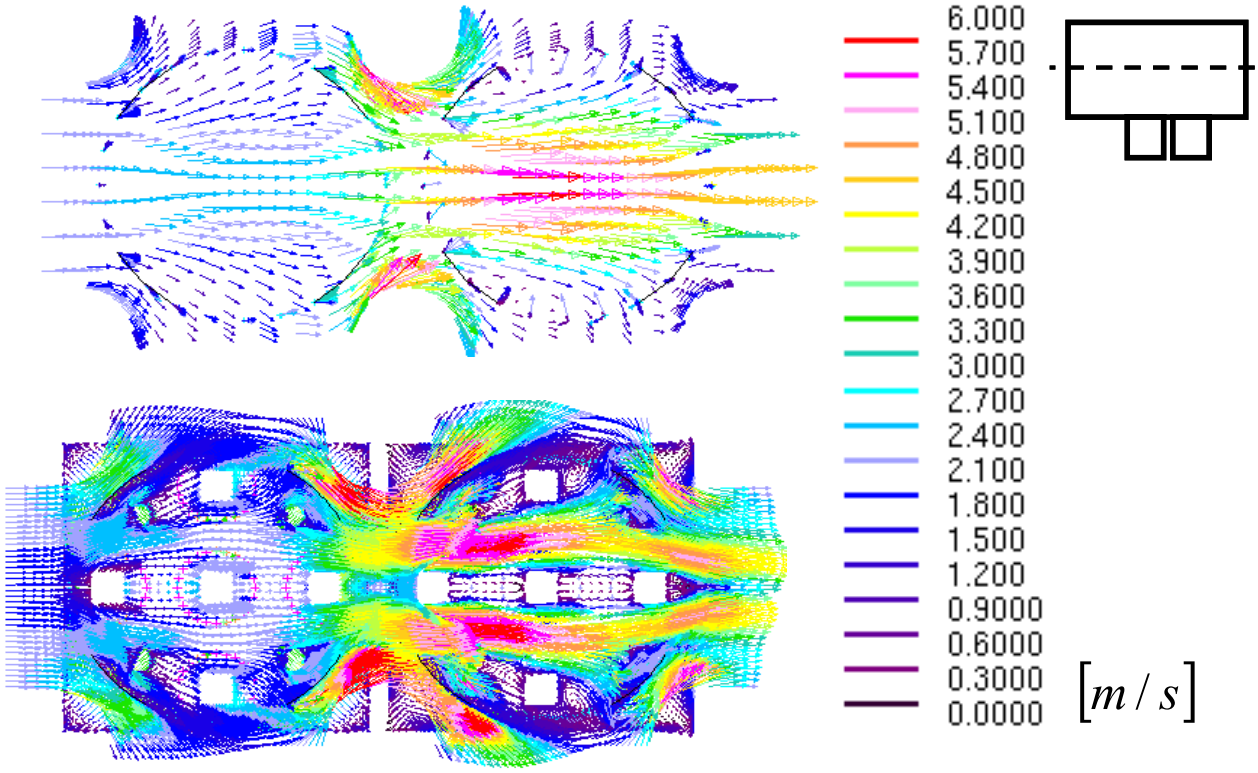

Fig. 5-9 Velocities in a horizontal cross section of the simplified (top) and detailed headpiece model (bottom)

5.2 Introduction of the Headpiece Influences

As described in chapter 3.1, the effect of the omitted structures on the mixing is introduced into the Reynolds equations according to (3.1). The idea is to introduce source terms resembling the effects of the omitted structures.

5.2.1 Insertion of Local Forces

An idea to introduce the effects of the initially disregarded moderator boxes in the model, without actually introducing their geometry, is to insert local forces at the positions of the moderator boxes. This idea is outlined in Fig. 5-10 and the forces to be introduced are indicated exemplarily for the central moderator boxes.

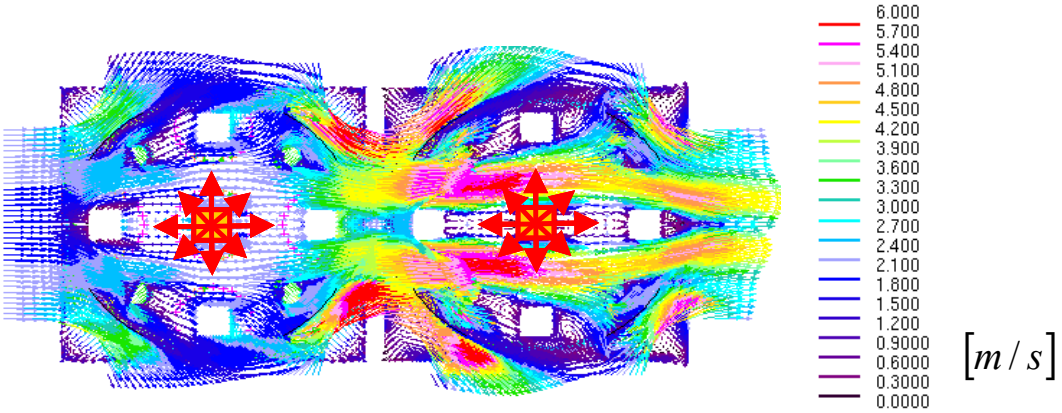

Fig. 5-10 Introduction of local forces to replace waterboxes

Merely to see if this approach can be generally successful, the detailed headpiece model has served as a basis and additional cells are introduced where the moderator boxes had been in the model. Thus, “the holes in the model (moderator boxes) are filled” and a detailed model without struts as flow obstacles has been built. The created model is shown on the left side of Fig. 5-11 from above. While the cells of the detailed headpiece model are depicted in red, the additional cells representing the moderator boxes can be seen in a light brown color. On the right side of the figure below, the additional almost 50.000 cells for the moderator box structures are shown. Overall the model size has been increased to 300.000 cells.

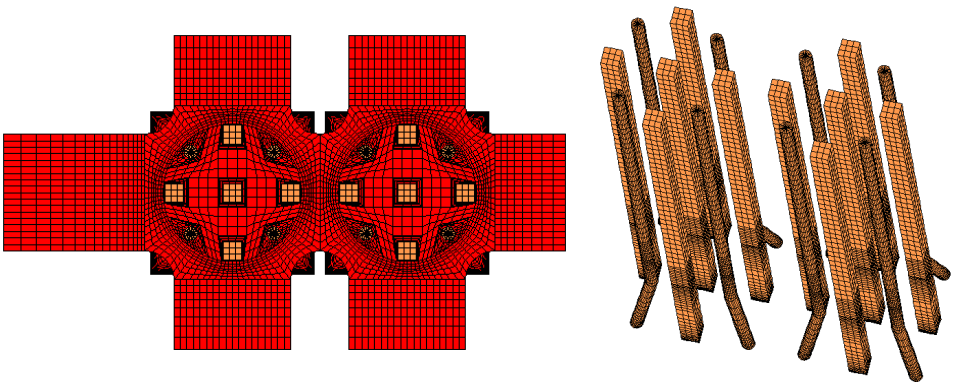

Fig. 5-11 Detailed model with cells filling the positions of the moderator boxes, thus creating a model without distinctive flow obstacles

For this created model without distinctive flow obstacles, which resembles the simplified headpiece model, analogue results are obtained. To add the effects of the detailed headpiece model to this model, source terms have been added to the newly introduced cells representing the moderator boxes. Since in reality no water can pass through these cells, the applied source terms are calculated with the pressure drop imposed by the omitted obstacles. For the steady-state analyses presented, the source terms are forces divided by unit volume with the unit N/m^3. The geometrical entities are taken from the quadratic shaped moderator boxes that have a width of approximately $a = 0.03m$ and a height of $h = 0.48m$ and are applied for all additionally introduced cells. To calculate the pressure drop, the pressure drop coefficient of a rectangular tube in a transverse flow $\varsigma = 1.05$ is applied according to [50] (page 149). The pressure drop can be calculated as:

$$\Delta p = \varsigma \frac{1}{2} \rho (u)^2 . \tag{5.1}$$

For the source term and a constant value for the density $\rho = 215 kg/m^3$ this leads to:

$$\frac{F_R}{V} = \frac{A \Delta p}{V} = \underbrace{\frac{A}{V} \varsigma \frac{\rho}{2}}_{C} (u)^2 . \tag{5.2}$$

On the left side of (5.2) F_R / V is the force per unit volume to be introduced, while F_R is the resting force. A is the area of the flow obstacle represented by the introduced force (width a times height h of the rectangular moderator box) and V is its volume.

Since all values are known, a general pre-factor can be introduced that defines the introduced source term as a function of velocity. For the definition of the local forces, this leads to a pre-factor of $C = 4000 kg/m^4$. The source term as function of the velocity is plotted in Fig. 5-12.

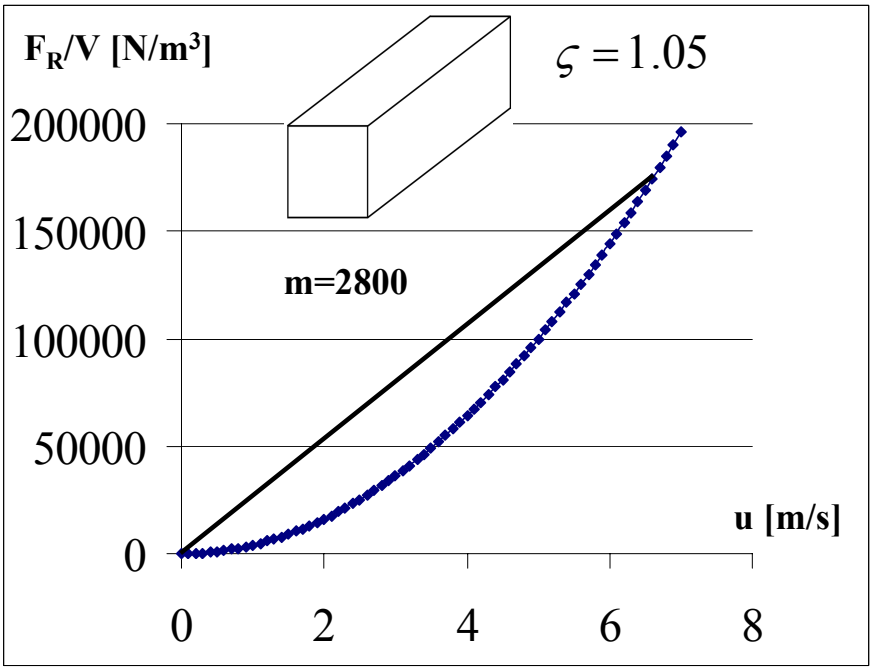

Fig. 5-12 Source term as a function of the velocity for local forces

Star-CD requires a linear function at this point, therefore the function is approximated with a straight line that has slope of $m = 2800$ and starts at the origin. The introduced force represents the rectangular pipe in the transverse flow field. Applying a linear function leads to an additional error. In newer versions of the code, it should be possible to apply quadratic functions, thus reducing the error. When looking at the results obtained for this detailed model with source terms, analogue results are obtained compared to the results for the detailed model. In a horizontal cross section at half of the height, the flow structure is very similar to the detailed model. This is shown in Fig. 5-13, in which the detailed model with source terms (top) is compared to the detailed model (bottom).

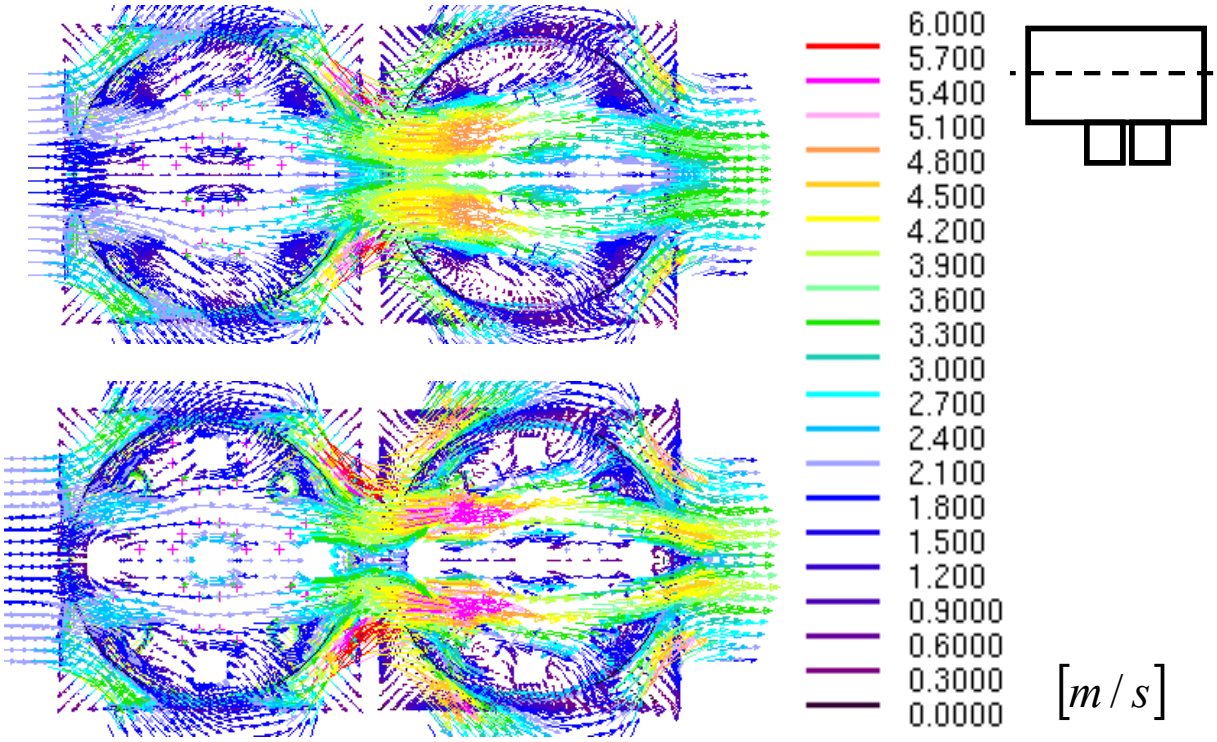

Fig. 5-13 Velocity plotted for the detailed model, top: waterboxes introduced with source terms, bottom: waterboxes geometrically resolved

When comparing the two velocity plots in the figure above, the same two noticeable velocity jets are found. For the detailed model with the resolved moderator box geometry, these jets are slightly more pronounced and the velocity gradients between the accelerated water in between the waterboxes and the regions with small velocities are slightly higher.

In Fig. 5-14 the scalar distribution at the outlet is shown for the detailed model (bottom) and the detailed model with introduced cells charged with source terms representing the moderator boxes (top). The scalar distribution is very similar and shows the same structure, but the values are generally higher for the model with applied source terms. In the detailed model, 35.5% of the neighboring inlet scalar is detected at the analyzed outlet with a local maximum of 44% and a local minimum of 29.7%. For the model with the applied source terms, 38.5% of the neighboring inlet scalar is detected at the outlet and the local maximum and minimum vary between 35.1% and 44.6%.

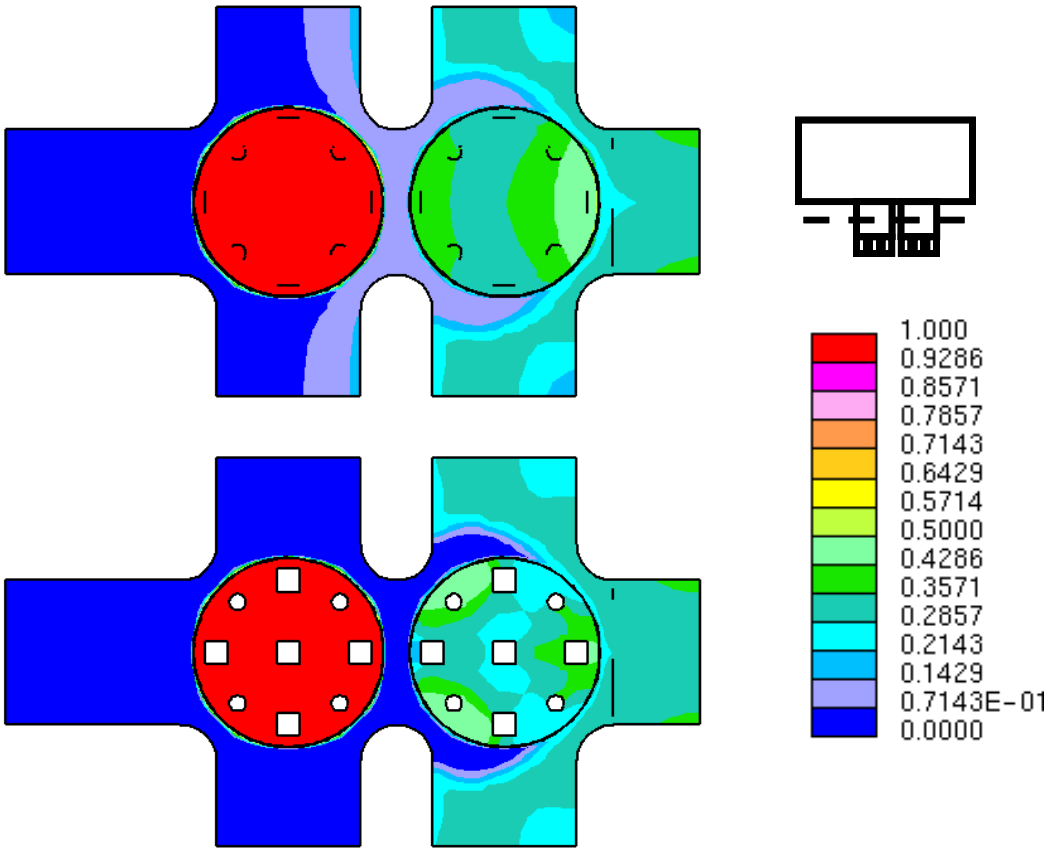

With source terms:

Sc1 – averaged: 38.5%
Min: 35.1% Max: 44.6%

Geometrically resolved:

Sc1 – averaged: 35.5%
Min: 29.7% Max: 44.0%

Fig. 5-14 Scalar distribution plotted for the detailed model, top: moderator boxes introduced with source terms, bottom: moderator boxes geometrically resolved

The agreement between the two models is significantly better than the predictions of the simplified model as depicted in Fig. 5-14. Not only the results for the scalar distribution are almost the same, but also the flow structure is very similar.

Reasons for the small discrepancy between the two approaches might be the approximation of the quadratic function describing the applied source term by a linear function or the coarse resolution, especially of the cells filling the moderator box structures.

Even though these results are promising, adding additional cells that are then charged with sources terms does not lead to a reduction in the numerical effort as intended. The additional cells increase the numerical effort and the added source terms deteriorate the convergence of the simulation. Therefore, the derived source terms are added to the simplified headpiece model in order to combine the good results for the mixing and the much decreased numerical effort. Due to the very coarse local discretization of the simplified headpiece model, an exact local application of the source terms could not be achieved and the position of the moderator boxes had to be approximated. The positions of the introduced source terms are indicated in Fig. 5-15 with the red cells.

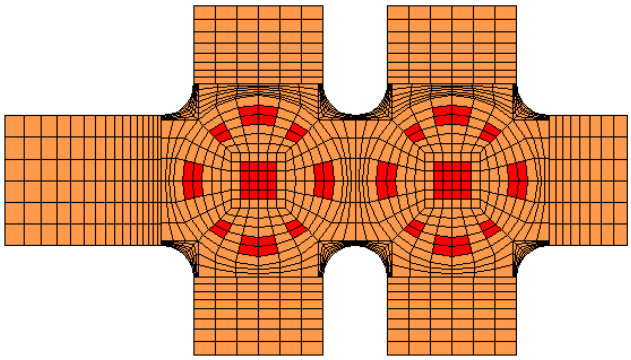

Fig. 5-15 Position of cells with local source terms representing the initially omitted moderator box structures

The results of this model, however, vary significantly from the results obtained for the detailed headpiece model. In Fig. 5-16 the velocities and the scalar distribution for the two models are plotted. For the simplified headpiece model with local source terms, almost twice as much of the neighboring inlet scalar is detected at the analyzed outlet and the range between the minimum and maximum value for the scalar is much higher.

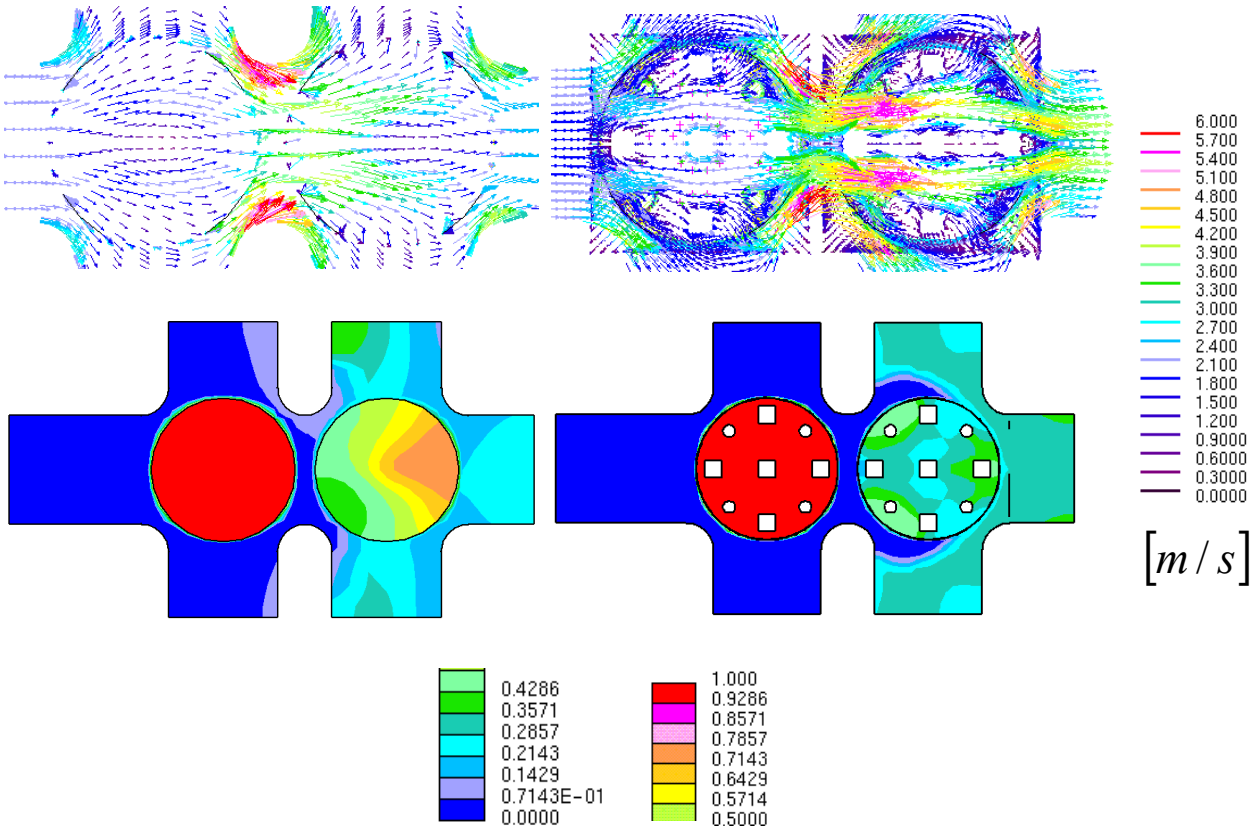

With source terms:

Sc1 – averaged: 53.1%
Min: 35.5% Max: 79.8%

Geometrically resolved:

Sc1 – averaged: 35.5%
Min: 29.7% Max: 44.0%

Fig. 5-16 Velocities and scalar distribution – left: simplified headpiece model with local source terms, right: detailed model

The reason for this very significant discrepancy between these models lies within the coarse discretization of the simplified headpiece model, rather than in the rough approximation of position of the moderator boxes represented by the applied source terms. This can be seen when looking at the velocity plots for each model for a cross section at half its height as depicted above. The flow structure stays the same, again two jets can be seen in the simplified headpiece model, but since the very high gradients imposed on the flow by the strong forces cannot be reproduced between only two cell layers. To achieve a better reproduction of these gradients, local refinement of the grid (as performed for the detailed headpiece model) becomes necessary.

The result of this failure to reproduce strong gradients leads to a general deceleration of the flow within the entire headpiece not just locally and thus to a much higher scalar concentration in the neighboring outlet. Also, the scalar distribution to the sides is overestimated, since the entire headpiece acts now almost as a blockage. Using the higher order QUICK discretization scheme delivers analogue results.

To overcome these described disadvantages of the model, global forces are introduced to capture the effect of the headpiece geometry as a whole rather than locally.

5.2.2 Insertion of Global Forces

When introducing the effect of the headpiece geometry as a whole, claims to reproduce local effects cannot be met. The approach is similar to the presented approach for the insertion of local forces. Again, the applied source terms are derived with the pressure drop estimated for the headpiece geometry.

The two approaches using either local or global forces to outweigh the momentum are similar to the porous media approach, e.g. used by Kunik et al. [40]. In the porous media approach omitted structures are generally regarded by an additional pressure resistance. However, in contrast to the general porous media approach it is possible to introduce source terms only to specific regions of the grid, since no specifications for the boundary conditions between fluid cells and porous media cells are necessary.

Therefore, all cells framed by the window elements, representing the headpiece geometry in the simplified headpiece model are charged with source terms. The resulting simplified headpiece model with introduced global forces is depicted in Fig. 5-17 outlining the idea by indicating the region where the forces are introduced.

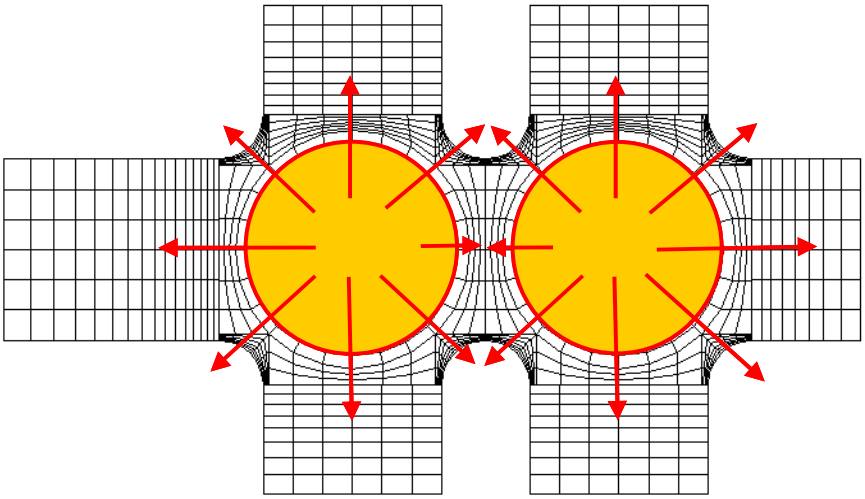

Fig. 5-17 Insertion of global forces representing an entire headpiece

To derive the forces which have to be introduced, the pressure drop of the headpiece geometry is approximated with a hand calculation using the pressure drop coefficient according to Kays [36]. When looking at a cross section of the headpiece geometry as depicted in Fig. 5-18, the flow coming from the side is canalized in two distinctive jets framed by the center and outer waterboxes. If only the upper (or lower) half of the headpiece geometry is regarded as shown in the figure on the right side of Fig. 5-18, the effect of the geometry on the flow can be reproduced by a very simple and abrupt change in the flow cross section.

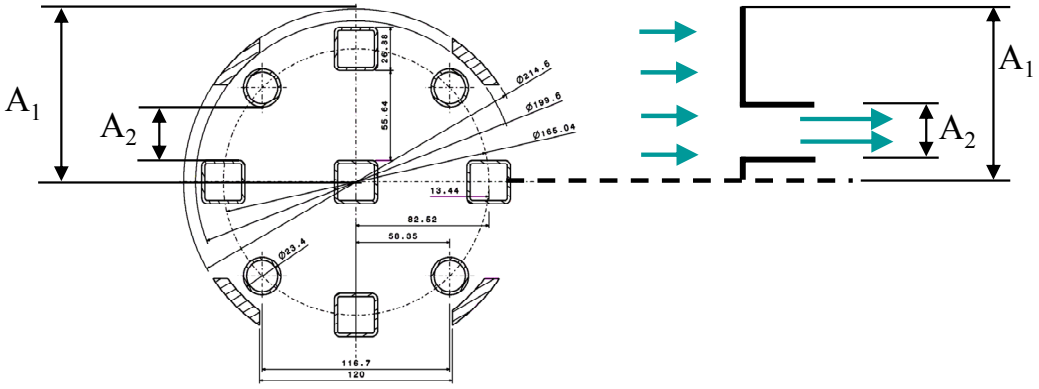

Fig. 5-18 Approach to model the headpiece with global forces

This approach is not only applicable if the flow approaches the headpiece from one distinctive side, but also if it approaches the headpiece with an angle. Due to its structure, certain channels can always be distinguished, framed by the central and outer moderator boxes.

For the simplified structure displayed on the right side of Fig. 5-18 a pressure drop coefficient has been defined according to Kays [36]. The pressure drop coefficient for flows across an abrupt contraction is given as a function of the ratio of the two cross sections A_1 / A_2. Here, a pressure drop coefficient of $\varsigma = 0.3$ is found. Applying the same hand calculations (5.1) and (5.2) as for the insertion of local forces, a global resistant force $F_{R,Global}$ is found with a prefactor $C = 160 kg/m^4$, leading to the depicted function in Fig. 5-19 for the source term. To approximate the quadratic function, a linear function starting in the origin with the slope $m = 750$, has been chosen.

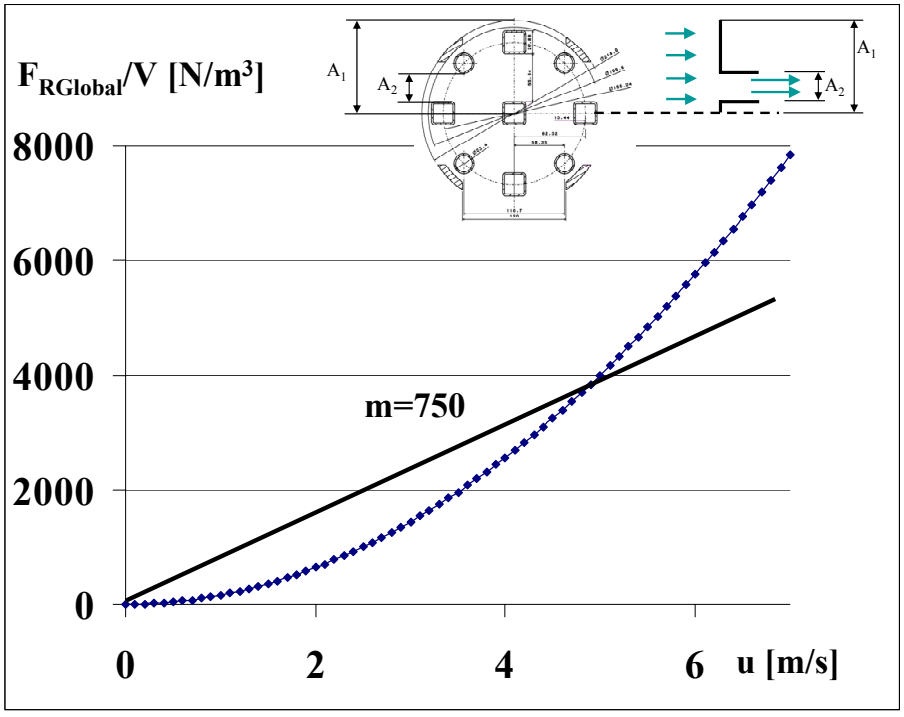

Fig. 5-19 Source term as a function of the velocity for global forces representing an entire headpiece

When applying the derived forces to each headpiece globally, the marker distribution shows large differences in comparison with the detailed headpiece geometry. The results for both cases are depicted in Fig. 5-20. The depicted velocity plots show that the flow is generally decelerated, which leads to an even higher marker concentration at the neighboring outlet.

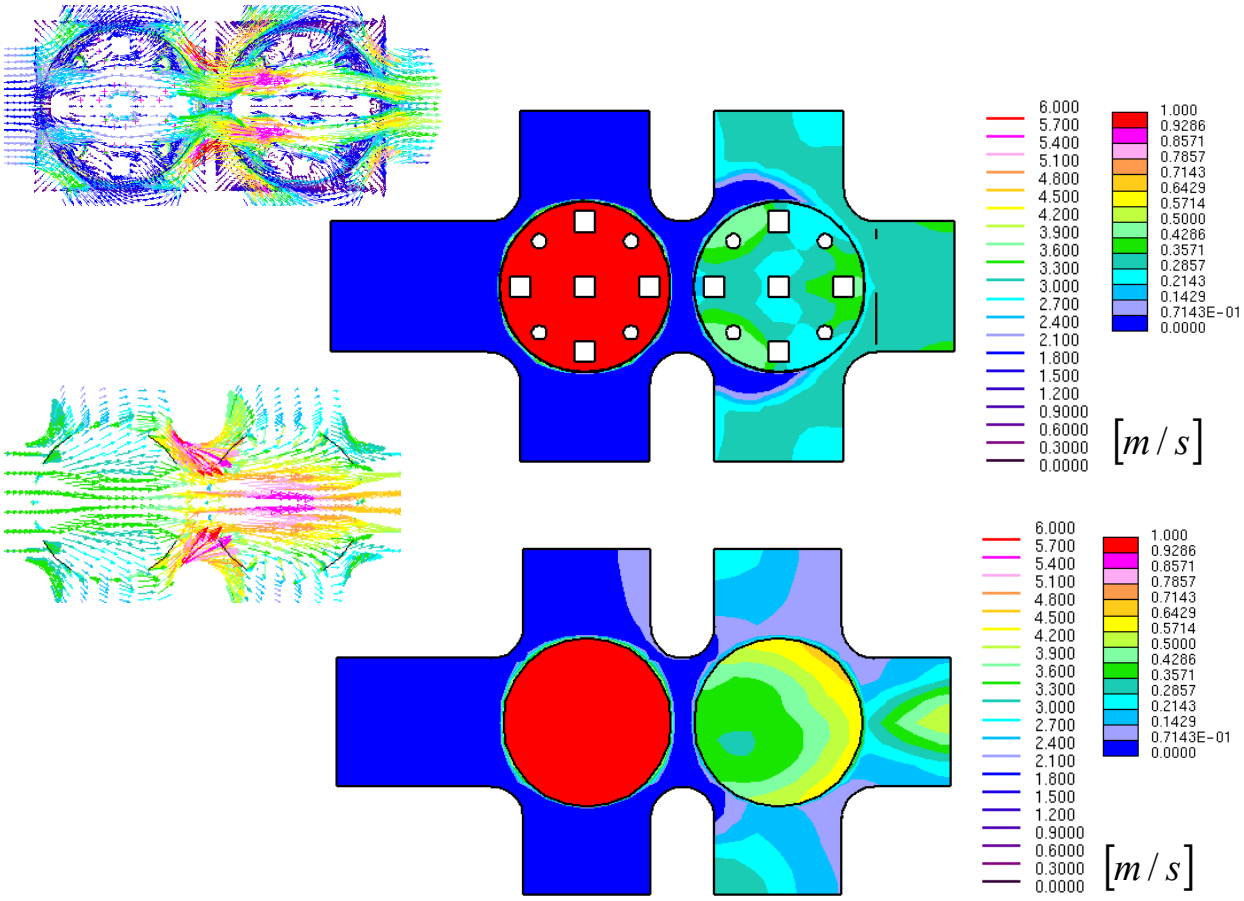

Fig. 5-20 Comparison of the results for the detailed headpiece model (top) and simplified headpiece model with global forces (bottom)

In this case, 43.7% of the inlet marker is transported directly to its neighboring outlet. The local minimum for this model with global forces is 33.2% and the local maximum is 67.9%, thus exceeding the values found for the detailed headpiece model and also for the simplified headpiece model.

In the here analyzed case, where global forces are introduced, the pressure drop imposed by the additional structure within the flow is captured. However, the forced deviation imposed on the flow by the waterboxes within the headpiece geometry accelerating the flow locally is neglected. This acceleration is responsible for the better mixing by transporting a larger fraction of the inlet scalar past its neighboring outlet and has to be regarded.

5.2.3 Insertion of Global Forces Accelerating the Flow

The distinctive velocity jets formed in the gaps between the moderator boxes lead to an acceleration of the flow. Since this effect is responsible for the better mixing in the detailed headpiece geometry, a force shall be introduced into the simplified headpiece geometry to generate this acceleration.

The local acceleration within the headpiece is based on continuity. The flow is accelerated between the moderator boxes by the forced deviation as a result of the reduction in the cross section. Further behind the headpieces, the velocity jets are dissipated. An approach to capture this effect is to add forces directed in the flow direction.

Himmel has used an analogue approach to accelerate the flow in [27], which is based on the balance of momentum. In comparison to the porous media approach, where the effects of geometries in the flow are introduced as resistances, here volumetric forces are introduced as momentum sources pointing in the direction of the flow.

In the previous chapter 5.2.2 (Insertion of Global Forces) only the resistance of the waterboxes has been introduced into the flow, while the accelerating effects due to the forced deviation has not been regarded. To add these effects, an acceleration force F_A has to be introduced, which can be derived by integrating the steady-state Reynolds equations (2.69) over the volume, where the forces will be applied:

$$\underbrace{\int_V \left(\rho \left(\overline{u}_j \frac{\partial \overline{u}_i}{\partial x_i} \right) \right) \mathbf{d}V}_{Convection} = \underbrace{-\int_V \frac{\partial \overline{p}_i}{\partial x_i} \mathbf{d}V}_{Pressure} + \underbrace{\int_V \left(\frac{\partial}{\partial x_i} \left[\left(\mu + \mu_t \right) \left(\frac{\partial \overline{u}_i}{\partial x_j} + \frac{\partial \overline{u}_j}{\partial x_i} \right) \right] \right) \mathbf{d}V}_{Resistance} . \tag{5.3}$$

The following simplifications are introduced in equation (5.3):

a. The flow is regarded as one-dimensional.

b. The velocities are constant over the in- and outlet cross section of the analyzed volume.

c. The pressures are constant over the in- and outlet cross section of the analyzed volume.

The different terms are indicated in the equation (5.3). Since the resistance of the omitted structure has already been included in the previous chapter, the resistance term can be replaced by the global resistance force F_R. Thus, the integration leads to the following momentum balance:

$$\underbrace{\left(\rho_1 A_1 u_1^2 - \rho_2 A_2 u_2^2 \right)}_{Acceleration} = \underbrace{-\left(A_2 p_2 - A_1 p_1 \right)}_{Pressure} + \underbrace{F_R}_{Resistance} . \tag{5.4}$$

Here the indices 1 and 2 represent the values at the in- and outlet cross section of the regarded volume.

The acceleration can be introduced with the acceleration force according to:

$$\left(\rho_1 A_1 u_1^2 - \rho_2 A_2 u_2^2\right) = F_A . \tag{5.5}$$

Assuming constant density, this leads to:

$$\rho\left(A_1 u_1^2 - A_2 u_2^2\right) = F_A . \tag{5.6}$$

F_A can be calculated with the same cross sections as shown in Fig. 5-18. The velocity u_2 can be calculated applying the continuity equation:

$$\rho A_1 u_1 = \rho A_2 u_2 , \quad u_2 = \frac{A_1}{A_2} u_1 . \tag{5.7}$$

Thus, the acceleration force F_A can be written as a function of the velocity:

$$F_A = \rho\left(A_1 u_1^2 - A_2\left(\frac{A_1}{A_2} u_1\right)^2 \right) = \rho\left(A_1 - A_2\left(\frac{A_1}{A_2}\right)^2 \right) u_1^2 . \tag{5.8}$$

Since a volumetric force has to be applied, equation (5.8) has to be divided by the volume, for which the force has been derived:

$$\frac{F_A}{V} = \frac{\rho}{V}\left(A_1 u_1^2 - A_2\left(\frac{A_1}{A_2} u_1\right)^2 \right) = \frac{\rho}{V}\left(A_1 - A_2\left(\frac{A_1}{A_2}\right)^2 \right) u_1^2 = C_A \cdot u_1^2 . \tag{5.9}$$

The constant pre-factor $C_A = -480 kg/m^4$ is found. It is negative, since the force is applied on the right side of the equation and points in flow direction.

To combine the source terms for the resistance and the acceleration in one simulation, a resulting global volumetric force has to be calculated. Therefore the two source terms $F_{SR} = F_R / V$ and $F_{SA} = F_A / V$ have to be added as shown in Fig. 5-21. The resulting source term for the entire headpiece is $F_S = F_{SA} + F_{SR}$.

The acceleration force is directed into the direction of the flow. Adding the resistant force acting in opposite direction slowing down the flow reduces the acceleration force in flow direction.

Applying the derived volumetric source terms leads to the following equation:

$$\rho\left(\overline{u}_j \frac{\partial \overline{u}_i}{\partial x_i} \right) = -\frac{\partial \overline{p}_i}{\partial x_i} + \frac{\partial}{\partial x_i}\left[\left(\mu + \mu_t\right)\left(\frac{\partial \overline{u}_i}{\partial x_j} + \frac{\partial \overline{u}_j}{\partial x_i} \right) \right] + F_{iSR} + F_{iSA} . \tag{5.10}$$

in which $F_{iSR} = F_{iR} / V$ and $F_{iSA} = F_{iA} / V$ are the volumetric source terms for the resistance and acceleration in different directions.

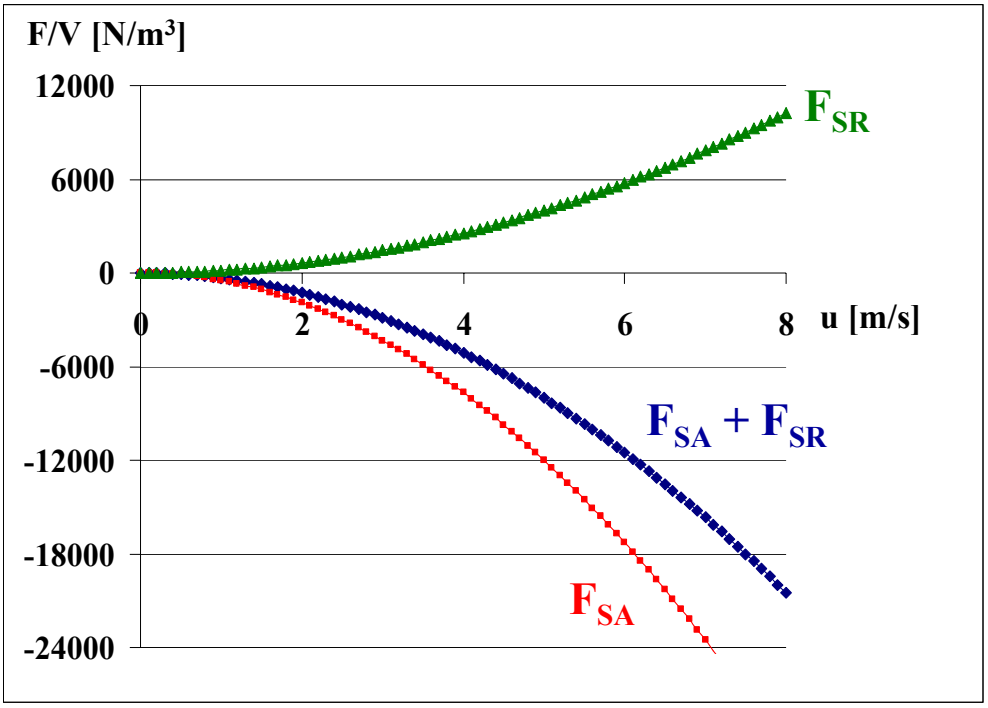

Fig. 5-21 Resulting source terms describing the different effects of the introduced structure

In the following Fig. 5-22 only the resulting source term $F_S = F_{SA} + F_{SR}$ is plotted. In the model it will be approximated with a straight line staring in the origin with a negative slope of $m = -1500$.

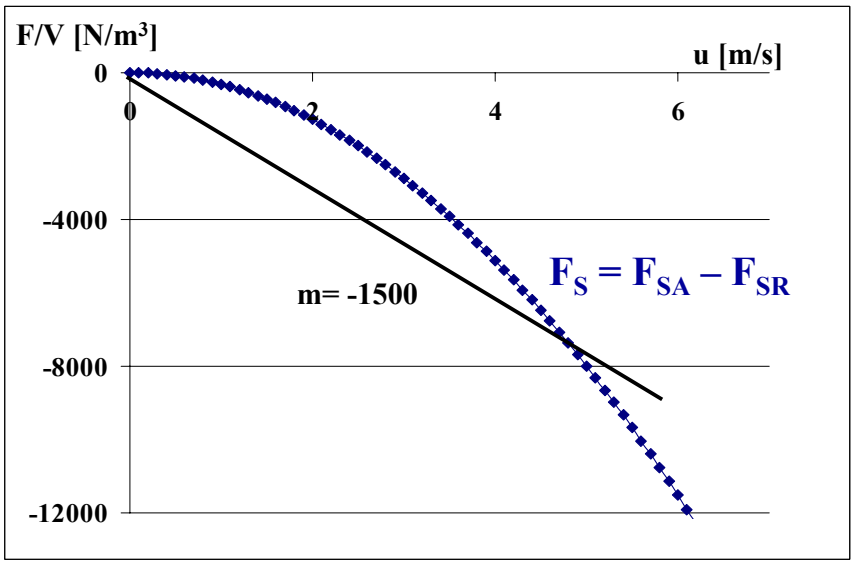

Fig. 5-22 Resulting source term accelerating the flow in the detailed headpiece structure

In the model, the resulting source term F_{iS} in the different directions is entered according to:

$$\rho\left(\overline{u}_j \frac{\partial \overline{u}_i}{\partial x_i}\right) = -\frac{\partial \overline{p}_i}{\partial x_i} + \frac{\partial}{\partial x_i}\left[(\mu + \mu_t)\left(\frac{\partial \overline{u}_i}{\partial x_j} + \frac{\partial \overline{u}_j}{\partial x_i}\right)\right] + F_{iS}. \qquad (5.11)$$

The results achieved with this method lead to good a prediction of the mixing. In Fig. 5-23, the results for the simplified headpiece model with introduced global forces in flow direction and the results for the detailed headpiece model are compared. The results for the model with global forces in direction of the flow reproduces even better results for the mixing than the detailed model with added local forces. Even though the local flow structure is entirely different, the scalar distribution at the analyzed outlet is very similar when comparing the distribution displayed in the figure below. In the center, spots with a very small scalar fraction are found, while regions with a higher scalar fraction are found on the corners and especially rather on the right. For the model with the introduced global forces accelerating the flow, 37.1% of the inlet scalar leave the model through the neighboring superheater I outlet, for the detailed model this value is only slightly smaller with 35.5%. For the differences of the peak values at the analyzed outlet, good agreement is achieved as well. The local minimum for the model with global forces in flow direction is 28.4% and the local maximum is 46.6%. Compared with values in between 29.7% and 44.0% for the detailed model, the agreement is more than satisfactory.

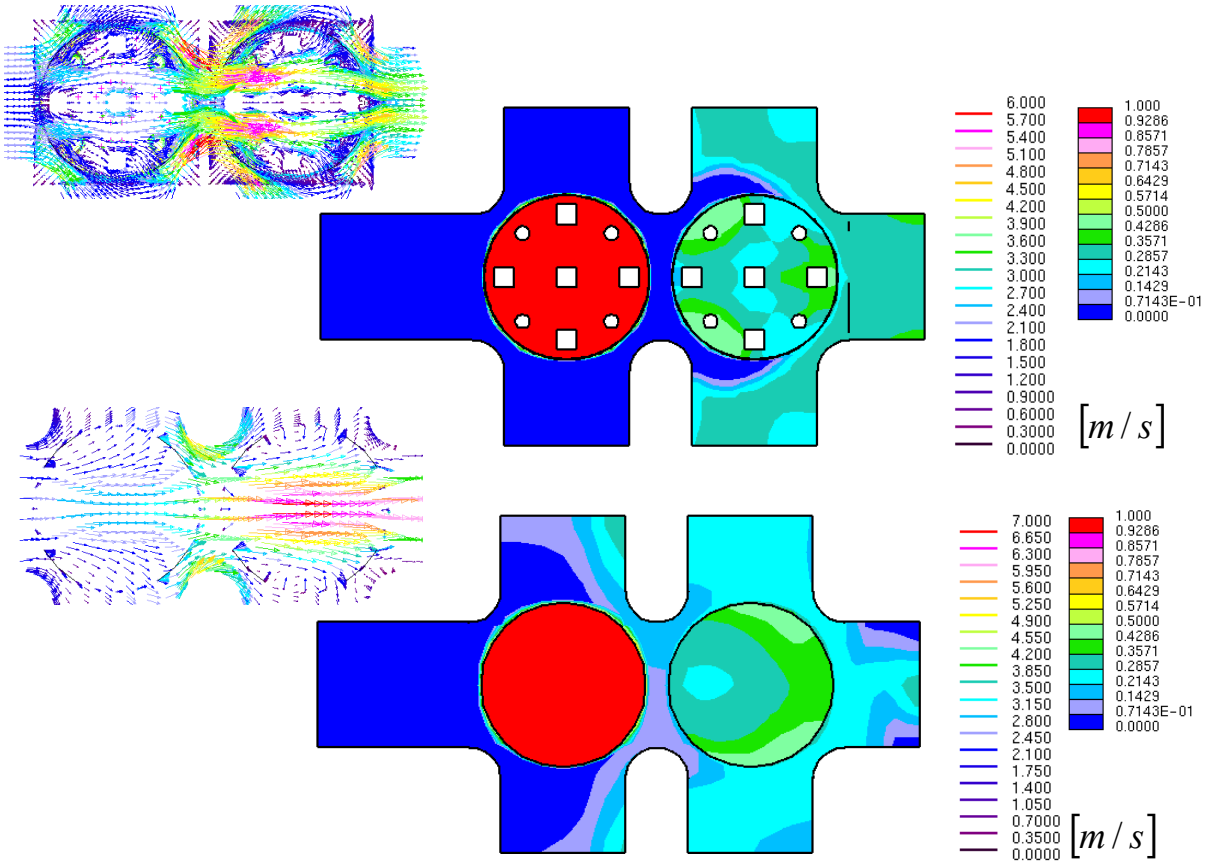

With source terms:

Sc1 – averaged: 37.1%
Min: 28.4% Max: 46.6%

Geometrically resolved:

Sc1 – averaged: 35.5%
Min: 29.7% Max: 44.0%

Fig. 5-23 Comparison of the results for the detailed headpiece model (top) and simplified headpiece model with global forces (bottom) accelerating the flow

Since only the effects of the headpiece geometry on the global flow field in the upper mixing chamber are analyzed and local differences can be disregarded, the distribution of the inlet scalar to the sides of the model has to be analyzed as well. Again, good agreement is achieved. While 9.6% of the inlet scalar exit the model on either side in the detailed model, 12.0% exit the model on the right and 10.7% on the left for the simplified model with global forces in flow direction (when looking at the model from below).

Due to the very good agreement of the mixing, the comparison of the two models can be interpreted as a validation of the approach using global forces in flow direction to represent the headpiece geometries in the upper mixing chamber. Therefore, the defined source terms, which have been derived exemplarily for the combination of the inlet 6 and outlet 1 headpieces, now have to be introduced in the simplified model of the upper mixing chamber. Since the source terms are defined as a function of the velocity, their introduction is valid for each headpiece position in the upper mixing chamber.

The results for the pressure drop, however, can not be further regarded, since the pressure drop of the additional structure is locally included as a resistance source term. This resistance source term then is summed up with the acceleration source term locally to capture the local acceleration effect. The resulting volumetric force pointing in the direction of the flow then artificially revokes the pressure drop of the detailed headpiece structure.

The defined global source terms are applied to the reference case of the simplified model as presented in chapter 3.2.2 and to the optimized case with meander alignment, presented in chapter 4.5. For analyzes with introduced source terms, a model with only 300.000 cells is used. As shown with the grid sensitivity study, the presented results also hold for this grid. The effects for the mixing are shown in the following diagrams depicted in Fig. 5-24.

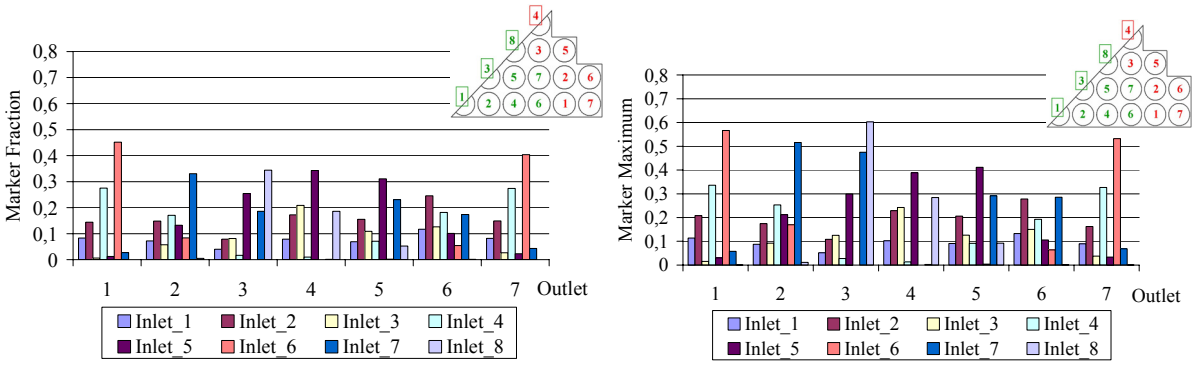

Fig. 5-24 Result for the scalar distributions for the simplified model with introduced forces representing the headpieces

A velocity plot for the simplified model with introduced global source terms in flow direction and for the simplified model without any introduced source terms at a horizontal cross section at half the height of the model are depicted in Fig. 5-25.

Due to the much larger flow velocities, the short cuts between the directly neighboring in- and outlets are slightly decreased and especially the peak values of the different inlet scalars at the

outlets are reduced significantly. For the simplified model without any included source terms, peak values reach almost 70 %, whereas here, the maximum peaks values stay just below 60%. For the standard deviation a value of $\sigma = 11.5\%$ is obtained.

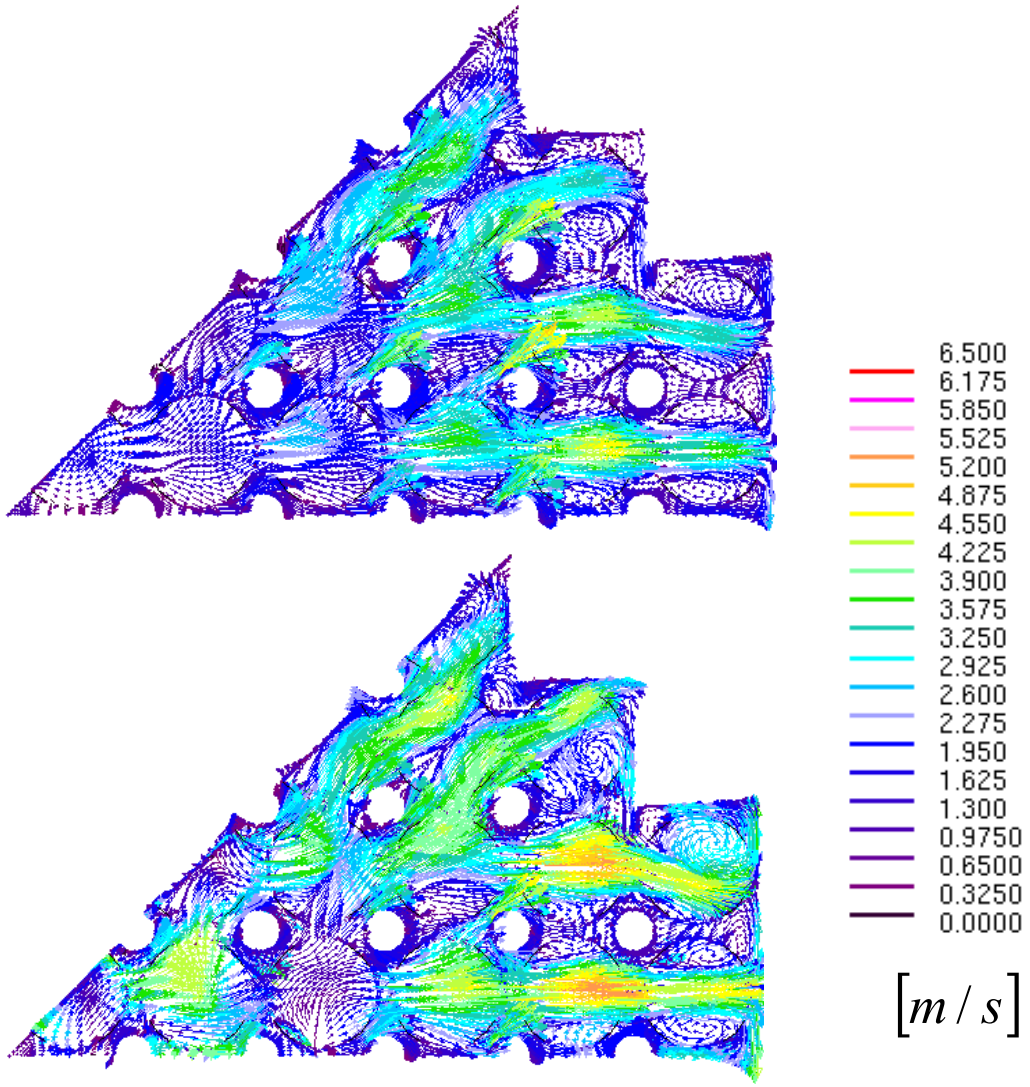

Fig. 5-25 Comparison of the results fort he u-,v-, w- velocity components at a horizontal cross section for the reference case of the simplified model without (top) and with global forces representing the headpiece geometries (bottom)

The jets formed by the headpieces are responsible for the reduction of direct short cuts between neighboring in- and outlets. The effects of the jets can be visualized as can be seen in Fig. 5-26. Here a cut through the model parallel to symmetry boundary II (as indicated on the right side of the figure) is shown. The plotted inlet scalar 6 forms a more pronounced streak past its neighboring outlet 1 and therefore, a smaller fraction is transported directly to outlet 1. In the case without source terms, 53.4% are detected at outlet 1, whereas in the case with applied source terms, this value is reduced to 45.2%. For the neighboring outlet 7, the inlet scalar 6 fraction, however, has been increased from 31.4% to 40.4 %.

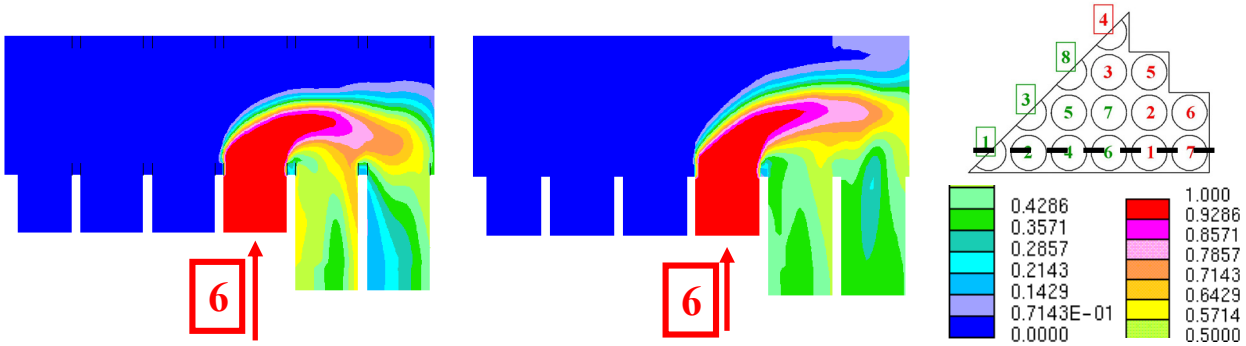

Reference case: without source terms **Reference case: with source terms**

Fig. 5-26 Comparison of the results for the scalar 6 distribution in a vertical cross section for the simplified model without and with source terms

Another distinctive influence of the headpieces is the better mixing of each inlet scalar itself. The improvement can be shown, by analyzing the differences between the minimum and maximum values for each scalar at each outlet. For the case with no introduced source terms, the mean difference between minimum and maximum at each outlet measured for each inlet scalar is 13.6%. The maximum difference in the peak values are found for inlet scalar 8 at outlet 3. Here, the maximum local concentration of inlet scalar 8 is 70.9% and the minimum is 7.6% resulting in a difference of 63.2%. For the case with introduced source terms, the mean difference between minimum and maximum is found to be only 8.5% with the maximum difference of 48.0%, again found for inlet scalar 8 at outlet 3.

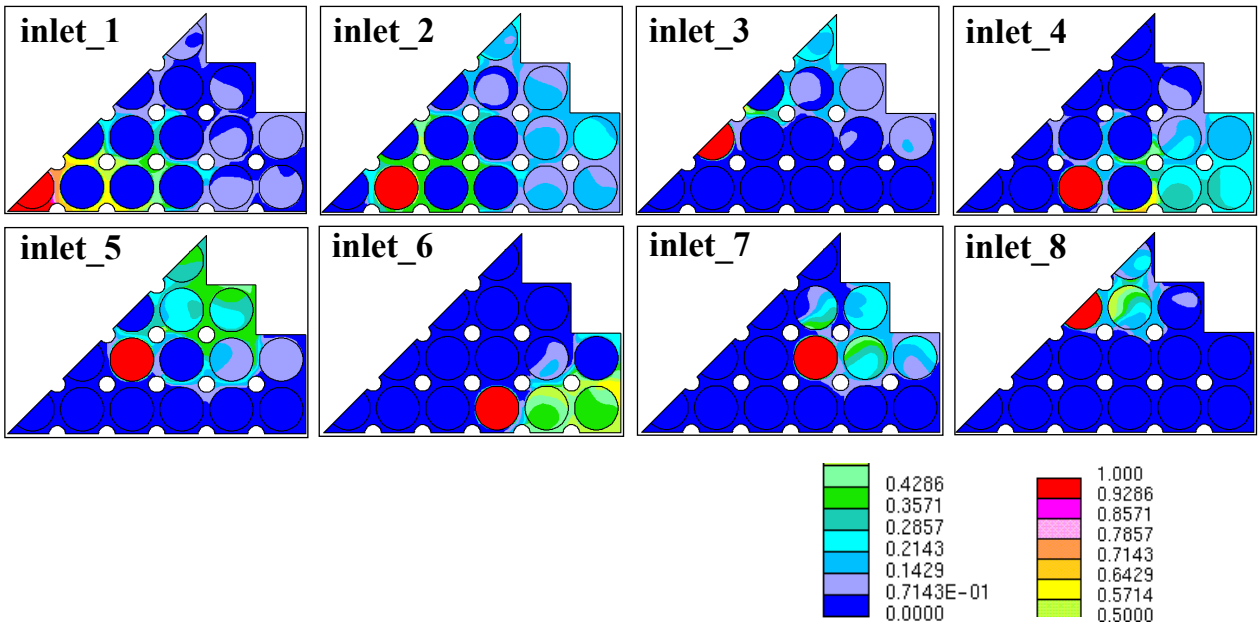

Fig. 5-27 Scalar concentration for the simplified model seen from underneath with introduced global source terms

To round up the application of the simplification method to the upper mixing chamber, the last step is to apply the determined source terms to the optimized case of the simplified model presented in chapter 4.5 (Collection and Re-distribution of the Inlet Flows –Meander Align-

ment). The effects due to introduced forces are not as significant for the optimized case with meander alignment. Very similar results are obtained for the optimized case without introduced source terms concerning the differences between the peak values for the different scalars at each outlet. In addition, almost no difference for the scalar distribution to the outlets is obtained. The overall mixing is slightly better at a standard deviation of $\sigma = 8.4\%$ compared to $\sigma = 8.8\%$ for the optimized case without source terms.

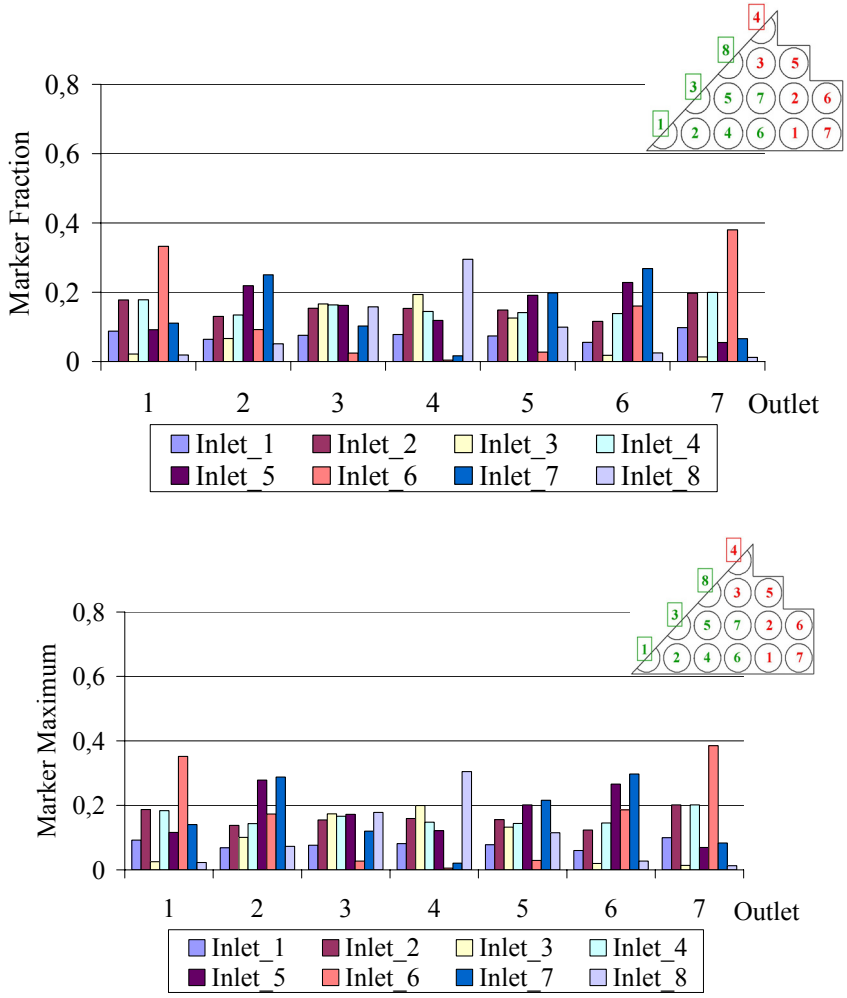

Fig. 5-28 Result for the scalar distributions for the optimized simplified model with introduced forces representing the headpieces

The increased effect of the headpieces in the reference case compared to the optimized case with meander alignment is explained by the significant change in the flow structure between the two alignments. The jets introduced by the headpieces are suppressed by the introduced vertical walls in the optimized case and different jets are introduced in the gaps between the mixing stages. In Fig. 5-29 the u-, v-, and w-velocities are plotted in the defined vertical cross section. Almost the same jets between the mixing stages are obtained, only for the case with source terms, shown on the bottom; the jets are slightly more pronounced showing less curvature towards the outlets.

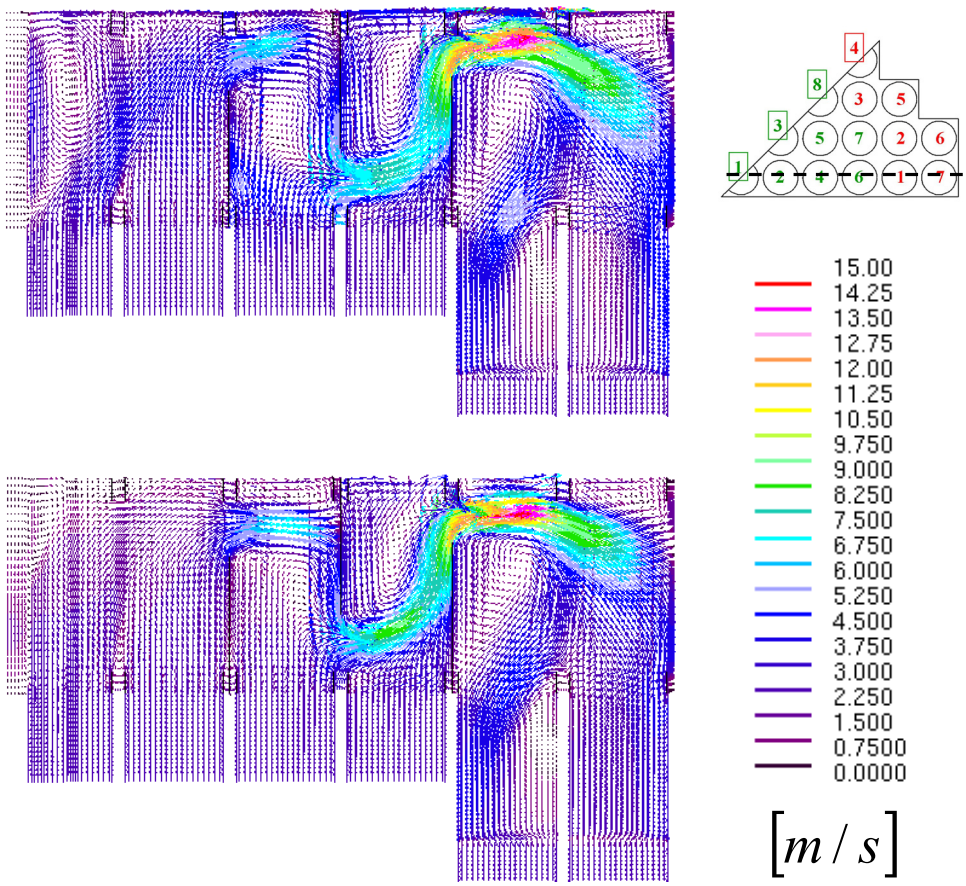

Fig. 5-29 Velocity plots for the optimized case without (top) and with (bottom) introduced source terms at a vertical cross section

5.2.4 Conclusions Regarding the Introduced Headpiece Influences

The better mixing and the better global scalar distribution in the detailed headpiece model are due to the distinctive velocity jets formed in the gaps between the moderator boxes These jets lead to a local acceleration of the flow due to the forced deviation as a result of the reduction in the cross section.

Since the acceleration effects outweigh the introduced resistance by the moderator boxes locally, a resulting volumetric force points in the direction of the flow. The resulting source term has been calculated and delivers good results concerning the mixing. However, the results for the pressure drop can not be further evaluated, since the resulting source term pointing in flow direction revokes the pressure drop of the detailed headpiece structure.

If the pressure drop introduced by the headpiece structures is of interest, the global resistant forces applied in chapter 5.2.2 (Insertion of Global Forces) must be used. In this case, the effect on the flow further behind the headpiece structure is of interest. Here the pressure drop is captured, while the velocity jets are dissipated.

6 Analysis of Temperature Depending Effects

So far all the analyses have been carried out for constant fluid properties and buoyancy influences have been disregarded. However, applying the in chapter 2.3 (Characterization of Buoyancy Influences) derived criteria leads to the assumption that buoyancy effects might play a significant role.

A Grashof-number of $\mathrm{Gr} = 1.1 \cdot 10^{14}$ is found when calculating it with the inner height of the upper mixing chamber as the characteristic length l, the temperature difference between the average coolant temperature and the peak coolant temperature of a hot channel according to [68], which is $\Delta T = 50K$, the acceleration due to gravity g, and the volumetric thermal expansion coefficient $\alpha = 0.008K^{-1}$, as well as the kinematic viscosity $\nu = 0.147 \cdot 10^{-6} m^2/s$ defined for water at a pressure of 25MPa and 390°C as given in the beginning of chapter 2.1 (Characterization of the Flow in the Upper Mixing Chamber). The Reynolds-number also has to be defined with the characteristic length l, the height of the upper mixing chamber and the mean inlet velocity $u = 3.997 m/s$.

Grashof-number:
$$\mathrm{Gr} = \frac{buoyancy\ \ force}{viscous\ \ force} = \frac{\alpha \mathrm{g} \mathrm{l}^3 (\mathrm{T} - \mathrm{T}_0)}{\nu^2} = 1.1 \cdot 10^{14}$$

Reynolds-number:
$$\mathrm{Re} = \frac{inertia}{friction} = \frac{\rho u l}{\mu} = \frac{u l}{\nu} = 1.3 \cdot 10^7$$

$$\frac{\mathrm{Gr}}{\mathrm{Re}^2} \approx 0.7$$

Due to the strong changes in the fluid properties, the Boussinesq approximation, where a volumetric lift term is added as described in chapter 2.3, does not hold for the here analyzed flow. The strong changes in the fluid properties have to be regarded as well. At supercritical pressure conditions the density, conductivity, specific heat and viscosity vary strongly with temperatures close to the pseudo critical point.

At a pressure of 25MPa, the density ratio changes by more than a factor of 8 in the temperature range of interest in the HPLWR and the heat capacity exhibits a very pronounced local maximum at the pseudo-critical temperature.

The strong change in density suggests that buoyancy effects in the flow field could be more pronounced. Therefore, temperature dependent effects on the mixing and on the pressure drop need to be analyzed and the temperature and enthalpy distributions at the outlet of the upper mixing chamber need to be calculated. The curve progressions according to the IAPWS-IF97 water and steam table [81] for the mentioned fluid properties are depicted in Fig. 6-1.

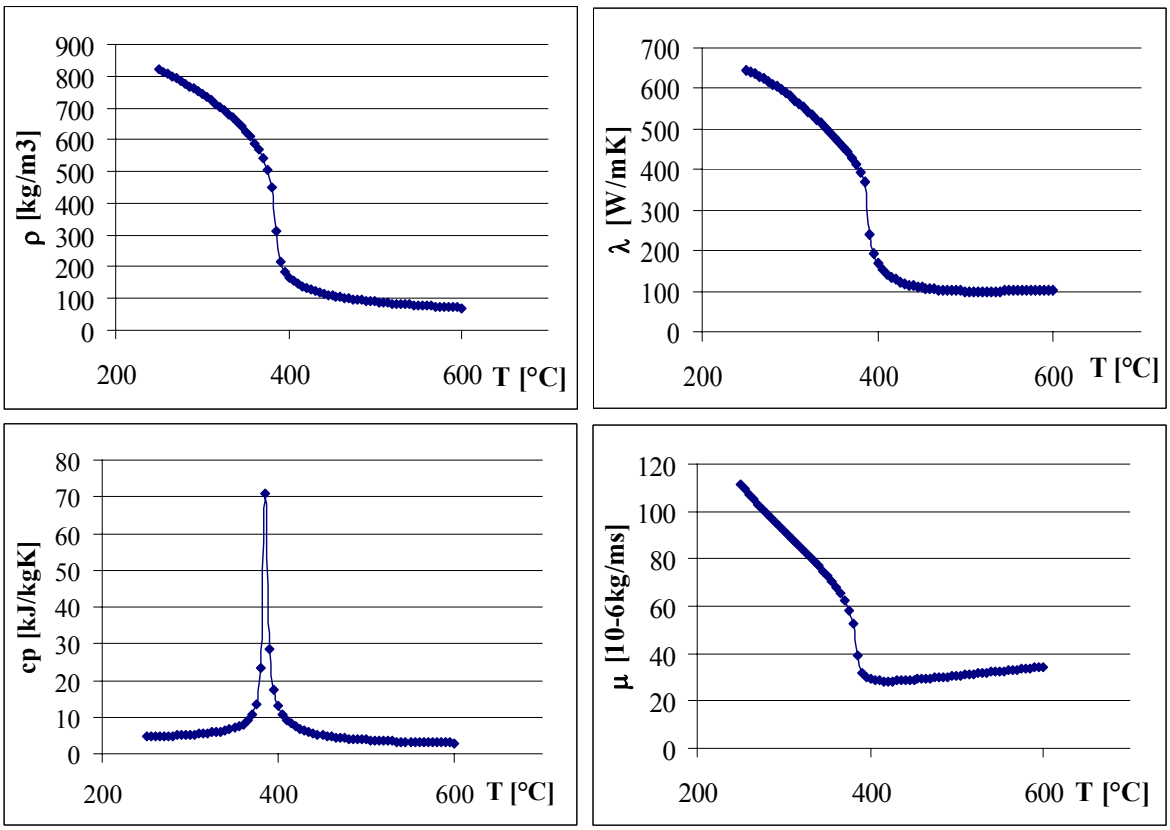

Fig. 6-1 Fluid properties for water at a pressure of 25 MPa

Laurien et al. have included these changes in the fluid properties in their model for a pressure of 24.5MPa in [44]. Analogue to their approach, Kunik et al. have introduced functions for a pressure of 25MPa in their model as presented in [39] and [40]. To include these functions in the here presented model, an additional function for the enthalpy as a function of temperature had to be included according to the relationship:

$$dh = cp(T)\,dt \tag{6.1}$$

The included function is shown in Fig. 6-2, where the dotted line represents the values taken from the IAPWS-IF97 water and steam table [81] and the straight lines g1 and g2 are used for the curve fit. The enthalpy h is approximated by the superposition:

$$h = g1f + g2\,(1 - f) \tag{6.2}$$

of two linear functions:

$$g1\,(T) = h1 + (h2 - h1) / (T2 - T1)\,(T - T1) \tag{6.3}$$

$$g2\,(T) = h3 + (h4 - h3) / (T4 - T3)\,(T - T3) \tag{6.4}$$

by the blending function f:

$$f = 1 / 1 + \exp((T - Tps) / w) \tag{6.5}$$

Here *Tps* is the pseudo-critical temperature and the enthalpies h1 to h4 as well as the temperatures $T1$ to $T4$ represent selected data points. The characteristic parameter w determines the width of the exponential transition and can be adjusted to achieve the best curve fit possible.

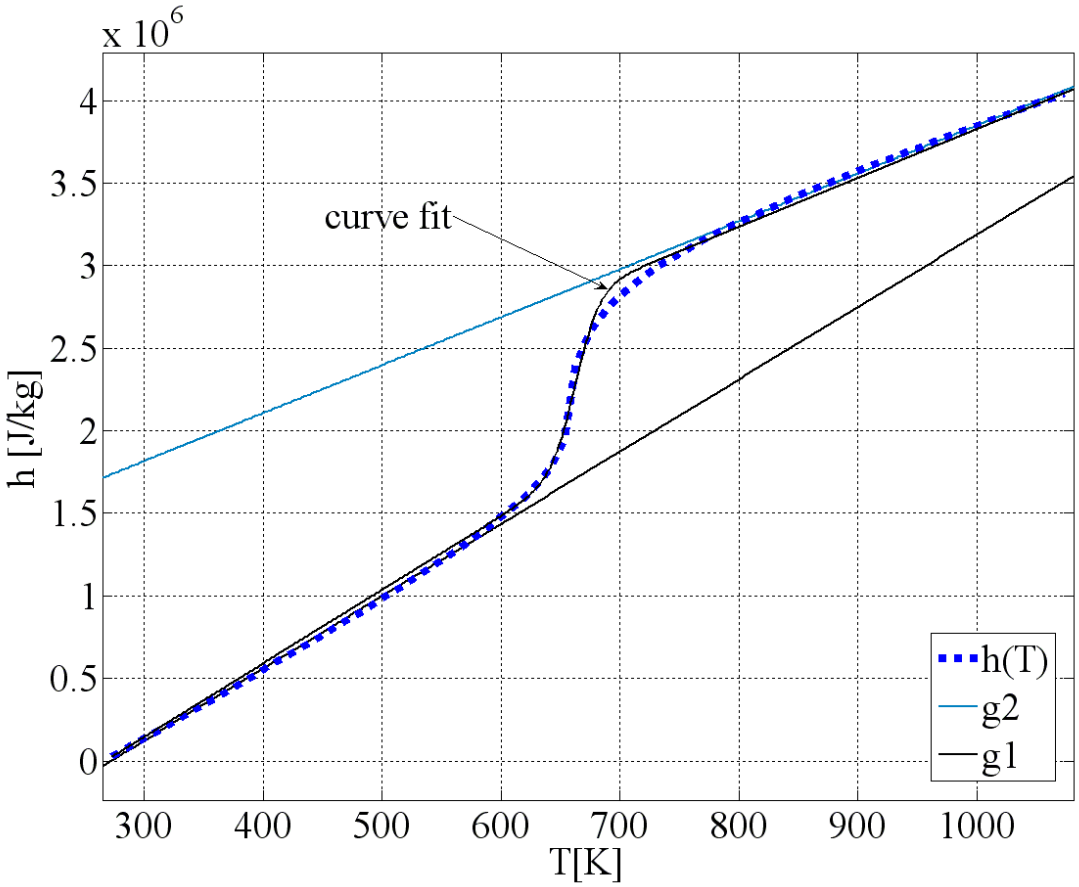

Fig. 6-2 Curve fit for the enthalpy at 25 MPa

The retrieved function describing the enthalpy at a pressure of 25MPa is found to be:

$$\begin{aligned} g1 &= 24964 + (1496284 - 24964)/(603 - 273) * (T - 273) \\ g2 &= 3127436 + (4044005 - 3127436)/(1073 - 763) * (T - 763) \\ f1 &= 1/(1 + \exp((T - 663)/10)) \\ h &= g1 * f1 + g2 * (1 - f1) \end{aligned} \tag{6.6}$$

To check the implemented functions, a test case has been defined in which a volumetric heat up has been applied to a horizontal, rectangular tube to verify that the predicted fluid properties correspond to the physical ones. A very thin, 2m long pipe has been chosen as test geometry. For the simulation a block profile has been applied at its inlet with a mean velocity of 0.5m/s and arbitrary values for K and ε in the same range as for the simulations of the upper mixing chamber. At the outlet, a regular outlet boundary has been applied, in Fig. 6-3, the results for all analyzed fluid properties over the temperature along the length of the test pipe are plotted. A very good correspondence between the values given for the water and steam table and the values obtained in the test case with the applied functions for the density, conductivity, heat capacity, and viscosity according to Kunik [40] and the additional function derived for the enthalpy as a function of temperature plotted in Fig. 6-2 as curve fit. The values given by the IAPWS-IF97 water and steam table [81] are depicted with the blue lines and the values according to the introduced functions are depicted by the pink lines.

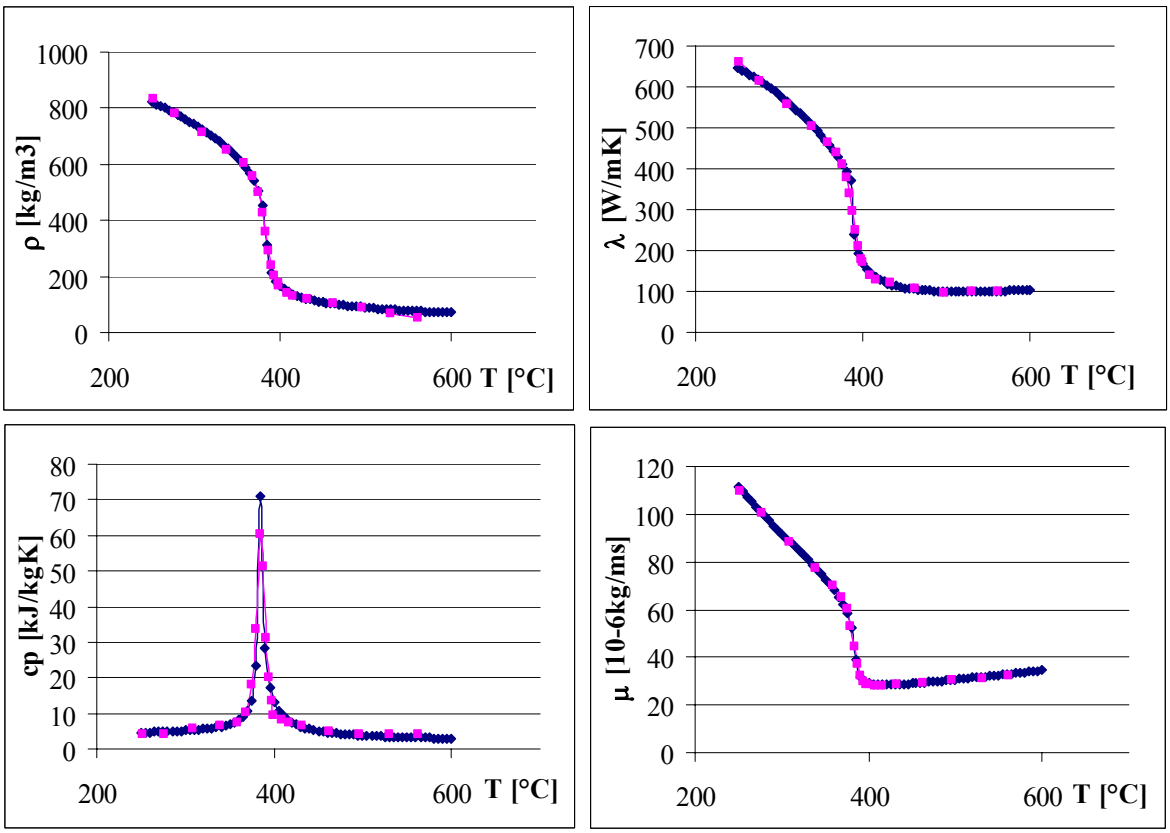

Fig. 6-3 Results for the test case with the introduced functions for the variable fluid properties introduced

To regard the temperature dependant effects in the flow, the functions describing the variable fluid properties as well as the additional volumetric lift term $g(\rho - \rho_\infty)$ to regard the effects of buoyancy are introduced into the model for further analyzes.

6.1 Characteristic Flow Patterns

For the analysis of temperature dependant effects, the simplified model as presented in chapter 3.2 is used. To draw principal conclusions about the influences of temperature dependant effects in the upper mixing chamber, one of the 8 inlets is charged with a higher temperature whereas the others are charged with the same temperature of 390°C. For the presented evaluation, inlet 6 is charged with a temperature of 490°C, thus being 100°C above the temperature of all the other inlets. Inlet 6 is chosen, since it represents the worst mixed inlet cluster. If a hot inlet streak occurs for this cluster, the worst case is obtained. A significantly overstated inlet temperature should make sure that possible buoyancy effects are detected. Two extreme cases can arise for this setting; either the mass flow rate or the volume flow rate in the hot cluster stays constant. In this sub-chapter the analysis of these two cases is presented to demonstrate and draw principal conclusions for the theoretical worst case, where the least mixed inlet flow is also the hottest, and to evaluate the principal influences of buoyancy effects on the mixing in the upper mixing chamber.

6.1.1 Constant Volume Flow

In the case with constant volume flow rate, the inlet velocity of $2.78 m/s$ is kept for all inlets despite their temperatures. This way, the most significant temperature dependant effects occur. Two different cases are simulated, one where the temperature of inlet 6 is 100K above the average inlet temperature and one where it is 100K below.

The results for these two cases, depicted in Fig. 6-4, show that buoyancy effects do not have the dominant influence as expected. In correspondence to the very high Grashof number and the criteria derived in 2.3, a noticeable acceleration of the hot flow entering inlet 6 in vertical direction has been expected due to buoyancy effects. However, for the case in which inlet 6 is hotter than the other inlets, the much lighter inlet flow with a much lower density is "overblown" by the other inlets entering in the center of the upper mixing chamber, as shown in Fig. 6-4. On the top, the reference case for the simplified model with constant fluid properties is depicted. On the bottom left, the case with a hot inlet 6 is depicted. No buoyancy effects can be seen for this configuration. Analogue results are obtained when inlet 6 is much colder than the other inlets, depicted on the bottom right side. The colder inlet flow has a much higher momentum when entering the upper mixing chamber due to its higher density. This way it is blocking all the other central inlets which have a very low density in comparison.

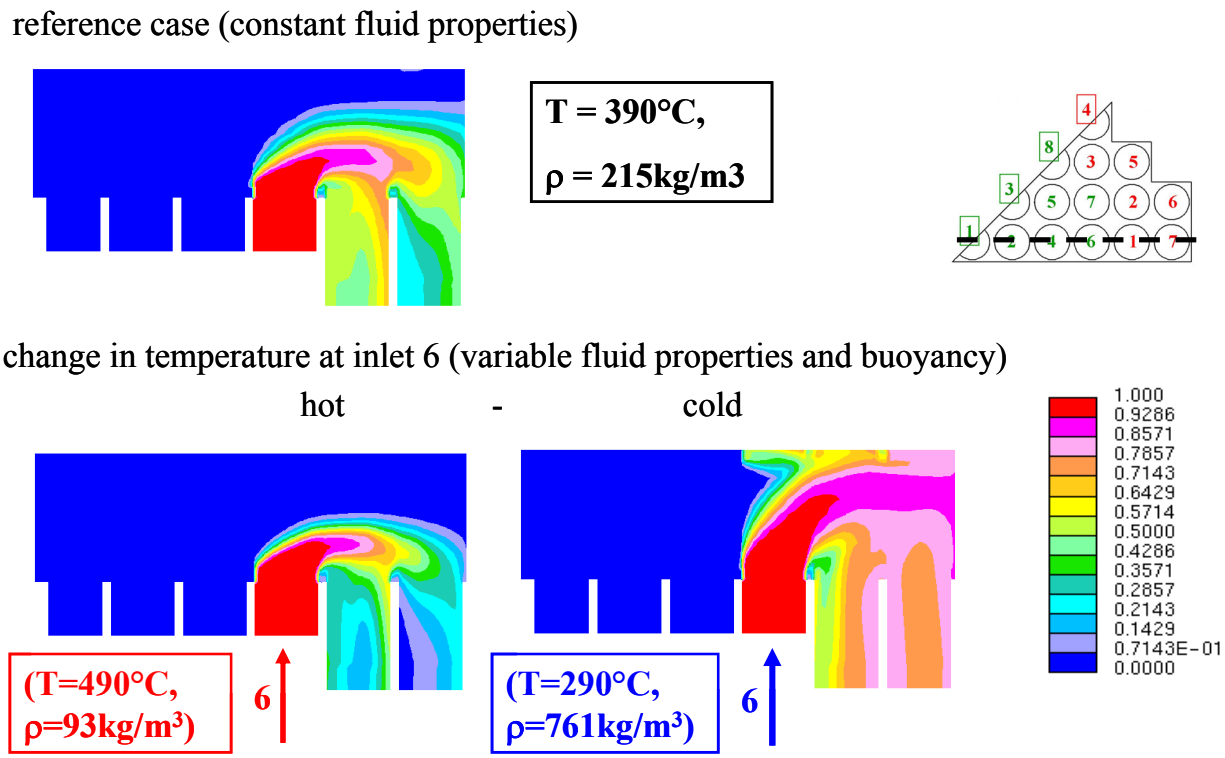

Fig. 6-4 Different temperatures applied to inlet 6 for the reference case of the simplified model with const. volume flow

The influence this change of the flow structure has on the mixing is significant. When looking at the results for the hot inlet 6, a much better mixing of the hot inlet streak is obtained, whereas the overall mixing evaluated with the standard deviation stay pretty much the same. The standard deviation for the case with a hot inlet 6 is $\sigma = 12.2\%$, while $\sigma = 12.1\%$ is obtained

for the reference case. In Fig. 6-5 the results for the scalar distribution are shown. While the scalar fraction of the hot inlet scalar 6 detected at the neighboring outlet 1 is decreased, higher fractions and peak values as in the reference case are obtained for other inlet scalars at the outlets.

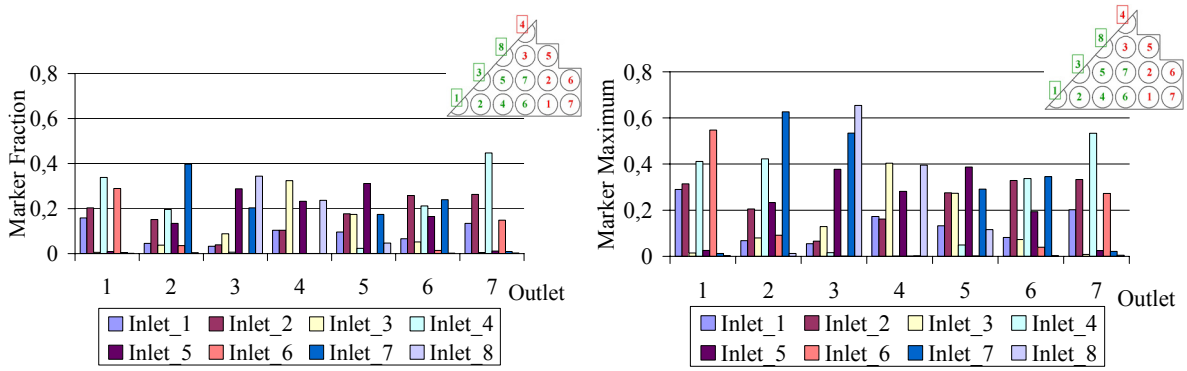

Fig. 6-5 Result for the scalar distributions for the simplified model for the case with const. volume flow and an inlet 6 temperature 100K above the mean temperature

Better mixing of the hot streak is the result of the effect described before as “over-blowing”. The fluid with the much smaller density is pushed aside by the fluid with the much higher density leading to a better distribution of the hot fluid to all outlets. However, this effect also leads to negative effects for the mixing of the neighboring inlets, especially for inlet 4, which now, due to the decreased obstructing effect introduced by its neighboring inlet 6, can reach outlet 7 in a more direct way. In Fig. 6-6, a vertical cut through the inlets 1, 2, 4, and 6 and the outlets 1 and 7 of the upper mixing chamber illustrates the more direct short cut between inlet 4 and outlet 7.

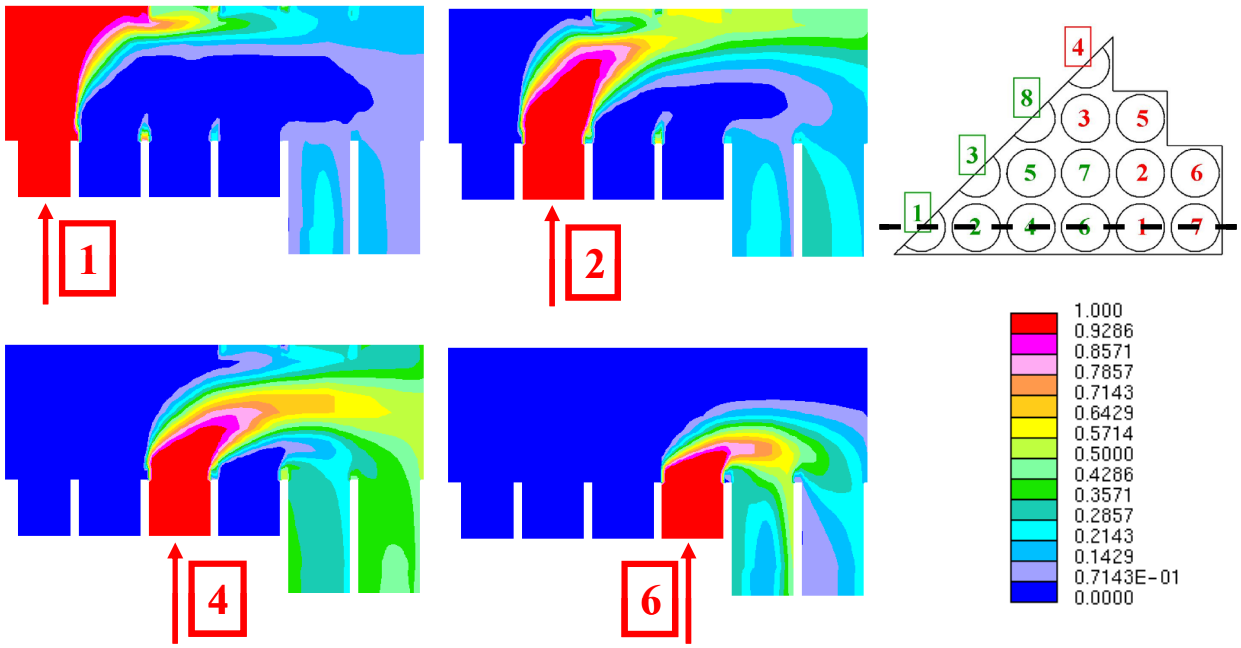

Fig. 6-6 Scalar distribution in a vertical cut through the upper mixing chamber with a hot inlet 6

As expected, a much worse result for the mixing is obtained in the case with an inlet 6 temperature 100K below the average inlet temperature. The obtained results are depicted in Fig. 6-7. A blockage of the colder fluid entering the upper mixing chamber through inlet 6 with a much higher density is established and suspends the flow from the other more central inlets. This can be seen by the very high values for the inlet 6 scalar at the outlets 1 and 7. The standard deviation is much higher at a value of $\sigma = 15.8\%$, compared to $\sigma = 12.1\%$ obtained for the reference case.

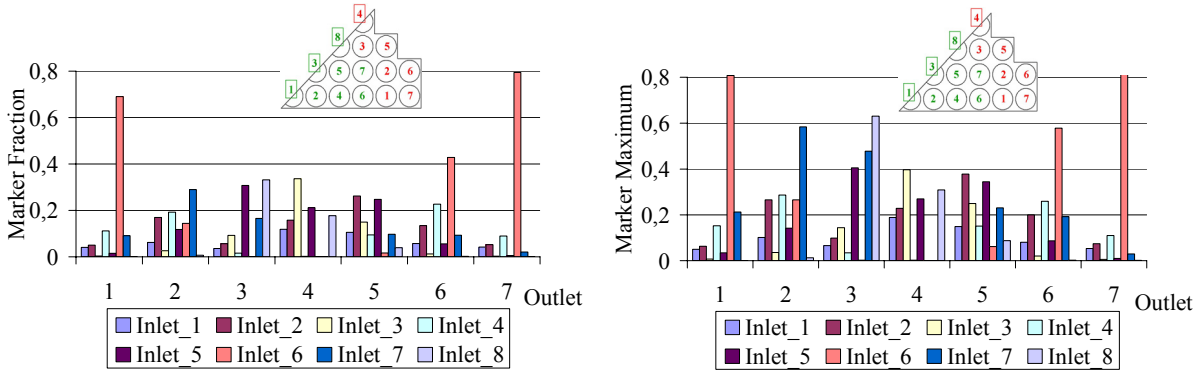

Fig. 6-7 Result for the scalar distributions for the simplified model for the case with const. volume flow and an inlet 6 temperature 100K below the mean temperature

At this point it can be concluded that buoyancy effects are not as dominant as expected. The inertial effects clearly outweigh the buoyancy effects and the hot inlet flow entering at inlet 6 is actually over-blown rather than showing an additional acceleration in vertical direction.

6.1.2 Constant Mass Flow

To analyze the case with constant mass flow through all inlets, the inlet velocity of inlet 6 has to be adjusted according the density change. For the case with an inlet temperature 100K above the average temperature, an inlet velocity of $6.31 m/s$ is obtained, for the case with an inlet temperature 100K below, the inlet velocity is much smaller at a value of $0.79 m/s$. In comparison, the inlet velocity for the mean temperature of $T = 390°C$ and the corresponding density of $\rho = 215 kg/m^3$ an inlet velocity of $2.78 m/s$ is obtained.

For this case, almost the same result is obtained as for the reference case without regarding the temperature dependant effects. Also, the difference due to the change in inlet temperature is small as can be seen in Fig. 6-8. The small differences in the flow are rather the result of the higher inlet velocity for the case with the hot inlet than of buoyancy effects.

The effects for the mixing are small, but also the same effect for the mixing of the hot leg can be observed. Due to the smaller density, the lighter fluid is distributed much better to the different outlets. The standard deviation for all three cases, the reference case, the case with an inlet 6 temperature 100K above the mean temperature, and the case with the inlet temperature 100K below the mean temperature stays the same at $\sigma = 12.1\%$.

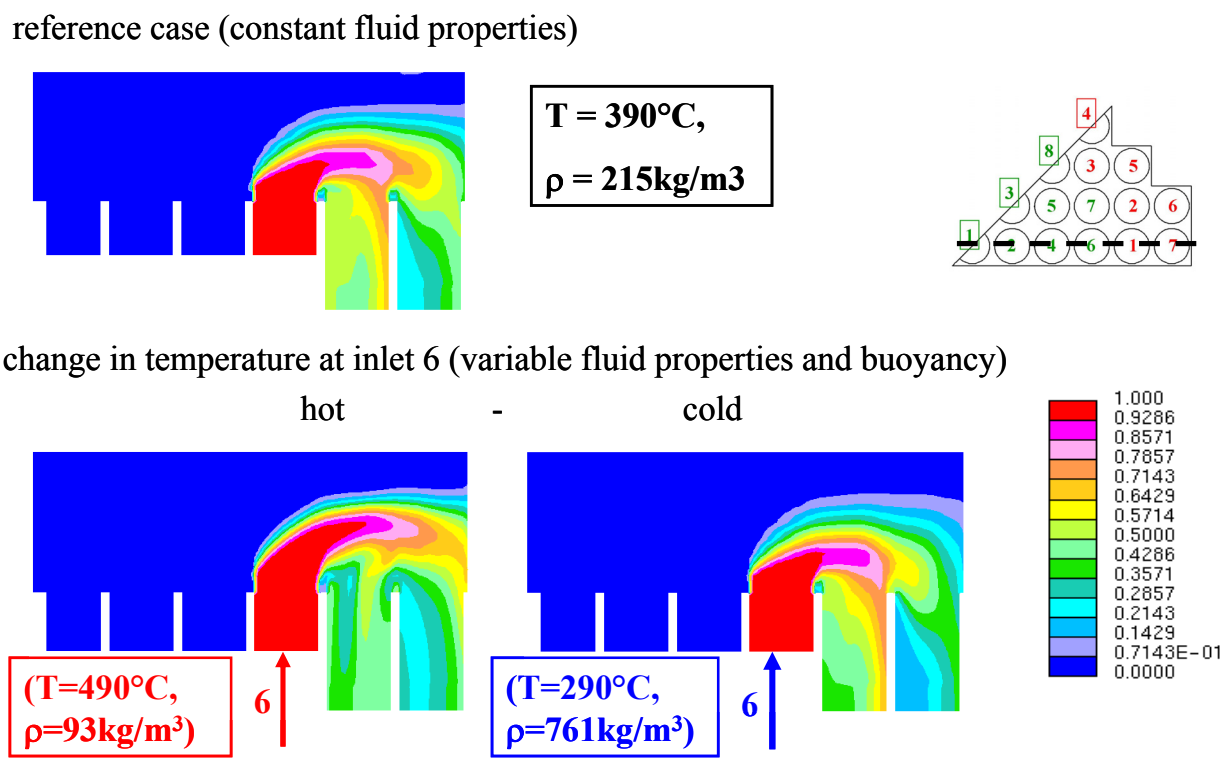

Fig. 6-8 Different temperatures applied to inlet 6 for the reference case of the simplified model with const. mass flow

When evaluating the results for the two analyzed cases, it is found that the case with the inlet 6 temperature 100K below the mean temperature delivers almost the same results as obtained for the reference case. For the case with the inlet 6 temperature 100K above the mean temperature, analogue results are obtained. The only significant difference is that the lighter inlet 6 fluid is now distributed better to the outlets, while the distribution of the other inlet scalars stays almost the same. The result for this case can be seen in Fig. 6-9.

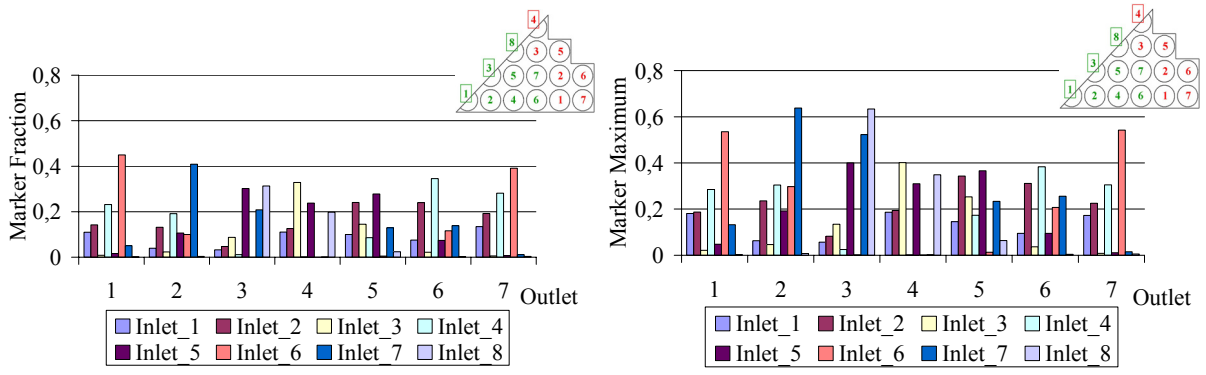

Fig. 6-9 Result for the scalar distributions for the simplified model for the case with const. mass flow and an inlet 6 temperature 100K above the mean temperature

Summarizing the observed results for these extreme cases with a temperature change imposed only at inlet 6, it can be concluded that temperature dependent effects do influence the mixing, but buoyancy effects do not become as dominant as expected.

6.2 Case with a Specified Inlet Temperature Distribution

In addition to the presented cases, where extreme assumptions have been made for inlet 6 representing the worst case, more realistic cases have been analyzed. The inlet boundaries have been defined according to the results for the thermal core analysis presented by Maráczy et al. from the Hungarian Academy of Sciences KFKI Atomic Energy Research Institute in [46]. The thermal core analyses have been carried out with the KARATE Code as presented in [45]. The given temperatures of the assemblies in each cluster have been averaged arithmetically to define the inlet temperature for each cluster. However, tolerances, burn-up, uncertainties, etc. have not yet been considered in these analyses.

The inlet temperatures, shown on the right side of Fig. 6-10, and the inlet enthalpies for the different inlets are listed on the left side of the figure. Here, inlet 7 is the inlet with the lowest inlet temperature marked in grey and inlet 4 has the highest inlet temperature marked in blue.

Inlet	T [°C]	T [K]	h [kJ/kg]
1	385,4	658,6	2188,5
2	389,4	662,6	2377,7
3	384,5	657,6	2125,0
4	389,4	662,6	2377,7
5	388,3	661,5	2340,8
6	387,7	660,8	2316,0
7	383,4	656,5	2055,4
8	386,9	660,1	2278,7

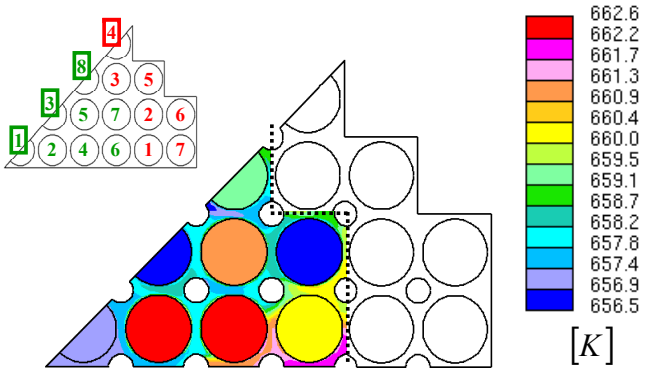

Fig. 6-10 Realistic inlet temperature and enthalpy distribution according to [46]

Due to a relatively homogeneous neutron flux in the center of the core, the temperature and the enthalpy at the outlets of the evaporator only vary between 383.4°C and 389.4°C for the temperature and between 2055.4kJ/kg and 2377.7kJ/kg for the enthalpy. This equals a temperature difference of 6K and an enthalpy difference of 322.1kJ/kg. When comparing the results for the mixing and for the temperature and enthalpy distribution at the outlet for the reference case, no significant differences are obtained for the assumption of constant volume flow or constant mass flow. For the case where the inlet velocities have been defined with the assumption of constant mass flow rate and the corresponding inlet density for each inlet temperature has been looked up, the new inlet velocity is calculated with the density fraction times the reference inlet velocity. When assuming a constant volume flow rate, all inlets are charged with the same inlet velocity and only the density and temperature varies. Two different cases are analyzed: the reference case of the simplified model as presented in chapter 3.2.2 and the optimized design of the upper mixing chamber with meander structure to enhance mixing as presented in 4.5. The results for the mixing are not significantly affected when comparing the cases in which temperature depending affects are considered with the cases where only constant fluid properties are applied and no temperature dependent effects are regarded.

For the standard deviation the same values are obtained for the case with constant mass flow rate: $\sigma = 12.1\%$ for the reference case and $\sigma = 8.8\%$ for the optimized case. In addition, almost no influence on the scalar distribution is noticeable for both cases. The achieved enthalpy and temperature distributions are depicted in Fig. 6-11 for both analyzed cases. Here, the upper mixing chamber is shown from the bottom and a dotted line is introduced to separate the inlet from the outlet side. Also, only the values on the outlet side are depicted to adjust the scale to smaller values for the enthalpy, for the temperature the scale remains unchanged. While the result for the reference case, which is depicted on the left side, shows a large variation in enthalpy and temperature, it can be seen that these differences in temperature and enthalpy largely disappear.

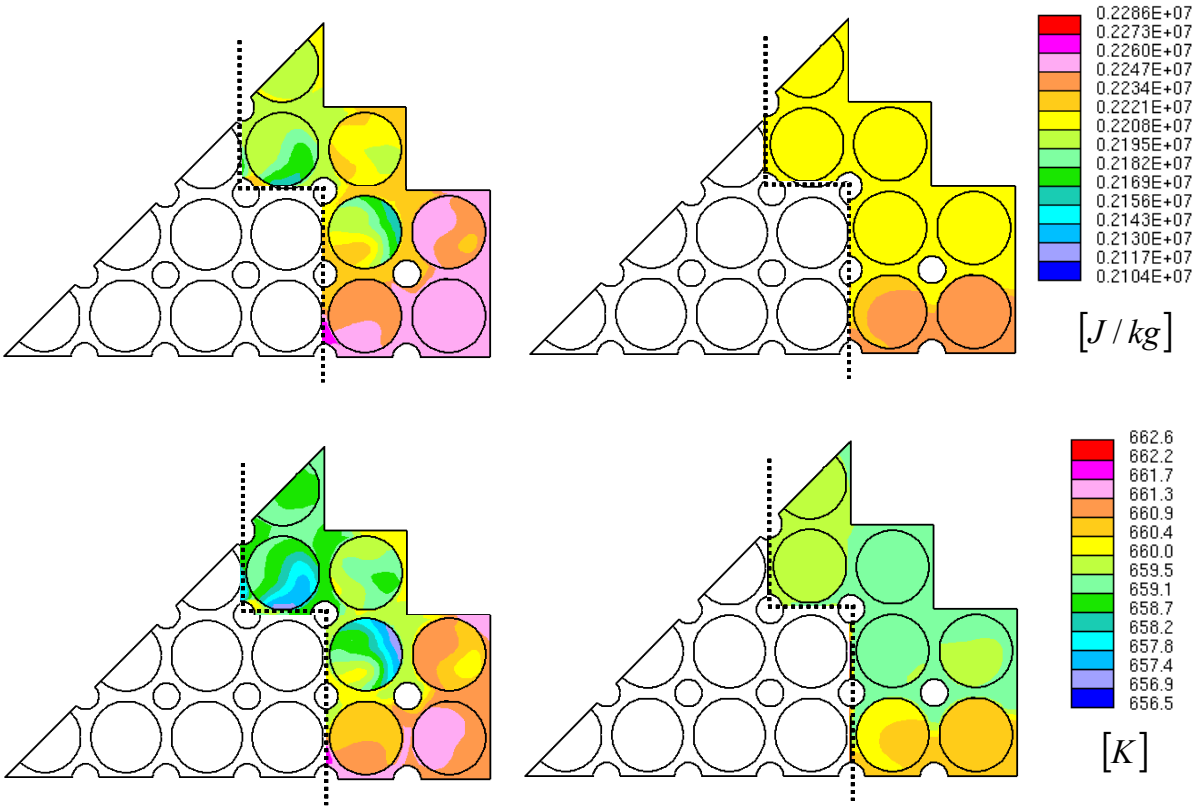

Fig. 6-11 Enthalpy (top) and temperature (bottom) distribution in the upper mixing chamber for the reference case (left) and for the optimized case (right) – const. mass flow

When looking at the outlet side of the optimized upper mixing chamber, the temperature varies between 386.8°C and 388.4°C and the enthalpy only varies between 2247kJ/kg and 2208kJ/kg. Thus, the variations in temperature of 6.1K and in enthalpy of 322.3kJ/kg at the mixing chamber inlets have been reduced to 1.1K and 73 kJ/kg at the outlet side, as summarized in Tab. 6-1.

ΔTin= 6.1K	**ΔTout= 1.1K**
Δhin= 322.3 kJ/kg	**Δhout= 39 kJ/kg**

Tab. 6-1 Comparison of inlet and outlet temperature/enthalpy differences in the upper mixing chamber (constant mass flow)

For the case with constant volume flow, slightly higher differences in the outlet temperature and enthalpy distribution are found. As depicted in Fig. 6-12. The standard deviation for the reference case is a little bit higher for the case with constant volume flow at a value of $\sigma = 12.6\%$ as for the case with constant fluid properties $\sigma = 12.1\%$. The same is true for the optimized case where the value for the standard deviation has been increased to $\sigma = 9.1\%$, compared to $\sigma = 8.8\%$. The scalar distribution has changed almost insignificantly.

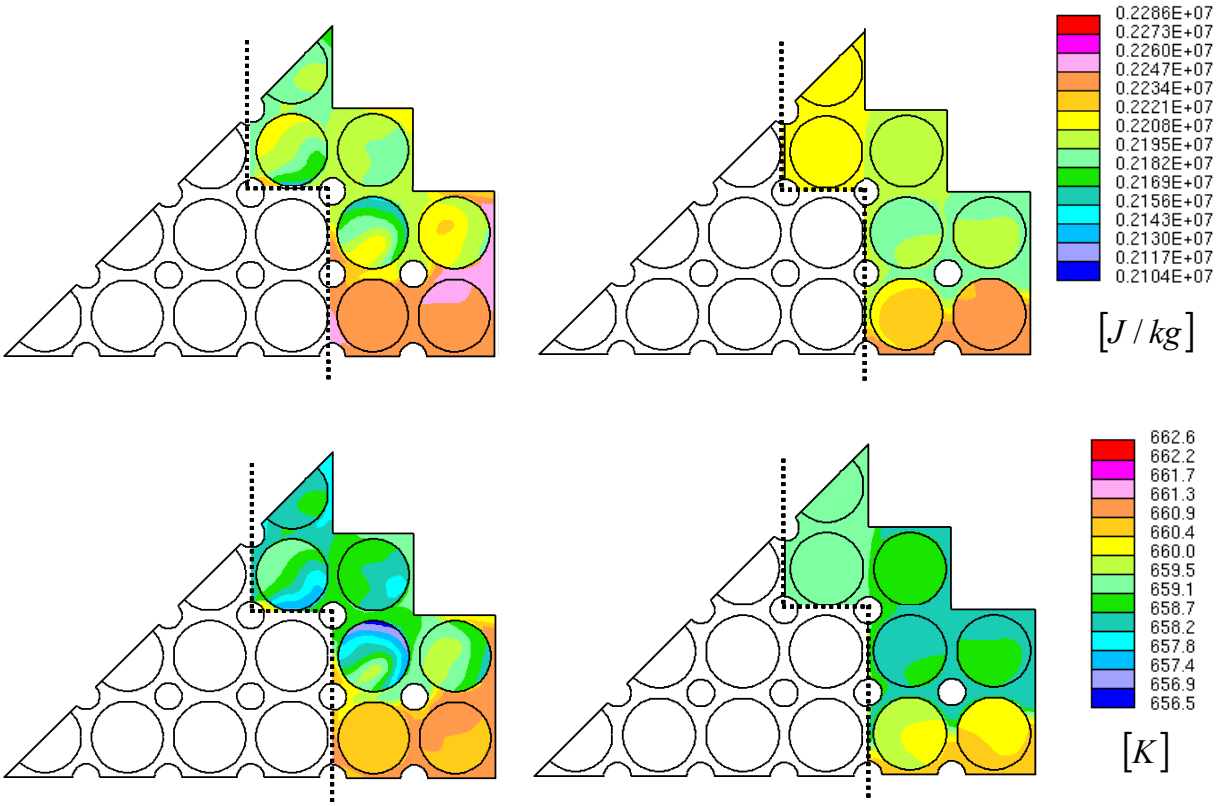

Fig. 6-12 Enthalpy (top) and temperature (bottom) distribution in the upper mixing chamber for the reference case (left) and for the optimized case (right) – constant volume flow

For this case, the temperature varies between 659.1K and 661.6K and the enthalpy varies between 2249kJ/kg and 2183kJ/kg. The differences in temperature and enthalpy are summarized in Tab. 6-2 for the optimized case with constant volume flow.

ΔTin= 6.1K	**ΔTout= 2.5 K**
Δhin= 322.3 kJ/kg	**Δhout= 66 kJ/kg**

Tab. 6-2 Comparison of inlet and outlet temperature/enthalpy differences in the upper mixing chamber (constant volume flow)

It can be concluded that buoyancy effects do not have as much influences as expected. When regarding the temperature dependant effects in the upper mixing chamber and applying them to a realistic inlet temperature distribution, it is found that the homogenization of temperature and enthalpy is successful and only small differences are calculated when comparing the cases of constant mass and volume flow.

7 Integrated Results for the Upper Mixing Chamber

In this chapter, the results for the upper mixing chamber will be presented including both, temperature dependant effects and the complex geometries, which had been disregarded in the simplified model. Thus, all necessary approaches to capture the effects on the mixing are integrated in one simulation only. However, the influence of the change in density has not been included for the derivation of the introduced source terms. In this chapter, the integrated solution for the mixing in the upper mixing chamber of the HPLWR is presented and the methods derived in the previous chapters are applied altogether.

Two models are analyzed: the reference case with no means to enhance mixing and the optimized case with the introduced meander structure as derived for the simplified model in chapter 4. The same calculated inlet temperature distribution delivered by AEKI as used in the previous chapter is also used. Constant volume flow is assumed, since slightly worse values are obtained for the mixing, leading to a slightly more heterogeneous temperature distribution.

Since the influences of the complex geometry are much more significant for the mixing than the inclusion of the temperature dependent effects, the integrated results are very similar to the results presented in chapter 5 (Including the Effects of the Omitted Structures). In Fig. 7-1, the results for the reference case with reproduced headpiece geometry and inlet temperature distribution are depicted.

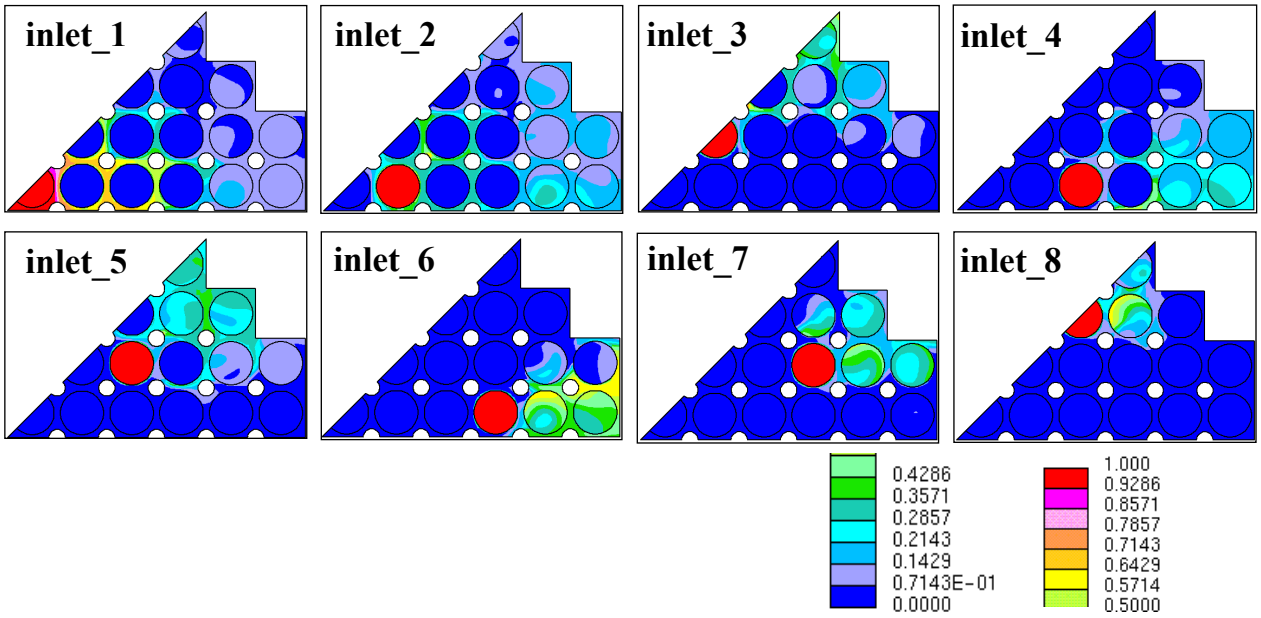

Fig. 7-1 Integrated results for the scalar concentration with introduced source terms representing the headpieces and a calculated inlet temperature distribution – reference case

The global flow structure is comparable to the results of the simplified model reference case. Inlet flows entering the upper mixing chamber in the center are distributed to the outer periphery, while the inlet flows entering the mixing chamber close to the outlet side are preferentially led to their neighboring outlets. However, these short cuts are decreased due to the

acceleration of the flow in radial direction by the simulated jets, which are generated by the headpiece geometries. Inlet scalar 6 for example is now better distributed between outlet 1 and 7 due to the acceleration of the flow in lateral direction. For one exemplary vertical cross section this is depicted in Fig. 7-2.

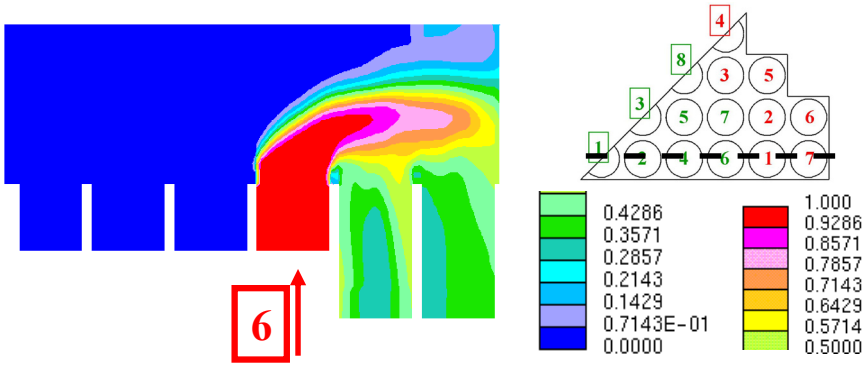

Fig. 7-2 Inlet scalar 6 distribution for the reference case

The better distribution of inlet scalar 6 can also bee seen in Fig. 7-3, where all inlet scalar distributions are depicted.

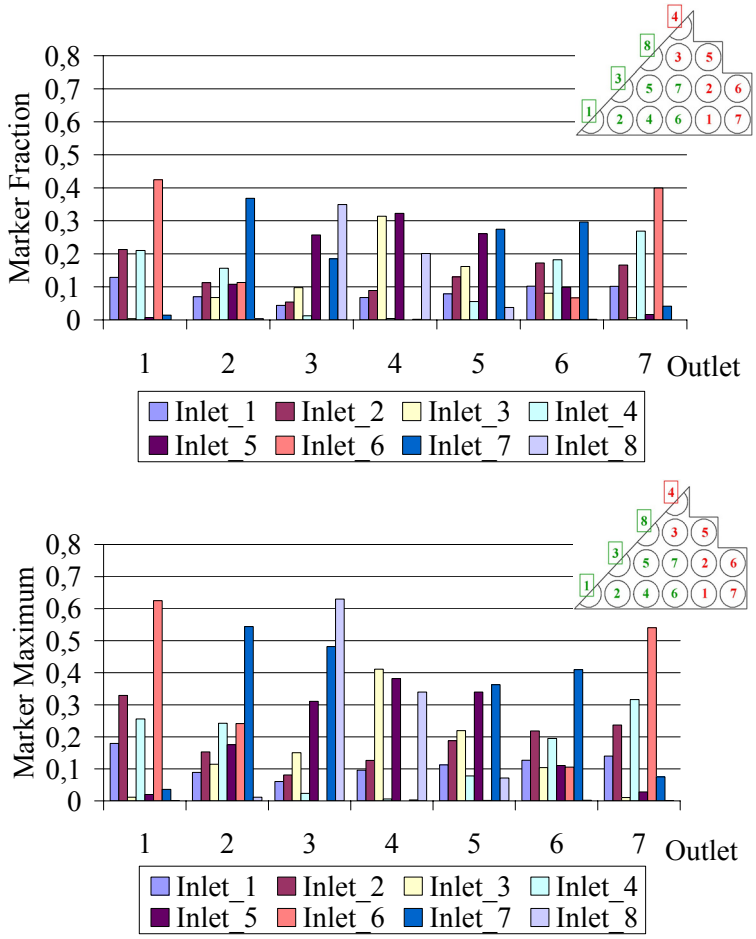

Fig. 7-3 Integrated results for the scalar concentrations, cross section averaged (top) and peak (bottom) in the upper mixing chamber – reference case

The cross section averaged scalar distribution, in general, shows better results for the mixing than in the simplified case. However, the high peaks are still not acceptable. Especially the local maxima for the inlet scalars are almost not affected when comparing the simplified case in chapter 3.2 with the integrated case. With a value for the standard deviation of $\sigma = 11.8\%$, the result for the mixing is noticeably better than for the previous analyses.

When comparing the inlet temperature and enthalpy distribution given in Fig. 6-10 to the outlet side as shown in Fig. 7-4, a more homogeneous temperature and enthalpy distribution is found than in the previous analyzed cases in chapter 6. In Fig. 7-4 the temperature distribution and the enthalpy distribution on the outlet side are shown. For the enthalpy, only the outlet side is depicted to adapt the scale in order to visualize smaller differences.

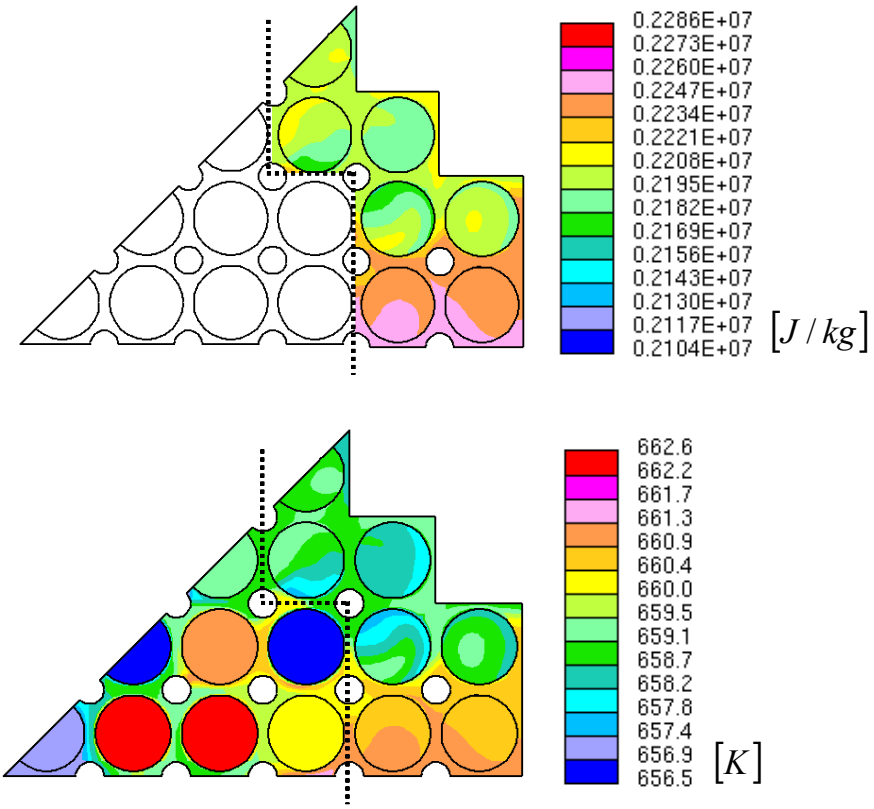

Fig. 7-4 Integrated results for the enthalpy (top) and temperature (bottom) distribution at the outlet side of the upper mixing chamber – reference case

The enthalpy and temperature at the outlets of the reference case for the upper mixing chamber thus vary between values of 2251kJ/kg and 2166kJ/kg for the enthalpy and between 661.4K and 656.8K for the temperature. Differences in the enthalpy and temperature distribution at the outlet are 85kJ/kg and 4.8K.

Since the local acceleration effects introduced into the flow field of the upper mixing chamber by the headpiece geometries is weakened by the introduced meander structure for the optimized case developed in chapter 4.5, the results for the mixing and temperature as well as enthalpy distribution are expected to be similar to the results found for the simplified model.

The results for the scalar distribution are plotted from underneath in Fig. 7-5. Direct short cuts are avoided by the wall welded into the upper mixing chamber between the inlet and outlet side, only leaving a determined gap at the top. Additional mixing is realized with the introduction of the other walls forming the formerly explained meander structure.

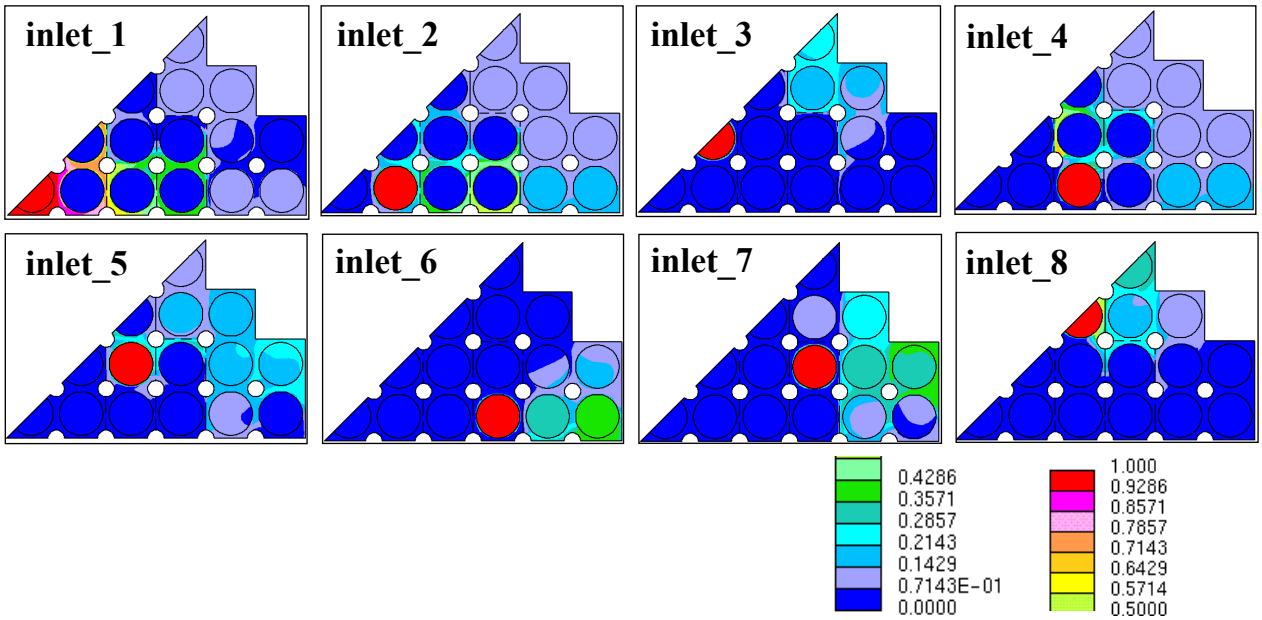

Fig. 7-5 Integrated results for the scalar concentration with introduced source terms representing the headpieces and a calculated inlet temperature distribution – optimized case

A vertical cross section shown in Fig. 7-6 illustrates the flow in the optimized mixing chamber with the meander structure.

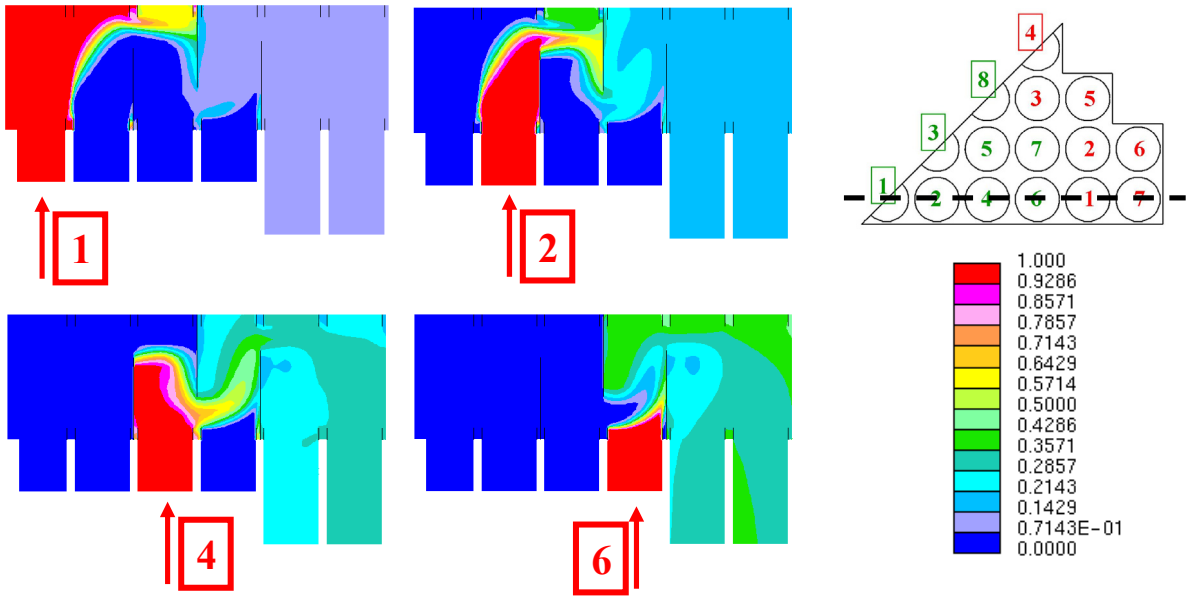

Fig. 7-6 Integrated results for the optimized case with meander structure dividing the upper mixing chamber in three stages

The flow structure in this optimized upper mixing chamber is almost the same, when simulated with headpiece geometries and temperature dependant effect as in the simplified model, where these effects are not regarded. This is due to the vertical walls decelerating the flow and forming defined jets in the horizontal gaps between the introduced mixing walls and the top or bottom wall of the upper mixing chamber. This is depicted in Fig. 7-7 exemplarily for one vertical cross section.

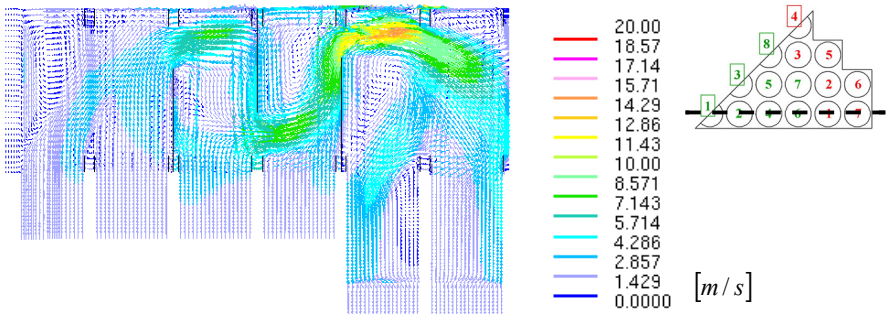

Fig. 7-7 Velocity plot in a vertical cross section of the optimized upper mixing chamber

The value for the standard deviation of $\sigma = 8.8\%$ remains unchanged in comparison to the optimized case analyzed for the simplified model. As shown in Fig. 7-8, the scalar distribution is almost identical to the scalar distribution presented for the simplified model.

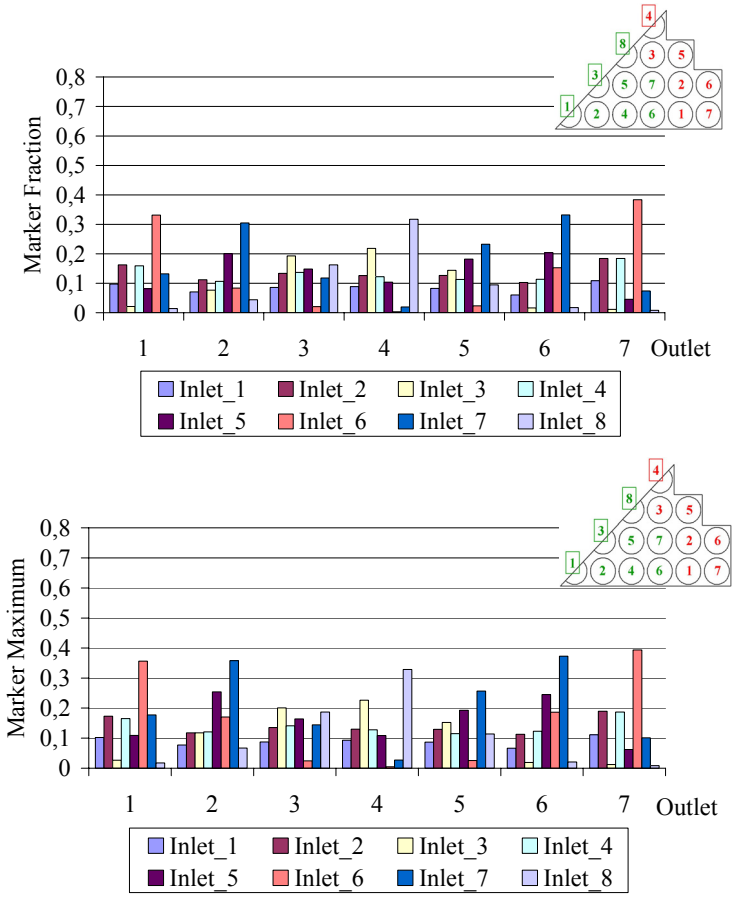

Fig. 7-8 Integrated results for the scalar concentrations, cross section averaged (top) and peak (bottom) in the upper mixing chamber – optimized case

Thus, the mixing achieved with the introduced meander structure is very successful and is also only slightly affected by the applied inlet temperature distribution.

For this case, representing the proposed technical solution for the upper mixing chamber, satisfactory results are achieved for the enthalpy and temperature distribution, which is shown in Fig. 7-9. The enthalpy at the outlet lies between 2238kJ/kg and 2191kJ/kg, while the temperature lies between values of 661.0K and 659.5K.

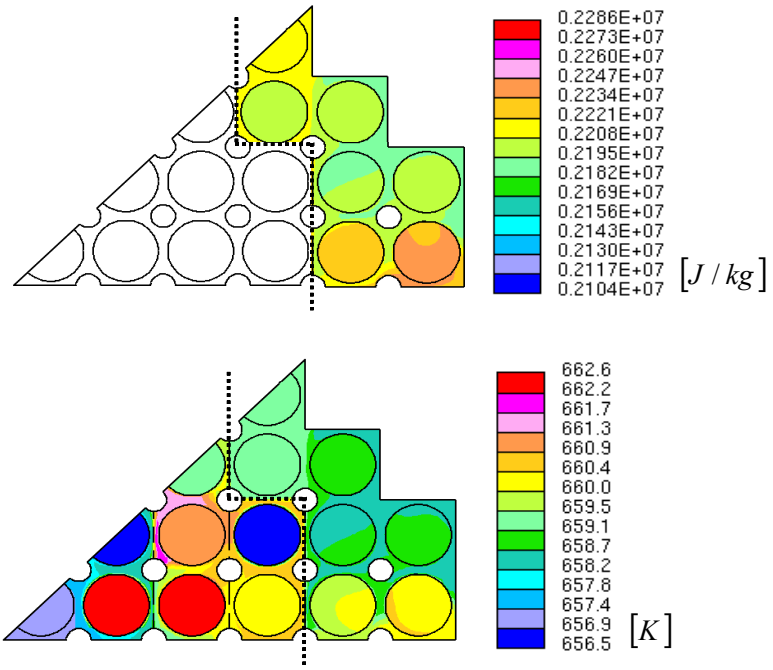

Fig. 7-9 Integrated results fort he enthalpy (top) and temperature (bottom) distribution at the outlet side of the upper mixing chamber – optimized case

The differences in temperature and enthalpy are summarized in Tab. 6-2 for the optimized case of the upper mixing chamber.

ΔTin= 6.1K	**ΔTout= 1.5 K**
Δhin= 322.3 kJ/kg	**Δhout= 47 kJ/kg**

Tab. 7-1 Comparison of inlet and outlet temperature/enthalpy differences in the upper mixing chamber (constant volume flow)

The here presented integrated results for the optimized case are the results proposed for the technical problem at hand, which is to enhance the mixing in the upper mixing chamber of the HPLWR to achieve an acceptable temperature distribution at its outlets.

Due to the value for the achieved standard deviation and a satisfactory scalar distribution at the outlets, with acceptable peak values, the meander structure as presented in chapter 4.5 can be proposed as technical solution. Considering the presented values for the enthalpy and temperature distribution at the outlet of the optimized upper mixing chamber, it can be concluded that the good mixing leads to a very satisfactory temperature homogenization.

8 Summary and Conclusions

A new method to analyze the mixing of fluids in complex mixing chambers has been presented in this work. The simplification method allows the numerical analysis of mixing chambers without geometrically resolving every complex detail of the geometry, while still capturing its effects. This leads to numerical analyses with much less necessary computation time. For this reason, the simplification method is an innovative approach in design processes, where many simulations are necessary for optimization.

The proposed simplification method has been derived for the upper mixing chamber of the HPLWR as an example for a very complex passive mixing chamber necessary for a temperature homogenization. In the upper mixing chamber, different water flows enter the mixing chamber with different temperatures at the supercritical pressure of 25MPa. The temperature of these different inlet flows has to be homogenized before the fluid enters the next heat up section to avoid the propagation of hot streaks in the core of the HPLWR. This task led to another important part in the analysis, which was to include the fluid properties of supercritical steam in the used CFD-code Star-CD to capture temperature dependant effects.

Both challenges were tackled independently from each other, before they were combined in one integrated simulation. The simplification method has been applied to model the complex geometry of the upper mixing chamber consisting of a large number of connection tubes and moderator boxes. To apply the simplification method, three steps are necessary, which are the simplification of the analyzed model, the quantification of the effects of the omitted geometry, and the introduction of these effects in the model. This strategy has been applied to the upper mixing chamber by omitting the complex geometry of the moderator boxes in the headpieces through which the fluid enters and exits the chamber. For the resulting simplified model, which consists of a much smaller number of cells, a design optimization has been performed which required much less computational time and effort. After finding the optimized design, the influences of the omitted geometry on the mixing have been determined. As last step in applying the simplification method, the influences of the omitted moderator boxes have been included into the model for the reference case as well as for the optimized case of the upper mixing chamber.

The influence of the detailed headpiece geometry with the moderator boxes on the flow has been added in the model with source terms in the momentum equations. Since only steady-state analyses have been performed, these source terms are volumetric forces, which have been derived with an integral balance of momentum and pressure drop correlations. The best performance of the method has been achieved, when regarding one headpiece as a whole and adding the effect globally. For the pressure drop coefficient, a simple approach has been chosen, describing the abrupt change of the flow cross section.

Additionally, a detailed CFD analysis of two neighboring headpieces has been performed. Hereby, an alignment with neighboring in- and outlet headpieces in a transverse flow field has been analyzed. Then the introduced forces have been applied to an extracted cutout of the simplified upper mixing chamber without the moderator boxes inside the headpieces and the results have been validated with the detailed CFD analysis.

An effective method to study a large number of different inlet temperature distributions with a single CFD analysis is the use of passive scalars as markers in an isothermal flow. Here, each inlet has been marked with a different passive scalar, allowing differentiation between the contributions of different inlet flows to the individual outlets. A disadvantage of this method, however, is that buoyancy forces will be neglected. Assuming a certain inlet temperature distribution instead of these markers, on the other hand, would require a separate CFD analysis for each case, so that mixing could only be studied exemplarily.

Characterizing the flow and by the Grashof- and the squared Reynolds- number suggests that buoyancy effects cannot be neglected a priori and temperature dependant effects also need to be included in the simulation. To include functions for the significant fluid properties, existing approaches have been extended with a direct relationship between the enthalpy and temperature. However, after including the strong changes in the fluid properties into the model, it has been found that buoyancy effects do not occur and only small influences on the mixing have been detected due to changes in the inlet temperature distribution.

For the integrated results of the upper mixing chamber, both temperature dependent effects and the effects of the headpiece geometries have been introduced. The results are presented for a reference case without means to enhance mixing as well as for an optimized case, representing the technical solution for the task at hand, which was to improve the mixing in the upper mixing chamber. Good mixing and thus an effective temperature and enthalpy homogenization are achieved in the optimized upper mixing chamber. A meander structure is introduced in the flow by including vertical walls leaving gaps at the top or bottom of the mixing chamber. This way, the inlet flows are collected and re-distributed.

The two components necessary to perform the analysis of this complex mixing chamber are the introduction of the temperature dependant effects and the simplification method. In principle it should be possible to apply these approaches to other technical tasks without major difficulties. In particular the simplification method is designed to be applicable to any complex flow structure. Although quantifying the adequate source terms might be a challenge.

Nomenclature

Latin symbols

a	$[m^2/s]$	Thermal diffusivity
a_t	$[m^2/s]$	Turbulent thermal diffusivity
c	$[m/s]$	Sound velocity
c_p	$[J/(kgK)]$	Specific heat
c_i	-	Scalar value in the analyzed cell
$\bar{c}_j$	-	Volume averaged inlet scalar at each outlet
$c_{j,\max}$	-	Maximum value of analyzed scalar per outlet
C	$[kg/m^4]$	Pre-factor for definition of local forces as source terms
d	$[m]$	Diameter
D	$[m^2/s]$	Diffusion coefficient of transported scalar
d_h	$[m]$	Hydraulic diameter
e	$[J/m^3]$	Inner energy
f	-	any magnitude
$\vec{F}$	$[N/m^3]$	Volumetric forces vector
$\bar{f}$	-	Magnitude is Reynolds averaged
f'	-	Fluctuation of a magnitude
f^*, f'	-	Star and prime usually represent dimensionless magnitude
F_x, F_y, F_z	$[N/m^3]$	Volumetric forces in x, y, z - direction
F_S	$[N]$	Resulting force
F_{iS}	$[N/m^3]$	Resulting volumetric force inserted as source term

F_R	$[N]$	Resistant force
F_{iSR}	$[N/m^3]$	Volumetric resistant force inserted as source term
F_A	$[N]$	Acceleration force
F_{iSA}	$[N/m^3]$	Volumetric acceleration force inserted as source term
g	$[m/s^2]$	Acceleration due to gravity
h	$[J/kg]$	Enthalpy
K	$[m^2/s^2]$	Turbulent kinetic energy
n	-	Number of evaluated values for inlet scalars (8 inlet scalars are evaluated at 7 outlets, $n = 56$)
N	-	Number of cells in model
p	$[MPa]$	pressure
p_c	$[MPa]$	Critical pressure
$\dot{q}_s$	$[W/m^2]$	Specific heat flux (per unit area), s denotes a source
$\dot{q}^t$	$[W/m^2]$	turbulent heat flux vector
s	$[kJ/(kgK)]$	Specific entropy
T	$[K]$ $[°C]$	Temperature
T_c	$[°C]$	Critical temperature
T_{cold}	$[°C]$	Temperature of cold inlet in validation experiment
u, v, w	$[m/s]$	Velocity component in x, y, z -direction
u^+	-	Dimensionless velocity
u_τ	$[m/s]$	Friction velocity
$\overline{u}_i$, $\overline{u}_j$	$[m/s]$	Reynolds averaged velocity components
u_i', u_j'	$[m/s]$	Turbulent fluctuations of velocity components
$\widetilde{u}_i$, $\widetilde{u}_j$	$[m/s]$	Favre averaged velocity components

u_i'' , u_j''	$[m/s]$	Turbulent fluctuations of mass averaged velocity components
V	$[m/s]$	Velocity magnitude ($V^2 = u^2 + v^2 + w^2$)
$\vec{v}$	$[m/s]$	Velocity vector
V_i	$[m^3]$	Volume of the analyzed cell
V_{total}	$[m^3]$	Sum of analyzed cell volumes per outlet
x_i	-	Value of each inlet scalar at each outlet
$\bar{x}$	-	Mean value of all inlet scalars at all outlets
y^+	-	Dimensionless wall distance
Y_m , $\overline{Y}_m$	-	Transported scalar
y	$[mm]$	Horizontal coordinate for measurements in outlet pipe of validation experiment
z	$[mm]$	Vertical coordinate for measurements inside mixing chamber of validation experiment

Greek symbols

α	$[1/K]$	Volumetric thermal expansion coefficient
ς	-	Pressure drop coefficient
ε	$[m^3/s^3]$	Turbulent dissipation
λ	$[W/(mK)]$	Conductivity
λ_t	$[W/(mK)]$	Turbulent conductivity
μ	$[kg/(ms)]$	Dynamic viscosity
μ_t	$[kg/(ms)]$	Eddy viscosity
ν	$[m^2/s]$	Kinematic viscosity

ν_t	$[m^2/s]$	Turbulent kinematic viscosity
ρ	$[kg/m^3]$	Density
τ_w	$[N/m^2]$	Wall shear stress
σ	[%]	Standard deviation
σ_{xx}, σ_{yy}, σ_{zz}	$[N/m^2]$	Normal stress in x, y, z - direction
Θ	-	Dimensionless temperature ($\Theta = 1$ is hot and $\Theta = 0$ cold water in inlet nozzles of validation experiment)
τ_{ij}	$[N/m^2]$	Shear stress tensor
τ_{xy}	$[N/m^2]$	Shear stress in xy - direction
τ_{xz}	$[N/m^2]$	Shear stress in xz - direction
τ_{yz}	$[N/m^2]$	Shear stress in yz - direction
τ^t	$[N/m^2]$	Turbulent shear stress tensor

Abbreviations

BWR	Boiling Water Reactor
CBS	Core Bottom Structure
CFD	Computational Fluid Dynamics
DNS	Direct Numerical Simulation
ERCOFTAC	European Research Community On Flow Turbulence And Combustion
HPLWR	High Performance Light Water Reactor
HTTR	High Temperature engineering Test Reactor
JAERI	Japan Atomic Energy Research Institute
KFKI	Atomic Energy Research Institute
LES	Large Eddy Simulation
LWR	Light Water Reactor
PWR	Pressurized Water Reactor
QUICK	Quadratic Upstream Interpolation of Convective Kinematics
RANS	Reynolds Averaged Navier Stokes
RPV	Reactor Pressure Vessel
SCWR	Supercritical Light Water Reactor
SIMPLE	Semi Implicit Method for Pressure Linked Equations
SST	Shear Stress Transport
Star-CD	Simulation of Turbulence in Arbitrary Regions
UD	Upwind Differencing

References

[1] ARIMOND, J., Erwin, L.: A simulation of a motionless mixer. Chemical Engineering Communications, Vol. 37, Page 105-126, 1985.

[2] ATKINS, W.: Consultants and Members of the NSC, Best Practice Guidelines for Marine Applications of Computational Fluid Dynamics, tech. report, Sirehna, HSVA, FLOWTECH, VTT, 2002.

[3] BAGLIETTO, CD-Adapco, personal note from Dr. Baglietto, Emilio, 2009.

[4] BAGLIETTO, E., Ninokata, H.: A Turbulence Model Study for Simulating Flow Inside Tight Lattice Rod Bundles, Nuclear Engineering and Design, Vol. 235 Page 773, 2004.

[5] BAGLIETTO, E., Ninokata, H.: Anisotropic Eddy Viscosity Modeling for Application to Industrial Engineering and Internal Flows, International Journal of Transport Phenomena, Vol. 8 Page 109, 2006.

[6] BERTOLOTTO, D., Manera, A., Prasser, H.-M., Chawla, R.: CFD Simulations of a Single-phase Mixing Experiment, Proc. IYNC Conf. 2008, Paper No. 422, Interlaken, Switzerland, 2008.

[7] BITTERMANN, D., Squarer, D., Schulenberg, T., Oka, Y.: Economic Prospects of the HPLWR, Proc. GENS4/ANP2003, Paper No.1003, Kyoto, Japan, 2003.

[8] BITTERMANN, D., Starflinger, J., Schulenberg, T.: Turbine Technologies for High Performance Light Water Reactors, Proc. ICAPP Conf. 2004, Paper No. 4195, Pittsburg, USA, 2004.

[9] BRANDAUER, M., Schlagenhaufer, M., J., Schulenberg, T.: Steam Cycle Optimization for the HPLWR, Paper No. 36, Proc. 4th Internat. Symposium of Supercritical Water-Cooled Reactors, Heidelberg, Germany, 2009.

[10] Bürkert Fluid Control Systems, personal note from Dr. Kabisch, Gunter, 2009.

[11] CASEY, M., Wintergerste, T.: Best Practice Guidelines. Version 1.0, European Research Community On Flow, Turbulence And Combustion, ERCOFTAG, 2000.

[12] CASEY, M.: Thematic Area 6: Best Practice Advice for Turbomachinery Internal Flows, Page 40–46, QNET-CFD Network Newsletter, 2, 2004.

[13] CD-ADAPCO, Baglietto, E.: Methodology - STAR-CD, Improved Anisotropic K-e modeling, Documentation for use on solver Star-CD 3.26., 2006.

[14] CD-ADAPCO: Methodology - STAR-CD Version3.26., 2005

[15] CHENG, X., Schulenberg, T., Bittermann, D., Rau, P.: Design analysis of core assemblies for supercritical pressure conditions, Nuclear Engineering and Design Vol. 223, Page 279-294, 2003.

[16] DOBASHI, K., Oka, Y., Koshizuka, S.: Conceptual Design of a high temperature power reactor cooled and moderated by supercritical light water, Ann. Nucl. Energy Vol. 25, No. 8, Page 487-505, 1998.

[17] FERZIGER, J. H., Peric, M.: Computational Methods for Fluid Dynamics, 3. edition, Berlin, Springer-Verlag, 2002.

[18] FISCHER, K., Guelton, E., Schulenberg, T.: Festigkeitsanalyse des Reaktordruckbehälters für einen Leichtwasserreaktor mit überkritischen Dampfzuständen, Proc. Jahrestagung Kerntechnik 2006, Aachen, Germany, 2006.

[19] FISCHER, K., Schneider, T., Redon, T., Schulenberg, T., Starflinger, J.: Mechanical Design of a Core Components for a High Performance Light Water Reactor with a Three Pass Core, Proc. GLOBAL Conf., Paper No. 175772, Boise, USA, 2007.

[20] FISCHER, K., Starflinger, J., Schulenberg, T.: Conceptual Design of a Reactor Pressure Vessel and its Internals for a HPLWR, Proc. ICAPP Conf., Paper No. 6098, Reno, USA, 2006.

[21] FOULON, H., Wank, A., Schulenberg, T.: CFD Analyse der Speisewasserströmung im HPLWR, Diplomathesis, Forschungszentrum Karlsruhe, Germany, 2008.

[22] FOULON, H., Wank, A., Schulenberg, T.: CFD Analysis of feedwater flow in the HPLWR Pressure Vessel, Proc. Internat. Students Workshop on High Performance Light Water Reactos, Karlsruhe, Germany, 2008.

[23] GROTE, K.-H., Feldhusen, J., DUBBEL - Taschenbuch fuer den Maschinenbau, 21.Auflage, Berlin, Springer-Verlag, 2001.

[24] HIMMEL, S., Class, A., Laurien, E., Schulenberg, T.: Determination of Mixing Coefficients in a Wire-Wrapped HPLWR Fuel Assembly using CFD, Proc. ICAPP conf. Paper No. 8053, Anaheim, USA, 2008.

[25] HIMMEL, S., Class, A., Laurien, E., Schulenberg, T.: Flow In A HPLWR Fuel Assembly With Wire Wrap Spacers, Proc. ANS/ENS Winter Meeting, Washington, USA, 2007.

[26] HIMMEL, S., Hofmeister, J., Starflinger, J., Schulenberg, T.: Mechanical Analysis of the Fuel Assembly Box of a HPLWR Fuel Assembly, Proc. ICAPP Conf. 2006, Paper 6229, Reno, USA, 2006.

[27] HIMMEL, S.: Modellierung des Strömungsverhaltens in einem HPLWR-Brennelement mit Drahtwendelabstandshaltern, Forschungszentrum Karlsruhe, Forschungsbericht FZKA, 2008.

[28] HOBBS, D., Muzzio, F.: Optimization of a static mixer using dynamical systems techniques, Chemical Engineering Science Vol. 53, No. 18, Page 3199-3213, 1998.

[29] HOFMEISTER J., Laurien E., Class A., Schulenberg T.: Turbulent Mixing in the Foot Piece of a HPLWR Fuel Assembly, Proc. GLOBAL Conf. 2005, Paper No. 066, Tsukuba, Japan, 2005.

[30] HOFMEISTER, J., Schulenberg, T., Starflinger, J.: Optimization of a Fuel Assembly for a HPLWR, Proc. ICAPP Conf. 2005, Paper No. 5077, Seoul, Korea, 2005.

[31] HOFMEISTER, J., Waata, C., Schulenberg, T., Starflinger, J.: Fuel assembly design study for a reactor with supercritical water. Nuclear Engineering and Design, Vol. 237, Page 1513, 2007.

[32] INAGAKI, personal note from Dr. Inagaki, Yoshiyuki from the Oarai Research and Development Center, Japan Atomic Energy Agency (JAEA), December 2008.

[33] INAGAKI, Y., Kunuki, T., Miyamoto, Y.: Thermal mixing test of coolant in the core bottom structure of a high temperature engineering test reactor, Nuclear Engineering and Design, Vol. 123, Page 77-86, 1990.

[34] JAERI, Japan Atomic Energy Research Institute, Design of High Temperature Engineering Test Reactor (HTTR), September 1994, JAERI 1332, http://httr.jaea.go.jp/eng/index_top_eng.html, 1994

[35] KAKAC, S., Aung, W., Viscanta, R.: Natural Convection - Fundamentals and Applications, Hemisphere Publishing Corporation, Washington, USA, 1985.

[36] KAYS, W.: Trans. ASME 72, Page 1067-1074, 1950. Found in VDI-Gesellschaft Verfahrenstechnik und Chemieingenieurwesen, VDI-Waermeatlas, 9th Edition, Section Lac1, Berlin, Springer-Verlag, 2002.

[37] KOTUMOS, P., McGuirk, J.: CFD predictions of lobed mixer performance, Computer Methods in Applied Mechanics and Engineering, Vol. 122, Page 131-144, 1995.

[38] KRAUME, M: Mischen und Ruehren: Grundlagen und moderne Verfahren, 1. edition, Wiley-VCH., Weinheim, Germany, 2003.

[39] KUNIK, C., Vogt, B., Schulenberg, T: Flow Phenomena in the Gap Volume between Assembly Boxes, Proc. 4th Internat. Symposium of Supercritical Water-Cooled Reactors, Paper No. 04, Heidelberg, Germany, 2009.

[40] KUNIK, C., Vogt, B.: Berechnung der Mischkonvektion im Moderatorspalt eines Kernreaktors mit einem Ansatz für poröse Medien, Forschungszentrum Karlsruhe, Forschungsbericht FZKA 7273, 2007.

[41] KUNITOMI, K., Inagaki, Y., Ioka, I., Suzuki, K., Nekoya, S., Miyamoto, Y.: Thermal and Hydraulic Tests in HENDEL T2 Supporting the Development of the Core Bottom Structure of the High Temperature Engineering Test Reactor (HTTR), Nuclear Engineering and Design, Vol. 108, Page 359-368, 1988.

[42] LAUNDER B.E., Spalding D.B.: The numerical computation of turbulent flows, Computer Methods in Applied Mechanics and Engineering, Vol. 3, Page 269-289, 1974.

[43] LAURIEN, E., Oertel jr., H.: Numerische Strömungsmechanik, 3.Auflage, Braunschweig, VIEWEG, 2009.

[44] LAURIEN, E., Rashid, M., McEligot, D., M.: Heat Capacity Model for Turbulent Heat Transfer at Supercritical Pressure, Proc. International Conference on Multiphase Flow, ICMF,Leipzig, Germany, 2007.

[45] MARACZY, C., Hegyi, G., Brolly, A., Vertes, P., Hordosy, G.: Application of the KARATE Code System to the High Performance Light Water Reactor, Proc. PHYTRA1,Marrakech, Marokko, 2007.

[46] MARACZY, C., Hegyi, G., Hordosy, G., Temesvari, E., Hegedos, C., Molnar A.: High Performance Light Water Reactor Core Design Studies, Proc. PBNC Conf 2008, Aomori, Japan, PaperID P16P1221, 2008.

[47] MENTER, F, Kuntz, M., Langtry, RTen Years of Industrial Experienece with the SST Turbulence Model, Turbulence, Heat and Mass Transfer Vol.4, 2003.

[48] MENTER, F.: Two-Equation Eddy-Viscosity Turbulence Models for Engineering Applications, AIAA Journal, Vol. 32, Page 1598–1605, 1994.

[49] MÖBIUS, M., Wank, A., Schulenberg, T.: CFD Analysis of mixing in the headpieces of the High Performance Light Water Reactor, Diplomathesis, Forschungszentrum Karlsruhe, Germany, 2008.

[50] OERTEL JR, H., Böhle, M., Dohrmann, U.: Strömungsmechanik, 5. Auflage, Braunschweig, VIEWEG, 2009.

[51] OERTEL JR, H., Delfs, J.: Strömungsmechanische Instabilitäten, 1. Auflage, Berlin, Springer-Verlag, 1996.

[52] OERTEL JR, H.:Prandtl's Essentials of Fluid Mechanics, 3.edition, Berlin, Springer-Verlag, 2009.

[53] OKA, Y., Koshizuka, S.: Conceptual Design of a Supercritical-Pressure Direct-Cycle Light Water Reactor, Proc. Int. Conf. Design and Safety of Advanced Nuclear Power Plants, Vol. 1, Page 1–7, Tokyo, Japan, 1992.

[54] OKA, Y.: Review of High Temperature Water and Steam Cooled Reactor Concepts, no. 104, Proc. SCR 2000 Symposium, Tokyo, Japan, 2000.

[55] OLDSHUE, J. Y.: Fluid Mixing Technologies, 1. edition, Chemical Engineering McGrawn-Hill Pub.Co., New York, USA, 1983.

[56] PAHL, M., H., Muschelknautz, E. Statische Mischer und ihre Anwendungen, Chemie Ingenieur Technik, Vol. 52, No. 4, Page 285-291, 1980.

[57] PAHL, M., H., Muschelknautz, E.: Einsatz und Auslegung statischer Mischer, Chemie Ingenieur Technik, Vol. 51, No. 5, Page 347-364, 1979.

[58] Pfaudler Werke GmbH, personal note from Heinzmann, Matthias, 2009.

[59] Pfaudler Werke GmbH, Pfaudler Mischkammer MK, 226-2 d, received 2009.

[60] POPE, S.: Turbulent Flows. 5. Edition, Cambridge University Press, New York, USA, 2008.

[61] RAHMANI, R., Keith, T., Ayasoufi, A.: Three-Dimensional Numerical Simulation and Performance Study of an Industrial Helical Static Mixer, Journal of Fluids Engineering, Vol. 127, Page 467-483, 2005.

[62] REISS, T., Foulon, H., Wank, A., Schulenberg, T.: Transient Stress Analysis of the HPLWR Pressure Vessel, Proc. 4th Internat. Symposium of Supercritical Water-Cooled Reactors, Paper No. 39, Heidelberg, Germany, 2009.

[63] ROACHE, P., Verification and Validation in Computational Science and Engineering, Hermosa Publishers, Albuquerque, United States, 1998.

[64] SCHLAGENHAUFER, M., Starflinger, J., Schulenberg, T.: Steam Cycle Analyses and Control of the HPLWR Plant, Proc. 4th Internat. Symposium of Supercritical Water-Cooled Reactors, Paper No. 38, Heidelberg, Germany, 2009.

[65] SCHLAGENHAUFER, M., Vogt, B., Schulenberg, T., Reactivity control mechanisms for a HPLWR fuel assembly, Proc. GLOBAL 07, Boise, ID, USA, Sept. 9-13, 2007.

[66] SCHLICHTING, H., Gersten, K.: Grenzschichttheorie, 10. edition, Springer-Verlag, Berlin Heidelberg, Germany, 2006.

[67] SCHUBERT, H: Handbuch der mechanischen Verfahrenstechnik , Band 1 und 2, 1. edition, Wiley-VCH., Weinheim, Germany, 2003.

[68] SCHULENBERG T., Starflinger J., Heinecke J.: Three Pass Core Design Proposal for a High Performance Light Water Reactor, Proc. INES-2 Conf. 2006, Yokohama, Japan, 2006; published in Progress in Nuclear Engineering, 2007.

[69] SCHULENBERG, T., Starflinger, J.: Core Design Concepts for High Performance Light Water Reactors, Nuclear Engineering and Technology Vol. 39, Page 249, 2007.

[70] SINGH, M., Galaktionov, O., Meijer, H, Anderson, P.: A simplified approach to compute distribution matrices for the mapping method, Computers and Chemical Engineering, Vol. 33, Page 1354–1362, 2009.

[71] SMIDT, D. Reaktortechnik - Band 1und 2, Karlsruhe, G. Braun, 1971.

[72] SQUARER, D., Schulenberg, T., Struwe, D., Oka, Y., Bittermann, D., Aksan, N., Maraczy, C., Kyri-Rajamäki, R., Souyri, A., Dumaz, P.: High Performance Light Water Reactor, Nuclear Engineering and Design, Vol. 221, Page 167-180, 2006.

[73] STRAUß, K.: Kraftwerkstechnik, 3.Auflage, Berlin, Springer-Verlag, 1997.

[74] TIRET, X., Wank, A., Schulenberg, T.: CFD Analysis of the Decay Heat Removal in a Three-Pass Core with Downward Flow, Diplomathesis, Forschungszentrum Karlsruhe, Germany, 2009.

[75] TODREAS, N., Kazimi, M.:Nuclear Systems I - Thermo Hydraulic Fundamentals. second printing, Levittown, PA, USA, Taylor and Francis, 1993.

[76] TODREAS, N., Kazimi, M.:Nuclear Systems II - Elements of Thermo Hydraulic Design. second printing, Levittown, PA, USA, Taylor and Francis, 1993.

[77] TURNER, J.: Buoyancy Effects in Fluids, Cambridge University Press, Great Britain, 1973.

[78] US DOE Nuclear Energy Research Advisory Commitee, A Technology Roadmap for Generation IV Nuclear Energy Systems, tech. report, Generation IV International Forum, 2002.

[79] VERSTEEG, H.K., Malalasekera, W.: An introduction to computational fluid dynamics - The finite volume method, Harlow, Essex, England, Pearson Education Ltd., 1995.

[80] VISSER, J., Rozendal, P., Hoogstraten, H., Beenackers, A.: Three-dimensional numerical simulation of fow and heat transfer in the Sulzer SMX static mixer, Chemical Engineering Science, Vol. 54, Page 2491-2500, 1999.

[81] WAGNER W., Kruse A.: The Industrial Standard IAWPS-IF97 for the Thermodynamic Properties and Supplementary Equations for other Properties: Properties of Water and Steam, Berlin, Springer-Verlag, 1997.

[82] WANK, A., Schulenberg, T., Class, A.: Coolant Mixing in the HPLWR Three pass core, Proc. ICAPP Conf., Paper No. 8100, Anaheim, USA, 2008.

[83] WANK, A., Schulenberg, T., Class, A.: Coolant Mixing in the HPLWR Upper Plenum, International Journal for Nuclear Power, Vol. 53, Page 549-551, 2008.

[84] WANK, A., Schulenberg, T., Laurien, E.: Analysis of the flow in the upper mixing chamber of a three pass core, Proc. 4th Internat. Symposium of Supercritical Water-Cooled Reactors, Paper No. 06, Heidelberg, Germany, 2009.

[85] WANK, A., Schulenberg, T., Laurien, E.: Mixing of Cooling Water at Supercritical Pressures in the HPLWR - Three pass core, Proc. NURETH 13 Conf., PaperID N13P1003, Kanazawa City, Japan, 2009.

[86] WILCOX, D.C.: Turbulence Modelling for CFD. 2nd edition, DCW Industries, Inc., 1998.

[87] YAMAJI, A., Kamei, K., Oka, Y., Koshizuka, S.: Improved core design of the high temperature supercritical-pressure light water reactor, Annals of Nuclear Energy, Vol. 32, Page 651–670, 2005.

[88] YAMAJI, A., Oka, Y., Koshizuka, S.: Three-dimensional Core Design of High Temperature Supercritical-Pressure Light Water Reactor with Neutronic and Thermal-Hydraulic Coupling, Journal of Nuclear Science and technology, Vol. 42, No. 1, Page 8–19, 2005.

[89] ZIEREP, J.:Grundzüge der Strömungslehre, 4. Auflage, Berlin, Springer-Verlag, 1993.

Annex A Lower Mixing Chamber

A.1. Numerical model and reference case

The simulation settings for the lower mixing plenum are identical to the simulations carried out for the upper mixing chamber. Only here, 1/4th of the geometry has been modeled. The grid consists of around 330000 cells. For the lower mixing chamber a hybrid mesh has been applied which consists of tetrahedral cells for most of the geometry and hexahedral cells for the outlet side, where the introduced passive scalars are evaluated. In analogy to the simulations for the upper mixing chamber, porous media cells are introduced to the outlet geometry to account for the pressure drop in the fuel element clusters in the following superheater II as shown in Fig. A-1.

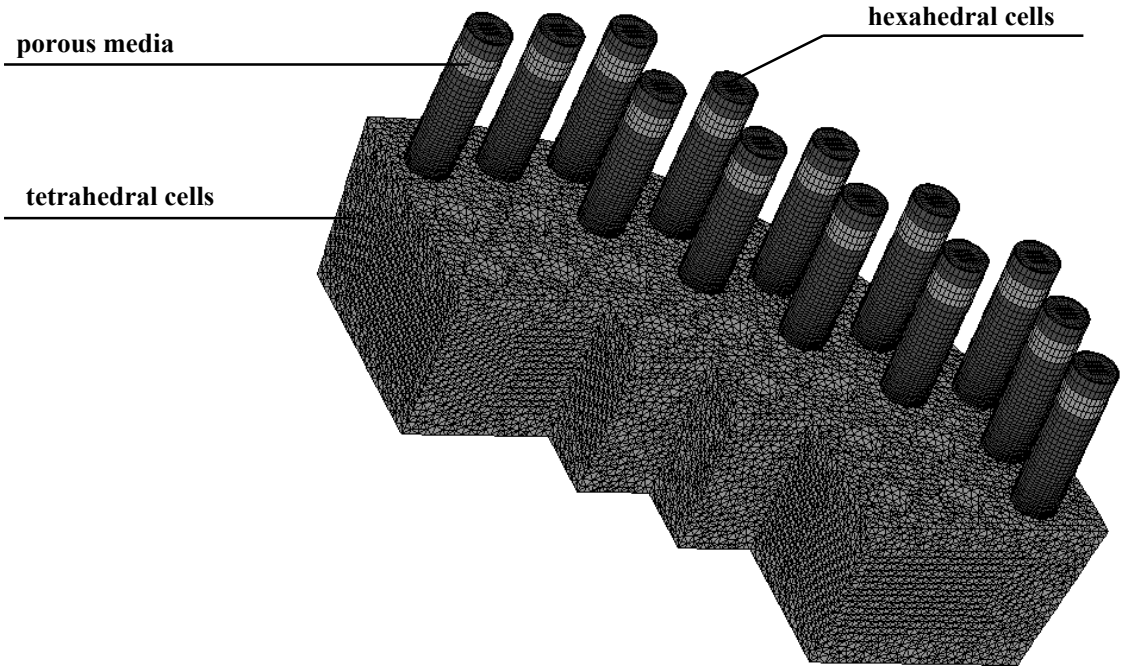

Fig. A-1 Tetrahedral grid for the lower mixing chamber with block structured, hexahedral elements for the outlet geometry and introduced porous media cells

The boundary conditions applied are shown in Fig. A-2. Since 1/4th of the lower mixing chamber is modeled, there are 13 inlets and 13 outlets defined in the model. The applied inlet velocity is higher, since the density of the supercritical steam is decreased. For each inlet a uniform inlet velocity of 11.7 m/s in vertical direction has been defined and the outlets are defined as pressure boundaries. The modeling of 1/4th of the geometry leads to geometrically identical cutting planes on both sides of the model, which allows the use of cyclic boundaries for these surfaces. Cyclic or periodic boundaries allow circumferential flow in the geometry, since the fluid leaving the model through one, re-enters through the other cutting plane. To simulate a global swirl in the lower mixing chamber, cyclic boundary conditions are applied requiring identical cutting planes at both sides of the model, which is why 1/4th of the geometry is modeled.

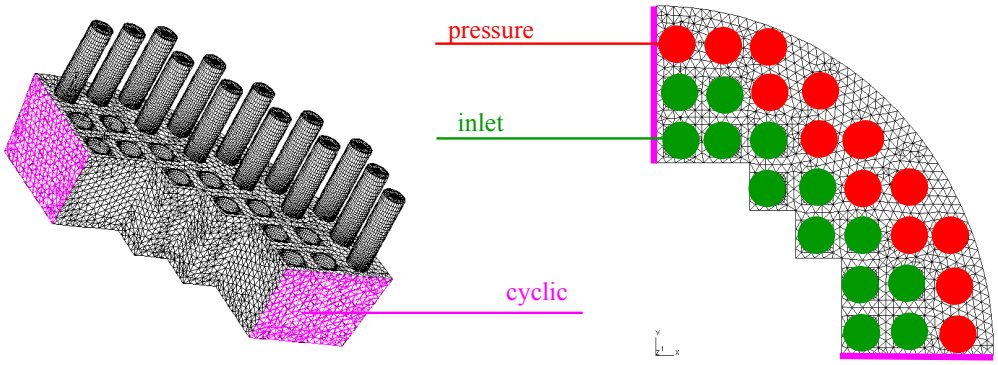

Fig. A-2 Boundary conditions applied to the lower mixing chamber

The scalar distribution is evaluated at each outlet, analogue to the upper mixing chamber. For the reference case, the inlet flows enter the lower mixing chamber without any tubes at the end of the footpieces of the superheater I clusters. In spite of the used cyclic boundaries for the cutting planes and the empty volume of the lower mixing chamber, the flow has no circumferential direction as can be seen in figure Fig. A-3. The results for only four exemplary scalars are shown in this picture. It can be seen that the scalars are bundled in radial direction and almost no mixing takes place. The different in- and outlets are numbered according to the picture on the lower left side of figure Fig. A-3.

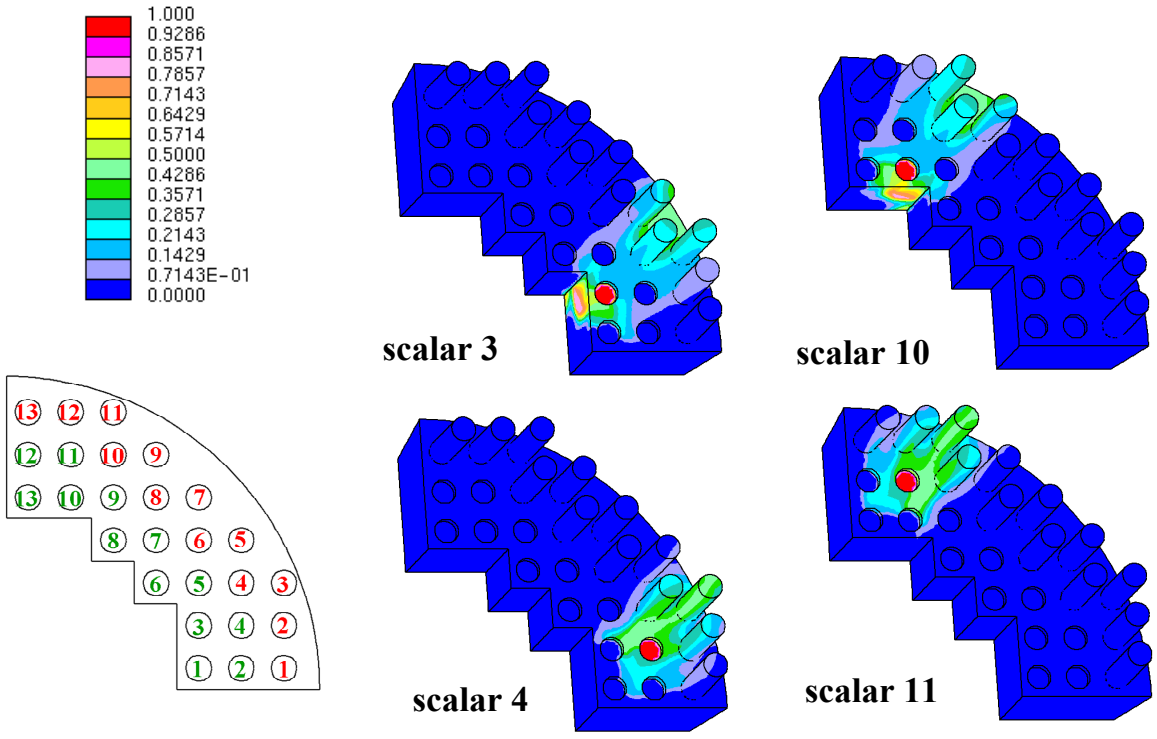

Fig. A-3 Lower mixing chamber: Results for the reference case and in- and outlet numbering

When comparing this case to the reference case of the upper mixing chamber, it is found that "short circuits" are obtained between all in- and outlets, whereas for the upper mixing chamber, critical in- and outlet pairs could be identified. The volume averaged scalar concentration is in general higher, at a value of around 40%, since each inlet scalar is distributed to only about three outlets, but the worst case here doesn't quite reach the worst case of the upper

mixing chamber, which is found to be between inlet 6 and outlet 1, where over 50% of the scalar is transmitted directly. Also the local peak values for the scalars, with about 50% aren't as high as in the upper mixing chamber where they reach local peak values over 70%.

A.2. Optimized design for the lower mixing chamber

Since the geometry of the lower mixing chamber is an empty volume, the mixing strategy differs significantly from the one chosen for the upper mixing chamber. To improve mixing, the chosen approach is to adjust the inlet flows, since the mixing volume is empty and a global swirl is easy to generate. This way it is possible to increase the mixing length significantly and to avoid short circuits between all in- and outlets. How this can be accomplished is demonstrated in Fig. A-4 on the left. On the right side it is shown how this approach can be simulated.

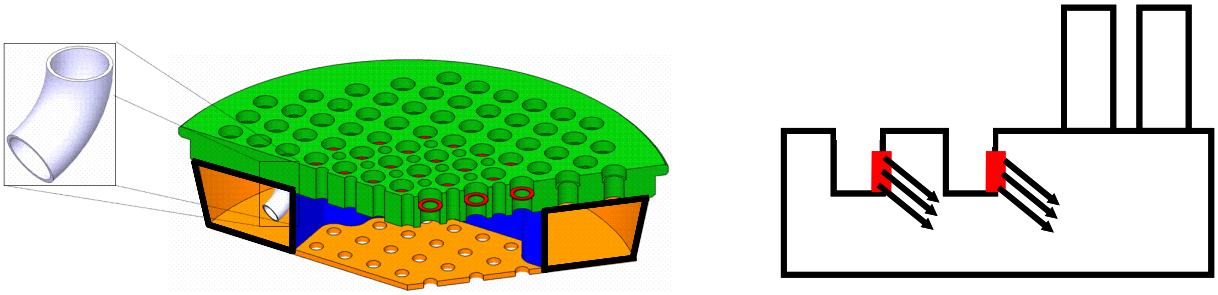

Fig. A-4 Design improvement for the lower mixing plenum

The inlet flow can be influenced by curved tubes or swirlers that can be welded to the holes in the core support plate (green) in which the footpieces of the fuel element clusters are entered. For the simulation of a case which is optimized in this way, round pockets are introduced into the grid, where the inlet tubes are located. This way, the inlet boundary conditions can be positioned inside the lower mixing chamber and the flow angle can be varied additionally, as shown on the right side of Fig. A-4.

The scalar distribution is evaluated at each outlet, analogue to the upper mixing chamber. For the reference case, the inlet flows enter the lower mixing chamber without any tubes at the end of the footpieces of the superheater I clusters. In spite of the used cyclic boundaries for the cutting planes and the empty volume of the lower mixing chamber, the flow has no circumferential direction It is found that the scalars are bundled in radial direction and almost no mixing takes place. When comparing this case to the reference case of the upper mixing chamber, it is found that "short circuits" are obtained between all in- and outlets, whereas for the upper mixing chamber, certain critical in- and outlet pairs could be identified. The volume averaged scalar concentration is in general higher, at a value of around 40%, since each inlet scalar is distributed to only about three outlets, but the worst case here doesn't quite reach the worst case of the upper mixing chamber, where over 50% of the scalar is transmitted directly. Also the local peak values for the scalars, with about 50% aren't as high as in the upper mixing chamber where they reach local peak values over 70%. The result for the optimized case for the lower mixing chamber is shown in Fig. A-5. The chosen angles for the inlet flows of the improved case are 45° in vertical direction. The radial direction for the other inlet flows is

orthogonal to the particular cutting surface, for the inlets 5 to 9 an angle of 45° between the inflow direction and the cutting planes is chosen in circumferential direction, according to the numbering shown in Fig. A-5 on the lower left side.

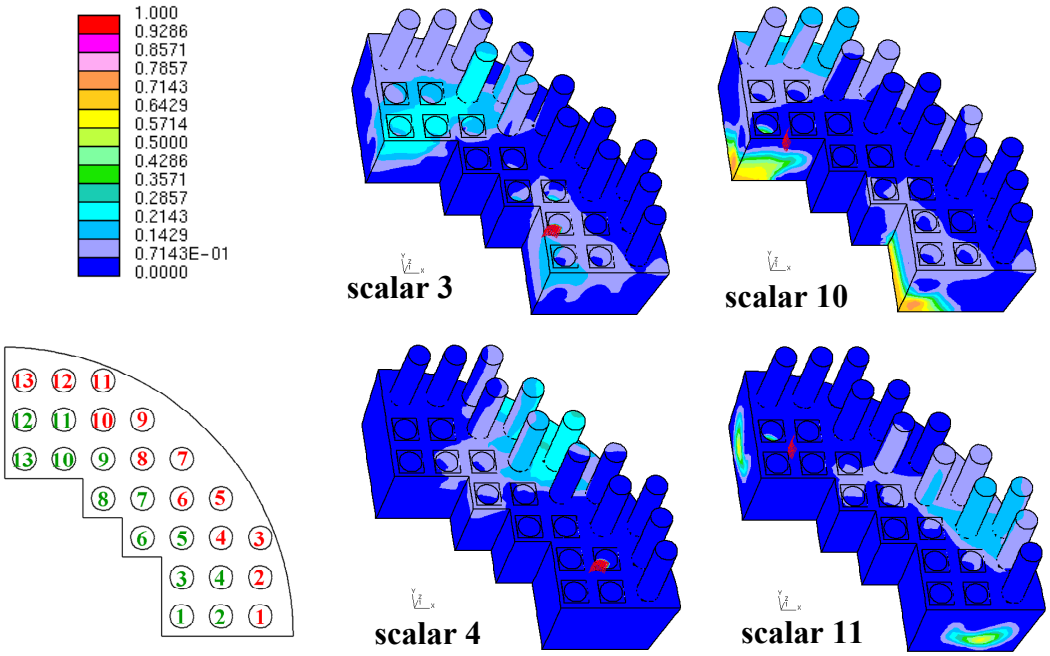

Fig. A-5 Results for the improved case of the lower mixing chamber

With this constellation, a global inlet swirl, which is superimposed with the local swirl between the in- and outlet side, is achieved. Thus, the local swirl parallel to the cutting surfaces is transported by the induced global swirl in circumferential direction and the mixing is improved significantly. The effect on the mixing can be seen when looking at exemplary scalar distributions. The inlet scalars are now distributed to at least five outlets and the mixing length has been increased visibly. The inlets in Fig. A-5 are accentuated with red windows.

Comparing the volume averaged scalar concentration, it is found that the global swirl in the lower mixing chamber leads to an improvement from 40% to just over 20% for most inlet scalars at the outlets. Peak values are also decreased by almost 30% from 50% to 20% in most cases. For the lower mixing chamber with enhanced mixing, a standard deviation of $\sigma = 5.5\%$ has been achieved. In general it can be stated that that the mixing improvement using the proposed swirlers is successful.

A.3. Temperature and enthalpy distribution in the lower mixing chamber

The inlet temperatures and enthalpies for the lower mixing chamber have been applied in analogy to the upper mixing chamber. For the superheater I outlets a higher discrepancy between the inlet temperatures and enthalpies of the different clusters has been found by Maraczy et al. in [46]. The influence of the introduced temperature dependant effects into the lower mixing chamber is insignificant. For the case with improved mixing, the variations in temperature of 26.4K and in enthalpy of 151.1kJ/kg at the mixing chamber inlets have been reduced to 7.1K and 40 kJ/kg at its outlets.

Annex B Dimensions of the Upper Mixing Chamber and Headpiece Geometry

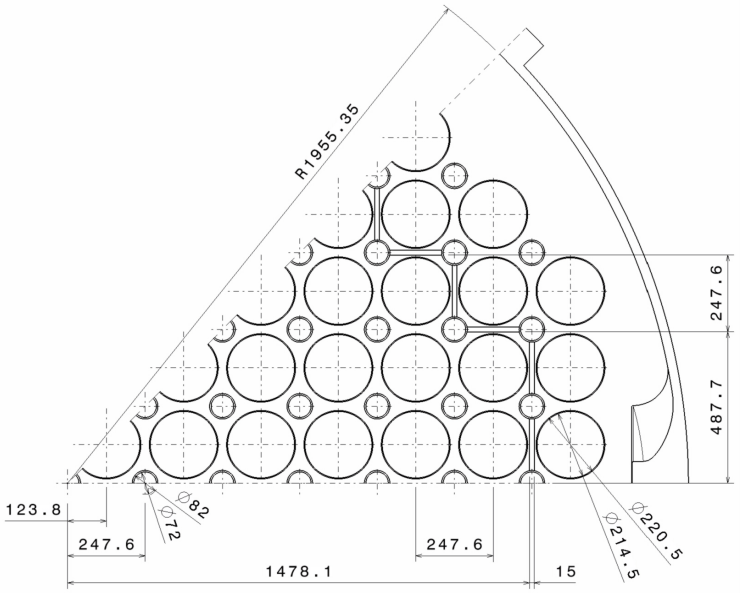

Fig. B-1 Dimensions of the upper mixing chamber reference case (without any measures to enhance mixing)

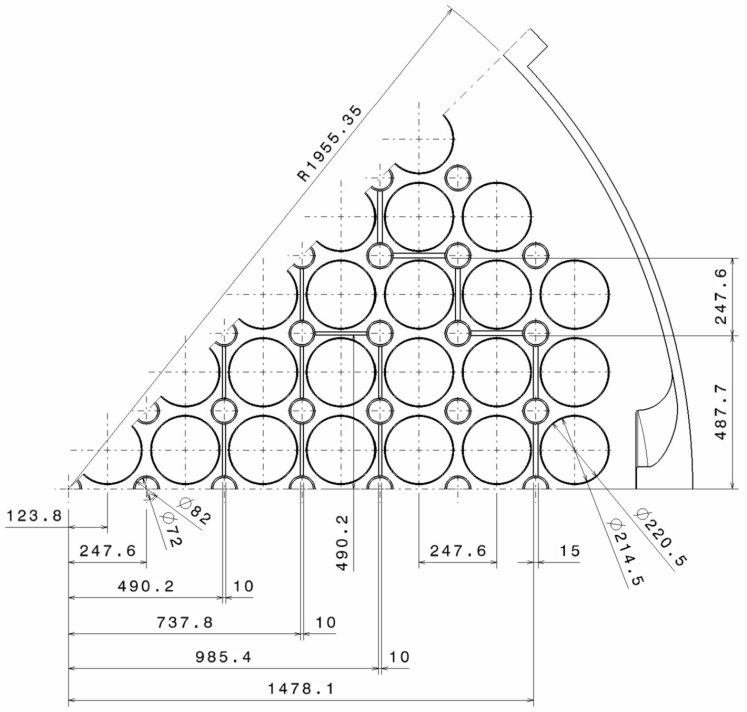

Fig. B-2 Dimensions of the upper mixing chamber optimized case (with meander alignment)

Inner height of upper mixing chamber: 480mm

Gap width for optimized case: 1st: 180mm, 2nd: 180mm, 3rd: 140mm

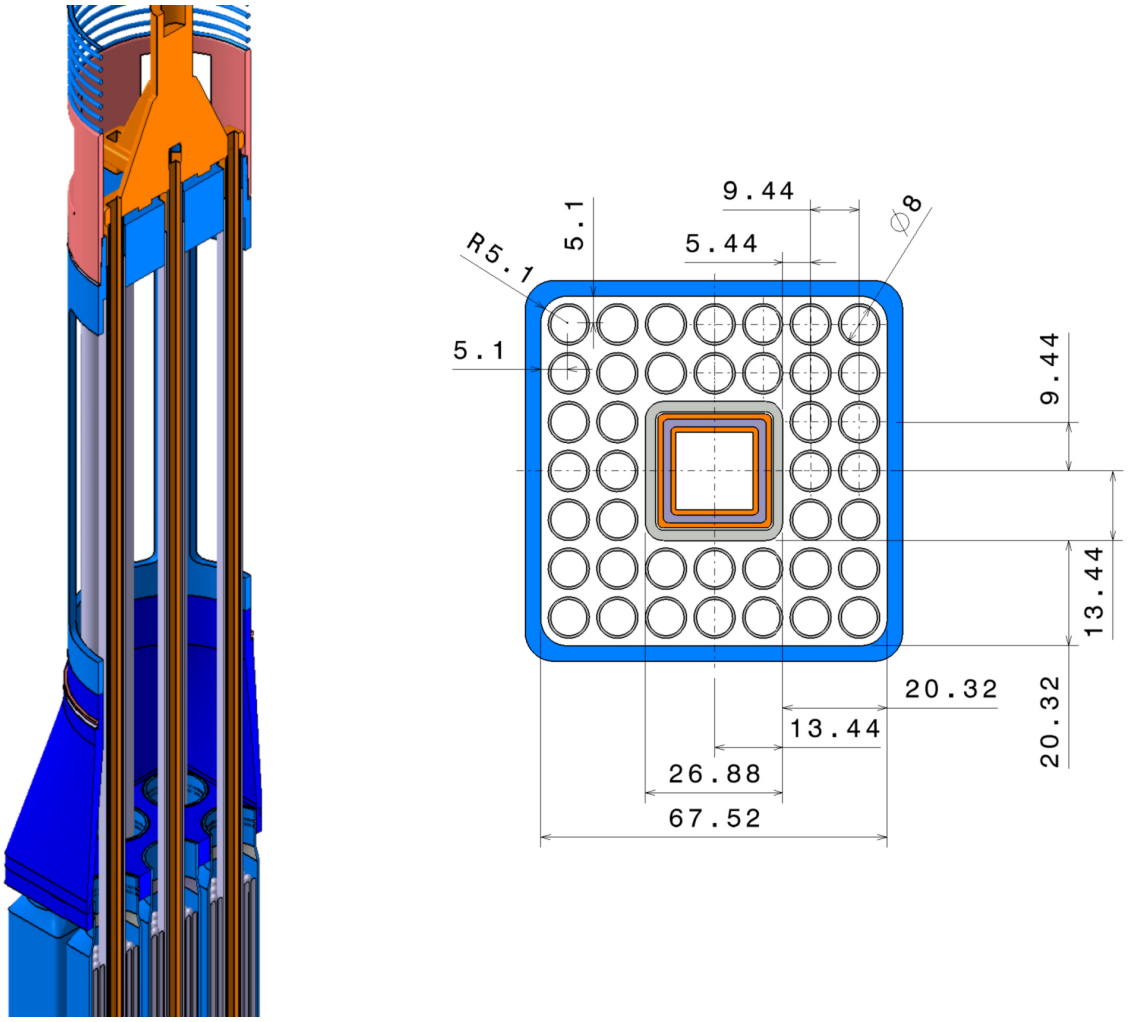

Fig. B-3 Dimensions of one cluster within the headpiece geometry

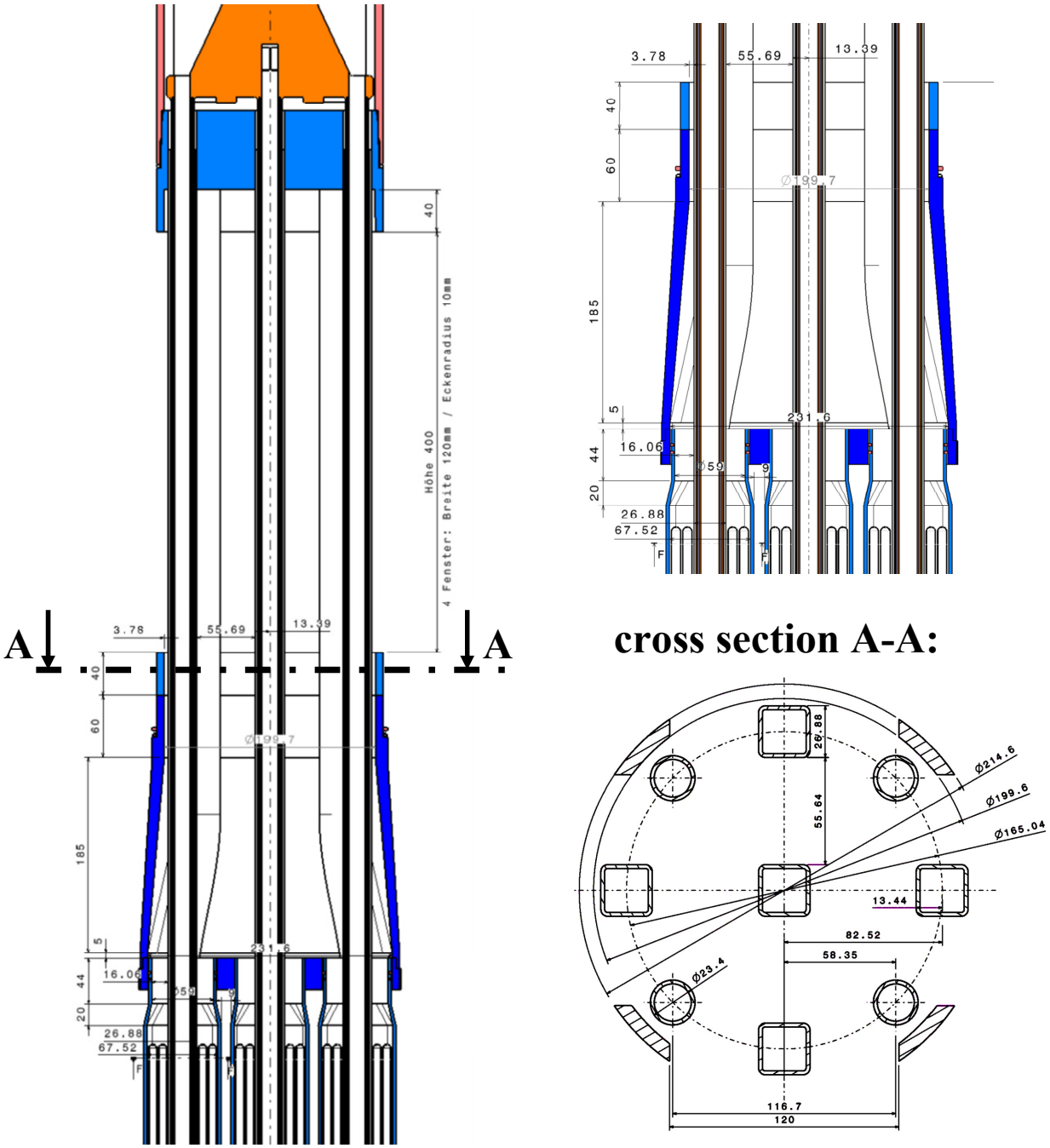

Fig. B-4 Dimensions of the headpiece geometry